

Radiation effects on airless bodies in space: radiolysis, sputtering, and sintering of regoliths

---

A Thesis

Presented to  
the faculty of the School of Engineering and Applied Science  
University of Virginia

---

In partial fulfillment  
of the requirements for the degree

Doctor of Philosophy

by

Micah J. Schalble

December

2016

APPROVAL SHEET

The thesis  
is submitted in partial fulfillment of the requirements  
for the degree of  
Doctor of Philosophy



---

AUTHOR

The thesis has been read and approved by the examining committee:

Robert E. Johnson

---

Advisor

Leonid V. Zhigilei

---

Pamela M. Norris

---

Eric Herbst

---

Alan D. Howard

---

Anne J. Verbiscer

---

Accepted for the School of Engineering and Applied Science:



Craig H. Benson, Dean, School of Engineering and Applied Science

December  
2016





# Abstract

Solar systems are interspersed with solids ranging in size from microscopic dust grains to moons. For Earth-like systems, rocks and minerals dominate the composition of inner solar system bodies, while surfaces in the outer solar system are predominantly ice covered. Small bodies, here meaning non-planetary bodies lacking appreciable atmospheres, are directly exposed to ambient radiation from numerous sources. Radiation of the solid state by ions, electrons and UV photons drives physical and chemical changes in the constituent materials, and understanding these effects is necessary to explain observations, guide spacecraft instrument design, and improve our understanding of the history of our solar system.

This thesis presents three case studies in radiation effects on airless bodies in space. First, laboratory experiments are used to estimate the formation rate of hydroxyl due to solar wind interactions with silicates on the surface of the Moon. Then, solar wind ion radiation and the subsequent ejection (sputtering) of surface species was studied by combining experimental measurements and Monte Carlo simulations of ion impact on lunar soil and meteorite compositions. Secondary ion fluxes produced by solar wind sputtering of small bodies are estimated, and it is shown that analysis of ejected ions can be used to determine composition and to classify small bodies according to the various known meteorite classes.

Incident plasma radiation can also modify the microstructure of a surface, and high energy ( $> MeV$ ) electron radiation-induced sintering of ice grains has been implicated in the formation of thermal anomalies on several Saturnian moons. Here, the basic theory for radiation-induced diffusion and grain sintering are presented, and the formation timescales for

anomalous features are estimated and compared with resurfacing rates due to grain impacts. Molecular dynamics (MD) simulations are used to obtain direct estimates for the number and average diffusion length of molecules mobilized by the incident electrons to further constrain the sintering model. Although the specific features considered are on the surfaces of the icy Saturnian moons, such processes occur throughout the outer Solar System and this work provides a template for quantifying radiation effects on other bodies within reach of human exploration.

*To Montana, you will always be home.*



# Acknowledgements

I first want to thank my family for always supporting me. There was a long time when I didn't know what I wanted to do, and you always encouraged me to keep trusting myself and to do the best at whatever task was in front of me. The distance hasn't been easy, but I have always felt you at my side. I want to say a special thank you to my brother John who has lived with me for several years in Charlottesville. You were a little piece of home and helped me feel a little less homesick. I want to say thank you to all of my co-workers at UVA, and especially to two of the best advisors a student could ask for: Prof. R. A. Baragiola and Prof. R. E. Johnson. You were two very different people, and I learned unique and valuable lessons from both of you. Thank you to Cathy, Adam, Ujwal, Caixia, Dabney, and Emma for all your help in the lab. I want to give a special thank you to Prof L. V. Zhigilei, and his students, as well as Justin and Hayley and others who have helped me learn how to be a competent programmer and computational scientist. All the remaining shortcomings are my fault alone.

I want to give my biggest thank you to UVA. I never could have expected such an experience as I have had here. The culture and promise of everyone, from the youngest students to the friendly custodian, you have made every minute of this experience enjoyable and I will never forget the wonderful time I have had. I want to especially thank Dean Norris, Prof Floro, and Prof Soffa who I have had the wonderful opportunity to work with closely. A special thanks is also due to Kim and Katherine for helping me out in a number of ways. You have all shown me a unique perspective of professionalism and academia that I hope to

emulate throughout the rest of my career.

Finally, thank you to Arnold. You're a pretty good boy.

# Contents

<b>Contents</b>	<b>ix</b>
List of Tables . . . . .	xiii
List of Figures . . . . .	xiv
<b>1 Introduction</b>	<b>1</b>
1.1 Space weathering by plasmas . . . . .	2
1.1.1 Case 1: Hydroxyl formation in lunar silicates . . . . .	6
1.1.2 Case 2: Solar wind sputtering and determination of small body composition using ion mass spectrometry (IMS) . . . . .	7
1.1.3 Case 3: Radiation-induced sintering and regolith thermal conductivity . . . . .	9
1.2 Thesis content and layout . . . . .	10
<b>2 Physical Processing Mechanisms</b>	<b>13</b>
2.1 Space Weathering Processes in Solids . . . . .	13
2.2 Photon Radiation . . . . .	14
2.2.1 Photostimulated desorption (PSD) . . . . .	14
2.2.2 Light penetration . . . . .	15
2.3 Ion sputtering of solids . . . . .	16
2.3.1 Ejected ion fluxes . . . . .	18
2.3.2 Sputtering of multicomponent materials . . . . .	19
2.3.3 Sputtering yield dependence on geometry . . . . .	21
2.4 High energy electron irradiation of ice . . . . .	22
2.4.1 Vacancy creation and ionization . . . . .	23
2.4.2 Penetration depth . . . . .	24
2.4.3 Estimation of excitation event length scale . . . . .	25
2.4.4 Surface desorption of molecules . . . . .	26
2.5 Thermal processing of volatile molecules . . . . .	27
2.6 Meteorite bombardment and surface age . . . . .	29
2.6.1 Crater size frequency distributions . . . . .	30
2.6.2 Regolith overturn rates . . . . .	32
<b>3 Case 1: Water on the Moon</b>	<b>35</b>
3.1 Introduction . . . . .	36
3.2 Background . . . . .	38
3.3 Experimental methods . . . . .	41

3.3.1	UHV simulation chamber . . . . .	41
3.3.2	Analysis techniques . . . . .	43
3.3.3	Sample and sample holder . . . . .	44
3.3.4	Data reduction . . . . .	45
3.4	Ion irradiation effects on lunar soil 15058 . . . . .	47
3.5	Discussion . . . . .	49
3.6	Conclusions . . . . .	50
<b>4</b>	<b>Case 2: Ion sputtering of airless surfaces</b>	<b>53</b>
4.1	Introduction . . . . .	54
4.1.1	Motivation . . . . .	56
4.1.2	Exosphere production around small bodies . . . . .	59
4.2	Sputtering yields: a brief review . . . . .	61
4.2.1	Experimental measurements for simple oxides . . . . .	62
4.2.2	Mineral sputtering yields . . . . .	64
4.2.3	Previous solar wind sputtering studies . . . . .	66
4.2.4	Secondary ion sputtering yields . . . . .	67
4.3	Monte Carlo simulations of solar wind bombardment . . . . .	69
4.3.1	Oxide sputtering yields . . . . .	70
4.3.2	Depletion of surficial oxygen . . . . .	72
4.3.3	Sputtering from regolith analog compositions . . . . .	74
4.4	Laboratory measurements of secondary ions from lunar soil . . . . .	77
4.4.1	Experimental system . . . . .	77
4.4.2	Measured secondary ion spectra . . . . .	78
4.4.3	Hydrogen bombardment chemistry . . . . .	80
4.4.4	Isotope fractionation . . . . .	82
4.4.5	Sputtered atom energies . . . . .	83
4.5	Modeling of secondary ion spectra . . . . .	85
4.5.1	Combining experimental and computational results . . . . .	87
4.5.2	Determination of small body classification . . . . .	88
4.6	IMS measurements around Phobos and Deimos . . . . .	90
4.6.1	Flux fall off with distance . . . . .	92
4.6.2	Calculations for NIMS-E . . . . .	94
4.6.3	Enhancement cell collection calculation . . . . .	96
4.7	Conclusions . . . . .	97
4.8	Future work . . . . .	98
<b>5</b>	<b>Case 3a: Thermal Conductivity of Regoliths</b>	<b>99</b>
5.1	Introduction . . . . .	100
5.1.1	Motivation: the PacMan thermal anomalies . . . . .	100
5.1.2	Regolith properties of the icy Saturnian moons . . . . .	103
5.2	Thermal conductivity in porous granular regoliths . . . . .	106
5.2.1	Radiative contribution to thermal conductivity . . . . .	106
5.2.2	Convective heat transfer . . . . .	107
5.2.3	Solid state thermal conductivity . . . . .	107

5.3	Thermal conductivity models applied to the icy moons . . . . .	110
5.3.1	Hertzian contact radius . . . . .	111
5.3.2	Grain size dependence . . . . .	112
5.3.3	Effective-medium thermal conductivity model . . . . .	114
5.3.4	Generalized regolith thermal conductivity model . . . . .	115
5.3.5	High parameter flexibility model: MaxRTCM . . . . .	116
5.3.6	Continuum modeling of cemented spherical grains . . . . .	117
5.4	Estimated grain contact sizes . . . . .	119
5.5	Conclusions . . . . .	122
<b>6</b>	<b>Case 3b: Radiation sintering of water ice regoliths</b>	<b>123</b>
6.1	Introduction . . . . .	124
6.1.1	Measured electron properties . . . . .	125
6.1.2	Basics of grain contact growth . . . . .	127
6.2	Preliminary surface modification timescales . . . . .	129
6.2.1	Ion compaction of water ice . . . . .	129
6.2.2	Regolith growth timescale . . . . .	131
6.3	Electron irradiation effects on icy regolith grains . . . . .	132
6.3.1	PENELOPE simulation software . . . . .	132
6.3.2	Electron energy profiles and excitation timescales . . . . .	134
6.3.3	Average heating per grain . . . . .	135
6.4	Radiation-induced sintering of spherical grains . . . . .	137
6.4.1	Sputtering and redeposition . . . . .	138
6.4.2	Diffusional sintering . . . . .	140
6.4.3	Spherical grain sintering timescales . . . . .	143
6.5	Void formation and enhanced UV scattering . . . . .	145
6.6	Summary . . . . .	146
6.7	Future work . . . . .	147
<b>7</b>	<b>Molecular Dynamics simulations of electron-induced excitations in water ice</b>	<b>149</b>
7.1	Introduction . . . . .	150
7.1.1	LAMMPS, Rivanna, and TIP4P-ICE . . . . .	150
7.1.2	Crystalline ice structures . . . . .	152
7.2	Simulation of electron excitations in water ice . . . . .	154
7.2.1	Excitations in bulk ices . . . . .	156
7.3	Conclusion . . . . .	159
<b>8</b>	<b>Conclusion</b>	<b>161</b>
<b>9</b>	<b>Appendices</b>	<b>165</b>
	Appendices . . . . .	165
A0.1	Meteorite gardening . . . . .	165
A	Meteorite impact production of secondary ions . . . . .	165
B	Cratering studies on the icy Saturnian satellites . . . . .	166

A0.2 Sintering at grain contacts: General processes . . . . .	169
A    Vapor phase sintering . . . . .	170
B    Solid state diffusion sintering mechanisms . . . . .	172
A0.3 Thermal spike estimates of the radiation-induced diffusion length-scale . . . . .	176
A0.4 Full listing of meteorite sample compositions . . . . .	177
<b>Bibliography</b>	<b>185</b>

# List of Tables

2.1	Electron penetration depths and energy deposited per unit length . . . . .	25
2.2	Thermal constants for water and carbon dioxide . . . . .	28
4.1	Published experimental sputtering yields for simple oxides . . . . .	63
4.2	Comparison of ion irradiation yields from minerals calculated by SRIM and SDTrimSP . . . . .	65
4.3	Published SRIM/TRIM sputtering yields for lunar soil compositions . . . . .	67
4.4	Published secondary ion sputtering yields for $SiO_2$ and extrapolated from lunar soil measurements . . . . .	68
4.5	Compositions measured by XPS and total yields determined from SDTrimSP for several lunar soil compositions . . . . .	75
4.6	Suite of meteorites compositions representative the various meteorite classes	76
4.7	Elemental $E_i^{SBE}$ , $E_i^{IE}$ and experimentally determined $R_i$ , $Y_i^+/Y_{Si}^+$ . . . . .	88
5.1	Thermal properties of the icy Saturnian moons . . . . .	104
5.2	Effective grain contact radii for the icy Saturnian moons . . . . .	121
6.1	Plasma measurements in the vicinity of the icy Saturnian moons . . . . .	126
6.2	First-order estimates of grain sintering and regolith overturn timescales . . .	130
6.3	Icy moon grain impactor fluxes . . . . .	132
6.4	Published values for thermal diffusion coefficients . . . . .	140
6.5	Electron-induced sintering timescales for the icy Saturnian moons . . . . .	145
A-1	Cumulative crater size distributions for the icy Saturnian moons . . . . .	167
A-2	Meteorite impact time scales . . . . .	168
A-3	Lunar compositions . . . . .	178
A-4	Mars compositions . . . . .	178
A-5	HED compositions . . . . .	179
A-6	Unique compositions . . . . .	179
A-7	Aubrite compositions . . . . .	180
A-8	Ureelite compositions . . . . .	180
A-9	Chondrite compositions . . . . .	181
A-10	Properties for various polymorphs, cubic, hexagonal, and low density amorphous (LDA), of water ice near versus temperature and calculated for 80K). Note R = gas constant = 8.134 J/mol/K. Temperature dependent equations use temperature in Kelvin (K). . . . .	183



# List of Figures

1.1	Weathering processes . . . . .	3
3.1	Water/hydroxyl absorption variations seen on the Moon . . . . .	37
3.2	Distinct 2.8 and 3 $\mu m$ absorptions on the Moon . . . . .	37
3.3	Experimental chamber used in the solar wind irradiation experiments . . . . .	42
3.4	Photo of LS15058 installed on sample holder . . . . .	45
3.5	FTIR spectra collected for LS15058 before and after ion irradiation . . . . .	48
3.6	Analysis of the 3 $\mu m$ region for $H^+$ irradiated LS15058 . . . . .	49
4.1	Color images of Phobos and Deimos . . . . .	57
4.2	Rendered illustration of the PADME spacecraft . . . . .	58
4.3	Comparison of computational and experimental total yields for simple oxides . . . . .	71
4.4	SDTrimSP sputtering yields vs. fluence determined for simple oxides . . . . .	73
4.5	SDTrimSP calculated surface compositions vs. fluence and depth . . . . .	74
4.6	Elemental sputtering yields for lunar soils and carbonaceous chondrites . . . . .	77
4.7	Experimental system used to collect secondary ion spectra for lunar soils . . . . .	78
4.8	Secondary ion spectra for solar wind ion bombardment of LS65901 . . . . .	80
4.9	Normalized secondary ion spectra for multiple experiments . . . . .	81
4.10	Comparison of elemental sputtered ion energy distributions . . . . .	83
4.11	Sputtered ion energy distributions determined by different methods . . . . .	84
4.12	Relative secondary ion yields for lunar soils . . . . .	86
4.13	Comparison of sputtered ion yields for various meteorite classes . . . . .	89
4.14	Ion ratio scatter plot for meteorite compositions . . . . .	90
5.1	The 'PacMan' anomalies . . . . .	102
5.2	Simple grain contact model for distinct grain and cementation phases . . . . .	110
5.3	Temperature dependent water ice parameters and Hertzian contact radius . . . . .	113
5.4	Continuum simulations showing heat flux for small grain contacts . . . . .	118
5.5	Bulk thermal conductivity derived from the continuum simulations . . . . .	119
6.1	PENELOPE interaction parameter with water ice . . . . .	133
6.2	Measured energy spectra and simulated energy deposition . . . . .	134
6.3	Radiation-induced grain temperature changes . . . . .	136
6.4	Primary diffusion paths leading to sintering of grains . . . . .	138
6.5	Radiation-induced diffusion coefficients and sintering rates . . . . .	144

7.1	Crystalline ice polymorphs used in the MD simulations . . . . .	153
7.2	Density for Ih and Ic ice during warming from 1 – 100 $K$ . . . . .	153
7.3	Radial distribution function and coordination number for Ih and Ic ice . . .	154
7.4	Visualizations $\sim 30$ $ps$ after a 10 $eV$ excitation in Ih ice . . . . .	156
7.5	Energies for Ih ice at 80 $K$ after 10 $eV$ excitation of a water molecule . . . .	157
7.6	Mean squared displacement for a typical 10 $eV$ excitation . . . . .	158
7.7	Average shell MSD as a function of distance from the IEM . . . . .	159

# Chapter 1

## Introduction

### Abstract

Space weathering is the cumulative effect of impacting asteroids and interplanetary dust particles (IDPs), micrometeorites, solar wind electrons and ions, ultraviolet photons, solar energetic particles, and cosmic rays on the physical properties of airless bodies in the space environment. This thesis presents several case studies in radiation-induced space weathering and compares theoretical, computational, and experimental results in a manner meant to provide context for the interpretation of the geologic history of small bodies in our solar system. By elucidating the paths through which surface materials interact and evolve under radiation conditions, the chemical and physical evolution of early solar systems and early history of Earth-like bodies can be better understood. Although the full scope of the effects produced by charged particles in the multitude of radiation environments in our solar system is beyond the scope of this work, the special cases considered here are (1) spectral changes and radiolysis induced in silicate bodies as a result of solar wind ion bombardment, (2) surface erosion and exosphere production by solar wind sputtering of silicate bodies, and (3) spectral and thermal conductivity changes produced by high energy electron sintering of water ice regoliths.

## 1.1 Space weathering by plasmas

Small bodies such as asteroids, planetesimals, and the majority of moons in the solar system lack a significant atmosphere, meaning that the ambient space environment interacts directly with surfaces composed of molecular ices, carbonaceous materials, and silicate minerals. By measuring the surface reflectance properties and sampling the composition of the collisionless atmosphere, called the *exosphere*, information about the composition and structure of small bodies can be obtained. Space weathering is the term commonly used to describe the physical effects of ambient plasma, photon radiation, and granular impacts with the solid phase surfaces of moons, asteroids and comets.

This thesis presents several case studies in radiation-induced space weathering and compares computational and experimental results in a manner meant to provide context for the interpretation of the geologic history of small bodies in our solar system. Changes in the surface are typically identified as differences in optical, thermal, and chemical properties between regions separated either spatially or compared to expected pristine materials. Furthermore, impacts by meteorites produce comminution - the breaking down of larger solids into successively smaller grains - and agglutination - the melting and subsequent bonding of adjacent particles. Impacts expose fresh surface, and intermix ices and minerals, ultimately creating a fine grained layer of loose material called the *regolith*.

As space weathering is a universal phenomenon, studying a few representative bodies in our Solar System can, in principal, yield general information about the formation and evolution of planetary systems containing life. However, each new mission yields surprising results, and the uniqueness of our solar system remains an open question. Using spacecraft and telescopic observations as guidance, experiments and theoretical modeling of the space environment can help predict specific surface properties and guide the design of next generation instruments. Furthermore, by elucidating the paths through which surface materials interact and evolve under radiation conditions we can better understand the history of our solar system and the

conditions leading up to the origin of life on Earth.

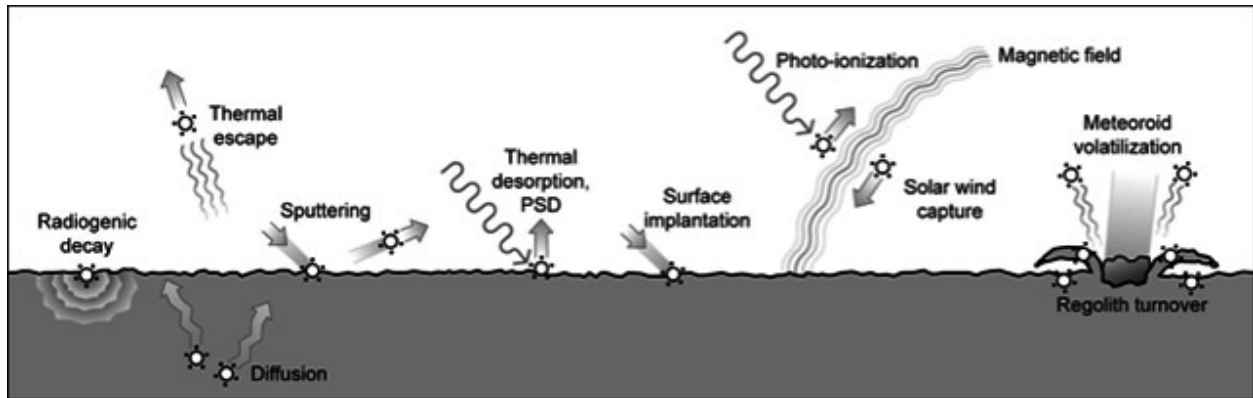


**Figure 1.1:** Numerous processes can occur in the upper surface of solid bodies in space, and depending on the composition and structure of the surface layer, processes may have very different efficiencies and effects, or may not occur at all. Common effects of incident radiation include amorphization of the surface, formation of new molecular species, and depletion/enrichment of various elements. These lead to changes in the bulk physical properties such as optical reflectance and thermal conductivity. Image credit: MESSENGER Mission

Early in the history of a solar system, the thick cloud of dust and gas surrounding the central star absorbs much of the radiation such that only material very near the central star or on the outer edges of the disk are exposed to radiation [Henning and Semenov, 2013]. As the material settles toward the disk midplane, ices of volatile species such as  $CO_2$ ,  $NH_3$  and  $H_2O$  condense onto the surfaces of silicate and carbonaceous grains, and the grains slowly grow into larger planetesimal sized objects. After larger planetary sized bodies have formed, materials near the central star may be exposed to heavy doses of solar radiation, while bodies further out receive a much smaller radiation dose. Plasma radiation of moons and dust grains can also occur in planetary magnetospheres where bombardment by ions and electrons may be inhomogeneous across a surface. Stellar and magnetospheric radiation ionizes molecules, breaks molecular bonds, ejects species from grain surfaces, and enhances diffusion rates. The effects of these processes in various radiation environments and on different surface compositions composes the topic of this thesis.

Space weathering is the cumulative effect of impacting asteroids and interplanetary dust particles (IDPs), circum-planetary grains, solar wind and magnetospheric plasma particles, ultraviolet photons, and cosmic rays on the physical properties of airless bodies in the space environment. Figure 1.1 shows a simple representation of the different space weathering

processes which can occur on airless surfaces. Radiation can ionize and excite surface atoms and molecules, break and rearrange chemical bonds, and induce molecular migration and diffusion. Radiolysis is the term often used to describe the molecular decomposition and bonding rearrangement induced by incident radiation. Depending on the age, location, size and history of the body, it may be exposed to very different radiation environments. For example, in addition to electromagnetic radiation (primarily UV photons), the sun emits a constant stream of energetic plasma called the solar wind with a flux of  $\sim 10^8 \text{ ion cm}^{-2} \text{ s}^{-1}$  at 1 *AU*.

Generations of telescopes and spacecraft have studied space weathering effects on small bodies in the solar system with sufficient detail to allow many optical and geologic phenomena to be explained. Changes in the optical features of the surface can be studied observationally [Clark et al., 2014] and in laboratory simulations [Bennett et al., 2013; Savin et al., 2012; Allodi et al., 2013]. For example, the solar wind has been shown to cause reddening of lunar-type silicates [Pieters et al., 1993; Hapke, 2001], and experiments using analog silicate materials suggest that solar wind  $H^+$  bombardment is sufficient to explain an observed *OH* absorption signal present at the lunar equator [Ichimura et al., 2012; Schaible and Baragiola, 2014]. Optical spectra of solar system bodies are typically determined through reflectance spectroscopy [Brown et al., 2004; Pieters et al., 2009, e.g.], although studying returned materials, meteorites, and analog samples in the laboratory [Pieters et al., 1993; Schaible and Baragiola, 2014] greatly aids interpretation. Additionally, computational methods can be used to simulate the weathering processes to explain various observed features [Hurley et al., 2012; Schaible et al., 2016], or more basic modeling can be carried out to predict what chemical and physical environments might be expected in early solar systems similar to our own [Hincelin et al., 2015; Drozdovskaya et al., 2016]. Simulations can be based on continuum descriptions of the micro-physical processes or directly simulate molecular level interactions [Arasa et al., 2010]. There is a need for laboratory work to provide detailed measurement of reaction rates relevant to different material environments and to constrain computational

models.

The case studies in space weathering considered here relate to surfaces composed of ices and silicate materials representative of the Moon, various asteroids, and the icy Saturnian moons. More complex bodies composed of dust/ice mixtures such as comets, and large moons with salts or carbonaceous species on the surface such as Europa, Titan and Triton are beyond the scope of this work. In Case 1 we consider solar wind  $H^+$  implantation into lunar regolith grains and the subsequent formation of silanol (SiOH) through radiolysis. This work was used to explain an observed absorption band at  $2.8 \mu m$  identified at the equator of the Moon [Pieters et al., 2009; Clark, 2009; Sunshine et al., 2009]. Although the bulk of the work presented in this section was completed as part of an M.S. thesis presented at UVA in Feb, 2014 [Schaible, 2014; Schaible and Baragiola, 2014], experimental data taken for  $5 - 15 keV H^+$  irradiation of lunar soil sample 15058 will be presented here for the first time. Case 2 presents a combined experimental computational analysis of solar wind sputtering of secondary ions from silicate dominated small bodies at  $1 - 3 AU$ . This work was originally motivated by an invitation to participate in a NASA Discovery Mission proposal for the Phobos And Deimos Mars Explorer (PADME), submitted in Feb 2015, and part of the work was used in the senior thesis of undergraduate astronomy student Adam Hutcherson. The primary work of this thesis is contained in Case 3, which provides a combined theoretical and computational description for electron induced sintering of water ice grains and shows that anti-corotational electrons in Saturn's magnetosphere are responsible for the so called PacMan thermal anomalies identified on the icy mid-sized moons Mimas, Tethys and Dione [Schaible et al., 2016]. Below we introduce each of the case studies presented in this thesis and discuss them in the context of their identification and accepted origin or, as in Case 2, their potential for new discovery.

### 1.1.1 Case 1: Hydroxyl formation in lunar silicates

Case 1 considers the surprising detection of a weak  $OH$  stretch vibration absorption at the lunar equator. During the four decades following the Apollo and Luna missions to the Moon, the lunar surface was considered to be anhydrous, with the exception of cold traps at the lunar poles that could potentially hold large deposits of water ice [Watson et al., 1961; Arnold, 1979]. While spectra obtained of the vapor plume produced by the crash of the LCROSS spacecraft into a permanently shadowed crater provided direct evidence for polar water [Colaprete et al., 2010], regions outside the poles, such as those sampled by the Apollo and Luna missions, were thought to be nearly completely anhydrous [Epstein and Taylor, 1974]. However, new results have challenged this conclusion as improved analysis of returned lunar samples suggests that the interior could hold hydroxyl or water at concentrations comparable to those in rocks formed on Earth [Saal et al., 2008; McCubbin et al., 2011; Liu et al., 2012], although evidence for a much (orders-of-magnitude) dryer Moon has been obtained from the isotopic abundance of chlorine in the regolith [Sharp et al., 2010].

Surficial  $OH/H_2O$  was identified on the lunar surface by remote infrared reflectance spectroscopy from three different instruments onboard the Chandrayaan-1, Cassini, and Deep Impact spacecraft [Pieters et al., 2009; Clark, 2009; Sunshine et al., 2009]. The reports of these observations show a  $2.8 \mu m$  absorption, attributed to bound  $OH$ , present at all latitudes but with an increasing absorption depth toward higher latitudes, and a  $3 \mu m$  absorption feature, attributed to molecular water, absent at the equator but increasing sharply above  $\sim 30^\circ$  latitude [McCord et al., 2011]. However, the spectra obtained from the various spacecraft differ slightly in the shape and depth of the absorption band and, in addition, are highly sensitive to the removal of the uncertain, location-specific, thermal emission background [Clark et al., 2011]. The relative absorption depth from the spacecraft measurements was measured to be 3 – 14%.

Since airless bodies like the Moon are constantly bombarded by energetic charged

protons from the solar wind, a suggested source of the observed absorptions is the reaction of implanted protons with oxygen in the regolith or deposited on the lunar surface as the Moon passes through Earth’s plasma tail. That  $OH$  bonds form by radiolysis induced during the implantation of oxides with energetic protons has been known for decades from experiments aimed at simulating the effects of the solar wind on the lunar surface and plasma interactions with materials inside prototype nuclear fusion devices. This thesis presents laboratory irradiation of Apollo lunar soil sample 15058 with  $5 - 15 \text{ keV } H^+$  is described and the effects on the IR spectra at  $\sim 2.8 \mu\text{m}$  are analyzed. The irradiated soils show clear spectral changes as a result of ion radiation. However, due to the opaqueness of the lunar soil and the weak transmitted IR signal through the sample, small changes in the  $2.8 \mu\text{m}$  absorption band expected due to combination of incident  $H^+$  ions with structural  $O$  [Schaible and Baragiola, 2014] could not be distinguished.

### **1.1.2 Case 2: Solar wind sputtering and determination of small body composition using ion mass spectrometry (IMS)**

Because the incident radiation and meteoroid impacts can drive ions and atoms from the regolith into the gas phase, it has often been suggested that information on surface composition can be obtained by collecting and analyzing the ambient gas in the vicinity of an otherwise airless body [Johnson and Baragiola, 1991; Elphic et al., 1991]. Therefore, in Case 2, the role of solar wind sputtering in creating a tenuous gas atmosphere, called an *exosphere*, around small silicate bodies is considered.

When an atom, ion or small particle impacts a surface, energy is transferred to the target material through momentum transfers and electronic interactions. The deposited energy spreads out from the point of interaction, locally heating the material and causing bond rearrangement, chemical reactions, and desorption of atoms and molecules from surfaces. The process of removing surface species through charged particle bombardment is known as *sputtering*. For silicate surfaces impacted by hydrogen ions at solar wind energies ( $\sim 1 \text{ keV}$ ),

the sputtering yield (ejected atoms per incident ion) is  $\sim 0.01$ . Sputtered atoms and molecules enter the exosphere, and if they are either ejected with (or subsequently gain) enough energy to exceed the escape velocity of the body, then they travel outward from the surface and are subjected to ambient fields. Ejected neutrals travel in large ballistic trajectories where they can eventually be ionized, and both ejected ions and ionized neutral ejecta can be swept up by the solar wind fields or, for a moon, by the fields of the parent planet. The ejected species which leave the surface in an ionized state are called secondary ions and make up  $\sim 1\%$  of ejected material on rocky bodies.

Detection and analysis of secondary ions in the laboratory provides a highly sensitive means of determining surface composition. The ejected ions can be directly analyzed using an IMS, thereby allowing detection of reactive metal ions and molecules which would otherwise stick to the instrument walls before they could be ionized and measured. It has long been suggested that secondary ions could be used to determine the composition of airless bodies in space [Johnson and Baragiola, 1991; Dukes and Baragiola, 2015; Johnson and Sittler, 1990], and recent spacecraft have shown promise by obtaining rough elemental analyses of both atmospheres [Waite et al., 2004; Fox, 2015] and surfaces [Mahaffy et al., 2014; Balsiger et al., 2007] using this technique. This work combines laboratory data and simulations to estimate the material ejection rates and the resulting neutral and ion fluxes as a function of altitude above a small body on which sputtering is occurring. The goal of this work is to demonstrate the discovery potential of an ion mass spectrometer (IMS) included on a spacecraft mission. It is shown that inclusion of an IMS on the proposed PADME mission to Mars' two rocky moons, Phobos and Deimos, would be able to determine the refractory composition and thereby constrain the origin of these bodies.

### 1.1.3 Case 3: Radiation-induced sintering and regolith thermal conductivity

A study of the exciting observation of anomalous features, often referred to as the PacMan thermal anomalies, on the icy Saturnian moons of Mimas, Tethys, and Dione comprises Case 3. The presence of an anomalous region on the surface of Tethys was first suggested during the Voyager-era when a dark equatorial band was observed in images [Buratti et al., 1990]. The Cassini spacecraft, a NASA flagship mission in orbit around Saturn since 2004, has allowed the moons to be imaged in much greater detail and at a variety of wavelengths. The moons are phase-locked to Saturn (like the Moon is to the Earth) so that the same side always faces in the forward moving direction. The anomalous features extend over the entire width of the leading hemisphere and  $\pm \sim 40^\circ$  and  $\pm \sim 20^\circ$  to the north and south at the center of the lens for Mimas and Tethys, respectively. The anomaly was first identified by the Cassini Imaging Science Subsystem (ISS) [Porco et al., 2004] as a region of low IR/UV color ratio ( $0.34 \mu m / 0.93 \mu m$ ) compared to the remainder of the leading hemisphere [Schenk et al., 2011]. Subsequently, Cassini InfraRed Spectrometer (CIRS) [Flasar et al., 2004] measurements of thermal emission in the mid-IR regime ( $9.1\text{-}16.7 \mu m$ ) showed that surface temperature variations during the day and night cycle were less in a lens shaped region. The boundaries of the thermal anomaly were surprisingly consistent with those identified in the color maps [Howett et al., 2011, 2012, 2014]. This anomalous behavior was interpreted as a greater thermal conductivity of the material in the anomalous region. The resulting CIRS images resembled the video game character PacMan when viewed from the Saturn-facing or anti-Saturn direction, and thus the anomaly became colloquially known as the 'PacMan Feature'.

The plasma electron energy distributions measured by the MIMI instrument on board Cassini [Krimigis et al., 2004] were used to calculate electron deposition profiles for high energy ( $\sim MeV$ ) electrons moving in the opposite direction of the icy moons. The resulting

energy contours matched the shape of the anomalous regions, thus suggesting an energetic source to form the anomalous features [Paranicas et al., 2012; Paranicas et al., 2014]. The physical mechanisms invoked to describe the electron effects in the regolith were radiation-induced diffusion and improvement in the quality of the contact, or *sintering*, between grains. Sintering occurs when material from the surface of a grain diffusionally migrates to the grain contact region where it remains, thereby improving the thermal contact between grains and providing a convenient explanation for the anomalous thermal conductivity. Furthermore, radiation induced-diffusion and accumulation of vacancies can create  $\sim nm$  sized scattering centers that can explain the enhanced UV reflectance of the anomalous regions. This thesis will provide a combined theoretical and computational consideration of electron radiation effects in water ice grains, and the temporal stability of the PacMan features will be shown to provide independent constraints on the regolith grain characteristics on the icy bodies.

## 1.2 Thesis content and layout

Before beginning the analysis of Case 1, I will briefly describe the physical processes involved with UV radiation, solar wind ion bombardment, energetic electron bombardment, thermal cycling and meteorite bombardment on the appearance and physical state of ice and silicate regoliths. For each of these processes, analytical means for calculating their effects will be presented and discussed in the context of the solar system bodies considered in this thesis. Then, in Chapter 3, solar wind hydrogen implantation into lunar soil and the formation of hydroxyl will be explored. The experimental system used to perform the experiments will be described and the results for hydrogen ion irradiation of an Apollo lunar soil sample will be discussed. The second case, using solar wind sputtered ions to determine the composition and classification of airless bodies, will be presented in Chapter 4. Experimental and computational estimates of sputtering from multi-component soils such as those found on airless solar system bodies will be used to derive estimates for solar wind sputtering rates of secondary ions from

small bodies and the required instrument sensitivities in order to make a distinction between primitive and evolved bodies. The final three sections will be used to present a complete picture of energetic electron induced sintering of water ice grains. In Chapter 5, the thermal properties of the icy Saturnian moons and relevant thermal conductivity models that can be used to determine the estimate the radius of contact between grains in the regolith will be reviewed. In Chapter 6, a model for electron induced sintering of ice grains will be developed, and standard equations used to describe thermal sintering of spherical grains will be coupled with estimates of radiation induced diffusion rates in crystalline water ice in order to calculate the growth rate of the contact radius between grains. Approximate sintering timescales, the time needed for the regolith thermal conductivity to increase from the minimum to the maximum measured values, are compared with rough estimates of the resurfacing rates due to meteorite bombardment of the moons in order to determine whether the observed anomalies should be stable on geologic timescales. In Chapter 7, preliminary Molecular Dynamics (MD) simulations of water molecule excitation in several water ice polymorphs will be presented and their utility for obtaining more accurate estimates of the radiation-induced diffusion rates will be discussed. Finally, in Chapter 8, the work presented in this thesis is summarized and future research directions are discussed.



# Chapter 2

## Physical Processing Mechanisms

### 2.1 Space Weathering Processes in Solids

In this section, I will introduce the primary drivers of space weathering on airless bodies in order to place the radiation processes that form the bulk of this thesis into the appropriate astrophysical context. Photon and plasma radiation, meteorite bombardment, and thermal processing are discussed in terms of their relevance either to small ( $\sim km$ ) sized silicate bodies or mid-sized, predominantly water ice moons such as Europa and Mimas which orbit in the magnetospheres around outer Solar System gas giants. A brief description of each of the processes is given, and their contribution to either surface modification or exosphere production is discussed. First, photo-desorption is briefly discussed, and it is determined to be important only for lightly bound metals (e.g. *Na* and *K*) or molecular solids ( $H_2O$ ,  $CO_2$ , etc.). Solar wind sputtering is introduced, and brief descriptions of ion transport processes through solids, sputtering of multi-component materials, and sputtering yield enhancements and decreases depending on surface morphology are given. High energy electron interactions with water are described and means of determining the vacancy formation and ionization rates in ice regoliths are presented. Finally, estimates of the thermal desorption of molecules in a regolith are given, and gardening processes caused by meteorite bombardment of airless

bodies are considered in order to place estimates on surface ages and material ejection rates.

## 2.2 Photon Radiation

The dominant radiation flux in the majority of space environments is photons from stars. It is the UV and X-ray photons that typically lead to photodesorption and chemical changes of interest here, particularly in the ices in the outer Solar System [Johnson and Quickenden, 1997; Loeffler and Baragiola, 2010; Westley et al., 1995]. The peak emission wavelengths from stars like the Sun, which is a G-type main-sequence star (G2V), are in the so-called visible light range, although up to  $\sim 10\%$  of the light is in the ultraviolet region of the spectra. Younger and hotter stars such as the O-, B- and A- type stars can emit much higher fluxes of UV radiation, while later K- and M- types stars emit predominantly in the infrared. Both solar and extrasolar photons can modify the uppermost surface of airless bodies; photons with energies  $> 5 - 10 \text{ eV}$  can penetrate up to  $\mu\text{m}$  into the regolith and are eventually absorbed through an interaction with the material causing excitations of the constituent atoms. The energy deposited in the surface can lead to heating, amorphization of the material, ejection of electrons, atoms, or molecules, diffusion along grain surfaces or through the bulk, rearrangement of molecular bonds, and the possible formation of new molecules.

### 2.2.1 Photostimulated desorption (PSD)

The absorption of a photon can give certain atoms and molecules such as  $\text{Na}$ ,  $\text{K}$  and possibly  $\text{H}_2\text{O}$  enough energy to desorb from the surface. Typically this is only an efficient process for species with a low surface binding energy. The flux of atoms or molecules of species  $i$  ejected by photostimulated desorption can be estimated by [Wurz and Lammer, 2003],

$$\phi_i^{PSD} = (1/4)\phi_{\text{photon}}Q_iC_in_0 \quad (2.1)$$

where  $Q_i$  represents the PSD cross-section of a given species,  $n_0$  is the number density of atoms or molecules in the regolith grains, and  $C_i$  is the atomic fraction of species  $i$  in the regolith. The flux of photons  $\phi_{photon}$  is found by integrating over a specified wavelength range and scaling to the subsolar distance of interest. The energy distribution of the desorbed species is often approximated by

$$f_{PSD}(E) = \eta(1 + \eta) \frac{EU^\eta}{(E + U)^{2+\eta}} \quad (2.2)$$

where  $E$  is the ejected particle energy,  $U$  is the characteristic energy or work function for PSD, and  $\eta$  is a shape parameter of the distribution.

The photodesorption cross-section of water has been calculated for the lunar surface and is likely the dominant mechanism for removal of surface adsorbed water molecules in the inner solar system [Mitchell et al., 2013]. However, photodesorption can be neglected for structurally bound  $OH$  such as that considered in Chapter 3 and for removal of refractory species such as the bulk of those considered in Chapter 4. This is because the surface binding energy for these species is larger than the UV photon energy. At the orbital distances of Saturn, UV light fluxes, although reduced by a factor of nearly 100 from those at 1  $A.U.$ , can still dominate plasma induced processes.

### 2.2.2 Light penetration

In addition to causing material changes and desorption of molecules in a regolith, the primary means of analyzing surfaces in space is through optical methods. Therefore, a large amount of data has been taken to determine the absorption structure and optical constants of surfaces similar to those found in space. The average penetration depth of incident light radiation can be estimated using the standard Beer-Lambert law and taking absorption coefficients typical of icy regoliths.

$$I(z) = I_0 e^{-z\alpha} = I_0 e^{-z/\delta} \quad (2.3)$$

where  $\alpha$  is the absorption coefficient and  $\delta$  is the penetration depth at which the incident wave decreases to  $\sim 37\%$  of its original intensity. However, this expression does not take into account the reduced density of a porous regolith or scattering from grain surfaces and voids. The Beer-Lambert law can be used to determine the column density of species formed by radiolysis such as those described in Chapter 3.

## 2.3 Ion sputtering of solids

In addition to photons, stars emit a constant stream of plasma called the solar wind which flows out from the solar corona. For a typical G2V solar type star, the ions of the solar wind consist mainly of hydrogen ( $\sim 95\%$ ) and helium ( $\sim 5\%$ ), with trace components of carbon, neon, argon and others. However, the composition and energy distribution of the solar wind can vary with stellar type and, for example, metal rich stars may have a much higher proportion of heavy ions. The ions and electrons of the solar wind impact a surface and penetrate the solid, subsequently losing energy through elastic (knock-on) and inelastic (electronic excitation) collisions leading to ionization, excitation, and nuclear displacement of the target material. Energy deposited by these processes causes radiation damage (amorphization, compaction, and void formation) in solid materials, and once the implanted and excited particles have lost sufficient energy to the medium they may participate in chemical reactions. Radiolysis is the term often used to describe the molecular decomposition and bonding rearrangement induced by incident radiation.

Charged particles in the vicinity of planets with strong magnetic fields can become trapped by the local, typically rotating, fields to form what is called a magnetospheric plasma. This plasma can come from the ionosphere of the planet and the solar wind. It can also be generated by material ejected from an airless surface, ring material that orbits in the magnetosphere, or by photoionization and pickup of ambient gaseous species. Such a plasma can flow onto surfaces of airless bodies causing changes similar to those produced by the solar

wind plasma. However, knowledge of the plasma composition and fluxes is needed in order to model the magnetospheric ion sputtering which vary depending on the planetary body of interest. Since the processes for solar wind and magnetospheric sputtering are similar, the focus in this thesis will be on solar wind energy ions in order to explain the general processes and estimate sputtering rates for airless bodies such as asteroids.

The primary effect of incident plasma ions considered here is the sputtering of surface materials. Sputtering occurs when the incident ion deposits energy near the surface of the target material, leading to the ejection of an atom or molecule, and is quantified by the *sputtering yield*. The sputtering yield is defined as the number of ejected target particles per incident ion and is usually assumed to be independent of the incident ion flux. In addition to the neutrals, some fraction of the ejected species leaves the surface in an ionized state, often referred to as *secondary ions*. Secondary ions are representative of the uppermost  $\sim 5 - 10$  monolayers of the surface from which species can be ejected and are routinely used in laboratory surface analysis.

Despite a long and rich history of sputtering studies and an interest in the results from the space science community, the bulk of the data and theoretical considerations has been obtained for sputtering of metals used in surface coatings and erosion of reactor walls. Experimental data for sputtering of oxides and minerals of relevance to planetary and asteroidal bodies with  $\sim keV H^+$  and  $He^+$  at solar wind energies is sparse. However, measurements of the ejected ion spectra due to solar wind ion bombardment have been carried out on a small number of returned lunar soils [Schaible, 2014; Dukes and Baragiola, 2015] and soil simulants [Elphic et al., 1991; Meyer et al., 2011]. These studies found that the sputtered ion composition for lunar soils can be correlated to the bulk composition using an ionization energy dependent relative yield. Furthermore, the total sputtering yields have been measured for several simple oxides [Roth et al., 1979], and these results are compared with computational studies discussed further in Chapter 4. The simulation parameters used to obtain a best fit to the simple oxide data were used to determine approximate sputtering yields

for a representative sample of silicate bodies found in the Solar System. Using the computed total yields together with the experimentally determined relative yields, the secondary ion yields around small silicate bodies such as the Moon and asteroids can be determined.

### 2.3.1 Ejected ion fluxes

Energy is transferred from the incident ion to the target through a series of primary (between the incident ion and target atoms) and secondary (between target atoms) collisions, and this series of energy transfer events is typically called a collision cascade. The collisions can transfer energy both through electronic excitations and through momentum transfer between nuclei, and the energy lost per unit length in the target, called the stopping power, is written

$$\left(\frac{dE}{dz}\right) = n_0(S_e + S_n) \quad (2.4)$$

where  $n_0$  is the number density of the target material and the quantities  $S_e$  and  $S_n$  are the electronic and nuclear stopping cross sections in  $eV \cdot cm^2$ , respectively. Although nuclear and electronic energy losses occur concomitantly, they are often treated as independent, additive processes.

The energy and spatial distributions of the ions ejected through sputtering can be described using the modified Sigmund-Thompson function [Thompson, 1968; Sarantos et al., 2012b]

$$f_{ej} = \frac{6E^{SBE}}{1 - 8\sqrt{E^{SBE}/E_{max}}} \frac{E_{ej}}{(E^{SBE} + E_{ej})^3} \left[1 - \sqrt{(E_{ej} + E^{SBE})/E_{max}}\right] \cos \theta_{ej} \quad (2.5)$$

where  $E_{ej}$  is the ejected energy,  $E^{SBE}$  is the surface binding energy,  $E_{max}$  is the maximum energy transferred during a collision between two particles minus  $E^{SBE}$ , and  $\theta_{ej}$  is the angle of the ejected species with respect to the local surface normal. This distribution is often used to calculate the exosphere density of sputtered species around bodies such as the Moon

[Sarantos et al., 2012b], and is compared with energy distributions derived from Monte Carlo simulations and ion irradiation experiments in Subsection 4.4.5.

For objects directly exposed to the solar wind, the total flux of species  $i$  leaving the surface,  $\Phi_i^{tot}$ , is a function of the incident solar wind flux,  $\Phi^{sw}$  and the sputtering yield of solar wind ions,  $Y_{sw \rightarrow i} = 95\%Y_{H \rightarrow i} + 5\%Y_{He \rightarrow i}$ , where  $Y_{H \rightarrow i}$  is the absolute yield for species  $i$  measured in sputtered atoms per incident ion for  $1 \text{ keV } H^+$  incident on a surface and likewise for  $4 \text{ keV } He^+$ . Although solar wind helium is doubly charged ( $He^{2+}$ ), the majority of experiments use single charged helium, so the small effects of the additional charge are ignored here. The sputtering yield is a function of the surface binding energy,  $E^{SBE}$ , the relative concentration of the species of interest,  $C_i$ , and a factor  $P(\phi)$  which accounts for effect of a granular regolith and depends on the regolith porosity,  $\phi$ . The sputtered secondary ion flux,  $\Phi_i^{ion}$  is found by multiplying the total species flux by the ionization fraction,  $\alpha_i$ , which is dependent on the elemental ionization potential of each species [Elphic et al., 1991; Schaible et al., in preparation].

$$Y^{tot} = \sum_i Y_i^{sw} \quad (2.6a)$$

$$\Phi_i = \Phi^{sw} Y_i^{sw} C_i P(\phi) \quad (2.6b)$$

$$\Phi_i^{ion} = \Phi_i \alpha_i \quad (2.6c)$$

### 2.3.2 Sputtering of multicomponent materials

When multi-component materials, e.g. oxides and minerals, are exposed to charged particle radiation, preferential ejection of a certain species can lead to an evolving surface composition in the uppermost several atomic layers ( $\sim nm$ ). For mixed, complex or alloyed materials, the sputtered composition become identical to the bulk composition only at high bombardment fluences, as required by conservation of matter [Betz and Wehner, 1983]. Momentum is transferred more efficiently between species of similar mass meaning that for solar wind bombardment the lighter elements are sputtered from the surface more efficiently. For

bombardment with light ions ( $H^+$ ,  $He^+$ ) at energies well above the displacement energy threshold, target atoms are predominantly sputtered by incident ions which have been backscattered from the interior. Furthermore, lower surface binding energies for species such as oxygen and sodium can lead to preferential ejection and depletion from the surface layers. Chemical bonding can also have an effect, although this can be difficult to quantify and depends strongly on the crystalline or amorphous structure of the material. In addition to preferential sputtering, transport processes such as thermal- or radiation-induced diffusion and segregation can occur, leading to a zone of altered composition larger than the implantation depth of the ions. However, at sufficiently low temperatures thermal diffusion can be neglected, the altered layer remains at a finite thickness, and steady-state conditions where the composition remains constant as a function of depth below the surface can be reached.

For surfaces of more complex silicates containing multiple refractory elements (i.e., *Ca*, *Mg*, *Fe*, etc.), preferential sputtering results in an enrichment in certain elements and depletion in others, and the total yield may change with fluence due to varying composition and cohesive energy of the surface. Surface compositional changes have been identified through X-ray photoelectron spectroscopy (XPS) measurements of sputter-induced surface compositional changes in minerals due to solar wind type ion irradiation. For example, the composition of San Carlos olivine in the uppermost several *nm* (the depth of sensitivity for the XPS technique) was seen to undergo a depletion in the atomic fraction of oxygen at the surface and the formation of elemental Fe [Pieters et al., 1993; Dukes et al., 1999; Loeffler et al., 2009; Dukes and Baragiola, 2015]. Specifically, metallic iron is enriched at the surface of Fe containing silicates bombarded with  $4\text{ keV } He^+$  ions and has been suggested to account for reddening of silicates such as the lunar soil [Hapke, 1965, 2001; Pieters et al., 1993]. Material can also leave the surface as molecular species as has been shown most dramatically in ice for which,  $H_2O$ ,  $O_2$  and  $H_2$  can be the dominant ejecta [Brown and Johnson, 1986]. Similarly,  $SiO$ ,  $Si_2$ ,  $SiO_2$ , and  $Si_2O$  are all sputter products from  $SiO_2$ , and similar molecules were seen in the ion spectra of lunar soils and simulants [Schaible, 2014; Dukes and Baragiola,

2015; Elphic et al., 1991].

In general, bonding in oxides seems to dominate over preferential sputtering due to mass effects (i.e., preferential enrichment of the heavier species). However, mass effects may dominate in the single knock-on regime (for light ions H+ and He+) due to more efficient energy transfer between the ion and oxygen. In the linear cascade regime, sputtering yield is roughly inversely proportional to the effective surface binding energy  $E^{SBE}$ . By choosing  $E^{SBE}$  based on the total ( $\Delta H^t$ ) and partial ( $\Delta H^p$ ) heats of atomization, the oxygen loss for a given oxide can be roughly approximated. Above  $\sim 200$  eV, the sputtering yields for light ion bombardment of oxides and nitrides are similar to or greater than those of the pure (elemental) refractory species [Roth et al., 1979]. The charge state of the emitted species depends strongly on the nature of the chemical bond and the elemental ionization potential, and sputtered ions represent a much larger fraction (orders of magnitude) of the sputtered flux for oxides than for metals. Additionally, molecular products can constitute up to 50% of sputtered products for oxides [Benninghoven, 1975; Benninghoven et al., 1979], and it was concluded that in this case the sputtering process is controlled by the partial molar enthalpies of vaporization for the various sputtered species.

### 2.3.3 Sputtering yield dependence on geometry

Because the molecular bonding environment is an important factor in determining the energy needed to remove an atom or molecule from the surface, the sputtering yield also depends on the local surface curvature [Urbassek et al., 2015; Wei et al., 2009]. Assuming that the collision cascade is symmetric and that the impact is perpendicular to the surface, the sputter yield of a curved surface,  $Y$ , can be related to the sputter yield of a flat surface,  $Y_{\text{inf}}$ , by

$$Y = Y_{\text{inf}}[1 + \lambda g_1(\theta)K_{11} + \lambda g_2(\theta)K_{22}] \quad (2.7)$$

where  $\lambda$  is the effective size of the excited region created by an ionization event,  $K_{11}$  and  $K_{22}$  are the principal surface curvatures measured along the axes perpendicular to the surface normal, and the sputter-yield correction functions  $g_1(\theta)$  and  $g_2(\theta)$  depend on the angle of incidence  $\theta$ . The correction functions are given by Urbassek et al. [2015] as a function of the longitudinal and lateral widths of the energy deposition profile, and for normal incidence  $g_1 = g_2 = 1/2$ . For a flat surface,  $K_{11} = K_{22} = 0$ , and for a sphere of radius  $R$ ,  $K_{11} = K_{22} = 1/R$ . By convention, raised curvatures (e.g. the outer surface of a sphere) are measured as positive curvature ( $R > 0$ ) while dips in the surface (e.g. the contact neck between grains) represent negative curvature ( $R < 0$ ).

In contrast to enhanced sputtering yields from curved or rough surfaces, Cassidy and Johnson [2005] found that the net sputtering yield from a granular regolith should be reduced from that expected from a flat surface. This is due to the distribution of ejection angles from the randomly oriented grain surfaces and subsequent shadowing by nearby grains. They noted that shadowing effects could be especially important for  $keV$  bombardment of silicates where the incident ions can be heavily forward scattered.

## 2.4 High energy electron irradiation of ice

For electrons and high-energy ( $> keV$ ) ions incident on water ice, the dominant energy loss mechanism is through ionization of the water molecules, which in a solid is referred to as electron-hole pair production. Following an ionization, recombination and dissociation occur and energy spreads from the site of the initial interaction, driving molecular motion. However, the energy released directly into molecular motion is only a fraction of the initially deposited energy and the remainder is lost through vibrational excitations, conduction, and small momentum transfers.

### 2.4.1 Vacancy creation and ionization

When the kinetic or repulsive energy,  $\Delta E$ , transferred to a molecule by the incident radiation is greater than the cohesive energy of the solid,  $U$ , a molecule breaks free from its position in the lattice and becomes mobilized. Mobilized molecules subsequently lose energy in a cascade of molecule-molecule collisions, here called a mini-cascade, until they return to thermal equilibrium with the solid, typically in  $< 10 ps$ . In a uniform molecular material such as water ice, the total number of secondary recoils with an energy between  $E$  and  $E + dE$  produced by an excited molecule of initial energy  $\Delta E$  can be approximated from transport equations using

$$dN \sim \beta \frac{\Delta E}{E^2} dE \quad (2.8)$$

where  $\beta$  is a constant given as  $\sim 6/\pi^2$  in Sigmund [1969a] and 0.8 in Myers [1980]. These results are roughly consistent with Molecular Dynamics (MD) simulations and have been used to describe electronic sputtering of ices and silicates [Johnson and Liu, 1996; Bringa and Johnson, 2004]. As the electrons penetrate the ice regolith, they interact with the water molecules and energy is deposited through elastic and inelastic collisions as well as ionization of the constituent atoms, thus creating vacancy/interstitial pairs which can disrupt the crystal structure and molecular bonding arrangements.

A full treatment of the rate of vacancy formation as a function of depth into the regolith,  $R_{disp}(z)$ , depends on the incident particle flux,  $\Phi$ , the energy transferred per interaction,  $\Delta E$ , the depth-dependent electron energy,  $E(z)$ , and the cross-section for interaction between the incident particle and a lattice atom/molecule,  $\sigma_{int}$ . For instance, when a fast electron penetrates a solid, a track of excitations results resembling a column of 'hot' atoms and molecules, and additional secondary collisions continue until the energies drop below the threshold displacement energy,  $E_{disp}$ . This is the minimum energy for an atom or molecule to be displaced from a lattice site. Based on Equation 2.8, a simplified solution to transport equations shows that the average number of molecules,  $N$ , which overcome a given activation

energy,  $E_a$ , due to energy released during the cascade is roughly

$$N \sim \frac{\beta \Delta E}{E_a} \quad (2.9)$$

which is consistent with the well-known Kinchin-Pease estimate of defect (vacancy / interstitial pair) production in the bulk

$$N_{KP} = \frac{\beta \Delta E}{2U}$$

where  $\Delta E$  is the energy deposited into molecular motion following an ionization event and  $U$  is the material cohesive energy. Understanding the vacancy formation rate in solids is important in determining the rate of nano-scale void formation and subsequently altered scattering behavior measured by UV through NIR reflectance. Although the above is true for both ions and electrons, the only section where radiation-induced vacancies and diffusion of molecules are discussed is in Chapter 6 where electrons are the only incident particles. Therefore, the following will focus solely on electrons.

## 2.4.2 Penetration depth

As electrons enter the ice grains, energy is lost through momentum transfer and electronic excitations. The ESTAR (Electron STopping And Range) database [Berger et al., 2005] gives total path-length traveled by the electron,  $d_{CSDA}$ , determined using the Continuous Slowing Down Approximation (CSDA) which integrates the stopping power ( $dE/dz$ ) from  $E_{inc}$  to zero. Values for 0.5 – 10 MeV electrons are given in Table 2.1. However, due to electron-nucleus and electron-electron scattering, the CSDA approximation gives an upper bound to the projected depth of penetration (depth below the surface at which the electron comes to rest). A more reliable means of calculating vacancy and ionization effects in solids is to use Monte Carlo computational techniques. It is well known that programs such as SRIM/TRIM and Geant-4 give good agreement with experimental data for a large variety of material compositions and incident particle energies [Ziegler et al., 2008; F. Salvat and

Sempau, 2011]. As described in Chapter 6 the program PENELOPE was used to simulate the penetration of  $\sim MeV$  electrons into water ice regoliths.

**Table 2.1:** Penetration depths calculated by PENELOPE (Chapter 6) and CSDA path lengths. The average energy deposited per unit depth into the regolith,  $\langle D_{dep} \rangle$ , was calculated by dividing the incident energy by the implantation depth, and the average energy lost per unit length traveled through the solid,  $\langle D_{len} \rangle$ , can be roughly estimated by dividing the initial energy by the CSDA range.

$E_{Inc}$	PENELOPE		ESTAR	
	$d_{pen}(\text{cm})$	$\langle D_{dep} \rangle(\text{MeV/cm})$	$d_{CSDA}(\text{cm})$	$\langle D_{len} \rangle(\text{MeV/cm})$
10 MeV	10.16	0.90	10.65	0.939
5.0 MeV	5.35	0.93	5.460	0.916
2.5 MeV	2.64	0.95	2.670	0.936
1.0 MeV	0.92	1.08	0.935	1.070
0.75 MeV	0.64	1.17	0.651	1.152
0.5 MeV	0.37	1.35	0.378	1.323

The average number of vacancies or ionizations created per grain per incident electron can be approximated by determining the energy deposited per grain, found by multiplying the energy deposited per unit length,  $\langle D_{len} \rangle$ , by the average distance traversed by an electron through a grain,  $d_g = 4/3r_g$ , and then dividing by the activation energy,  $E_a$ , for vacancy or ionization

$$N_{vac/grain/electron}(z) = \frac{D_{dep}(z) \times d_g}{E_a}. \quad (2.10)$$

The average distance traversed by an electron can be given also in terms of the number of ice grains penetrated. Assuming an average grain size  $r_g = 25 \mu m$ , the number of water ice grains traversed by the impinging electrons is  $\sim 100 - 3000$  for  $0.5 - 10 MeV$  electrons.

### 2.4.3 Estimation of excitation event length scale

Johnson and Liu (1996) give an approximate analytic expression for the average number of recoils produced by an energy release,  $\Delta E$ , in a condensed gas solid. Assuming that a collision occurs in every layer following the energy release, the extent of the cascade can be estimated by multiplying the mean number of sufficiently energetic collisions by the average atomic layer thickness  $\ell_0$  for recoil energies greater than the material cohesive energy. The

weighted average distance from an energy release event,  $\lambda$ , was estimated to be,

$$\lambda \approx \frac{l}{4} \left[ \frac{\eta E_i}{2U} - \frac{\eta}{\kappa} + 1 \right] \quad (2.11)$$

where  $\eta$  is the number of particles involved in a collision ( $\eta = 2$  in the binary collision approximation),  $\kappa$  is the fraction of energy transferred in the collision ( $\kappa = 1$ ). To rough approximation, this equation can be written as

$$\lambda \approx \frac{\ell_0}{4} N \quad (2.12)$$

where  $\ell_0 \sim 0.3 \text{ nm}$  is the approximate lattice spacing for water ice. It is important to note that the cohesive energy of water ice is lower at the surface than in the bulk so that vacancies form more readily in the near surface region leading to a higher vacancy concentration. Watkins et al. [2011] found vacancy formation energies of  $\sim 0.2 - 0.5 \text{ eV}$  per molecule in the uppermost complete monolayer. These decreased further as additional vacancies were added to the surface with vacancy formation energies as low as  $\sim 0.1 \text{ eV}$  found for some vacancy complexes. This is compared to a cohesive energy of  $\sim 0.75 \text{ eV}$  for bulk crystalline water [Watkins et al., 2011]. In order to diffuse into a nearby site, a molecule must overcome both the vacancy formation and vacancy migration energies, and a range of activation energies for bulk and surface diffusion of pure water ice are given in Table 6.4.

#### 2.4.4 Surface desorption of molecules

In addition to producing excitations in the bulk of the ice grains, if sufficient energy is deposited near the grain/pore boundary, molecules can be desorbed from the surface. The electronic structure of ice at the interface of large porous cavities in amorphous ice may resemble that of the free surface interface, and therefore it might be expected that diffusion and desorption processes would occur there with increased efficiency. The total yields due to electron ionization of molecules near grain surfaces are generally much higher from amorphous

ice than from crystalline. The increased yields have been attributed to increased defect density and an increase in excitation localization due to disruption of long range order in the matrix [Sieger and Orlando, 2000].

## 2.5 Thermal processing of volatile molecules

Surface temperature can drive the release of volatiles into the vacuum above the surface of an airless body. For volatile rich bodies such as those in the outer asteroid belt and for the Galilean moons, surface temperatures can reach  $> 100 K$ , in which case sublimation can be the primary source of gas species to the exospheres surrounding the bodies. Alternatively, for silicate rich bodies or for icy bodies far from the Sun where temperatures remain well below the sublimation temperature of water ice, sputtering or meteorite bombardment can dominate the exosphere production processes. However, for bodies such as Pluto which contain abundant volatile species with sublimation temperatures much lower than water ice, or for surfaces containing a mixture of volatile and refractory species, transport and migration of molecules can occur. This has been seen for cold traps on the lunar poles containing significant water [Colaprete et al., 2010], and additional examples of transport can be found for hydrocarbons on Titan [Mitri et al., 2007] and volatiles on Pluto [Stern et al., 2015]. Additionally, molecules formed by radiolysis due to incident radiation such as  $H_2$  and  $O_2$  found on icy surfaces in the outer Solar System are more prone to thermal diffusion than their parent molecules.

The equilibrium vapor pressure can be estimated via the Clausius-Clapyron equation

$$P_v(T) = a_1 \exp(-a_2/T), \quad (2.13)$$

for which several experimentally determined coefficients are given in Table 2.2. The equilibrium vapor pressure  $P'_v$  of a curved surface, such as a spherical grain in a regolith, differs from that

**Table 2.2:** In order to calculate the thermal desorption rates for volatile gases, experimental measurements are used to determine the coefficients used in the Clausius-Clapyron equation.

Reference	$a_1[\times 10^{12} Pa]$	$a_2[K]$
	$H_2O$	
Fanale and Salvail (1984)	3.56	6141.667
Mauersberger and Krankowski (2003): $T > 169K$	$3.44 \pm 0.09$	$6132.8 \pm 1.8$
Mauersberger and Krankowski (2003): $T < 169K$	$758.58 \pm 313$	$7044 \pm 60$
Gundlach et al (2011): $T > 164K$	$3.23 \pm 0.73$	$6134.6 \pm 17$
	$CO_2$	
Fanale and Salvail (1987)	0.123	3167.8

of a flat surface, and these can be related using the Gibbs-Thompson formula [Mullins, 1957]

$$\ln \left( \frac{P'_v}{P_v} \right) = K \frac{\gamma_s}{n_0 k T} \quad (2.14)$$

where  $K$  is the sum of the two principle surface curvatures,  $\gamma_s$  is the surface energy, and  $n_0$  number density. Noting that the right hand side of the equation is typically small, this equation can be expanded giving

$$P'_v = P_v \left( 1 + K \frac{\gamma_s}{n_0 k T} \right) \quad (2.15)$$

and it can be seen that the equilibrium vapor pressure depends on the local surface curvature and will be large where curvatures are small and positive, similar to the sputtering dependence on curvature described in Subsection 2.3.3. The condensation rate of molecules onto a point on the grain surface is determined by integrating

$$\phi_{con} = \frac{1}{\pi} \int_{gra} \phi_{sub}(\Omega) \cos \theta d\Omega + \frac{\phi_{gas}}{\pi} \int_{gas} \cos \theta d\Omega \quad (2.16)$$

over the whole grain surface where  $\phi_{sub}(\Omega)$  is the sublimation rate from the surface located in the direction  $\Omega$  viewed from the surface onto which the molecule condenses,  $\cos \theta$  is the angle between the incident molecule and the surface normal, and  $\phi_{gas}$  is the condensation

rate due to a background gas pressure of  $P_{gas}$ . The contribution from the first integral is due to desorption from neighboring grains with a straight line-of-sight path to the condensation point, and the second integral is due to the background gas and is negligible for low pore pressures. The velocity distribution of desorbed molecules can be estimated using

$$f(E_{ej}, \theta) = 4\cos\theta \left[ \frac{E_{ej}}{(k_b T)^2} \right] e^{-\frac{E_{ej}}{2\pi k_b T}} \quad (2.17)$$

where  $E_{ej}$  is the ejected energy and  $\theta$  is the angle with respect to the surface normal.

Assuming pure ice surface and using the gas emission rate where dominance between sublimation and solar wind sputtering is estimated to transition, it can be shown that  $\phi_{H_2O}(4.0AU) \approx 2 \times 10^7$  molec/( $cm^2s$ ) and  $\phi_{CO_2}(14.6 AU) \approx 1 \times 10^7$  molec/( $cm^2s$ ) [Johnson, 1990]. Similar to sputtering, outgassing rates of a specific species depend on the fractional abundance in the uppermost several atomic monolayers of the surface material. Additionally, implanted solar wind is expected to outgas from the bodies at roughly their implantation rate, depending on surface maturity or solar wind exposure times. Taking a 10 – 15% reduction in SW fluxes to account for ions backscattered from the surface, trapped in crystal defects in the solid, or chemically reacted with surface atoms, and further assuming the gasses are thermalized and  $H$  reacts to form  $H_2$  before escaping, these escape rates of  $H_2$  and  $He$  are  $\sim 10^8$  and  $\sim 10^7$  at 1  $A.U.$ , respectively. More sophisticated treatments of outgassing of airless bodies account for the variable surface temperature [Schläppi et al., 2008] and reductions in outgassing rates from ice as a function of an overlying dust layer [Gundlach and Blum, 2012].

## 2.6 Meteorite bombardment and surface age

Meteorite impacts on the surfaces of asteroids, comets and moons can eject and scatter materials, and the persistent comminution or breaking up of larger rocks and boulders by the impactors creates a fine grained regolith on rocky silicate bodies. However, the effects are more uncertain for icy bodies due to lack of observational evidence or laboratory

studies and can depend sensitively on temperature [Parmentier and Head, 1981]. Each grain impact with the surface excavates some small volume while burying surrounding regions, and this process is commonly referred to as meteorite gardening. Due to the stochastic nature of the bombardment, some regions will be progressively buried while others are freshly exposed and the regolith will be vertically mixed. It is shown below that, using measured impactor fluxes and size distributions, the surface age at a given depth can be estimated. In addition to gardening, meteorite impacts can also eject material into the exosphere which can subsequently be detected by spacecraft.

Crater counting is a 'top down' technique that is often used to estimate the ages of surfaces. However, the spatial resolution of the imaging for airless bodies other than the Moon often limit the estimates to  $\sim km$  sized features, and extrapolation of the crater size distributions is likely inaccurate in the  $cm$  size scales of interest for radiation processing. A brief discussion of crater counting methods is given below and derived surface ages for the Saturnian moons is given in Subsection B. Additionally, a 'bottom up' approach to estimating surface ages at  $\sim cm$  depth scales and regolith overturn rates due to IDP grains is presented and used in Chapter 6 to estimate surface ages at depths relevant to incident plasma induced changes.

### 2.6.1 Crater size frequency distributions

The resurfacing rates are ultimately determined by the number of impactors onto the surface and the impact energy distributions. High resolution ( $\sim 100 m$  per pixel) mapping over the entire body can be used to count the number of craters of a given size and scaling laws can be used to derive an approximate regolith depth. Assuming the surfaces of the satellites are in approximate equilibrium and using measured impactor size and frequency distributions, the surface age of a body can be estimated [Melosh, 2011]. In general, the cumulative crater

distribution, given as the number of craters with diameter  $> D$ , follows the form

$$N_{cum}( > D) = cD^{-b} \quad (2.18)$$

where  $c$  is a constant and  $b$  should be related to the impactor size distribution. If it can be assumed that  $b$  is constant over some interval, then the incremental number density between craters of size  $D$  and  $\sqrt{2}D$  is  $N(D, \sqrt{2}D) = c(1 - 2^{-b/2})D^{-b}$ , from which the relative crater population over the interval can be defined

$$R(D) = \frac{2^{3/4}}{\sqrt{2} - 1} D^2 \left[ N_{cum}(D) - N_{cum}(\sqrt{2}D) \right] \quad (2.19)$$

where, up to a factor of 3.65,  $R(D)$  is equal to the fraction  $f_c(D)$  of the total area covered by craters in the diameter interval  $D$  to  $\sqrt{2}D \Rightarrow R(D) = 3.65f_c(D)$  [Melosh, 2011].

Typical treatments of regolith growth are based on the evolution of crater populations with size distributions described by  $b \geq 2$ , and these models do reasonably well in predicting the regolith thickness for bodies such as the Moon. For a  $b > 2$  type distribution, the crater population is in equilibrium for all diameters less than some maximum crater diameter  $D_e$  which increases as  $(\text{time})^{1/(b-2)}$ . Then, the maximum thickness of a regolith layer at equilibrium is taken to be  $h_{eq} = D_{eq}/4$  where the equilibrium crater diameter  $D_{eq}$  can be determined by equating the cumulative number of craters in the production population given by Equation 2.18 to the number of craters in the equilibrium population,  $N_{ceq} = c_{eq}D_{eq}^{-2}$ , such that

$$D_{eq} = \left( \frac{c}{c_{eq}} \right)^{1/(b-2)}. \quad (2.20)$$

The differential size frequency distribution is given by

$$dN(\geq D)/dD = c'D^b \quad (2.21)$$

where  $c'$  is a constant and  $b'$  is the differential slope. The cumulative crater distribution slopes for the icy Saturnian satellites are given in Table A-1 [Kirchoff and Schenk, 2010, 2015].

A minimum regolith thickness can be used to compute regolith growth rates and depends on the fraction,  $f_c$ , of the total area covered by craters with a diameter between  $D$  and  $D_{eq}$  which is given by

$$f_c(D, D_{eq}) = -\frac{\pi}{4} \int_D^{D_{eq}} D^2 \frac{dN_{cum}}{dD} dD. \quad (2.22)$$

Substituting Eq. 2.20 and letting the overturn timescale  $\tau_{ovr} = t_{surf}/f_c$ , the rate at which the regolith will be renewed at a depth  $h$  below the surface is

$$\tau_{ovr} = t_{surf} \frac{4(b-2)}{\pi b c_{eq}} \left[ \left( \frac{h_{eq}}{h} \right)^{(b-2)} - 1 \right]^{-1} \quad (2.23)$$

where  $h_{eq}$  is the equilibrium regolith depth. The typical regolith depths produced by  $\sim \mu m$  sized particle bombardment are on the order of meters.

## 2.6.2 Regolith overturn rates

One means of estimating the surface overturn timescale is to use the influx of material onto the surface of a satellite to determine the depth of regolith affected as a function of time [Cooper et al., 2001]. The amount of material ejected from the surface depends fundamentally on the incident projectile flux and also on the distance from the planet due to gravitational focusing. The gravitational focusing factor increases the overall magnitude of the impacting flux as a function of distance  $r$  from the planet as [Spahn et al., 2006a].

$$f_g(r) = \frac{1}{2} \sqrt{V(r)} \left[ \sqrt{V(r)} + \sqrt{V(r) - \frac{R_p^2}{r^2} V(r)} \right] \quad (2.24)$$

where  $V(r) = 1 + [v_{esc}(r)/v_\infty]^2$  and  $R_p$  is the radius of the planet,  $v_{esc}(r)$  is the escape velocity from the planetary system and  $v_\infty \sim 14 \text{ km/s}$  is the typical interplanetary grain velocity far from the planetary body [Poppe, 2016]. Then, the ejected flux due to impacting

interplanetary dust particles is [Cuzzi and Estrada, 1998]

$$\dot{\sigma}_{ej}(r) = f_g(r)\dot{\sigma}_\infty Y_0 \quad (2.25)$$

where  $\dot{\sigma}_\infty$  is the interplanetary meteorite flux and an average ejecta yield at  $v_\infty$  is  $Y_0$ . The growth of the regolith is then driven by the mass flux onto the surface and the rate of growth is given by

$$g_0 = \frac{\dot{\sigma}_{ej}}{\rho_{reg}} \quad (2.26)$$

where  $\rho_{reg}$  is the density of the upper regolith. The depth of the regolith,  $h(t)$ , grows with time and can be written

$$h(t) = g_0 t (1 + t/t_0)^{(-0.55)} \quad (2.27)$$

where  $h$  is in  $\mu m$  and the mixing timescale  $t_0 \sim 1.7 \times 10^5$  years was given for Jupiter [Cooper et al., 2001].



# Chapter 3

## Case 1: Water on the Moon

### Abstract

In 2009, an unambiguous OH absorption band was seen across the entire surface of the Moon [Pieters et al., 2009; Clark, 2009; Sunshine et al., 2009]. The work presented here experimentally tested the role of solar wind hydrogen in the formation of an *OH* band in Apollo soil 15058. Experiments were performed in ultrahigh vacuum (UHV) and used a mass analyzed ion beam to eliminate contamination from spurious oxygen, water or other OH sources. Analysis was performed using a Fourier transform infrared (FTIR) spectrometer in transmission. Although some spectral changes were measured as a function of ion fluence, the sensitivity of the analysis was insufficient to detect changes in the OH band of the lunar soil.

### 3.1 Introduction

The lunar surface provides an ideal system for study of space weathering effects given its proximity to Earth and our ability to obtain a detailed knowledge of its composition and evolution through study of returned soil samples. The effects of solar wind bombardment on the physical and chemical make-up of the lunar surface have been studied for decades, but several fundamental questions remain unresolved. In particular, the issue of lunar water was revived in 2009 when data from three separate spacecraft making observations of the moon revealed an absorption feature in the infrared (IR) at  $\sim 3 \mu m$  [Pieters et al., 2009; Clark, 2009; Sunshine et al., 2009]. As shown in Figure 3.1a, the feature strength seen by the M3 instrument [Pieters et al., 2007] on board Chandrayaan-1 increased toward higher latitudes and was attributed to the *OH* stretch absorption due to hydroxyl or molecular water on the surface of soil grains in the top  $\sim 3 mm$  of the lunar regolith [Pieters et al., 2009]. Neither comet and asteroid impactors nor interior degassing were able to explain the variations in signal strength with composition [McCord et al., 2011] and time of day (Figure 3.1b) [Sunshine et al., 2009]. Therefore, the combination of solar wind hydrogen with oxygen from the lunar soil was hypothesized to explain the signal.

McCord et al. [2011] distinguished distinct absorptions at  $3 \mu m$  and  $2.8 \mu m$  as shown in Figure 3.2. The  $3 \mu m$  absorption, attributed to  $H_2O$ , was present only at higher latitudes while the  $2.8 \mu m$  absorption, attributed to structurally bonded  $-OH$ , although less intense, was present even at the equator. Complicating the interpretation of the signal were the effects of surface geometry and thermal emission corrections [Besse et al., 2013; Clark et al., 2011]. Thermal emission from the lunar surface becomes significant above  $3 \mu m$ , thus complicating the background fitting and band depth determinations. Furthermore, uneven heating of surfaces due to surface morphology at  $\sim m$  size scales can lead to uncertainty in the thermal background.

Previous work to understand the role of solar wind in the formation of water and

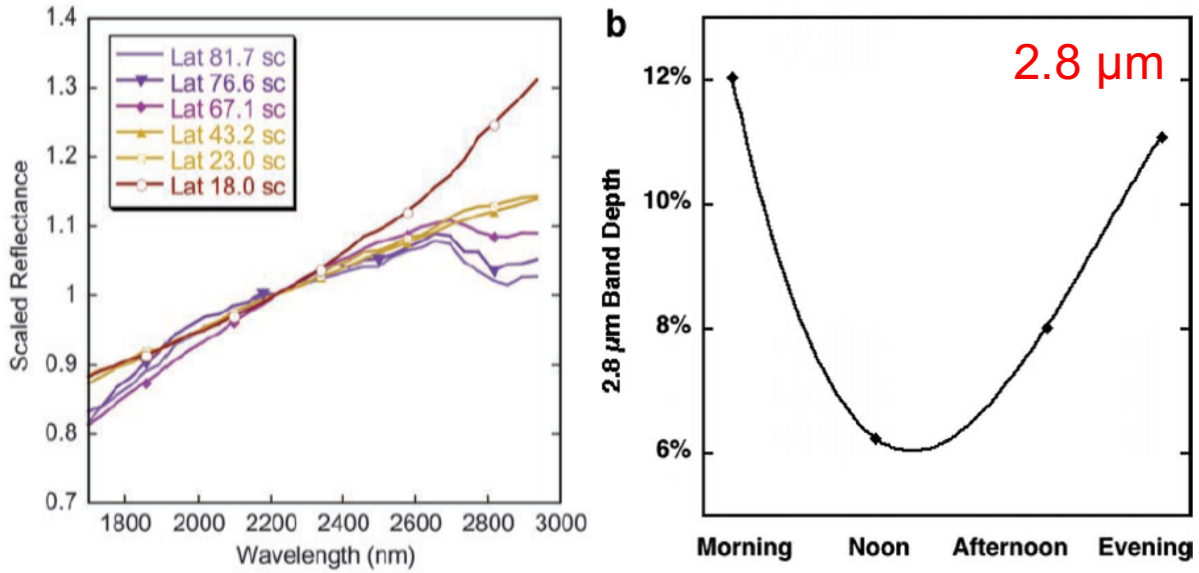


**Figure 3.1:** (Left) Absorption created by the  $OH$  stretch vibration as a function of latitude on the Moon seen by the M3 instrument on board the Chandrayaan-1 spacecraft. Image from Pieters et al. [2009]. (Right) Variation in the absorption strength as a function of lunar time-of-day seen by the Deep Impact spacecraft. Image from Sunshine et al. [2009].

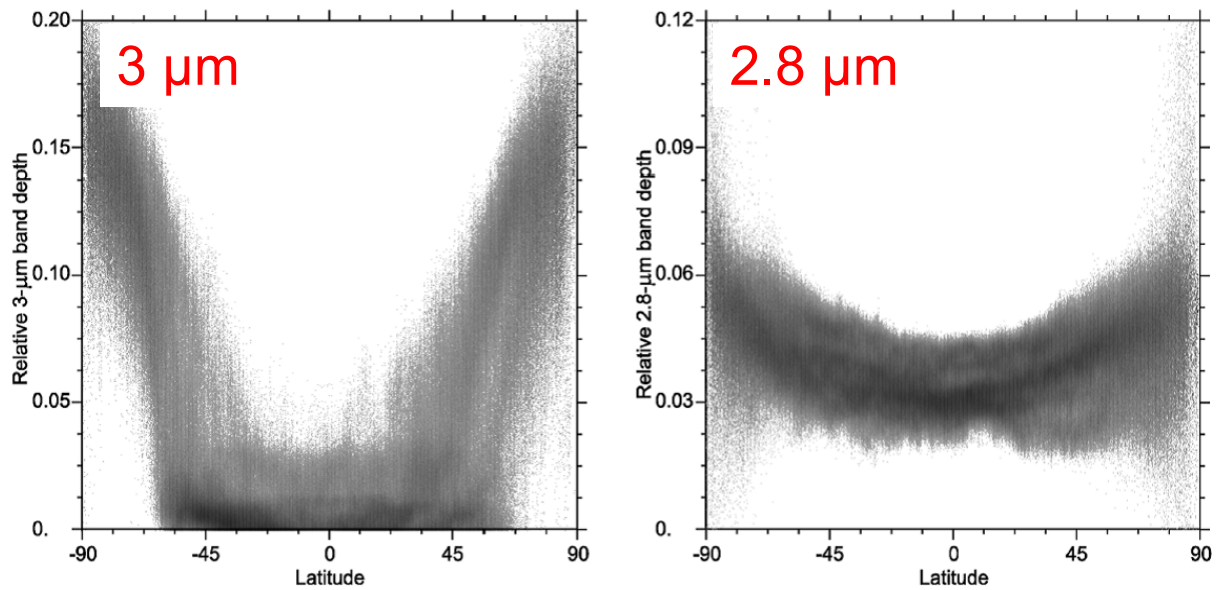


**Figure 3.2:** The distinct 2.8 and 3 μm absorption features seen by M3 on the Moon. The 3 μm absorption is absent at the equator and strongest at the poles, while the 2.8 μm absorption is present at all latitudes and less strongly varying. Image from McCord et al. [2011].

hydroxyl on the lunar surface consisted of a series of experiments that monitored the strength of the 2 – 4 μm region of the IR spectrum to determine changes in the  $-OH$  content in amorphous  $SiO_2$  ( $a-SiO_2$ ) and olivine. As discussed further in Schaible [2014], the goal of this work was not to directly reproduce spacecraft observations but to carry out simple

laboratory experiments to understand and quantify the chemistry of silicates irradiated by  $\sim keV H^+$ . Chemical reactions occur through the implantation depth, while surface reactions are likely suppressed due to preferential removal and depletion of oxygen at the surface as described further in Subsection 2.3.2. Analysis was performed using transmission Fourier transform infrared (FTIR) spectroscopy and the samples used were well-characterized mineral slabs suitable for comparison with standard geophysical methods of studying hydrogen in nominally anhydrous materials.

## 3.2 Background

For several decades following the Apollo missions to the Moon, the lunar surface was considered to be anhydrous and largely devoid of volatile species. Though it was thought since the 1960s that cold traps at the lunar poles could potentially hold large deposits of water [Watson et al., 1961; Arnold, 1979] analysis of returned lunar samples from the Apollo era led to a general consensus that the bulk of the moon was nearly completely anhydrous [Epstein and Taylor, 1974; Taylor et al., 1995]. This was partly due to Earth atmosphere contamination of the returned lunar samples and partly due to limitations in the analytical techniques available at the time. In the last decade this view has changed, and a new paradigm containing three distinct collections of lunar water - bulk, surficial, and polar - has emerged. Measurements of volatile species in returned lunar soils and mineral grains led to predictions that the bulk Moon could hold water concentrations from  $\sim 10 ppmw$  (parts per million of water) in lunar volcanic glasses [Saal et al., 2008; Liu et al., 2012]. Concentrations as high as 5000  $ppmw$  have been found in lunar apatites [McCubbin et al., 2011], a phosphate mineral formed in volcanic outflows, as high as found in the Earth's mantle. Additionally, the existence of polar water was confirmed when the LCROSS (Lunar CRater Observation and Sensing Satellite) spacecraft was crashed into the permanently shadowed crater Cabeus on the lunar south pole resulting in a vapor plume which showed water present at an estimated 5.6% by mass

[Colaprete et al., 2010].

Hydrogen makes up over  $\sim 95\%$  of the solar wind composition and reacts with many atoms that make up the bulk of solid objects in space (i.e. carbon, nitrogen and silicon). Therefore, understanding what bonds can form and determining reaction cross-sections is necessary to explain the molecular content of silicates of the lunar regolith. For example,  $MeV$  hydrogen implanted into lunar simulant glasses can become trapped by bonding to oxygen atoms to form  $OH$ , thereby creating a distribution of hydroxyl molecules throughout the implanted region [Zeller et al., 1966]. While in principle it is possible for hydrogen to bond directly to silicon as well [Moore et al., 1991], the formation of  $SiH$  in silicates due to ion implantation has not been detected [Buemi et al., 1994; Djouadi et al., 2011]. Thus, trapping of implanted hydrogen as a result of radiation induced chemical bonding can be thought of as limited by the volume concentration of oxygen,  $n_O$ , in the silicate sample ( $n_O \sim 2 \times 10^{22} SiO_2/cm^3$ ). At implantation energies of  $150 - 300 keV$ , the formation rate of bound hydrogen decreases after implantation fluences  $\geq 2 \times 10^{17} H^+/cm^2$  indicating a saturation in the formation of  $OH$  bonds, and with further irradiation the hydrogen either accumulates in radiation induced ‘bubbles’ or diffuses through the material and escapes, likely as  $H_2$  or  $H_2O$  [Mattern, 1976]. Though it has long been established that high energy ( $\sim MeV$ ) hydrogen implantation can produce hydroxyl in silicates, energy loss mechanisms and physical effects are energy dependent and studies are needed at solar wind energies.

Several recent laboratory experiments performed in ultra high vacuum (UHV) have attempted to produce  $OH/H_2O$  bands by  $H^+$  implantation of silicates. Previous studies obtained an upper limit for  $OH$  produced by  $\sim 100 keV H^+$  implantation that corresponded to 0.5% absorption band depths in the Moon [Burke et al., 2011], much lower than the 3 – 14% reported for the lunar surface [Pieters et al., 2009]. It was argued that such low  $OH$  production in laboratory samples was related to the relative lack of chemical reactivity in laboratory samples compared to the lunar surface, which the authors presumed to contain “a myriad of unsatisfied bonds, most of which are those of oxygen” [McCord et al., 2011].

However, as discussed in Subsection 2.3.2 and further in Chapter 4, the surfaces of lunar grains are expected to be deficient in oxygen due to preferential sputtering [Loeffler et al., 2009; Schaible et al., in preparation].

Other reports also show  $OH/OD$  formation after irradiating lunar soil simulants with H (D) ions [Managadze et al., 2011; Ichimura et al., 2012]. Managadze et al. [2011] used secondary ion mass spectrometry (SIMS) to detect sputtered water ions from lunar simulants but did not correlate them to IR measurements and could not conclude that the detected  $OH/H_2O$  species were formed in the bulk silicates and not due to contamination. SIMS is orders of magnitude more sensitive than IR absorption and thus a small SIMS signal may not give an observable signal in IR. Ichimura et al. [2012] used only modest vacuum conditions (not UHV) and multiple exposures to air during their experiment, and although the signal formed was stable over long time periods, contamination from atmospheric exposure and large differences in the radiation fluences from those found in space make direct comparison of this work with observation difficult. Furthermore, the possible contamination of the ion beam with  $OH^+$  ( $OD^+$ ) ions in both studies make it difficult to assert that ion irradiation under lunar conditions can produce sufficient  $OH$  to account for the remote IR observations of lunar soil.

In addition to changes in the  $3\ \mu m$   $OH$  band, the  $Si - O$  stretch band at  $\sim 10\ \mu m$  also changes as a result of ion irradiation. Minerals irradiated with keV energy  $H^+$  and  $He^+$  ions become predominantly amorphous at fluences  $< 1 \times 10^{18}\ cm^{-2}$  [Demyk et al., 2004] as evidenced by the smoothing of  $Si - O$  bands from  $9 - 13\ \mu m$ . An increased OH concentration of plasma deposited  $SiO_2$  causes a shift in the  $Si - O$  peak towards lower wavenumbers and a narrowing of the band [Gupta and Parsons, 2000]. The hydroxyl peak at  $2.7\ \mu m$  was found to shift peak position depending on whether the hydroxyl molecules were present in large enough concentrations for significant interactions between molecules to be present. The  $OH$  peak at  $\sim 2.7\ \mu m$  is typically assigned to ‘un-associated’  $Si - OH$  bonds, meaning that no significant hydrogen bonding is present, while the symmetric stretch at  $\sim 2.9\ \mu m$  is assigned

to associated *SiOH* bonds [Gupta and Parsons, 2000].

### 3.3 Experimental methods

A major effort towards completing the proposed experiments consisted of constructing an experimental UHV system, installing the various instruments necessary for the analysis, many of which were new or untested, and commissioning the system in a series of calibration measurements. The experimental system consists of a UHV chamber capable of maintaining pressures below  $1 < 10^{-9}$  Torr and is equipped with a sample transfer flag, purchased from VG Scienta, that can rapidly transfer samples into and out of vacuum through a 'load-lock', thereby greatly reducing the amount of time needed to change samples while maintaining system cleanliness. A Janis closed-cycle helium cryostat was installed and under full cooling power was able to cool the sample holder to less than  $10\text{ K}$ . In order to simulate the solar wind, a Peabody duo-plasmatron ion accelerator was assembled and attached to the UHV chamber. This accelerator contains a mass filter to separate out the  $H^+$  ions and can provide a current of several hundred nano amps at the sample. The analysis equipment attached to the system consists of the following: a Thermo-Nicolet Fourier Transform Infrared (FTIR) spectrometer for detecting chemical changes in the samples as evidenced by changes in IR absorption bands that can be used in either transmission or reflection mode; a Hiden Analytical SIMS for detecting sputtered species and ejected secondary ions during bombardment; and a Quartz Crystal Microbalance (QCM) for accurately measuring the mass or thickness of deposited gaseous species. A detail showing the chamber and sample holder is presented in Figure 3.3.

#### 3.3.1 UHV simulation chamber

Ion irradiations were performed in the UHV chamber at a base pressure of  $< 1 \times 10^{-9}$  Torr, and during irradiation the dominant gas species in the chamber was whichever gas was being ionized in the accelerator source region (typically  $H/H_2$ ,  $He$ , or  $Ar$ ). Performing the

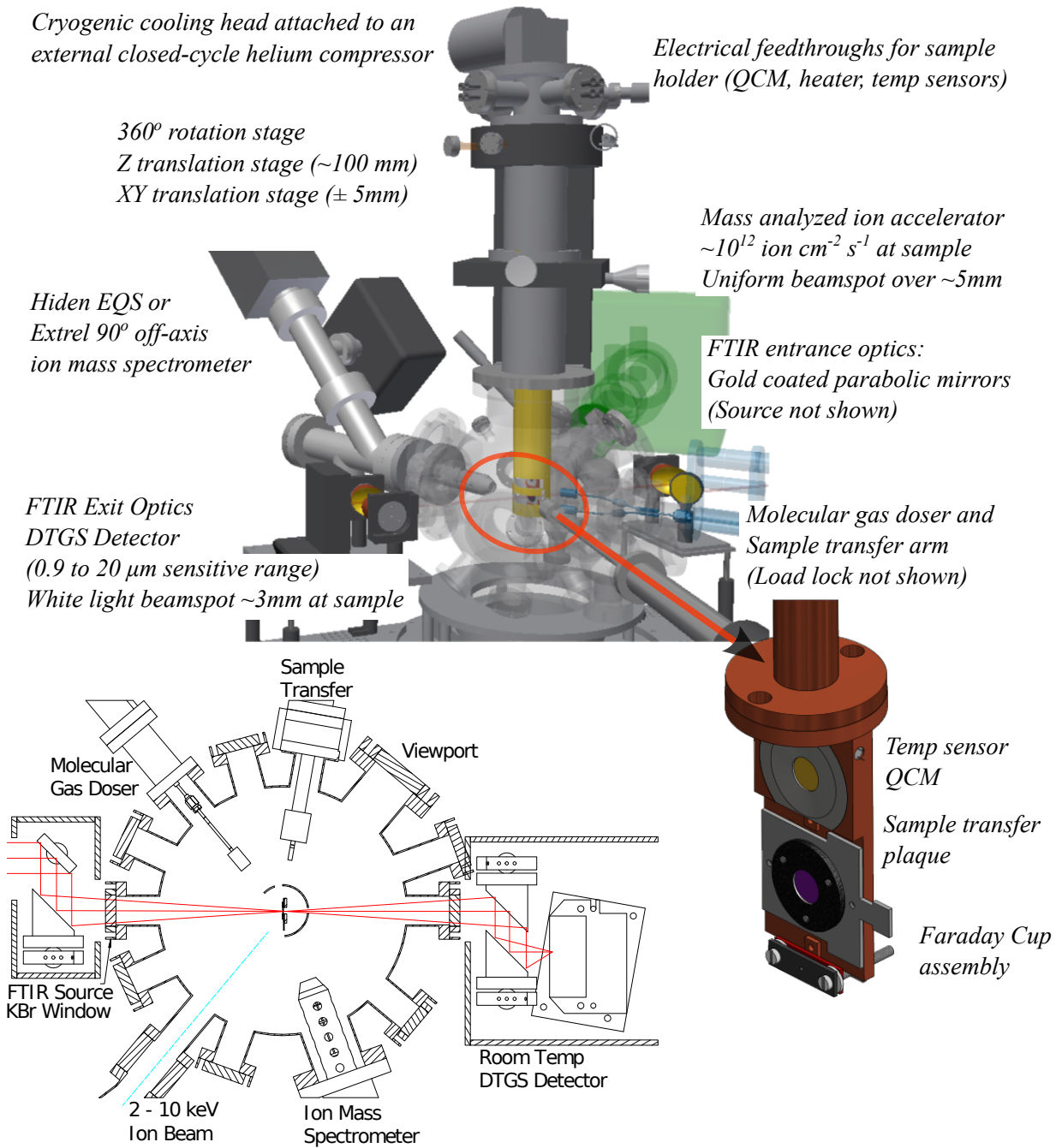


**Figure 3.3:** (top) Solid model of 'Monte', a UHV chamber designed and housed in the Laboratory for Atomic and Surface Physics at the University of Virginia. Experiments were performed under UHV and lunar soil samples were irradiated with 1 – 15 keV  $H^+$  ions. (bottom right) Sample holder design. The entire ensemble can be cooled to  $< 10 K$  and samples are pressed against the Cu body using either two clips or a wire screen. The Faraday cup assembly has a 1mm aperture in the front plate, and the cup entrance is 5mm. (bottom left) Layout of the hydrogen irradiation experiments where  $H^+$  ions were used to bombard lunar soil 15058. The red lines represent the FTIR beam, and a DTGS detector with a sensitivity range of  $\sim 1 - 20 \mu m$  was used in the experiments.

sample preparation and analysis entirely under vacuum conditions ensured that no water adsorbed on/diffused into the material or altered bonding between implanted hydrogen and

structural atoms. Samples were irradiated at normal incidence with 5 – 15 keV  $H^+$  ions. Mass-analyzed ion beams were produced by a Peabody ion accelerator connected to the UHV chamber through a differentially pumped stage. A Wien filter provided ion mass analysis and post-deflection was used to prevent fast neutrals from reaching the samples. The ion beam was scanned uniformly over an area larger than the IR analysis area.

Previous experiments used 2 keV  $H_2^+$  ions from ion beams without mass analysis capabilities, meaning that the incident ion beam contained a mixture of ion types (e.g.,  $H^+$ ,  $H_2^+$ ,  $H_3^+$ , and  $O^+$ ) [Burke et al., 2011; Ichimura et al., 2012]. Although molecular species are expected to split on contact with the surface with an equal amount of energy (1 keV) partitioned to each atom, using a mass-analyzed proton beam avoids the assumption that the  $OH$  production is the same regardless of molecular effects or oxygen contamination in the ion beam. Ion fluxes were on the order of  $\sim 2 \times 10^{12} cm^{-2} s^{-1}$  which, while larger than typical solar wind fluxes ( $\sim 2 \times 10^8 cm^{-2} s^{-1}$ ), lead to negligible heating (fraction of a degree) due to the very low power densities ( $\sim 0.3 mW/cm^2$ ). The ion current density was measured using a the Faraday cup located on the sample holder with a 1 mm diameter aperture. The ion accelerator was allowed to reach a stable beam flux before samples were irradiated, and the fluence of ions implanted into the sample was determined by integrating the beam flux over the irradiation time.

### 3.3.2 Analysis techniques

The structural and/or chemical changes were monitored using a Thermo-Nicolet Nexus 670 Fourier Transform Infrared (FTIR) spectrometer. Unpolarised infrared spectra were collected from  $\sim 1 - 10 \mu m$  with the Thermo-Nicolet Omnic software at  $16 cm^{-1}$  resolution and averaged over 1024 scans. An advantage of the transmission IR setup vs. previous experiments is that the column density,  $\nu$ , of new OH bonds produced along the path of the protons can be directly quantified. A series of gold coated mirrors is used to focus and collect the light from the sample and redirect it to the detector, and an internal mirror redirects the

light from the spectrometer bench to the chamber sample holder. The beam path after it leaves the spectrometer as shown in Figure 3.3. The windows used to admit the light into the chamber were *KBr* with a transmittance range from 0.4 to 20  $\mu m$ . The spectrometer was coupled to the chamber through dry-air purged paths containing focusing mirrors and a Deuterated TriGlycine Sulfate (DTGS) detector, sensitive to a total wavelength range from 0.9 to 20  $\mu m$ , was used to eliminate the water absorption problems found using cooled detectors. Transmission through the sample holder is limited by a 5 *mm* hole in the transfer flag which works as an aperture to constrain the analysis area to only the irradiated region. The analysis proceeded by first lifting the sample holder clear and acquiring a background spectrum with only the optics and *KBr* windows in the IR beam path. The sample was then lowered so that the IR beam was centered on the transfer flag aperture, and another spectrum taken. Between irradiation and transmission IR measurements, the sample must be rotated 50°.

### 3.3.3 Sample and sample holder

The sample used in the experiments was a thin section taken from lunar pigeonite basalt rock sample 15058 obtained from the NASA curation facility at Johnson Space Center. The parent rock is predominately composed of pyroxene - an inosilicate mineral with the general composition  $(Na, Mg, Ca, Fe)_2(Si, Al)_2O_6$  - and plagioclase - a solid solution series varying from albite,  $NaAlSi_3O_8$ , to anorthite,  $CaAl_2Si_2O_8$  - silicate minerals (95%) with minor amounts of other phases incorporated into the solid matrix. The sample was delivered on a glass slide to which it was adhered using a soluble epoxy. The sample was removed from the slide by placing it in a container of acetone for > 48 *hrs*, and the acetone was exchanged several times until the sample was free and the epoxy dissolved. The sample contains abundant micro-crystalline grains and was not self-supporting upon removal from the glass slide. However, the experimental chamber requires vertical sample orientation. Therefore, in order to hold the loose grains vertically so that they could be irradiated and

analyzed, the sample was loosely pressed between two 90% transmittance *Ni* metal grids. A picture of the sample after installation on the sample holder is given in Figure 3.4. This configuration allowed the sample to remain undisturbed as the main chamber sample holder was rotated from irradiation to FTIR analysis positions and as the sample was lifted and lowered to measure the ion beam current.

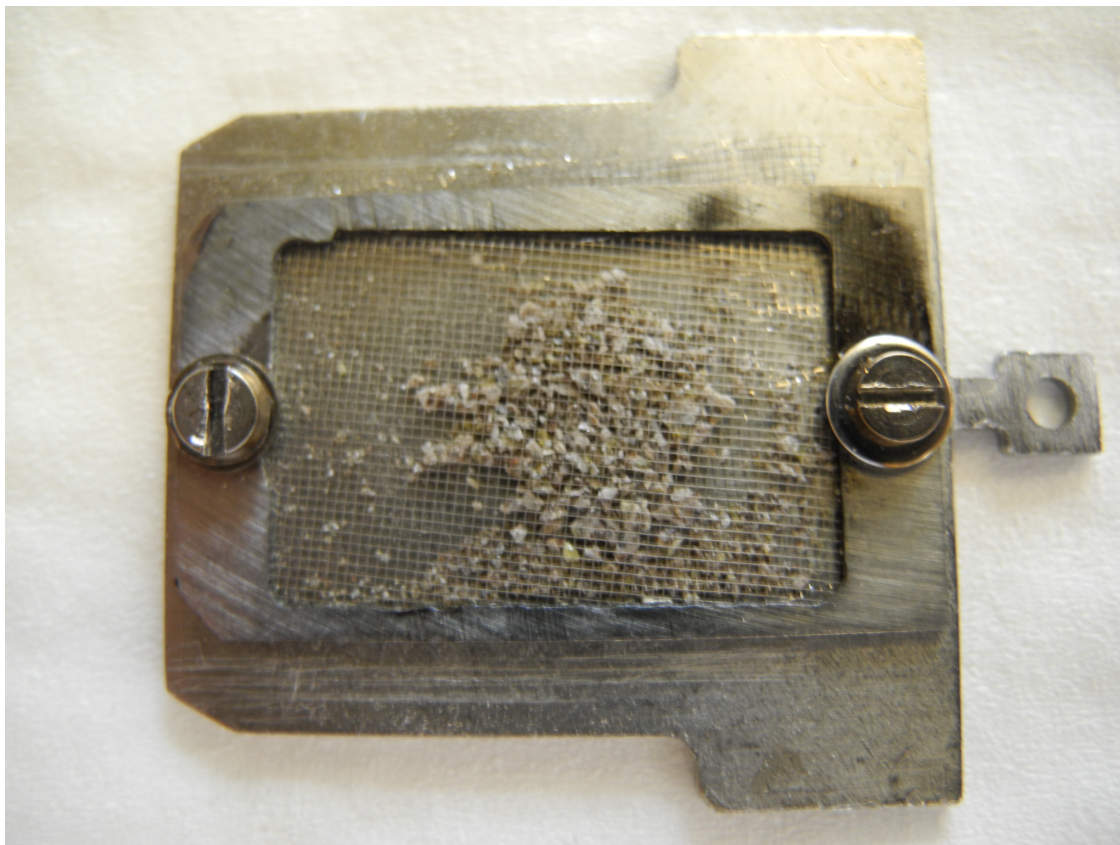


**Figure 3.4:** Lunar soil 15058 was delivered as a thin section, but upon removal from the glass slide the sample crumbled and it was necessary to sandwich the material between two *Ni* metal grids and manually arrange the grains to cover the transfer flag transmittance aperture. Although the grains were still somewhat mobile, this configuration was seen to hold the sample relatively stable after vertical mounting in the UHV chamber. However, small shifting of the grains as the sample was rotated to face the beam and FTIR could have resulted in changing spectral features.

### 3.3.4 Data reduction

Absorbance, a dimensionless quantity hereafter given in terms of dimensionless absorbance units (a.u.), is calculated for the pristine (unirradiated) samples by taking the negative log

base-10 of the ratio of the two spectra

$$A(\nu) = -\ln(i/i_o) \quad (3.1)$$

where  $\nu$  is the column density of the absorbing species and  $i/i_o$  is the ratio of the intensities of the infrared beam after passing through the sample to that with the sample removed. Note that  $A(\nu) = A_{10}(\nu)\ln(10)$  where  $A_{10}$  is the decadal absorbance typical of the chemistry literature. For the irradiated samples, we likewise obtain  $A'$ , and then the difference can be calculated,  $\Delta A = A' - A$ , which cancels instrumental effects such as the presence of the wire grid in front of the sample.

The *OH* column density can be determined either from the height of the absorption band (BH) in  $\Delta A$  and the molar absorption coefficient  $\epsilon$ , or from the band area (BA) and the integrated molar absorption coefficient,  $\epsilon_{int}$ . The column density is given by

$$\nu = \frac{BH \times N_A}{\epsilon} = \frac{BA \times N_A}{\epsilon_{int}} \quad (3.2)$$

where  $N_A$  is Avogadro's number. The sensitivity of the FTIR measurements is  $\sim 10^{-4}$  for minerals in transmission, corresponding to a column density  $\nu \sim 1 \times 10^{15} \text{ OH/cm}^2$ . Band height and area measurements are taken after using standard software to subtract smooth baselines from the absorption spectra  $A$  and  $A'$  so that there is a common basis from which to measure the peak differences (height or band area). Subtraction is carried out over the spectral range  $\pm 1000 \text{ cm}^{-1}$  from the water band peak position so that the high absorbance *Si-O* bands, which are several orders of magnitude larger than the *OH* bands, do not affect the baseline. The baseline subtraction procedure was carried out using the OMNIC software package which uses a quadratic line fit to the absorbance data  $A(x)$  by the least squares method following

$$A(x) \sim Y(x) = ax^2 + bx + c \quad (3.3)$$

where  $Y(x)$  is the fit function and  $x$  represents the wavenumber. The maximum difference between  $A(x)$  and  $Y(x)$  is then determined, and all points in  $A(x)$  that differ from the corresponding point in  $Y(x)$  by more than half of this maximum value are dropped to create a subset of data with the tops of the major peaks missing. The same procedure - fit, compare, and drop - is subsequently repeated for diminishing subsets of the data 20 times. After the 20 iterations, the final subset  $Y(x)$  is subtracted from the original spectrum  $A(x)$  to produce the baseline corrected spectrum. Finally, the lowest point on the corrected spectrum is automatically set to zero.

### 3.4 Ion irradiation effects on lunar soil 15058

The mounted sample, LS15058, was installed in the UHV chamber and preliminary (pristine) spectra of the sample were taken using both IR and visible (WL) light sources. Background corrected FTIR spectra collected before irradiation (pristine), after *Ar* sputter removal of adsorbed atmospheric species, and after irradiation with 5 – 15 keV  $H^+$  ions to fluences greater than  $10^{17} \text{ cm}^{-2} \text{ s}^{-1}$  are shown in Figure 3.5. Although there appears to be a general increase in absorbance for decreasing wavenumber (increasing wavelength) representing a general ‘blueing’ of the spectra, the spectral backgrounds do not appear to be consistent between measurements.

The spectral changes are in contrast to what would be expected based on previous measurements of ion radiation of Fe-bearing olivine where spectral reddening (decreased absorbance at IR wavelengths) was observed [Loeffler et al., 2009]. However, it has been seen that in some instances, e.g. for carbonaceous meteorites or pure forsterite ( $Mg_2SiO_4$ ) minerals, that the sample can blue as was observed here. However, the bulk composition of LS15058, given in Section A0.4, contains  $\sim 5\%$  *Fe* and therefore would be expected to redden. The variances in the spectra shown in Figure 3.5 are possibly due to shifting of the sample as it was rotated between the irradiation and analysis positions, or while moving up

and down to take baseline IR spectra and to measure the ion beam current. Unfortunately, these spectra are unable to give any indication whether the ion irradiation caused general trends in the spectra as a function of implantation fluence.

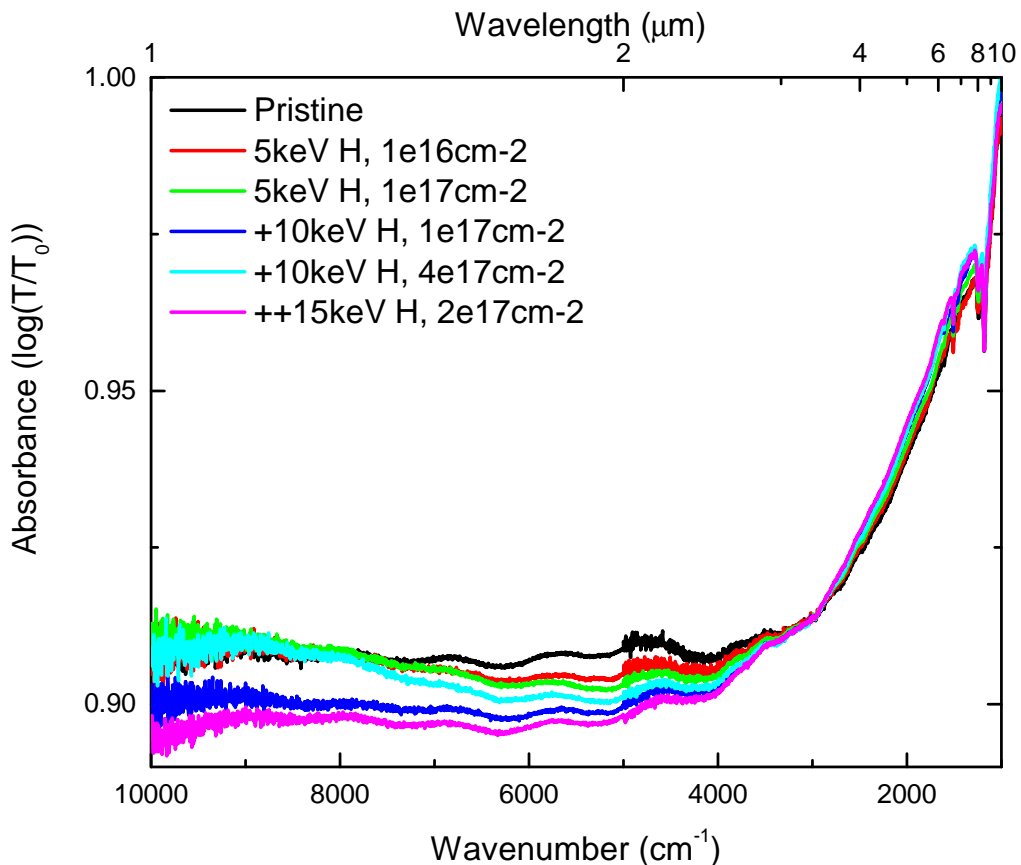


**Figure 3.5:** Combined infrared and white light spectra for lunar soil sample LS15058 mounted as shown in Figure 3.4. The fluences at each energy are indicated and are not cumulative, but the irradiation were performed sequentially so that after the 15 keV irradiation step the total  $H^+$  fluence to the sample was  $> 7 \times 10^{17} \text{ cm}^{-2}$ . The sample was rotated between irradiation and analysis, and lifted/dropped before each irradiation step to measure the ion beam flux. The movement of the sample likely led to jostling of the grains and ultimately caused significant variations in the spectra.

Lunar soil samples are nominally anhydrous, small amounts of residual water vapor condensed on the sample need to be removed either by sputtering or by subtracting pristine spectra from irradiated spectra. In order to determine whether the  $H^+$  irradiation of LS15058 produced an increase in absorbance at  $\sim 3 \mu\text{m}$ , the sample was first sputter cleaned with 5 keV  $Ar^+$ . The spectra taken after  $Ar^+$  sputter cleaning was subtracted from the subsequent spectra taken after  $H^+$  bombardment so that spectral changes produced by the reaction of

$H^+$  with  $O$  in the lunar sample could be evaluated. The spectra were background corrected as described above, and the spectral differences are shown in Figure 3.6. There is no change in the absorbance over this wavelength range at the level of the measurement noise.

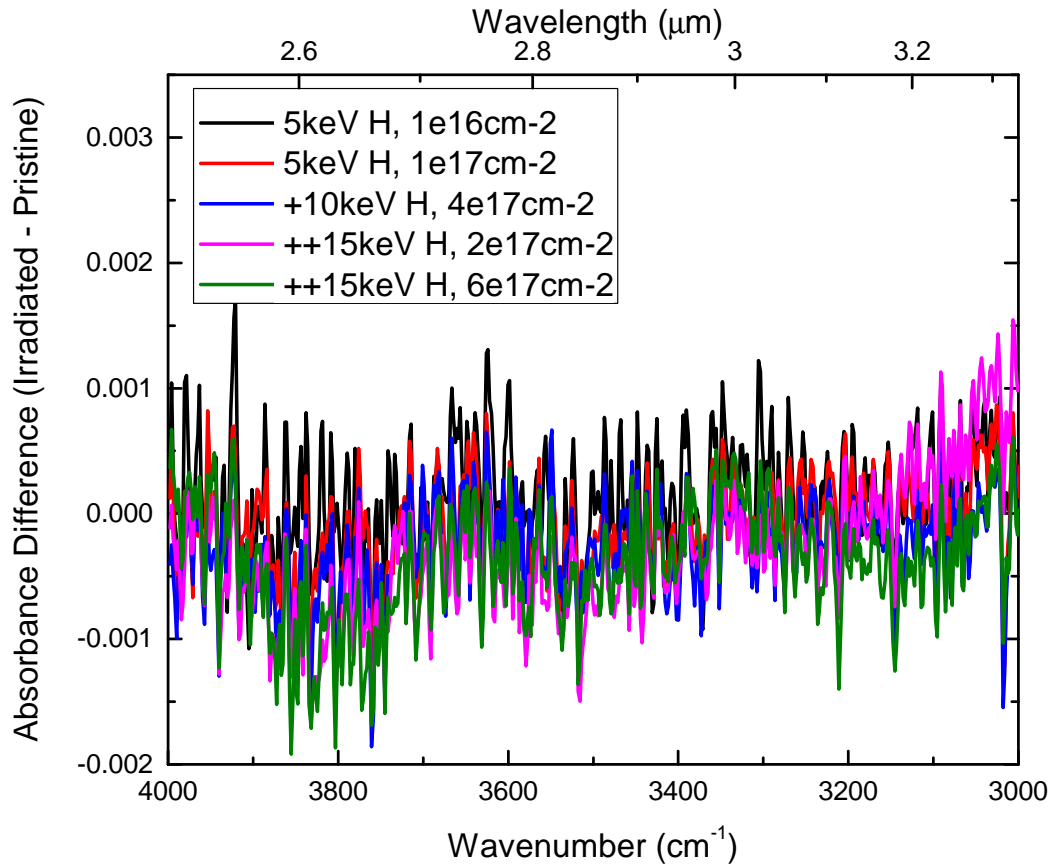


**Figure 3.6:** Analysis of the  $\sim 3\mu\text{m}$  spectral region for LS15058. The irradiation fluences are indicated in the legend, and no significant change in the absorbance region could be detected at the sensitivity of the measurements.

### 3.5 Discussion

Although clear spectral changes were seen after  $H^+$  irradiation of amorphous  $\text{SiO}_2$  and olivine thin sections [Schaible and Baragiola, 2014], no radiation induced spectral changes could be clearly discerned from the data for LS15058. The samples used in the two experiments were very different. In the earlier experiments, the samples were optically flat thin sections

and only a single metal grid was needed to hold the sample against the sample holder. The  $a - SiO_2$  and olivine samples were homogeneous without visible grain boundaries, much different than the ‘pebble’ like sample LS15058. Although LS15058 was delivered as a  $50 \mu m$  thick section, upon removal from the glass plate the sample crumbled due to the large number of discontinuous grain boundaries. This led to a less well defined optical path for the FTIR, and increased scattering from grain surfaces. Furthermore, the individual ‘pebbles’ were highly opaque, limiting the light transmittance through any single irradiated solid surface. It is possible that, due to the opaqueness of the lunar sample, the granularity, and shifting of the sample during analysis, hydroxyl formed as a result of  $H^+$  irradiation was either obscured or insufficient to create a distinguishable signal.

### 3.6 Conclusions

It has been shown previously that irradiation of  $a - SiO_2$  and olivine solids with  $2 - 10 keV H^+$  ions leads to the formation of  $OH$  molecules which can be identified using transmittance FTIR spectroscopy [Schaible and Baragiola, 2014]. The results of the earlier experiments showed that both the depth and area of the  $OH$  absorption band were seen to grow with an exponentially decaying rate up to a fluence of  $\sim 2 \times 10^{17} cm^{-2}$ , at which point the band saturated. Furthermore, no evidence for formation of water ( $H_2O$ ) was observed. The increase in  $OH$  band absorption measured was sufficient to explain the lunar reflectance signals at the equator. However, repeating these experiments using LS15058 did not lead to any discernible spectral changes with fluence. This does not imply that no  $OH$  was formed as a result of the  $H^+$  irradiation, but only that it was below the detection limits of the experiments. The lunar soil was significantly more difficult to work with, and the grains were far more opaque than the previously used samples. Due to the ‘pebbly’ nature of the sample, it is possible that the bulk of the reflectance signal was seen from single scattering events on grain surfaces and did not probe the implanted regions. Further experiments with more

rigidly mounted samples are needed to quantify the rate of  $OH$  formation in lunar samples resulting from solar wind hydrogen bombardment.



# Chapter 4

## Case 2: Ion sputtering of airless surfaces

### Abstract

Due to the lack of appreciable atmospheres around most moons and asteroids in the Solar System, the ices and minerals that compose the upper surfaces are exposed to ambient gases, impacting particles, and radiation. Plasma ion bombardment of the surfaces drives the subsequent removal of material through collisional energy loss processes, a process known as sputtering. The surface composition can be determined by detecting sputtered material and spatial mapping of the compositional differences can be used to understand the geologic history of the body. Here, sputtering yields from simple oxides, minerals, lunar samples, and a suite of meteorite compositions will be considered using both experimental and computational techniques. Results are used to estimate solar wind sputtering yields on airless bodies, and it is shown that analysis of ejected ions can be used not only to determine composition but also to classify a body according to the various known meteorite classes. Conclusions are used to suggest design considerations for an ion mass spectrometer (IMS) flown near the surface of an airless body subject to solar wind bombardment.

## 4.1 Introduction

The solar wind, a constant outflow of energetic charged particles from the Sun composed predominantly of  $H^+$  and  $He^{2+}$ , and magnetospheric ions can impact the surface of airless bodies causing chemical and physical changes to occur [Hapke, 2001; Madey et al., 2002; Pieters et al., 1993]. On impact, charge and momentum transfer processes lead to the ejection of particles from the surface in a process called sputtering, and the interaction of sputtered material with ambient gas and radiation leads to the formation of a dynamic exosphere about such bodies. A small fraction of the ejected species ( $\sim 1\%$ ) leaves the surface in an ionized state and these, commonly called secondary ions, can be detected with a high sensitivity using standard ion mass spectrometry (IMS) techniques. Predictions for ion energy and spatial distributions in the exospheres around moons and asteroids provide a useful tool in the design of spacecraft IMS instruments. However, ions are deflected by the randomly oriented solar wind magnetic field and thus, if there is significant deflection, the probability of detecting sputtered ions becomes independent of the spacecraft orientation and the source location of the ejecta is difficult to determine. Therefore accurate yield estimates should be combined with measurements or models of ambient plasma fields in the vicinity of small bodies and moons to determine accurate exosphere density as a function of time. The term small bodies is used here to refer to asteroids and comets in the inner Solar System with diameters  $\lesssim 100 \text{ km}$ .

The purpose of this work is to estimate the exosphere density close to the surface of an airless body in an environment produced by particle and grain impacts and provide design suggestions for a spacecraft IMS. Using known meteorite compositions, the measured secondary ion counts can be used to place constraints on the geologic history of the parent body. Although reflectance spectroscopy can give surface information to depths of  $\sim \mu\text{m}$  ( $\propto$  wavelength of the light), it is prone to weathering effects that change the chemical state of the surface and can modify the spectra. For exosphere densities produced predominantly by

solar wind sputtering, the composition of the exosphere depends on the elemental abundances of the exposed surface. However, direct detection of all but the least reactive neutral species is unlikely without relatively long integration times and increased densities caused by ram pointing of the mass spectrometer. The ram enhancement is due to pointing of the instrument in the forward moving direction of the spacecraft (the ram direction) and a corresponding increase in the pressure in the instrument ionization chamber. Secondary ion mass spectrometry is highly surface sensitive, but less sensitive to the chemical state of the surface and better suited to determining the elemental atomic composition of the exposed material. Although the flux of ejected ions is only  $\sim 1\%$  that of the neutrals, ion spectrometry provides a more sensitive detection technique due to low background ion counts. Furthermore, an IMS can be pointed toward the surface and, by limiting the acceptance aperture, rough spatial mapping can, in principle, be obtained.

After a brief introduction and review of published literature relating to solar wind sputtering of silicate surfaces in Section 4.2, the results from modern Monte Carlo techniques are used to simulate the transport of ions through solid targets whose compositions are similar to those of representative parent bodies in the solar system. As described in Section 4.3, the open source Monte Carlo program SRIM/TRIM [Ziegler et al., 2008] and the program SDTrimSP v. 5.07, developed at the Max Plank Institut fer Plasmaphysik [Mutzke et al., 2011], were used to simulate ion bombardment of numerous astrophysical analog compositions and give estimates for the elemental sputtering yields. Comparisons were made with sputtering measurements of several simple oxide materials to test the validity of the computations. Experimental measurements of the secondary ion ejection produced by solar wind bombardment of lunar soils are described in Section 4.4 and, using the combined results from computation and experiment, the predicted secondary ion fluxes and relative yields for several major meteorite classes are given in Section 4.5. Finally, in Section 4.6, the change in ion flux as a function of altitude from a small body surface is estimated using analytical equations and assuming average solar wind conditions.

### 4.1.1 Motivation

This work was originally carried out in support of the NASA Ames research center proposal for a NASA Discovery class mission to explore Phobos and Deimos, the moons of Mars, and to constrain their origins. The Discovery class of missions is a low-cost ( $\sim$  \$450 million), highly focused series of NASA missions to Solar System targets of interest. The Phobos And Deimos & Mars Environment (PADME) mission proposal was submitted in response to the 2014 NASA Discovery Announcement of Opportunity (NNH14ZDA014O) led by Anthony Colaprete as the mission PI and Pascal Lee as the deputy PI. Phobos is  $\sim 22$  km in diameter and the surfaces features are dominated by the  $\sim 9$  km Stickney crater visible in Figure 4.1. Phobos has an orbital period of just 7.66 hr and is inside the Roche limit meaning that the orbital distance is decreasing with time and the moon will eventually be broken up by tidal forces. Deimos is slightly smaller with a  $\sim 13$  km diameter and an orbital period of 30.35 hr. Both moons have nearly circular orbits and are tidally locked to Mars. The spectral characteristics of Phobos and Deimos are most similar to C- and D-type asteroids in that they have very low albedo and featureless, reddish reflectance spectra.

The origins of Phobos and Deimos are unknown, with various possibilities being that they are captured asteroids, remnants from the formation of Mars, or impact ejecta produced by a planetesimal collision with Mars. The proposed PADME spacecraft, shown in Figure 4.2, would explore these moons and their environment, and the mission instruments are intended to provide information about the structure and composition of the moons through complimentary measurements of the internal structure, near surface and surface features, and external environment of the moons. The hydrogen content and composition of the uppermost  $\sim 1$  m will be probed using the neutron spectrometer (NS) instrument. The dust environment and possible transport of material from Deimos to Phobos will be studied using the Mars dust experiment (MDEX) detector. Additionally, the optical imaging system (OIS) will be used to determine the libration amplitude to determine internal structure, as well as to analyze



**Figure 4.1:** Color enhanced images of Phobos and Deimos (not to scale). The Phobos image clearly shows distinct 'red' and 'blue' units which could be suggestive of underlying materials of differing composition from Phobos' uppermost surface. Both Phobos and Deimos are spectrally similar to D-type asteroids with dark, reddish spectra lacking any major spectral absorptions. Image credit: NASA Mars Reconnaissance Orbiter.

the surface geologic features for possible dynamics.

A final instrument, the Neutral/Ion Mass Spectrometer with Enhancement cells (NIMS-E), is proposed as a means of constraining the surface composition, especially the metallic component of the regolith. The instrument would detect the sputtered and desorbed surface ejecta using a combined closed source neutral and open source ion mass spectrometer. Furthermore, enhancement cells containing a high surface area silica materials can capture dust particles and volatiles, and heating of these cells to  $> 600^{\circ}\text{C}$  can provide information on both the volatile composition and mineral type composing the uppermost surfaces of Phobos and Deimos. The enhancement cells provide complimentary measurements to the proposed dust detector (MDEX) and closed source detection mode. By comparing signal from all spacecraft instruments, not only can the surface composition and the geologic history be constrained, but novel insight would be gained into the various degassing modes of airless bodies and whether out-gassing, micrometeorite impacts, or sputtering due to solar wind ions dominates the exosphere production.

The primary observations of the sputtered ion composition to be carried out by the

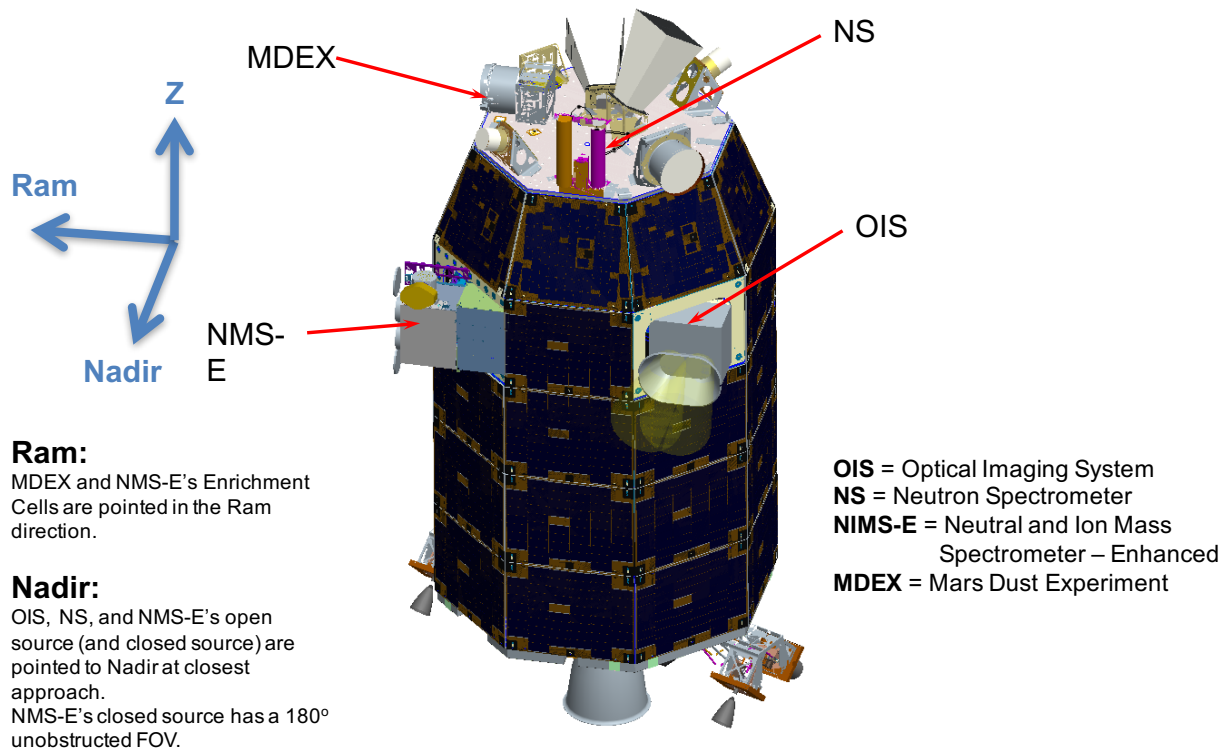


**Figure 4.2:** The Phobos And Deimos & Mars Explorer (PADME) spacecraft with the instruments labeled and their pointing directions indicated.

PADME NIMS-E instrument were in the ion detection mode since neutral refractories quickly stick to the detector walls and, due to low volatility, require either very high partial pressures or long dwell times in order to be detected. It has long been suggested that secondary ions could be used to determine the composition of airless bodies in space [Johnson and Sittler, 1990; Johnson and Baragiola, 1991; Dukes and Baragiola, 2015]. Recent spacecraft have shown the promise of obtaining detailed elemental analysis of ions from both atmospheres such as those of Titan [Waite et al., 2004] and Mars [Fox, 2015] and from airless surfaces such as the Moon [Mahaffy et al., 2014] and comets [Balsiger et al., 2007].

Detection and analysis of secondary ions in the laboratory provides a highly sensitive means of determining surface composition [Hofmann, 1976]. In the space environment, ejected ions can be directly analyzed using an Ion Mass Spectrometer (IMS), thus allowing detection of reactive metal ions and molecules which would otherwise stick to the instrument walls before they could be ionized and measured. When Phobos is directly exposed to the solar

wind, ion sputtering is expected to dominate over micrometeorite bombardment, and the average total ejection flux including volatiles, refractories, and molecules is  $\sim 5 \times 10^{10} m^{-2}s^{-1}$  [Cipriani et al., 2011]. During the transit through the plasma wake, on the opposite side of Mars from the sub-solar point, solar wind ion sputtering drops off significantly as the plasma is deflected around Mars. However, oxygen pick-up ions from the Mars atmosphere can produce sputtered fluxes up to an order of magnitude larger [Poppe and Curry, 2014]. Therefore, in the absence of meteoroid streams, sputtering is expected to be the dominant source of neutrals and ions throughout the moon’s orbits.

Although the spectral properties of the moons are most similar to C- and D-type asteroids, with the exception of water bands which are much smaller or non-existent on Phobos and Deimos, various end member compositions representative of a suite of meteorite types are considered for completeness. By measuring the composition of the sputtered material in flight and comparing this with experimental and computational results, the atomic and chemical composition differences between the two bodies such as Phobos and Deimos can be determined. In particular, using a mass spectrometer with a narrow field of view can provide spatial mapping of compositional differences between distinct regions on Phobos, namely, the ‘blue unit’ expected to be representative of the native composition, and the ‘red unit’ thought to be deposited dust and possibly resulting from migration of Deimos surface material.

### 4.1.2 Exosphere production around small bodies

Surface-bound exospheres are produced when short wavelength photons (UV), solar wind ions, pick-up ions, and micrometeorite bombardment eject atoms, molecules, and ions from the top  $\sim 1 nm$  of the regolith [Schläppi et al., 2008; Sarantos et al., 2012b,a]. Around airless bodies, ejected atoms and molecules travel away from the surface in ballistic trajectories, escaping the body and becoming subject to the background solar radiation and planetary magnetosphere effects. If the ejection velocity is less than the escape velocity, the atoms and

molecules will redeposit and can subsequently migrate across the surface. The exospheric column density  $N_i$  for species on escape trajectories is determined by dividing the ejected flux by the average ejection velocity of the particles

$$N_i = \int \frac{\phi_i(v)}{v_i} dv \quad (4.1)$$

where  $v_i$  represents the velocity of species  $i$  and  $\phi_i(v)$  is the ejected surface flux per unit velocity for the ejection process of interest. For sputtering, the velocity distribution depends on incident ion energy and mass as described in Subsection 2.3.1, and for thermal desorption it depends on temperature as described in Section 2.5. For radiation release processes, it is common to forgo the integral in this formula and instead use an absolute yield (ejected species/incident particle) of monoenergetic ejecta and an approximate incident radiation flux to calculate the sputtered fluxes of species near the surface.

Several attempts have been made to measure the exospheres of moons and comets, and recent data from the NASA Cassini and LADEE (Lunar and Atmospheric Dust Environment Explorer) missions as well as the ESA Rosetta mission to comet 67P/CG have shown the power of mass spectrometry in providing detailed compositional information. Because exospheres are produced by outgassing and sputtering processes, measuring the exosphere composition provides direct evidence of the surface composition. Investigations by Rosetta ROSINA (Rosetta Orbiter Spectrometer for Ion and Neutral Analysis) and Ptolemy instruments into proposed water vapor outgassing mechanisms during fly-bys of asteroids (21) Lutetia ( $\sim 100 \text{ km}$  effective radius,  $\sim 3000 \text{ km}$  closest approach) and (2867) Steins ( $\sim 5 \text{ km}$  effective radius,  $\sim 800 \text{ km}$  closest approach) did not detect any unambiguous signal of a neutral exosphere [Altwegg et al., 2012; Andrews et al., 2012; Morse et al., 2012; Schläppi et al., 2008, 2010]. However, once the spacecraft approached the comet 67P/CG during its active phase, a rich variety of atomic and molecular species were detected [Le Roy et al., 2015]. Surface-bound exospheres have also been observed on the Moon [Benna et al., 2015; Halekas

et al., 2015], Mercury [Burger et al., 2014], Europa [Hall et al., 1995; Cassidy et al., 2007; Johnson et al., 1998], and the icy Saturnian moons [Tokar et al., 2012; Waite et al., 2006], and are expected to be present around much smaller bodies as well given the ubiquitous nature of their formation process.

Although the sole ejection mechanism considered in the following is solar wind ion sputtering, as discussed in Chapter 2, photodesorption, thermal degassing, and meteorite impacts can generate significant fluxes of ejected material and should be fully considered for any complete model of secondary ion density in small body exospheres. The production of detectable amounts of material by impacts has been verified around the Moon in LADEE neutral mass spectra where periodic spikes in the exosphere density correlate with known orbital crossing meteorite streams [Szalay and Horányi, 2015]. While dust impacts may generate detectable amounts of ejecta, they are neglected in this analysis since the calculations have already been carried elsewhere out for the martian moons [Cipriani et al., 2011]. Furthermore, it is currently unknown what fraction of vaporized ejecta created during meteorite impacts escapes the surface in an ionized state.

## 4.2 Sputtering yields: a brief review

The total sputtering yield for all elements ejected through the sputtering process,  $Y^{tot} = \sum_i Y_i$ , is defined as the total number of atoms for all species ejected per incident solar wind ion as discussed in Subsection 2.3.1. The component yield,  $Y_i$ , is the number of atoms of species  $i$  ejected per incident ion. In the absence of abundant experimental data, estimates of solar wind sputtering yields from surfaces in space have typically extrapolated values for  $Y^{tot}$  from sputtering yield measurements from metals and used stoichiometric yield ratios to determine the sputtered material composition [Cipriani et al., 2011], or have determined yields for solar wind energy ion bombardment of surfaces simulated using the popular simulation tool developed by Zeigler and colleagues called Stopping/Transport and Range of Ions in Matter

(SRIM/TRIM) [Ziegler et al., 2008; Wurz et al., 2007; Poppe and Curry, 2014]. SRIM/TRIM is based on extensive data sets and models of the interaction potentials between a fast incident ion and a neutral in the solid and uses an efficient Monte Carlo algorithm to simulate ion collision cascades through amorphous, uniform stoichiometry solids. As discussed further in Section 4.3, a more recently developed program, SDTrimSP [Mutzke et al., 2011], which is based on the TRIM.SP and Tridyn programs, is also used here to simulate sputtering yields. Although the results from Monte Carlo methods are only approximate, such simulations are used extensively in the radiation effects community to extrapolate the limited experimental data sets. Experimental measurements of the total or relative sputtering yields are often not available for multi-elemental, heterogeneous solids, but sputtering of simple oxides such as  $SiO_2$  and  $CaCO_3$  can yield insight and guidance into understanding the more complex materials.

#### 4.2.1 Experimental measurements for simple oxides

A review of the available laboratory and theoretical sputtering literature shows that there are considerable uncertainties in the yields and ejection energies for materials that would be expected to make up the bulk of silicate bodies in space. Table 4.1 gives a representative example of sputtering yields measured experimentally for solar wind bombardment of oxides similar to those expected in meteorites and small Solar System bodies. Yields were obtained by a variety of different experimental methods which typically utilized either measured weight loss or other absolute methods to determine the amount of material removed. Such methods require very large beam fluxes, many orders of magnitude larger than the solar wind, such that sample heating effects may become important. The total sputtering yields obtained using SDTrimSP are given for several species for comparison. The total yield measured by experiments performed using heavy ions at high energy has been shown to be roughly proportional to the material stopping power,  $dE/dz$ , defined as the energy-loss per unit path length for an ion entering a solid. Thus, results for different incident ions can be compared

by dividing the absolute yield by the stopping power,  $Y^{tot}/(dE/dz)$ . In order to directly compare results, yields are given in terms of sputtered atoms per incident ion divided by the theoretical stopping power.

**Table 4.1:** Published sputtering yields for several oxide samples and comparisons with various estimates used in the literature. The experimental yields can be scaled by the incident ion stopping power for a more direct comparison of yields. In calculating the stopping powers no correction was made for Bragg reflection or compound effects, and only nuclear stopping powers are given here. However, the contribution of electronic stopping may be significant for  $H^+$  ions.

Ion $\rightarrow$ Target	Experimental Yield (atoms/ion)	Stopping Power <sup>1</sup> (eV/ang)	Scaled Yield $Y^{tot}/(dE/dz)_n$	SDTrimSP Yield (atoms/ion)
5 keV $Ar^+ \rightarrow SiO_2$ bef $H^+$	1.05 <sup>2</sup>	5.84	0.18	$\sim 1.5$
5 keV $H^+ \rightarrow SiO_2$	0.08 <sup>2</sup>	0.167	0.48	0.015
5 keV $Ar^+ \rightarrow SiO_2$ aft $H^+$	1.3 <sup>2</sup>	5.84	0.22	$\sim 1.5$
5 keV $Ar^+ \rightarrow SiO_2$	1.05 <sup>3</sup>	5.84	0.18	$\sim 1.5$
1 keV $He^+ \rightarrow SiO_2$	0.15 <sup>4</sup>			0.15
5 keV $Ar^+ \rightarrow Al_2O_3$	0.1-0.9 <sup>3</sup>			
1 keV $He^+ \rightarrow Al_2O_3$	0.17 <sup>4</sup>			0.2
5 keV $Ar^+ \rightarrow MgO$	0.7-0.82 <sup>3</sup>			
5 keV $Ar^+ \rightarrow TiO_2$	0.9 <sup>3</sup>			
5 keV $Ar^+ \rightarrow CaCO_3$	1.15 <sup>3</sup>			

One of the main parameters controlling the sputtering yield for each element is the Surface Binding Energy,  $E^{SBE}$ , which depends on the local bonding environment in the outermost atomic layers. Published estimates of sputtering yields using SRIM/TRIM often simply use a default  $E^{SBE}$  value [Barghouty et al., 2011; Poppe and Curry, 2014; Wurz et al., 2007], although this quantity may be different for a particular atom in a metal or mineral silicate, and can differ between an amorphous or crystalline solid. Several efforts have been made to account for crystallinity and composition of the target based on the enthalpy of sublimation  $\Delta H^s$ , the enthalpy of formation  $\Delta H^f$ , and the enthalpy of dissociation  $\Delta H^d$  for a given mineral species [May et al., 2000]. SDTrimSP incorporates several different surface binding models appropriate for different sample types [Mutzke et al., 2011]. The simplest of these is the same as that used in SRIM/TRIM and treats  $E^{SBE}$  as a constant for each

<sup>1</sup>Determined using SRIM computational software [Ziegler et al., 2008]

<sup>2</sup>FTIR - Fourier Infrared Spectroscopy, yields measured in terms of  $Si - O$  bonds, not total atomic yield. [Schaible and Baragiola, 2014]

<sup>3</sup>SV - Sputtered Volume [Schirwitz, 1962; Bach, 1970]

<sup>4</sup>WL - Weight loss [Roth et al., 1979]

species regardless of the surface composition. Both programs allow the  $E^{SBE}$  of each element in the sample to be varied independently.

## 4.2.2 Mineral sputtering yields

Thiel et al. [1982] measured the total sputtering yield for a number of mineral and glass compositions irradiated with  $\sim 50 \text{ keV}$  noble gas ions (e.g., *Xe*, *Ar*, *He*). Since details on the mineral origin and precise sample composition were not given, reference compositions based on natural Earth abundances for

- Bytownite [ $(Ca, Na)(Si, Al)_4O_8$ ]
- Andesine [ $(Na, Ca)Al_{1-2}Si_{3-2}O_8$ ]
- Albite [ $NaAlSi_3O_8$ ]
- Augite [ $(Ca, Na)(Mg, Fe, Al, Ti)(Si, Al)_2O_6$ ]
- Olivine [ $(Mg, Fe)_2SiO_4$ ]
- Ilmenite [ $Fe^{2+}TiO_3$ ]

were taken from <http://www.webmineral.com/>. The experiments measured total yield by employing Tolansky multiple beam interferometry which could measure the surface position to within  $\sim 7 \text{ nm}$  [Thiel et al., 1982]. Details of the relative sputtering yields and surface composition changes were not included in these results.

Table 4.2 compares experimental yields with yields calculated using the Monte Carlo codes SRIM/TRIM, described in more detail in Section 4.3, for the minerals considered in Thiel et al. (1982). Two sets of simulations were run. The first used the default SRIM/TRIM default energies for the elemental surface binding energies,  $E_i^{SBE}$ , for all elements  $i$ . Maintaining  $E^{SBE}$  for the metal species equal to their sublimation energies and setting the surface binding energy of oxygen,  $E_O^{SBE} = 2 \text{ eV}$ , the SRIM program overestimates the sputtering yields by a

**Table 4.2:** Ion irradiation yields for several mineral and glass compositions as measured by Thiel et al. [1982]. All irradiations were performed using 50 keV ions. The computational results were obtained using the SRIM and SDTrimSP simulation software. The surface binding energies were modified to be proportional to the total mineral formation enthalpy which resulted in typically larger  $E^{SBE}$  and better agreement with the experimental results.

Ion	$Y_{Expt}$ [atoms/ion]	$Y_{SRIM}$ $E_O^{SBE} = 2.0 \text{ eV}$	$Y_{SRIM}$ $E_O^{SBE} \propto \Delta H^f$
Bytownite			
$Xe^+$	2.27±0.34	6.95	1.38
$^{40}Ar^+$	1.45±0.12	3.30	0.54
$^{20}Ne^+$	0.42±0.06	1.13	0.28
$^{14}N^+$	0.18±0.02	1.13	0.17
$^4He^+$	0.01±0.001	0.06	0.01
Olivine			
$Xe^+$	1.97±0.21	8.42	1.20
$^{20}Ne^+$	0.18±0.04	2.07	0.32
$^{14}N^+$	0.14±0.05	1.24	0.19
Andesine			
$Xe^+$	2.42±0.21	6.92	1.15
$^{40}Ar^+$	1.46±0.13	3.25	0.55
$^{20}Ne^+$	0.47±0.07	1.74	0.29
Albite			
$Xe^+$	2.56±0.27	6.86	–
$^{40}Ar^+$	1.73±0.14	3.19	0.55
$^{20}Ne^+$	0.49±0.05	1.73	0.29
Augite			
$Xe^+$	2.31±0.27	8.35	1.38
Ilmenite			
$Xe^+$	5.20±0.54	8.57	1.42

factor of several. Modified surface binding energies were obtained by first calculating the total heat of atomization for the mineral, e.g.  $\Delta H^f(SiO_2) + \Delta H^s(Si) + \Delta H^d(O_2)$ , and then determining the average heat of atomization in eV/atom. This average value is then used to calculate the percent difference from the default value for  $Si$  and the same percent difference then applied to the default  $E^{SBE}$  for all species following

$$E_i^{SBE} = \frac{\Delta H_i^s}{\Delta H_{Si}^s} \times \frac{1}{n} \left( \sum_i \Delta H_i^s + \Delta H^f + \Delta H^d \right) \quad (4.2)$$

where  $n$  is the number of atoms in a stoichiometric unit of the compound. Using the modified values of  $E^{SBE}$  to account for the total heat of atomization of mineral species brought compu-

tational results into better agreement with experiment, but still gave large disagreements with many of the measured sputtering yields. It is possible that this disagreement originates from SRIM's static nature, and that accounting for preferential sputtering and surface composition changes gives a better agreement with experiment. Alternatively, the disagreement could be due to the varying  $E_i^{SBE}$  for the metal species in the minerals that was not accounted for using the simple correction procedure described. Additional laboratory measurements and simulations using dynamically updated surface compositions are needed to better understand the effects of crystallinity, composition, and incident ions to guide the computational efforts and improve agreement between experimental and simulated sputtering yields.

### 4.2.3 Previous solar wind sputtering studies

Wurz et al. [2007] used SRIM/TRIM to estimate sputter yields for various compositions of lunar soil (Low Ti, High Ti, Highland and KREEP = Potassium, Rare Earth Elements, Phosphorus). Both  $H^+$  and  $He^{++}$  ions were considered and the incident ion angle was  $45^\circ$  to account for a rough surface. The sputtering yield for KREEP (Potassium, Rare Earth Elements, Phosphorus) soil is shown in Table 4.3, and the total sputtering yield for  $< 1 \text{ keV}/amu$  incident ions is  $Y_{tot} \sim 0.10$  atoms/ion. Additionally, Barghouty et al. [2011] simulated solar wind erosion of lunar KREEP soil using SRIM/TRIM using  $1 \text{ keV}/amu$  solar wind ions including the trace solar wind species and found that including sputtering contributions from heavier solar wind ions (e.g.  $O^{6-8+}$  and  $C^{4-6+}$ ) increased the total sputter yield 26% over  $H^+$  alone. However, the total yield calculated by Barghouty et al. [2011] is  $\sim 10\%$  less than that calculated by Wurz et al. [2007]. This is likely due to the use of lower energy solar wind in the Wurz simulations. As discussed further below, SRIM/TRIM gives increasing sputtering yields as the incident ion energy approaches zero and disagrees significantly with experimental data below  $\sim 10 \text{ keV}$ .

Barghouty et al. [2011] also calculated the percent change in the surface composition of KREEP type lunar soil as a function of incident ion fluence using the model of Starukhina

**Table 4.3:** The top rows give the average KREEP composition and SRIM sputtering yields calculated for solar wind ions ( $300\text{m/s}$ ,  $95\%H^+ + 5\%He^+$ ,  $45^\circ$  incidence angle) and given in terms of the number of ejected atoms per incident ion [Wurz et al., 2007]. The total computational yield is on the order of what would be expected based on experimental measurements from simple oxides shown in Table 4.1. The bottom rows give composition and SRIM sputtering yields calculated for lunar KREEP composition soils determined for normal incidence and including sputtering contributions from all solar wind ions [Barghouty et al., 2011]. The total yield scaled to a  $45^\circ$  incidence using  $\cos^{1.6}\theta$  is also given.

	O	Si	Mg	Ca	Al	Na	Ti	Fe	K	Mn	Cr	Total
$At\%$	60.82	17.35	5.39	4.43	6.48	0.44	0.62	4.47	0.19	0.06	0.10	100%
$Y_i$	0.07	0.01	0.008	0.007	0.004	0.001	0.0003	0.003	0.0004	$< 10^{-4}$	$< 10^{-4}$	0.104
$At\%$	58.1	17.2	4.8	5.2	6.5	0.4	2.4	5.1	0.1	0.10	0.10	
$Y_{sw}$	0.030	0.005	0.004	0.005	0.003	0.0005	0.002	0.0005	$< 10^{-4}$	$< 10^{-4}$	$< 10^{-4}$	0.051
										$Y_{tot}(\theta = 45^\circ) = 0.087$		

[2003] and total yield estimates derived from SRIM/TRIM. They found that the atomic abundance of *O* and other elements with low  $E^{SBE}$  decreases by  $\sim 17 - 40\%$ , while strongly bound species such as *Si* and *Ti* can be enhanced in a surface by as much as 80% of their original value. Including the additional effects of potential sputtering (due to the multiply charged states of the incident ions) led to a further enhancement in the total yield and more pronounced surface composition changes. Dukes and Baragiola [2015] measured surface oxygen abundance decreases of  $\sim 5 - 10\%$ , somewhat less than that predicted by Barghouty et al. [2011]. However, this can be explained by the geometry of the experiment and shadowing of the ion beam by the granular soil sample. Meyer et al. [2011] measured a factor of 2 enhancement in the total sputtering yield of multiply charged *Ar* ions ( $Ar^{6+}$  and  $Ar^{9+}$ ) over singly charged  $Ar^+$  incident on lunar soil simulants, and Barghouty et al. [2011] estimated an approximately 25% enhancement in total solar wind yield when including potential sputtering.

#### 4.2.4 Secondary ion sputtering yields

When silicates are bombarded by solar wind or magnetospheric ions, material is typically ejected in decreasing abundance as (a) neutral atoms, (b) ions and (c) molecules/clusters, and the ion yields given in Table 4.4 are  $\sim 2$  orders of magnitude smaller than the neutral (total) yields. The total yield dependence on the atomic surface abundance  $C_i$  (%) and the elemental surface binding energy  $E_i^{SBE}$ , the secondary ion yield,  $Y_i^+$ , additionally depends on the elemental ionization potential,  $E_i^{IE}$ , of each species. Ion sputtering yields from simple

oxides are estimated to compose 1 – 10% of the total sputter yield [Maul and Wittmaack, 1975; Elphic et al., 1991]. Unfortunately, absolute measurements of ion yields are difficult to measure accurately due to a large number of variable parameters, and often only ratios of various elements are given.

**Table 4.4:** Measurements of the total secondary ion yield, summed over all elements, from  $\text{SiO}_2$  and lunar soil simulant under  $\text{Ar}^+$  and  $\text{H}^+$  bombardment. Difficulty in comparing yields between different experimental systems suggests that a new set of self-consistent measurements could be useful.

Authors	Incident Ion $\rightarrow$ target	Ion Yield, $Y^{+,tot}$
Maul and Wittmaack [1975]	5 keV $\text{Ar}^+ \rightarrow \text{SiO}_2$	$2.5(\pm 1.3) \times 10^{-2}$
Maul and Wittmaack [1975]	1.5 keV $\text{H}^+ \rightarrow \text{SiO}_2$	$6.3(\pm 3.2) \times 10^{-4}$
Elphic et al. [1991]	5 keV $\text{Ar}^+ \rightarrow$ Lunar Simulant	$5.6(\pm 1.5) \times 10^{-2}$
Elphic et al. [1991]	1.5 keV $\text{H}^+ \rightarrow$ Lunar Simulant	$1.2(\pm 0.3) \times 10^{-4}$

A significant experimental contribution to our understanding of ion ejection from fine grained regoliths composed of predominantly silicate materials came over two decades ago [Elphic et al., 1991]. In these experiments lunar soil simulants (compositions given in Section A0.4) were irradiated on a commercial sputtering+SIMS system (Leybold SS-200) using several different incident ion+energy configurations and the ejected secondary ions were collected in a SIMS instrument. No energy data were collected, but by integrating the total signal and plotting vs. the stopping power (calculated following Ziegler, 1984) they were able to show that for noble gas ions the total yield, scaled to a 60 nA beam current (100  $\mu\text{m}$  beam, rastered over  $2 \times 2 \text{ mm}$  area, incident at  $50^\circ$ ) decreased with decreasing stopping power. However, an increase in the sputtering rate over the expected for  $\text{H}^+$  bombardment was left unexplained. Scaling the Si yield to the absolute yield measured from  $\text{SiO}_2$ , the expected elemental yields for 1.5 keV  $\text{H}^+$  bombardment of lunar soil composition materials range from  $\approx 9 \times 10^{-6}$  (Ca) to  $\approx 2 \times 10^{-5} \text{ ion}/\text{H}^+$  (Mg/Al/Si). The secondary ion fluxes given in Table 4.4 are for a typical solar wind flux of  $3 \times 10^8 \text{ ion}/\text{cm}^2 \cdot \text{s}$ .

### 4.3 Monte Carlo simulations of solar wind bombardment

The elemental component yield,  $Y_i$ , is the number of atoms of species  $i$  ejected per incident ion and can be readily calculated from Monte Carlo techniques. Typical Monte Carlo programs designed to simulate particle bombardment compute the ion-solid collision cascade using experimentally measured values for the collision cross-sections. The freeware program SRIM/TRIM is often used to simulate the radiation induced effects on a given sample composition with a wide range of ions and energies [Biersack and Eckstein, 1984]. SRIM is well proven for calculating net yields, penetration depths, and sputtered atom energy distributions for ion bombardment of metals at incident ion energies  $> 10 \text{ keV}$  [Ziegler et al., 2008].

However, SRIM/TRIM results are less certain for oxides and minerals where cohesive energies and bond strengths depend on the composition and structure of the solid and preferential sputtering leads to relative abundances in the target surface region which cannot be assumed to remain constant. Additionally, SRIM/TRIM has been shown to give inaccurate results even for metals when solar wind energy ( $\sim \text{keV}$ ) ions are considered [Wittmaack, 2004]. A more recently developed program, SDTrimSP [Mutzke et al., 2011], has been shown to accurately reproduce sputtering yields at low energies [Hofsäss et al., 2014]. In addition, SDTrimSP dynamically updates the target surface composition to account for preferential sputtering and also accounts for the re-emission of implanted atoms through diffusion. However, neither the SRIM/TRIM nor the SDTrimSP program is able to account for material crystallinity, chemical effects or surface topography, and this may influence comparisons with experiment.

Simulations using SRIM/TRIM and SDTrimSP were carried out to simulate solar wind bombardment of a wide variety of regolith analog materials. Extensive simulations were run for the simple oxide materials  $\text{SiO}_2$  and  $\text{Al}_2\text{O}_3$  in order to determine the simulation options

that best matched the experimental data [Roth et al., 1979]. A suite of meteorite and lunar soil compositions meant to be representative of the variety of silicate dominated solar system bodies were then used as initial conditions and simulations of  $> 50k$  incident ions were used to determine the elemental sputtering yields. The computational yields give the total number of sputtered atoms regardless of their charge state or possible molecular form. As discussed further in Section 4.5, the component yields,  $Y_i$ , determined from the simulations can be used together with experimentally determined ionization correction factors to predict the solar wind sputtered secondary ion fluxes and relative yield ratios from small bodies in the Solar System.

### 4.3.1 Oxide sputtering yields

Figure 4.3 gives the total sputtering yield for several simple oxide targets as a function of incident ion energy obtained using both the SRIM/TRIM and SDTrimSP simulation codes. For the SDTrimSP simulations, the metals were assumed to have  $E^{SBE} = \Delta H_i^s$  (e.g.  $Si(s) \rightarrow Si(g)$ ), while for oxygen  $E_O^{SBE}$  was varied between 1 – 3 eV. The SRIM/TRIM simulations were run using both the default  $E^{SBE}$  and modified values based on the formation enthalpy of the oxides obtained using Equation 4.2. However, it was seen that even for the increased  $E^{SBE}$  calculated using this method, SRIM/TRIM consistently overestimated the experimental total sputtering yields. Furthermore, the sputtering yields continued to increase at the lowest energies simulated ( $E^{inc} = 500$  eV) as opposed to decreasing following the experiments. Therefore it was concluded that SRIM/TRIM could not give a good match to the experimental data at solar wind energies and should not be used to estimate solar wind sputtering rates from rocky bodies.

The computational yields are compared against total sputtering yield measurements for simple oxides determined using large incident ion beam fluxes and removal of  $\mu g$  of material. The Wehner and KenKnight [1967] total sputtering yields were obtained using hydrogen and helium mass analyzed ion beams to drill holes through thin oxide foils. These yields are

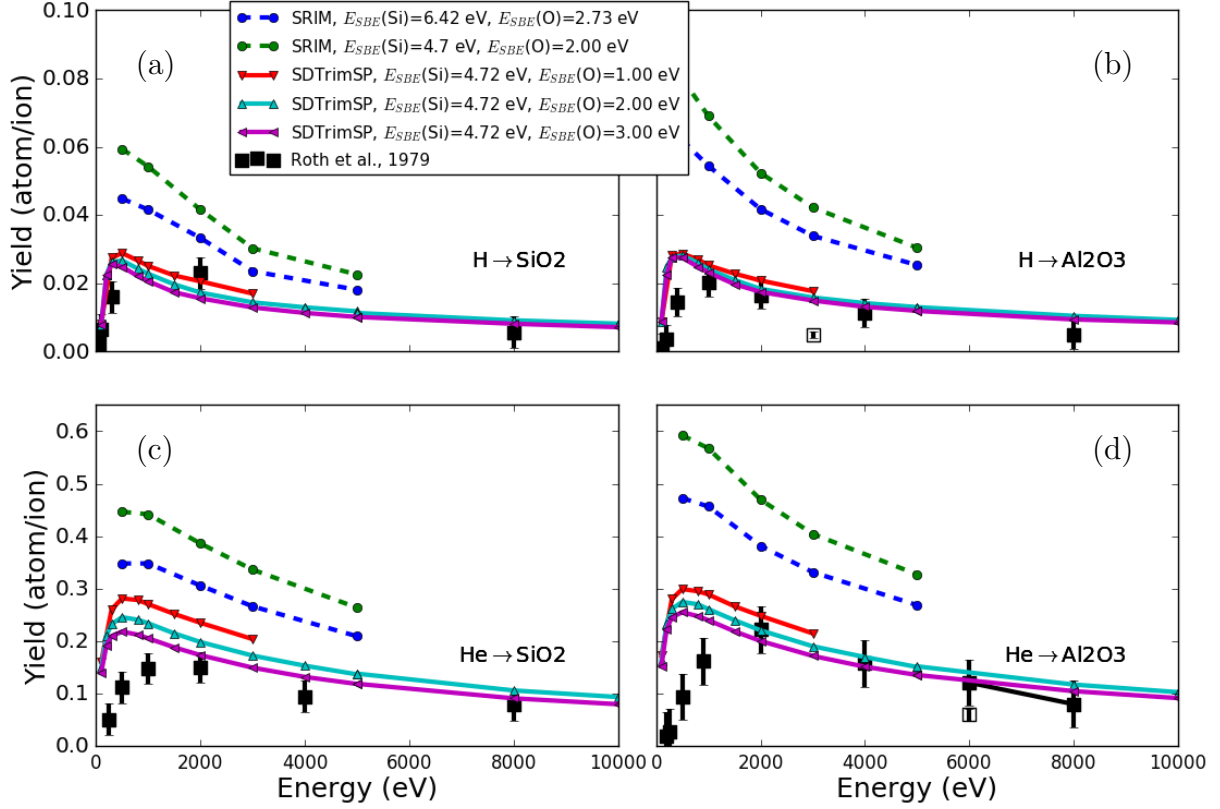


**Figure 4.3:** Total yields obtained from laboratory irradiation experiments of simple oxides by 0.1-10 keV  $H^+$  and  $He^+$  ions and compared with simulation results for SRIM and SDTrimSP. The oxides simulated were  $SiO_2$  (a and c) and  $Al_2O_3$  (b and d) and the ions used were H and He.

estimated to be uncertain by at least  $\sim 20\%$  [Wehner and KenKnight, 1967]. The Roth et al. [1979] results were taken using a 1 – 15 keV, mass analyzed ion accelerator, and samples were irradiated at fluxes of  $\sim 10^{15}$  ion/cm<sup>2</sup>/s to fluences  $> 10^{19}$  cm<sup>-2</sup>. Total yields were determined through weight loss measurements of the sample with a sensitivity of  $< 1 \mu g$ . Additionally, the hydrogen irradiations were performed using  $H_2^+$  since the beam currents obtained were much larger than for  $H^+$ , and low energy ( $< 4$  keV) beams were obtained by decelerating a 4 keV beam through a collimator system directly before the target [Bay et al., 1977]. Neutral atoms formed in collimation region were not separated from the incident ion beam and, since they could have a large influence on the measured total yields for low irradiation energies, were measured and correction factors applied to the total sputtering yields [Bay et al., 1977]. Unfortunately, a full analysis of experimental uncertainty is not available for the  $SiO_2$  and

$Al_2O_3$  data. A uniform uncertainty of 20% of the largest measured yield for each data set is applied to all experimental data in Figure 4.3. However, the true uncertainties in the measured total sputtering yields may be much larger, especially at energies  $< 4 \text{ keV}$ .

Although SRIM/TRIM agrees well with experimental measurements for elemental metal yields at  $E_{inc} > 10 \text{ keV}$  [Ziegler et al., 2008], it over-estimates the total sputtering yields from oxide and silicate materials by a factor of 2 – 3 at solar wind energies. This disagreement stems, at least in part, from the inability of SRIM to account for depletion of oxygen from the surface at high incident ion fluences. The dynamic code, SDTrimSP [Mutzke et al., 2011], matches the experimental data for  $H^+$  and  $He^+$  to within  $\sim 50\%$  for  $SiO_2$  and  $\sim 30\%$  for  $Al_2O_3$ . Deviations are smaller for energies  $> 1 \text{ keV}$ . Setting  $E_O^{SBE} = 2.0 \text{ eV}$ , slightly less than the molecular dissociation energy of  $\Delta H_d(O_2) = 2.73 \text{ eV}$ , gives slightly better agreement with data than  $E_O^{SBE} = 1.0 \text{ eV}$  or  $3.0 \text{ eV}$ . The uncertainties in the SDTrimSP calculations at high fluence, calculated from the variance at fluences  $> 10^{19} \text{ cm}^{-2}$  shown in Figure 4.4, are of the same order as the size of the data markers.

### 4.3.2 Depletion of surficial oxygen

As discussed in Subsection 2.3.2, ion irradiation tends to change the surface composition by preferentially sputtering weakly bound elements, thus resulting in an enrichment of strongly bound refractory species. Changes in surface composition caused by preferential sputtering can be studied using the SDTrimSP program. The program periodically updates the target composition in 1 nm depth sections, on the order of the depth from which the majority of sputtered material originates ( $\sim 2 \text{ nm}$ ). The total and elemental sputtering yields plotted as a function of fluence are shown in Figure 4.4 for  $1 \text{ keV } H^+$  and  $4 \text{ keV } He^+$  bombardment of  $SiO_2$  and  $Al_2O_3$ . It is seen that oxygen is rapidly depleted from the surface and  $Si/Al$  are enriched. An equilibrium state is reached at fluences of  $\sim 10^{19} \text{ cm}^{-2}$ , corresponding to solar wind exposure time of  $\sim 10^4 \text{ yr}$  at  $1 \text{ A.U.}$ , at which point the yields are approximately stoichiometric. This timescale implies that yields are expected to be approximately stoichiometric for the

majority of inner solar system bodies. For all simulations presented here, it was assumed that the incident ions were removed from the target after their energy dropped below the minimum system threshold displacement energy  $E_{Disp}$  which is  $\sim 15-25\text{eV}$  for most elements. Therefore, no accumulation of the incident ions occurred. A second set of simulations was run where  $H$  and  $He$  were allowed to accumulate in the sample. However, these did not improve the fits to the experimental data and, due to uncertain diffusion coefficients and structural effects on the solids, these simulations are neglected here.

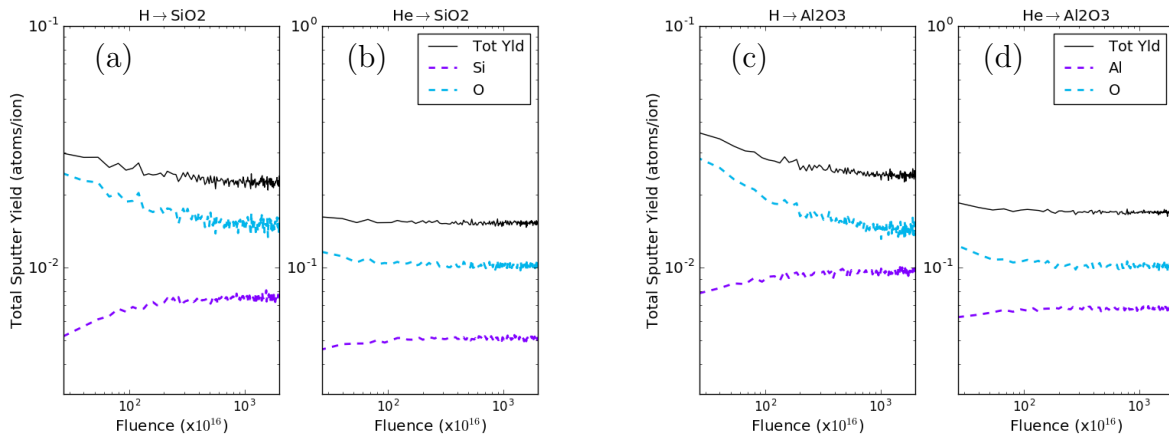


**Figure 4.4:** Total and individual element sputtering yields as a function of incident ion fluence obtained from SDTrimSP simulations. Figures (a/b) show respectively H/He irradiation of  $SiO_2$ , and figures (c/d) irradiation of  $Al_2O_3$ . The yields are approximately stoichiometric after a fluence of  $\sim 1 \times 10^{19}$  ions/cm<sup>2</sup>. The total (neutral+ion+molecular) for  $Si$  is on the order of 0.01  $Si$  per incident  $H$  and 0.05  $Si$  per incident  $He$ . Note the different scales used for the  $H$  and  $He$  incident ions.

The dominant changes in sputtering yields of  $SiO_2$  are for oxygen where the elemental yield,  $Y_O$ , decreases by  $\sim 20\%$  and, while  $Y_{Si}$  can increase by up to  $\sim 50\%$ , the total yield decreases. This indicates a changing surface composition for the material where oxygen is depleted and the refractory species is enriched. Although the actual computed surface compositions for the simulations presented here were not fully analyzed, the surface abundance of  $Si$  and  $O$  for initially stoichiometric  $SiO_2$  were provided by A. Mutzke (personal communication) as a function of fluence and depth. In Figure 4.5a it is seen that  $Si$  is enriched and makes up  $\sim 70\%$  of the total surface abundance at high fluences. However, in Figure 4.5b, it is seen that for depths of  $\sim 2\text{nm}$  the oxygen abundance can be enriched above its stoichiometric value. Due to the difficulty in understanding combined radiation

and thermally induced diffusion in crystalline versus amorphous solids, it is unclear whether the enrichment of  $O$  at depths of  $1\text{ nm}$  ( $\sim 2$  atomic monolayers) also occurs in astrophysical silicates subjected to solar wind bombardment. The final oxidation state of the surface is of interest as it may have implications for understanding the origins of protoplanetary silicate grains and their catalytic effects on chemical reactions of volatile molecules such as  $H_2O$  and  $CO_2$  [Gontareva et al., 2009].

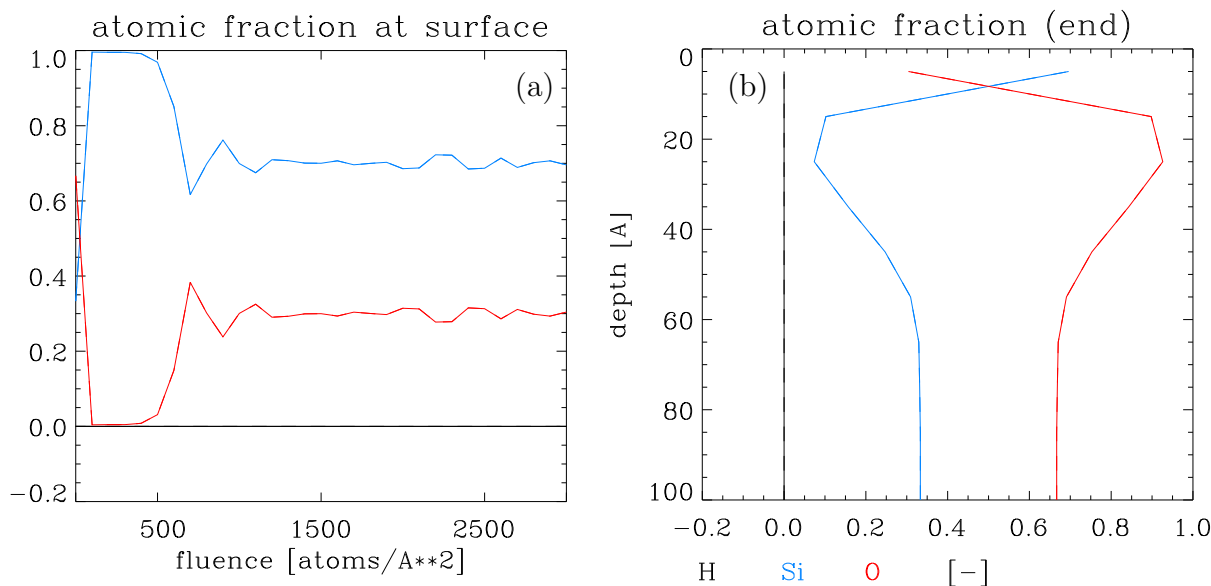


**Figure 4.5:** From A. Mutzke. (a) The atomic fraction of  $Si$  and  $O$  in the uppermost surface of initially stoichiometric  $SiO_2$ . The  $Si$  abundance increased to  $\sim 70\%$  at high fluences. (b) Atomic surface abundance as a function of depth below the target surface calculated after large fluences ( $> 10^{19}\text{ cm}^{-2}$ ).

### 4.3.3 Sputtering from regolith analog compositions

Using published bulk compositions for the suite of meteorites representative of the variety of silicate bodies found in the solar system, the elemental component yields,  $Y_i$ , due to solar wind sputtering of flat, amorphous targets were determined using Monte Carlo programs. Although all simulations were also run for SRIM/TRIM, due to the inaccuracy of this program at solar wind energies these results are not included here. The atomic abundance of the major elements for the lunar soil samples, given in Table 4.5, were taken from the lunar sample compendium for bulk composition and measured in situ prior to irradiation using

X-ray Absorption Spectroscopy (XPS) spectroscopy [Dukes and Baragiola, 2015; Housley, 1992]. Lunar soils 65901 (LS65901) and 62231 (LS62231) are mature highland samples of similar composition, while 10084 (LS10084) is typical of mare soils. The total yields  $Y^{tot}$  calculated by SDTrimSP are given for these lunar soils in Table 4.5. It is seen that  $Y^{tot}$  is a factor of  $\sim 2$  less than the SRIM/TRIM results given in Table 4.3, consistent with the yield results discussed for simple oxides above. This implies that previous solar wind sputtering rates and exosphere density calculations that have relied on SRIM/TRIM simulations have been systematically overestimated by a factor of  $\sim 2$ .

**Table 4.5:** Compositions  $C(i)$  given in atomic fraction for returned Apollo 16 and Apollo 11 mature lunar soil samples for which secondary ion spectra have been collected [Schaible, 2014; Dukes and Baragiola, 2015]. Bulk sample compositions were taken from the Lunar Sample Compendium [Korotev et al., 1981; Korotev, 1982; Korotev and Gillis, 2001], and the XPS compositions representative of the uppermost several monolayers were taken from Housley [1992] for LS65901, and from Dukes and Baragiola [2015] for LS62231 and LS10084. The elemental yields  $Y_i$  were determined from SDTrimSP calculations and are given for solar wind composition incident ions (95%  $1\text{ keV } H^+$  and 5%  $4\text{ keV } He^+$ ). The yield ratios determined by SDTrimSP are approximately stoichiometric for high fluences ( $> 10^{18}\text{ cm}^{-2}$ ).

	LS65901			LS62231			LS10084		
	Mature Highland Soil			Mature Highland Soil			Mature Mare Soil		
	Bulk [At. %]	XPS [At. %]	$Y^{tot}(i)$ [atom/ion]	Bulk [At. %]	XPS [At. %]	$Y^{tot}(i)$ [atom/ion]	Bulk [At. %]	XPS [At. %]	$Y^{tot}(i)$ [atom/ion]
Na	0.16	0.16	0.0001	0.14	0.20	0.0001	0.16	0.20	0.0001
Mg	3.21	2.10	0.0004	3.19	0.70	0.0003	4.38	1.20	0.0004
Al	5.42	9.40	0.0026	5.35	9.60	0.0024	2.98	7.00	0.0024
Si	15.70	18.50	0.0058	15.53	18.40	0.0055	15.68	15.80	0.0055
K	0.02	0.02	<0.0001	0.03	0.03	<0.0001	0.03	0.03	<0.0001
Ca	5.58	5.30	0.0018	5.69	3.10	0.0011	4.78	2.20	0.0008
Ti	0.16	0.16	0.0001	0.16	0.10	<0.0001	2.12	0.80	0.0003
Mn	0.02	0.02	<0.0001	0.03	0.03	<0.0001	0.07	0.30	0.0001
Fe	1.68	3.10	0.0022	1.41	2.30	0.0008	4.93	6.10	0.0022
O	68.06	61.24	0.0243	68.48	65.54	0.0229	64.87	66.37	0.0229
$\sum_i Y^{tot}(i)$	0.034			0.035			0.035		

The remaining analog compositions were taken from published values for the representative suite of meteorite compositions listed in Table 4.6, and the tabulated compositions are given in Section A0.4. Several of the published meteorite compositions (e.g., carbonaceous chondrites) contained a significant amount of structurally bound non-refractory species such as hydrogen, carbon, and nitrogen, in addition to structural oxygen. Since sputtering occurs from only the uppermost several monolayers, a region expected to be hydrogen saturated due to solar wind bombardment, structural hydrogen was neglected in the simulations. Nitrogen

makes up only a small atomic percentage of the total composition and, due to its unknown chemical state in the target, nitrogen was also neglected in the simulated compositions. For target compositions containing carbon,  $E_C^{SBE} = 7.37 \text{ eV}$  was used. The defaults for  $E_i^{SBE}$  given in Table 4.7 were used for the metal refractory species, and  $E_O^{SBE} = 2 \text{ eV}$  was taken for oxygen. The remaining SDTrimSP target and incident ion settings used in the lunar soil and meteorite composition simulations were the same as those used to obtain the best match to experimental data for  $SiO_2$  and  $Al_2O_3$  discussed above. The total yields for each individual class of parent bodies are given in Table 4.6 for both total and secondary ion sputtering yields.

**Table 4.6:** Meteorite types and sample compositions considered. The Mars meteorite compositions are given in Lodders (1998) and Gellert et al. (2006). The HED and Ureilite compositions are taken from Jarosewich (1990). The chondrite compositions are based on group averages and given in Lodders and Fegley (1998). The aubrite compositions are taken from Easton (1985). The average total yield and variance determined from SDTrimSP simulations are given in (atoms/ion) for each of the indicated groupings.

Martian	HED	Ureilites	Carbonaceous Chondrites	Enstatite+ Ordinary Chondrites	Aubrites
EETA79001 A	Sioux County	ALH84136	CM	EL	Bishopville
EETA79001 B	Serra de Magé	ALHA77257	CV	EH	Bustee
Shergotty	Y-791195	North Haig	CO	L	Khor Temiki
ALH 84001	Johnstown	Dingo Pup	CK	LL	Mayo Belwa
Nakhla	Bholghati	Donga	CR	A	Norton County
Chassigny	EET 87503		CH	K	Pena Blanca Sp.
Adirondack	Bialystok		CI	H	Shallowater
Humphrey	Petersburg			R	Aubres
Mazatzal Brook. ALHA77005	Haraiya				
$Y^{tot} =$ 0.0325	0.0322	0.0341	0.0322	0.0305	0.0370
$Y^+ =$ $6.4 \times 10^{-4}$	$4.8 \times 10^{-4}$	$6.4 \times 10^{-4}$	$5.5 \times 10^{-4}$	$6.1 \times 10^{-4}$	$7.7 \times 10^{-4}$

As shown in Table 4.5, the elemental yields in terms of the average number of atoms of species  $i$  ejected per incident ion can be determined directly from the Monte Carlo simulations. As with the simple oxides discussed above, the yields of oxygen and other weakly bound species are seen to decrease with increasing fluence, while the yield of strongly bound refractories is seen to increase with fluence until a steady state is reached at fluences  $> 10^{17} \text{ cm}^{-2}$ . Plots of the  $1 \text{ keV } H^+$  and  $4 \text{ keV } He^+$  elemental yields as a function of fluence are shown for lunar soils and carbonaceous chondrites in Figure 4.6.

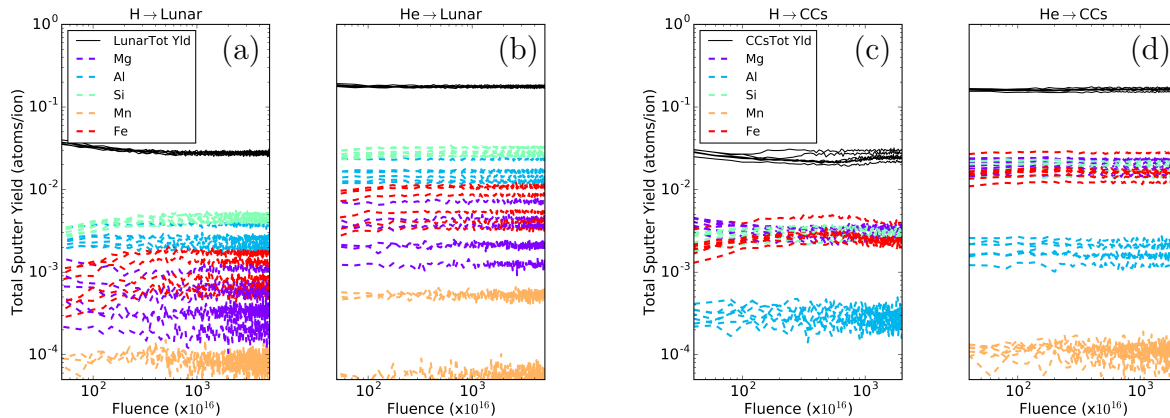


**Figure 4.6:** Total and individual element sputtering yields for the lunar samples listed in Table 4.5, in addition to the lunar soil analog compositions given in Elphic et al. [1991] as a function of incident ion fluence obtained from SDTrimSP simulations. Also shown are the elemental sputtering yields for the carbonaceous chondrite compositions given in Section A0.4. Note hydrogen and nitrogen present in the measured compositions were neglected in the simulated compositions.

## 4.4 Laboratory measurements of secondary ions from lunar soil

During my Master’s Thesis work, I participated in a series of experiments aimed at studying sputtering processes from soils obtained during the Apollo missions [Schaible, 2014]. The soils were obtained on loan from the NASA Curation Facility for studies of water formation and removal processes. During the course of these experiments, SIMS spectra were collected for a variety of incident ions. Although these data were never formally published, appearing only as part of yearly progress reports submitted to NASA in fulfillment of requirements for a NESSF research fellowship, at the time they consisted of the first full ion spectra collected from the bulk (multigranular), loose lunar soils. I had the good fortune to encounter a problem in my PhD work that allowed me to revisit these data and use them as a calibration for simulation results of solar wind sputtering of regolith analog materials.

### 4.4.1 Experimental system

The experiments were carried out at the Laboratory for Atomic and Surface Physics in collaboration with Cathy A. Dukes and Prof. R. A. Baragiola. Samples were placed in an

Ultra High Vacuum (UHV) chamber pumped to pressures of  $\sim 10^{-10}$  Torr using an ion pump. The chamber was equipped with a low energy ion gun (non-mass analyzed) capable of irradiating samples with 1 – 5 keV ions of any easily ionized gas (e.g.,  $H_2$ ,  $He$ ,  $Ar$  etc.). The sample, lunar soil 65901 (LS65901), the composition of which is given in Table 4.5, was bombarded with 1 keV  $Xe^+$ , 4 keV  $He^+$ , and 2 keV  $H_2^+$  ions. Sample surface compositions were measured in situ by X-ray photoelectron spectroscopy (XPS) and SIMS spectra were taken with a Hiden Analytical EQS mass spectrometer. For this study, positive SIMS spectra were measured at ejected ion energies over the range of 2 to 36 eV, a range where the instrument transmission is expected to be roughly constant as a function of energy. The extraction lens voltages were optimized for ions of mass 27 (Al+) before collecting spectra. Because the lunar soils charged significantly under ion bombardment, the sample surface was charge neutralized during SIMS data collection using low energy ( $\leq 4$  eV) electrons. A schematic of the chamber used is shown in Figure 4.7.

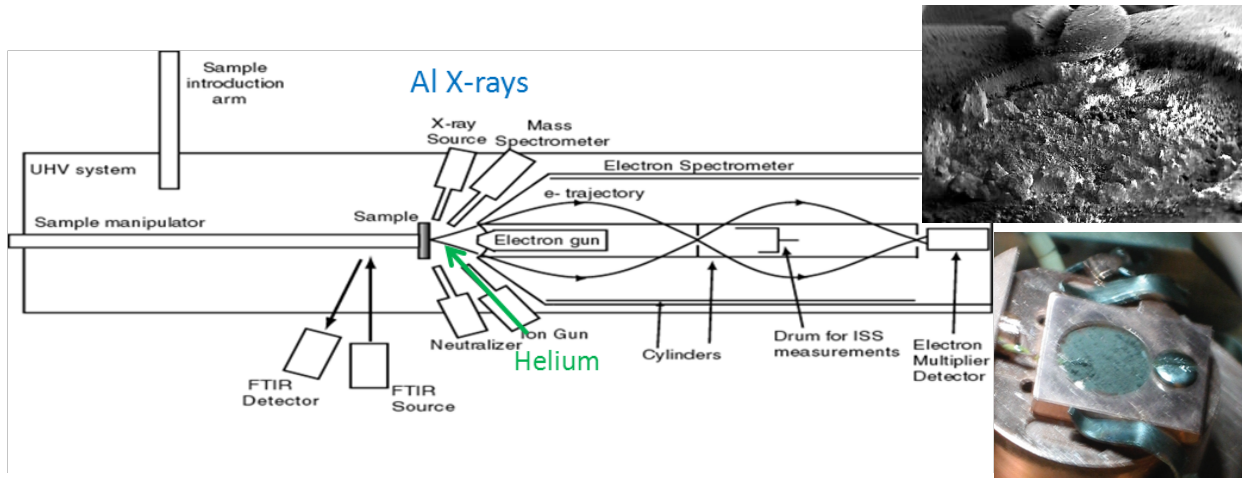


**Figure 4.7:** Schematic of the Surface Science Chamber (SSC) housed in the Laboratory for Atomic and Surface Physics at the University of Virginia. A photo of the in-situ sample and a SEM magnified image of the soil collected prior to irradiation are shown on the right hand side. Sample compositions were determined in situ using XPS, and SIMS spectra were collected using a Hiden Analytical EQS. The FTIR instrument was not used in this study

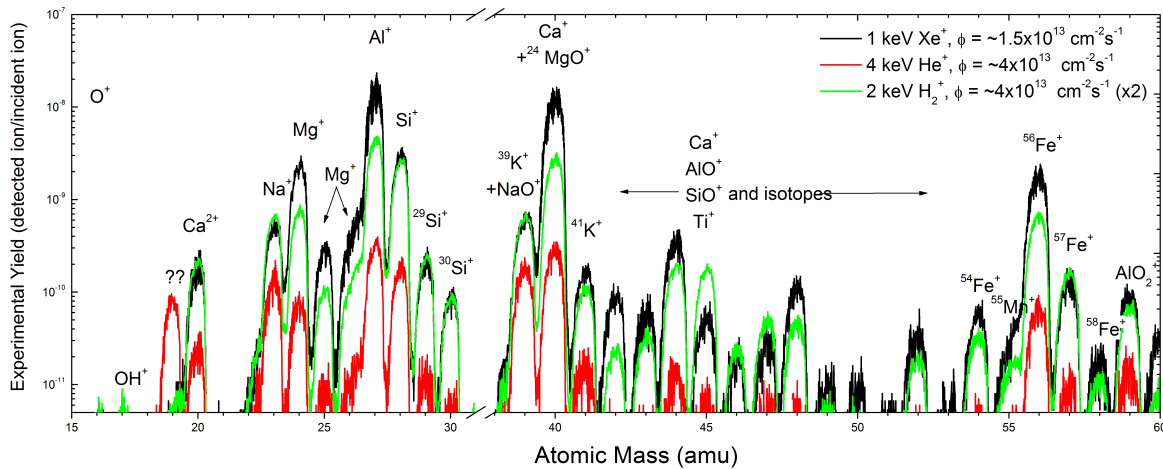
#### 4.4.2 Measured secondary ion spectra

Figure 4.8 shows a comparison of the raw counts obtained for solar wind ion bombardment of LS65901 [Schaible, 2014] for various incident ions. The peaks have been labeled with the

most probable ion type and the relative peak heights were used to determine the isotope and oxide ratios for several species. The raw counts obtained in the experiment were converted into an approximate yield (ejected ions/incident ion) by dividing by the incident ion flux and the approximate spot size of the beam:  $Y_{exp} = Y_{raw}/(\phi_{ion} \cdot A_{beam})$ . For the hydrogen irradiation the signal was further divided by a factor of two to account for the additional atom in  $H_2^+$ . The heights of the curves represent the relative sputtering yields for each of the incident ions. The hydrogen yield relative to the noble gas ions is much higher than expected, similar to the results found by Elphic et al. [1991].

The total ion yield  $Y_i^+$  given in Figure 4.8 is much lower than total yield values given in Table 4.4. This reduced yield can be explained by a limited instrument aperture and orientation of the instrument with respect to the peak of the distribution. Ejecta from a rough surface are expected to leave in a cosine distribution oriented normal to the surface regardless of the ion beam incidence angle [Cassidy and Johnson, 2005]. Due to spreading, few atoms pass through the narrow aperture of the SIMS detector. Incident ion flux and spot size measurements limit yield measurements to at best an order of magnitude approximation. Total count rates for a unit mass range measured in the laboratory are typically on the order of  $10^6 s^{-1}$  for incident ion fluxes of  $10^{13} cm^{-2}s^{-1}$  [Elphic et al., 1991; Schaible, 2014]. Crudely extrapolating to solar wind fluxes at 1 AU ( $\sim 10^8 cm^{-2}s^{-1}$ ) implies that secondary ion fluxes of only  $\sim 0.1 cm^{-2}s^{-1}$  are available at spacecraft altitudes of 40 km due to solar wind bombardment of small airless bodies. However, using spacecraft instruments with a larger aperture opening than the laboratory instrument would lead to further enhancements in the count rates.

A comparison of normalized SIMS spectra for lunar simulants [Elphic et al., 1991] and for lunar soils [Schaible, 2014; Dukes and Baragiola, 2015] is given in Figure 4.9. The total count intensity in the Schaible [2014] measurements was approximately an order of magnitude greater than the Elphic et al. [1991] results, even though the incident flux in atoms/( $cm^2s$ ) was approximately an order of magnitude less. This is likely due to a larger flux of ejected



**Figure 4.8:** Experimental SIMS yields for lunar soil sample 65901 obtained during 1 keV Xe<sup>+</sup>, 4 keV He<sup>+</sup>, and 2 keV H<sub>2</sub><sup>+</sup> ion bombardment of the loose (un-adhered and un-compressed) soil using the system shown in Figure 4.7.

ions being captured or greater instrument sensitivity. Unfortunately, further experimental details of the Elphic et al. [1991] experiments are not available for comparison. Although the fraction of sputtered species that leave the surface as oxide molecules is not well known, the data in Figure 4.9 indicate that it is at least 10 times smaller than the elemental ion yield. Therefore, contributions from molecular species to the SIMS intensity are neglected in the calculations below. Although the radiation fluxes used were much greater than those expected in the interplanetary medium, these results indicate that high quality laboratory mass spectra can be obtained in a short time-scale (minutes for the fluxes used in these experiments) and using the resolving power of such an instrument with long integration times in the environment around an airless bodies should allow an abundance of compositional information to be obtained.

#### 4.4.3 Hydrogen bombardment chemistry

It is important to note that incident H<sup>+</sup> can chemically react with the target material, and experiments seem to indicate that hydrogen sputtering of oxide targets such as lunar soil may effect both total and secondary ion yields. Figure 4.9 indicates that the raw hydrogen

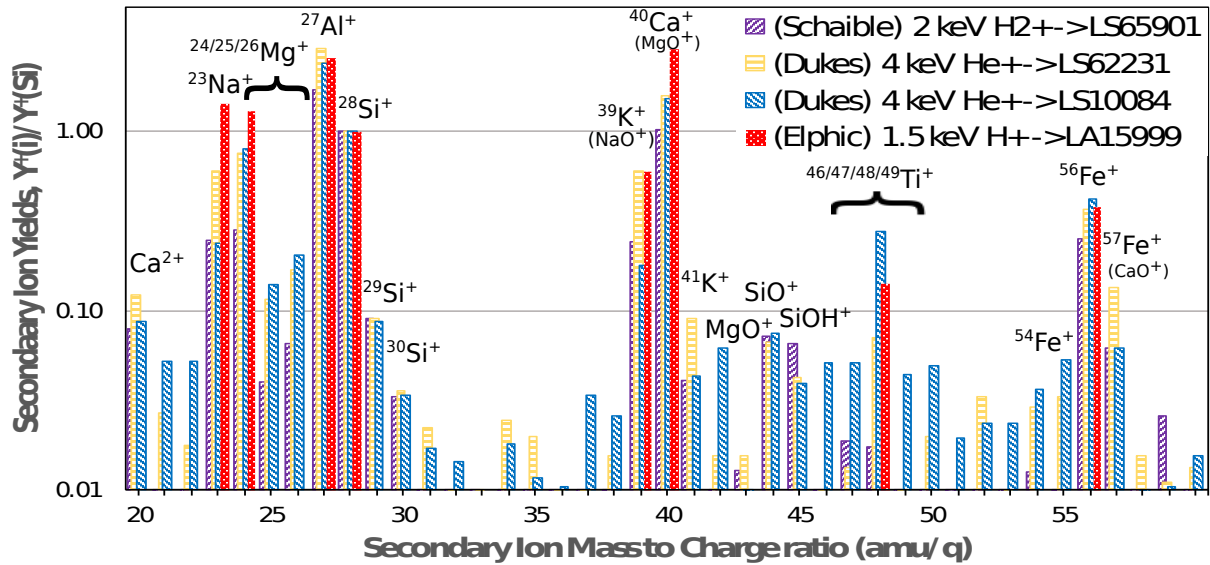


**Figure 4.9:** Comparison of the normalized experimental yields obtained in the Elphic et al. and LASP measurements for ion bombardment of lunar soil obtained during the Apollo missions and lunar soil simulants. The more recent measurements contain abundant isotopic and oxide peak information. Oxide ions are detected in all experiments.

yield is greater than the helium yield, although it would be expected to be a factor of  $\sim 10$  less. This has been seen previously in measurements at UVA and was ascribed to ‘molecular effects’, but the effects were never well studied (C. Dukes, private communication). Elphic et al. [1991] cited a similarly enhanced secondary ion yield for  $H$  bombardment of lunar soil simulants compared to what was expected based on scaling the nuclear stopping power from noble gas secondary ion yields. One possible explanation for the enhancement would be the formation of hydroxides in the solid which effectively decrease the bond energies/lower the surface binding energies. It is not currently understood whether lowering the surface binding energies of refractory species through chemical bond formation is a sufficient effect to make up the large difference between expected and measured secondary ion yields for  $H$ . Alternatively, or perhaps additionally, efficient reflection and scattering of incident  $H$  in the solid can lead to enhanced upward movement of energetic hydrogen atoms leading to increased knock-on collisions near the sample surface and resulting in an enhancement in the secondary ion sputtering yield.

Suggestions of the importance of hydrogen chemistry are also given in Schaible and

Baragiola [2014] where it is shown that total 5 keV  $Ar^+$  sputtering yield, determined via FTIR spectroscopy, was larger after  $> 10^{17} H^+ / cm^2$  irradiation fluences. The increased total yield was interpreted as a weakening or breaking of the  $Si - O$  bond strength due to the reaction of  $H$  with the oxygen to form silanol ( $SiOH$ ) [Schaible and Baragiola, 2014]. This is a potentially important result, and could imply that secondary ions are more abundant than would be suggested based on Monte Carlo models which do not include hydrogen chemistry such as the methods described above. However, the experiments were performed with molecular hydrogen while solar wind hydrogen is atomic, and although it appears that there is some sputtering enhancement above what is expected from extrapolation of data taken for heavy ions, care should be taken in extrapolating this assumption to atomic hydrogen. The effects of  $H^+$  bombardment of silicates and oxides are not well understood and further experimental investigation is needed.

#### 4.4.4 Isotope fractionation

For IMS instruments with a resolving power  $\Delta m/m < 1$ , individual mass peaks may be deconvolved through knowledge of the isotope ratios for each element. Theoretically, the measured height of an abundant isotope (i.e.  $^{41}K^+$ ) can be used to determine the elemental contribution to a shared peak (i.e. mass 39 =  $^{39}K^+ + NaO$ ) and place constraints on the oxide ion contribution. Alternatively, resolving powers  $\Delta m/m \ll 1$  are needed to distinguish small nuclear mass differences in each mass unit. Comparisons were made with Earth abundances, and although the isotope ratios may be somewhat different for Earth and lunar soils, the estimates are accurate to  $\sim 1\%$ . However, this is much greater than any of the isotopic differences between Earth and the Moon [Poitrasson et al., 2004], and such results are of limited value.

### 4.4.5 Sputtered atom energies

In order to predict sputtered densities and optimize instrument pointing angles, the velocities of the ejected ions must be known. Experimental data from LS65901 are shown in Figure 4.10 and Figure 4.11 for several ion irradiation types. It is seen that the ejected ions have broad energy distributions that peak at  $\sim 10$  eV and have roughly the same shape distribution for all elements and incident ion types. The heights of the curves in Figure 4.10 represent the ion counts for each species obtained under the same experimental conditions. The peak positions vary within  $\sim 3$  eV and it is seen that elements with a high  $E^{IE}$  such as *Si* peak at higher energies, while easily ionized species such as *Na* peak at lower energies. The precise relationship between  $E_i^{IE}$  and the peak position of the sputtered secondary ion energy distribution was not fully analyzed, but could be important for the design of spacecraft IMS.

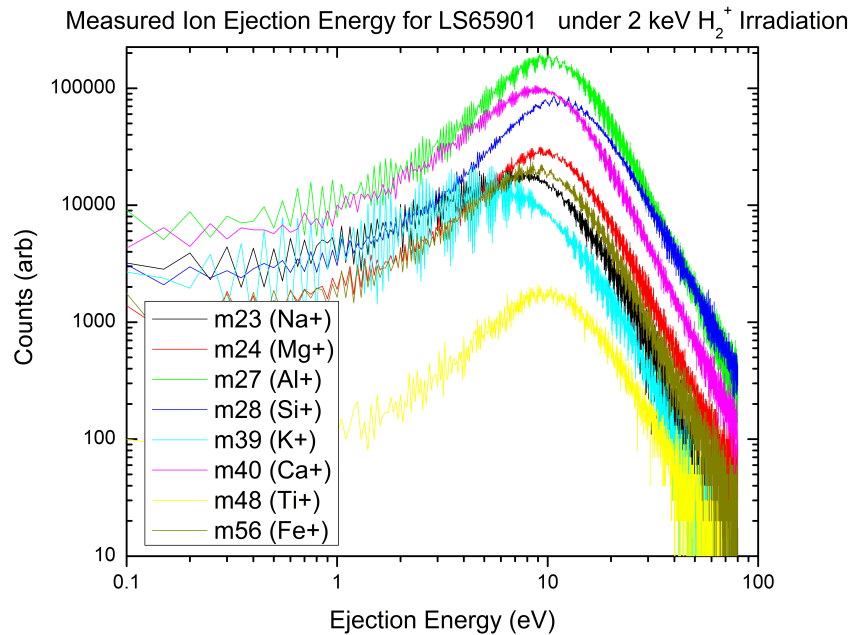


**Figure 4.10:** Raw energy distribution for ejected ions from LS65901 under 2 keV  $H_2^+$  irradiation. Comparison of the normalized ejection energy distribution for Si ions from LS65901.

The normalized sputtered ion energy distributions of  $^{28}Si^+$  are shown for 2 keV  $H_2^+$ , 4 keV  $He^+$  and 1 keV  $Xe^+$  bombardment of LS65901 in the top panel of Figure 4.11. The

energy distribution for  $H_2^+$  bombardment is more narrowly peaked and maximum at a lower energy than the  $He^+$  or  $Xe^+$ . As described further below, the precise energy distribution for sputtered ions becomes important far from the surface of an airless body where ambient fields can modify the ion energy and trajectory. Further experiments are needed to determine the precise relationship between a sputtered ion energy distribution and incident ion mass, energy or surface composition.

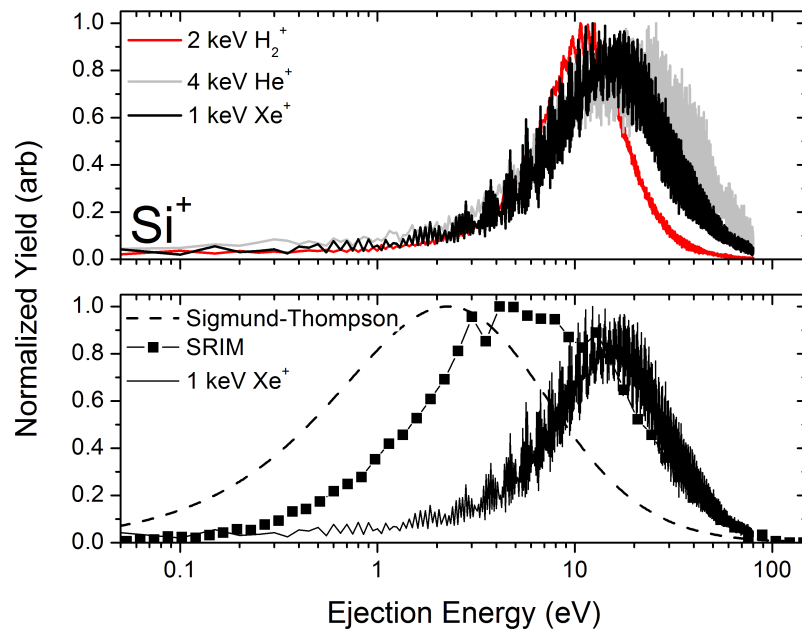


**Figure 4.11:** Comparison of the normalized ejection energy distribution for Si ions from LS65901 (top) irradiated by different ions and (bottom) for experimentally measured, from SRIM calculations, and estimated from theoretical considerations (ST), all assuming 1 keV  $Xe^+$  irradiation.

Density estimates around airless bodies present in the literature typically assume that sputtered neutral species leave with a Sigmund/Thompson (ST) energy distribution as described in Subsection 2.3.1. Cassidy and Johnson [2005] modeled sputtering from a grainy regolith and found the same broad distribution of sputtered species for Na. The energy distribution of sputtered species peaked near  $0.01 eV$  while there was still a significant fraction of sputtered ions with low energies  $< 0.001 eV$  and the fraction of sputtered species with energies near  $1 eV$  was negligible. However, comparison with measured ejection energies from

ion bombardment experiments on lunar soil [Schaible, 2014] and ejected energy distributions calculated by SRIM show that the maximum yield occurs at much higher energies than predicted by the Sigmund distribution. A comparison of the ejected energy distributions due to 1 keV  $Xe^+$  irradiation of LS65901 calculated using Equation 2.5 and energy distribution output from SRIM/TRIM simulations is given in the bottom panel of Figure 4.11. It can be seen that both the SRIM/TRIM and Sigmund distributions greatly underestimate the sputtered energy distribution for ions, and therefore should not be used to make predictions for sputtered ions.

## 4.5 Modeling of secondary ion spectra

The secondary ion yield is related to the total sputtering yield by  $\alpha_i = Y_i^+/Y_i$ , where  $\alpha_i$  is the ionization probability. By knowing  $\alpha_i$  for each species in a sample, the secondary ion spectra and corresponding ion fluxes under solar wind bombardment conditions can be calculated using the total yields determined from Monte Carlo methods. However, measuring  $\alpha_i$  independently for each element in a complex, multi-component material is experimentally difficult. Therefore, we define relative yields with respect to  $Si$  which, due to its presence in roughly equal amounts in all meteorite types, serves as a convenient fiducial. The relative yield,  $R_i$ , for element  $i$  with respect to  $Si$  can be determined from measured secondary ion spectra and target compositions, and is defined as

$$R_i = \frac{Y_i^+ C_{Si}}{Y_{Si}^+ C_i} \quad (4.3)$$

where  $C_i$  is the composition of species  $i$ . As discussed above, at high fluences the total sputtering yield ratio  $Y_{Si}/Y_i$  is constant and equals the sample composition  $C_{Si}/C_i$ .

The relative yield correction factors calculated from secondary ion spectra of several lunar soil and analog targets and for numerous ion types and energies are shown in Figure 4.12. The relative ion yields have been found to roughly obey the relation  $Y_I^+ \propto C_i \exp(-E_i^{IE}/E_c)$

where  $E_i^{IE}$  is the first ionization energy and  $E_c$  is a characteristic energy [Andersen and Hinthorne, 1972; Elphic et al., 1991]. The exponential dependence in the first ionization energy, given for several elements in Table 4.7 so that easily ionized species (e.g., *Ca*) come off with relatively larger fluxes than could be expected based on atomic abundance alone. This same trend is observed here. The sputtering results for a variety of samples and incident ions [Elphic et al., 1991; Schaible, 2014; Dukes and Baragiola, 2015] were used to determine the approximate relative yield dependence on ionization potential, and these results will be used to correct the computational total yield predictions and determine secondary ion fluxes due to solar wind sputtering of silicate surfaces in space.

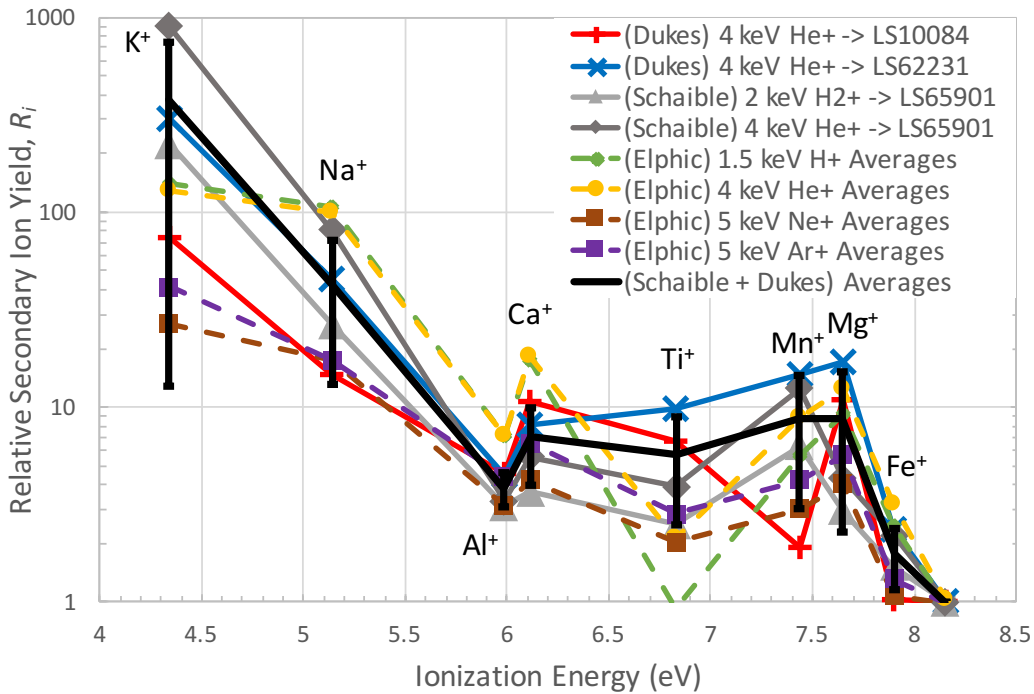


**Figure 4.12:** Relative secondary ion yields calculated for the lunar soil compositions given in Table 4.5 (LS65901, LS62231, and LS10084) bombarded by  $2\text{keV } H_2^+$  and  $4\text{keV } He^+$  incident ions [Schaible, 2014; Dukes and Baragiola, 2015]. The relative yields show a roughly exponential dependence on the elemental ionization energy. Results from [Elphic et al., 1991] are also shown. Results for multiple incident ions are shown, and the values are averaged for three Apollo soil analogs (LA10899, LA15999, LA69999) such that only limited compositional effects are taken into account. The average was calculated including only the results for actual lunar soils and SW ions, and the error bars represent the  $1\sigma$  variance in the calculated relative yields. Oxygen is not shown since it sputters primarily as a negative ion and thus is not easily measured simultaneously with the positively charged metal ions.

The source of the experimental variance between targets may be due to differences in  $C_i$  and  $E_i^{SBE}$  for a given species or differing chemical effects of the incident ion. It has long been known that the presence of oxygen tends to increase the secondary ion yield from

metals and semiconductors [Benninghoven, 1975]. When targets containing  $Si$  are bombarded by  $\sim keV Ar^+$  in the presence of a controlled oxygen atmosphere,  $\alpha_{Si} \sim 0.2$  for  $SiO_4$  stoichiometry, and  $\alpha_{Si} \sim 0.01$  for 40%  $O$  in the presence of a controlled oxygen atmosphere [Franzreb et al., 2004]. Since sputtering depletes oxygen from the uppermost surface and at large fluences the total yield is stoichiometric with the bulk composition, the concentration  $C_O$  in the uppermost  $nm$  of the target can be significantly depleted, thereby complicating estimates of the ionization efficiencies. Ultimately, the dependence on composition, crystalline structure, and incident ion remains uncertain. Although there are large uncertainties in the  $R_i$  determined from experimental SIMS spectra, a roughly exponential decrease is seen in the relative yield with increasing ionization energy. Additional experiments on a variety of mineral and amorphous samples would allow structure and composition dependence to be better understood. However, the experimental data in Figure 4.12 can be used to roughly predict relative secondary ion yields corrected for target composition.

### 4.5.1 Combining experimental and computational results

The average relative yield,  $\langle R_i \rangle$ , and variance for  $2 keV H_2^+$  and  $4 keV He^+$  irradiation of lunar soils measured using the experimental system in Figure 4.7 are given in Table 4.7. Since only  $\sim nm$  of surface material is removed during irradiation, we use the compositions determined from XPS measurements which have a comparable sampling depth of  $< 5 nm$ . The SIMS technique can easily separate mass to charge ratios of order unity, and thus relative abundances of the isotopic ratios can be determined (e.g.,  $\Gamma(^{29}Si)/\Gamma(^{28}Si)$  where  $\Gamma$  is the isotopic fractional abundance). The bulk compositions in Table 4.5 do not distinguish the isotopic fractions, and therefore it is necessary to account for the relative isotope abundances when deriving the relative yields from the experimental SIMS spectra. Isotopic abundance corrections were done by taking the SIMS intensity of the most abundant isotopic mass for each element in Table 4.5, determined by integrating over a single  $m/q$  unit, and dividing by the average solar system isotopic abundance. Comparing the derived secondary ion yields

relative to  $Si$  given in Table 4.7 with experimental results [Dukes and Baragiola, 2015] shows that the agreement for most elements is within the errors.

**Table 4.7:** Elemental surface binding energies and average relative yields for the major elemental species present in lunar soil compositions given in Table 4.5. The  $E^{SBE}$  used in all SDTrimSP simulations were calculated from elemental sublimation energies (e.g.,  $Fe(s) \rightarrow Fe(g)$ ) and  $E^{IE}$  is the first ionization energy for each species. The average  $R_i$  and variance were calculated using only the experimental data  $2keV H^{2+}$  and  $4keV He^+$  bombardment of lunar soil samples shown in Figure 4.12. The yield ratios  $Y_i^+/Y_{Si}^+$  for  $4keV He^+$  bombardment of LS62231 were found experimentally [Dukes and Baragiola, 2015], and determined using total yields from SDTrimSP multiplied by  $R_i$ .

$4 keV He^+ \rightarrow LS62231$					
Element	$E^{SBE}$ (eV)	IE (eV)	$R_i$	Expt.	SDTrimSP
Na	1.11	5.139	$44.2 \pm 29$	$0.57 \pm 0.51$	$0.56 \pm 0.43$
Mg	1.51	7.646	$10.7 \pm 9.3$	$0.72 \pm 0.22$	$0.32 \pm 0.19$
Al	3.39	5.986	$4.14 \pm 1.1$	$2.61 \pm 0.53$	$2.43 \pm 0.87$
Si	4.72	8.152	$1.0 \pm 0.0$	$1.0 \pm 0.0$	$1.0 \pm 0.0$
K	0.93	4.341	$395 \pm 353$	$0.44 \pm 0.35$	$0.38 \pm 0.47$
Ca	1.84	6.113	$7.49 \pm 3.5$	$1.35 \pm 0.19$	$1.57 \pm 0.97$
Ti	4.84	6.828	$7.40 \pm 6.2$	$0.04 \pm 0.03$	$0.02 \pm 0.02$
Mn	2.92	7.434	$10.1 \pm 7.1$	$0.02 \pm 0.01$	$0.01 \pm 0.01$
Fe	4.28	7.902	$1.95 \pm 0.8$	$0.24 \pm 0.09$	$0.24 \pm 0.1$

## 4.5.2 Determination of small body classification

By assembling a large number of bulk elemental compositions for meteorites, Nittler et al. [2004] found that elemental ratios can be used to discriminate between many meteorite classes. It was determined that the major elements - oxygen, magnesium, aluminum, silicon, sulfur, calcium and iron - “reflect to differing degrees nebular elemental fractionations and parent-body igneous processes and can be used together to distinguish most classes and sub-classes of meteorites” [Nittler et al., 2004]. Although oxygen isotope measurements or measurements of trace species are often preferred in the lab setting, instrument sensitivity and numerous background sources make meeting the required detection limits for these low abundance species difficult in space. The use of readily detected metal ions for which background sources are negligible represents a more robust method to identify composition and carry out parent body classification.

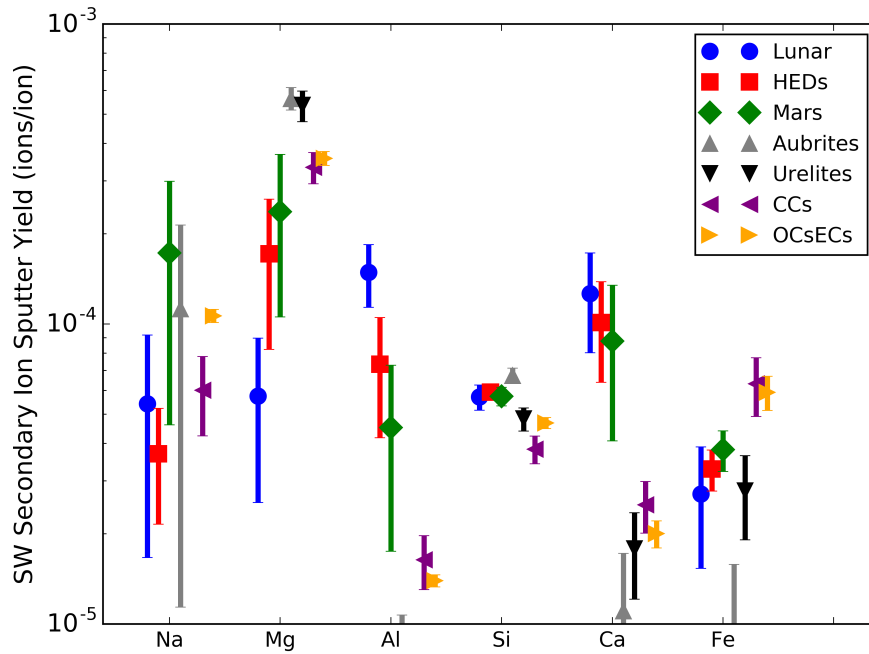


**Figure 4.13:** Sputtered ion yields for different species are distinguishable such that the parent body can be classified according to meteorite type. Although this technique is not powerful enough to distinguish between all meteorite types, grouping shows clear separation between the primitive-type and geologically evolved parent bodies.

The relative secondary ion yields  $Y_i^+/Y_{Si}^+$  for the meteorites were determined using the correction factors in Table 4.7, and high-fluence yields for each of the major elements are compared in Figure 4.13 and Figure 4.14. It is seen that individual meteorite classes tend to be grouped and some distinction between major meteorite classes can be made based on the estimated ion ratios. Noting that the lunar, HED (howardite–eucrite–diogenite), and Mars compositions are more typical of geologically evolved parent bodies, while the chondrite, aubrite, and urelite meteorite types likely represent more primitive solar system materials, the simulated meteorite compositions can be broadly grouped into evolved and primitive types. The elements Mg, Al, Ca, and Fe show the clearest separation between the various meteorite types.

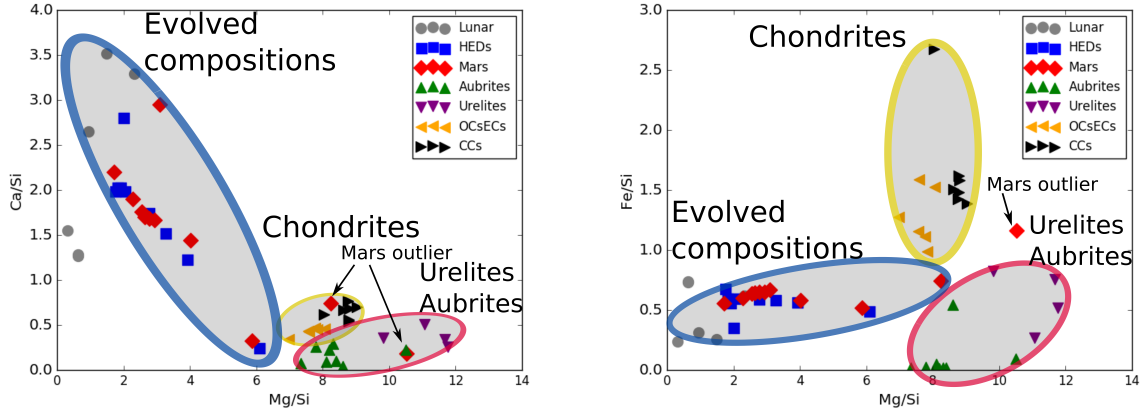


**Figure 4.14:** The scatter plots for secondary ion ratios show significant grouping between the evolved and primitive meteorite types

## 4.6 IMS measurements around Phobos and Deimos

Since the ejecta escape to space due to the low surface gravity of Phobos and Deimos, exosphere densities depend mainly on the energy and incident flux of the impactors. However, small body exospheres are expected to be tenuous. As mentioned previously, the ROSINA and Ptolemy mass spectrometer instruments on-board Rosetta attempted to measure the exosphere densities using neutral mass spectrometry during close flybys of asteroids (2867) Steins and (21) Lutetia [Altwegg et al., 2012; Andrews et al., 2012; Morse et al., 2012; Schläppi et al., 2010]. Ion mass spectrometry (IMS) provides orders of magnitude better sensitivity than neutral mass spectrometry and suffers from relatively low spacecraft background contamination. IMS can rapidly sample and measure the abundance of key exospheric ions over a wide range of masses and allow the bulk composition of surface materials to be inferred or constrained [Johnson and Baragiola, 1991; Schaible et al., in preparation].

The expected ion fluxes in close proximity to small bodies can be estimated using  $Y^{tot}$  determined from SDTrimSP simulations estimates for  $\alpha_{Si}$  and the incident solar wind flux,  $\Phi_{sw}$ . Such flux estimates greatly aid in determining the needed IMS sensitivity and threshold requirements to adequately distinguish elemental compositions using the secondary ion spectra. Here, we assume that all sputtered species that escape the moon's surface

can in principle be measured by the mass spectrometer. Regolith effects and variations in binding energy can create a distribution as seen in Figure 4.10 , and in order to maximize the probability of detecting surface ions instruments should be designed to be sensitive to as wide an energy range as possible. Effectively this entire distribution of ejection energies yields velocities much greater than the escape velocity of a Vesta sized body ( $\sim 10^{-3} eV/amu$ ).

The ratio  $Y_i/Y_{Si}$  derived from SDTrimSP simulations at high fluence ( $> 10^{19} \text{ ion}/\text{cm}^2$ ) give nearly identical results to stoichiometric yield predictions. Thus, taking the total yield for a given meteorite class from Table 4.6, the elemental ion yield can be determined by  $Y_i = Y^{tot}C_i$ . Then, the secondary ion flux at the surface of a body of radius ( $r_{sb}$ ) for element  $i$  is given by

$$\Phi_i^+(r_{sb}) = \Phi_{SW}Y^{tot}C_iR_i\alpha(Si^+)P \cos^{1.6} \theta' \quad (4.4)$$

where  $r_{sb}$  is the radius of the small body and represents a point on the surface,  $\theta'$  is the incident ion angle, and  $P \sim 1/3$  is the reduction in sputtering yield due to the porosity of the regolith [Cassidy and Johnson, 2005]. The average solar wind ion flux is  $\Phi^{SW} \sim 10^7 \text{ cm}^{-2}\text{s}^{-1}$  at 3  $A.U.$ , and the total yields obtained from the SDTrimSP simulations are  $Y^{tot} \sim 0.03$  atom/ion. Based on the available data [Franzreb et al., 2004], we here take  $\alpha_{Si} = 0.005$  as a conservative estimate of the ionization fraction for  $Si$ . The relative yields given in Table 4.7 are used to determine the ejected fluxes of the remaining refractory species. Irradiation of flat surfaces at angles away from the local surface normal are typically accompanied by an increase in the sputtering yield and reach maximum values at  $\theta = 60 - 90^\circ$  from the local surface normal [Behrisch and Eckstein, 2007].

Irradiation at angles increasing from the surface normal cause an increase in the sputtering yield up to a cutoff angle depending on the material ( $\sim 80^\circ$ ), and yields typically follow a  $\cos^{-1.6}(\theta_{inc})$  dependence [Cassidy and Johnson, 2005], though it may be narrower for ions. Thus, results obtained for normal incidence are often scaled using an average incidence angle of  $\theta_{inc} = 45^\circ$  to account for both isotropic incidence and the roughness of the surface. Here, in order to account for the granular nature of the small body regoliths and the variation

in solar incident angle based on time-of-day, a cosine distribution of incident ion angles is assumed. Although ejected ions tend to be more forward peaked than the neutrals, a cosine distribution of ejection angles is used here as a conservative estimate. Using the calculated yields for LS62231 in Table 4.5 and the solar wind flux and porosity reduction factor given above, the flux of  $Si^+$  leaving a regolith is  $\sim 76 \text{ cm}^{-2}\text{s}^{-1}$  at 3  $A.U.$  These estimates match well with previous ion flux estimates given in Table 4.4.

### 4.6.1 Flux fall off with distance

As ions move away from the surface ( $r > r_{sb}$ ), their trajectories are modified by ambient electromagnetic fields and momentum transfer from plasma ions. Since the interplanetary magnetic field (IMF) is carried by the solar wind, its direction is randomly oriented, and thus at large distances from the surface the origin of an ion entering the detector cannot be determined. The gyroradius is given by

$$r_{gr} = \frac{mv_{\perp}}{qB} \quad (4.5)$$

where  $B$  is the IMF strength,  $m$  is the sputtered ion mass,  $q$  is the ion charge, and  $v_{\perp}$  is the ion velocity perpendicular to the B-field. For ions ejected at greater angles with respect to the IMF, the gyroradius will be much larger. Ions also gain energy due to the IMF influence depending on the ion ejection velocity, the average SW velocity, the magnitude of the IMF, and the distance from the surface as given by

$$\Delta v = \frac{h_{sc}}{m_i \langle v_i \rangle} \left( q_i \times B \sqrt{(\langle v_i \rangle)^2 + v_{sw}^2} \right) \quad (4.6)$$

where  $h_{sc}$  is the altitude of the spacecraft above the surface of the small body. The gyroradius and change in ejected ion velocity at Mars' orbit can be estimated using a  $\sim 0.15$  nTesla magnetic field strength, measured by the PHOBOS spacecraft [Russell et al., 1990]. Then, taking an ejection energy of  $\langle v_{Si^+} \rangle \sim 10 \text{ eV}$  oriented  $1^\circ$  off of the IMF so that  $v_{\perp} = \langle$

$v_{Si^+} > \sin(1^\circ)$ , the gyroradius for a recently ejected  $Si^+$  ion is  $\sim 40 \text{ km}$ . For a spacecraft  $40 \text{ km}$  from a surface bombarded by the solar wind ( $v_{sw} \sim 500 \text{ km/s}$ ), the estimated change in velocity for an  $Si^+$  ion ejected at  $\sim 10 \text{ eV}$  ( $\sim 8 \text{ km/s}$ ) is  $\sim 10 \text{ eV}$ , effectively doubling the ion energy but still well within the acceptance energy ranges for most IMS instruments. Therefore, close to a body embedded in a weak magnetic field, an IMS instrument can detect the majority of ejected ions without the need for complicated sensor designs.

Assuming that the gravitational attraction of the body is negligible, neglecting any velocity variations, and taking the surface flux as calculated above, the flux at distance  $h_{sc}$  is given as

$$\Phi_i^+(h_{sc}) = \Phi_i^+(r_{sb}) F \left( \frac{r_{sb}}{r_{sc}} \right) \quad (4.7)$$

where  $r_{sc} = r_{sb} + h_{sc}$  and

$$F \left( \frac{r_{sb}}{r_{sc}} \right) = \left[ 1 - \left( 1 - \left( \frac{r_{sb}}{r_{sc}} \right)^2 \right)^{1/2} \right] \quad (4.8)$$

accounts for radial expansion as the sputtered species move away from the surface [Johnson, 1990]. Using the surface flux calculated for  $Si^+$  above, the flux of ions at a spacecraft altitude of  $40 \text{ km}$  above a  $10 \text{ km}$  sized body is  $\sim 1.5 \text{ cm}^{-2}\text{s}^{-1}$ . The count rate for an IMS instrument depends on the instrument sensitivity, aperture opening, and acceptance angle, and these are typically given in terms of a geometric factor  $g = NG/\Phi^+$  where  $N$  is the instrument count rate and  $G$  is the solid angle for which the instrument is sensitive to ions. Therefore, in order for an instrument with uniform sensitivity over  $\pi/4$  radians from the detector axis (corresponding to  $\sim 1.8 \text{ s.r.}$ ) to collect a minimum of 1 count per second for an incoming ion flux of  $\sim 1 \text{ cm}^{-2}\text{s}^{-1}$ , the geometric factor should be  $g \sim 2$ . The error on the ion measurements follows Poisson statistics is calculated by taking the square root of the total number of counts.

It is seen in Figure 4.13 that the expected yields for  $Si^+$ , and therefore exosphere density, are similar for all meteorite species, thus providing a convenient fiducial. However, contamination from  $CO$ , such as would be expected on the surface of Phobos due to deposition

during passage through the Mars plasma wake, may complicate signal interpretation. One means of alleviating this concern is to use an IMS with sufficient mass resolution to distinguish the small nuclear mass differences. Alternatively, for bodies such as Phobos, which is tidally locked, deposition should occur preferentially on the Mars facing hemisphere, and IMS measurements can be taken when the moon is outside the plasma wake and exposed only to the solar wind to determine the  $CO$  background.

#### 4.6.2 Calculations for NIMS-E

The expected ion fluxes entering the NIMS-E instrument were calculated by integrating over the solid acceptance angle of the instrument and multiplying by the instrument sensitivity function. A large acceptance angle allows more ions to be collected and thus more detailed statistics of the global ion composition to be determined, while a narrow acceptance angle yields more precise spatial information at the expense of total ion counts. The acceptance angle for the proposed NIMS-E instrument falls off as a Gaussian away from the detector axis and the Full-Width-Half-Max (FWHM) =  $5^\circ = \pi/36 \text{ rad}$ . As a first order approximation, we assume the flux arrives at the instrument with a cosine distribution. The detection rate for an IMS detector at a distance  $h_{sc}$  above the surface is given by

$$R_i^{ion} = \Phi_i(h_{sc}) \times S_{IMS} \times \int_0^{\pi/2} G(\theta) [\sin(\theta) \cos(\theta)] d\theta \quad (4.9)$$

where  $S_{NIMS-E} = 2.5 \times 10^{-3}$  is the instrument sensitivity in (counts/s)/(ion/cm<sup>2</sup>/s) and

$$G(\theta) = \frac{1}{\sigma * \sqrt{2 * \pi}} * \exp\left(-\frac{\theta^2}{2\sigma^2}\right) \quad (4.10)$$

is a typical angular sensitivity factor. Since the instrument is nominally sensitive from 0 to 90°, we normalize the Gaussian distribution by dividing by  $\int_0^{\pi/2} G(\theta) d\theta = 0.5$ . The standard deviation  $\sigma$  can be found according to  $FWHM = 2\sqrt{2 \ln 2} \sigma$ .

Finally, the expected ion fluxes entering the instrument can be calculated using

$$N_i(1km, \theta') = N_i(r) \int_{\theta'-\Omega}^{\theta'+\Omega} \frac{\cos(\theta)}{\cos^{1.6}(\theta)} d\theta \quad (4.11)$$

where  $\theta'$  is the angle between the surface normal and the solar wind incidence angle, the cosine factor in the numerator accounts for the cosine distribution of ejecta angles. The total number of counts per flyby can be determined by integrating the count rate over an entire flyby. Assuming the instrument will dwell on only two elements per fly by (Si and one of Fe, Mg, Ca or Al), we divide the total number of counts for a given element by two. The effective area ( $A_{eff}$ ) of the detector is the detector sensitivity multiplied by the Gaussian factor.

Furthermore, ejecta flux drops as a function of distance from the surface of a small airless body. Therefore, we must account for the spatial distribution of the ejecta and the decrease in flux at distances away from the surface. Nearby points also contribute to flux at points above the surface, but this contribution is not considered here. A more accurate calculation would take into account the contribution of points not directly below the instrument and the curvature of the body.

The sputtered ejecta leaves the surface in approximately a cosine distribution. If we assume the surface is flat, there is no reduction in flux with distance from the surface. Gravitational attraction of the body is negligible. Taking the surface flux as calculated above, we can calculate the flux flowing into a solid angle at a point above the surface:  $\Phi_i^+ \times [2 * \sin(\theta)\cos(\theta)]d\theta$  where it is assumed that the ions arrive at the detector with a cosine distribution.

The sputtered component which results from SW and plasma wake ions impacting the surface of the bodies can be measured to determine the composition of the sputtered material in flight. Comparing this with experimental and computational results, one can, in principle, derive the atomic and chemical composition differences between the two bodies, as well as spatial differences between distinct regions on Phobos. As seen in Figure 4.1, Phobos' surface

is dominated by a ‘red unit’ which is spectrally similar to Deimos, but also contains a distinct ‘blue unit’ with much bluer spectra. The ‘red unit’ is thought to be deposited dust, possibly transported from Deimos, while the ‘blue unit’ is expected to be representative of the native composition. Differences in the composition of the red and blue units could be indicative of different origins for the two bodies.

The number of counts per flyby  $N$  estimated for the PADME mission was calculated following

$$N = D * [A_{eff} \Phi_i^+(r_{sb})(r_{sb})^2] / v_{sc} \int \frac{f(\alpha)}{z^2 + (r_{moon} + d)^2} dz \quad (4.12)$$

where  $A_{eff} = 1.27 \times 10^{-4}$  (counts/sec)(ion/cm<sup>2</sup>/s) and  $v_{sc} = 1 \text{ km/s}$ . Taking  $f(\alpha) = \cos(\alpha) = \frac{r_{moon} + d}{z^2 + (r_{moon} + d)^2}$ , meaning the flux decreases toward the edge of the illuminated hemisphere, we find  $N_{tot} \sim 26$  and  $N_{Si} \sim 4$ . The error on the Si counts is then  $\delta_{Si} = \sqrt{4} = 2$ , such that many flybys would be necessary to achieve high precision measurements of the sputtered surface composition.

### 4.6.3 Enhancement cell collection calculation

The enhancement cell works by passively collecting material during the flybys. The diameter of the cell is 6 cm and the collection efficiency is  $E = 50\%$ . Taking the total flux leaving the surface as calculated above, we then calculate the particle density as a function of distance from the body and integrate along the flyby trajectory to find a column density of collected material. Multiplying the column density by the area of the collector ( $A_{col}$ ) gives the total number of particles collected or ‘swept-up’ by the collector for a single flyby. In this case we consider all sputtered particles (ions + neutrals + molecules).

In order to calculate density, we need the velocity of the particles as they leave the surface. Neutrals are expected to be ejected at lower energies than ions, and we estimate an average ejection velocity of 2.5 km/s for all ejected species.

Atom ejection velocity:

$$\langle v_i \rangle = \left( \frac{2E_{eject}}{m_i} \right)^{1/2}$$

where  $E_{eject}$  is the energy with which the sputtered particle leaves the surface and  $m_i$  is the atomic mass of species  $i$ .

Average ejection velocity used for all atoms =  $\langle v \rangle = 2.5$  km/s. To find the density of a given species, the surface flux is multiplied by  $(4/\langle v \rangle)$ .

$$n_{tot} = \phi_{tot}^{atom} \left( \frac{4}{\langle v \rangle} \right) \approx 12 \times 10^6 \frac{part}{m^3}$$

Similar to the ions, the total number of particles collected is determined by integrating the density over an entire flyby and multiplying by the collector area.

The number of collected particles is:

$$N_{tot} = E * n_{tot} * A_{col} \times \frac{2*r_{moon}^2}{r_{moon}+d}$$

$$\Rightarrow N_{tot} \approx 3.16 \times 10^8 \text{ particles collected.}$$

For a regolith with 2% C (for example), this corresponds to  $6.3 \times 10^6$  C atoms collected.

## 4.7 Conclusions

Although we see that the sputtered densities are low, the above estimates show that, an ion mass spectrometer attached to a spacecraft with an orbital or flyby altitude of  $< 50$  km about a body located at  $< 3$  A.U. should be able to obtain a good deal of information about the bulk composition of the small body of interest. Further experimental study of ion sputtering of silicates is needed so that measurements of secondary ion spectra around small bodies can lead to a diagnostic measurement of their ages and origins. These estimates presented here are conservative, and surprising, unpredicted exosphere properties have been seen at other bodies such as the Moon [Benna et al., 2015; Halekas et al., 2015] and Mercury [Burger

et al., 2014]. It should be noted that the above estimates are subject to several relatively large uncertainties.

## 4.8 Future work

Additional study of sputter induced surface reduction of astrophysical silicates is needed to understand atom/molecule reactions occurring on grain surfaces. A depletion of oxygen may slow many chemical reactions and the presence of certain metal atoms such as *S* and *Fe* may catalyze otherwise unfavorable chemical reactions. Furthermore, studies of hydrogen reactions with surface atoms and the influence of *H* chemistry on both total and secondary ion yields would be interesting and useful for the space science community. Additional characterizations of the surface composition changes produced by ion sputtering in the target compositions simulated can be done using the data generated during the simulations described above. Analysis of these data could give insight into depletion and enrichment of elements in complex target compositions.

# Chapter 5

## Case 3a: Thermal Conductivity of Regoliths

### Abstract

The identification of the PacMan thermal anomalies on the surfaces of the Saturnian moons Mimas, Tethys, and Dione and their subsequent correlation with high energy electron deposition patterns presents a unique case of space weathering of an icy body for which both the regolith composition and incident radiation flux are reasonably well defined. Understanding the role of electron interactions with these predominantly water ice surfaces can provide insights into fundamental radiation effects at work on bodies in space, and a better understanding of the microphysical processes possibly allowing us to place constraints on the regolith properties (i.e., grain size, shape, crystallinity, and optical appearance). This in turn will enhance our ability to interpret the observed surface features on other icy bodies. This chapter introduces the PacMan features, discusses regolith thermal conductivity models, and gives estimates for the effective size of the contact radius between adjacent water ice grains at each of the icy moons.

## 5.1 Introduction

Radiation processing of ices occurs when ions, electrons or photons deliver energy to regolith grains, and the changes produced contribute to space weathering of surfaces. The deposited energy can break the molecular bonds in the ice structure, as well as between atoms in single molecules, and as energy spreads from the point of the initial excitation, excited species diffuse and react, changing the physical structure of the solid and forming new molecules. In order to interpret the surface features on small bodies and moons in the solar system, a fully quantitative description of the microphysical processes producing optical, chemical and physical changes is required. In this section and the following two, an ideal test case in radiation effects on icy bodies, the PacMan thermal anomalies, will be investigated through a combined computational and theoretical approach. Chapter 5 will introduce the PacMan thermal anomalies, review thermal conductivity models for granular, porous regoliths, and use the model of Sirono and Yamamoto [1997] to estimate the grain contact radii implied by the Cassini composite infrared spectrometer (CIRS) thermal inertia measurements. As shown in Subsection 5.3.6, the model chosen was validated using continuum simulations performed by S. Piqueux (JPL) for water ice grains in a simple cubic packing configuration. This work has been published in *Icarus* [Schaible et al., 2016].

### 5.1.1 Motivation: the PacMan thermal anomalies

Unique weathering features have been identified on the icy Saturnian moons Mimas, Tethys, and Dione and are referred to as anomalous regions due to their differing reflectance and thermal properties from surrounding regions [Elder et al., 2007]. Such features were first identified during the Voyager era when a dark equatorial band was observed in visible light images of Tethys [Stooke, 1989, 2002; Buratti et al., 1990]. More recently the IR3 (0.930  $\mu m$ ), GRN (0.568  $\mu m$ ), and UV3 (0.338  $\mu m$ ) filters in the imaging science subsystem (ISS) on Cassini, each with an effective bandwidth of  $\sim 0.1 - 0.15 \mu m$  [Porco et al., 2004], clearly

identified near-UV brightening of Mimas and Tethys in regions centered on the leading hemisphere and roughly symmetric about the equator [Schenk et al., 2011].

The anomalies were seen to be dark in the IR3 and GRN filters but bright in the UV3 (0.338  $\mu\text{m}$ ) filter as shown by albedo maps [Schenk et al., 2011]. The smaller IR/UV ratio in the anomalous regions as compared to the surrounding surface was explained as increased scattering at UV wavelengths due to a higher concentration of light scattering defects in the icy regolith grains. Additionally, the CIRS measurements of thermal emission in the mid-IR regime (9.1 – 16.7  $\mu\text{m}$ ) [Flasar et al., 2004] revealed that surface temperature variations during the day and night cycle were smaller in the anomalous regions on all three bodies [Howett et al., 2011, 2012, 2014] indicating increased thermal inertia. The morphology seen in the CIRS temperature maps, reproduced in Figure 5.1, led to the anomalies becoming colloquially known as the ‘PacMan’ anomalies. The spatial boundaries of the optical and thermal anomalies were similar, suggesting a common origin. However, these features were not seen in the far-UV data (170 – 190  $\text{nm}$ ) taken by Cassini’s ultraviolet imaging spectrometer (UVIS) [Hendrix et al., 2012] or in the near-IR wavelengths (0.8 – 5.1  $\mu\text{m}$ ) imaged by VIMS [Scipioni et al., 2015a]. This was explained by different sampling depths of the spectral data sets and different regolith properties as a function of depth.

As described further in Chapter 6, the boundaries of the thermal anomalies were seen to correspond with the deposition patterns for high energy ( $\sim \text{MeV}$ ) electrons moving with their net guiding center of motion in the opposite rotational direction of the moons. Despite the apparent correlation between the anomalous regions and high energy electrons, the physical mechanisms by which the electrons drive changes in UV scattering and thermal inertia have not previously been well described, and a quantitative comparison with theoretical and experimental results was lacking. One proposed mechanism for the increase in thermal inertia was growth or annealing of grain contacts produced by high energy electron interactions with the ice. Assuming that, initially, thermal transport between grains is inefficient due to poorly bonded molecules or small contact regions, the incident electrons ionize and mobilize

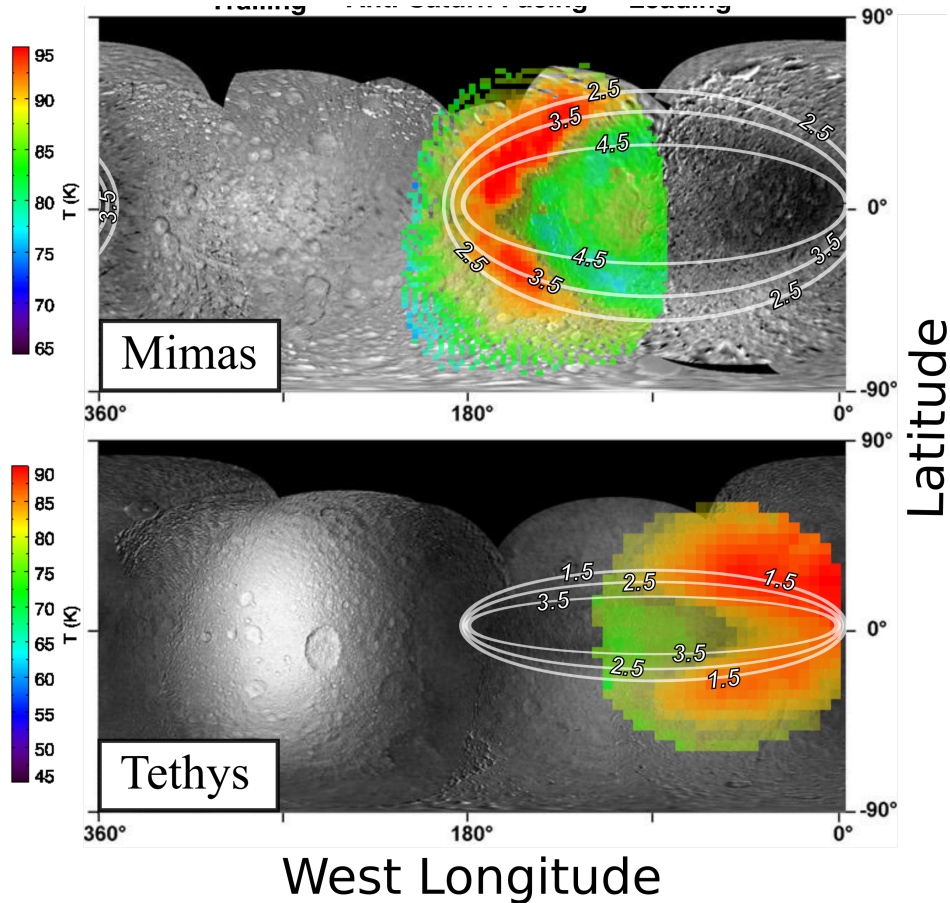


**Figure 5.1:** The panels show anomalous 'PacMan' features identified on the leading hemispheres of Mimas and Tethys. Energy flux contours calculated from MIMI measurements are given in units of  $\log_{10}(MeV/cm^2/s)$  [Paranicas et al., 2014]. Superimposed on the IR/UV ratio determined by the Cassini ISS [Schenk et al., 2011], the contour lines closely match the shape of the anomalous regions. The daytime surface temperatures for each of the bodies are given as color maps [Howett et al., 2011, 2012] and clearly show lower daytime temperatures (corresponding to higher thermal inertia) inside the anomalous regions with boundaries roughly consistent with the discolorations.

neighboring molecules driving diffusion and both forming and annealing crystalline defects. Defect annihilation is particularly effective in the contact region where the inverted surface curvature creates a surface energy minimum. Thus, molecules accumulate in the contact region and 'cement' grains together. Cementing or sintering of grains improves the thermal contact and, consequently, increases the effective thermal inertia of the regolith. The process of atoms or molecules migrating into the contact region between particles due to thermal or radiation-enhanced diffusion is called sintering and is well studied in materials processing (e.g. ceramics). However, due to the expected roughness of regolith grains, the unknown crystalline phase of the cementation, and the cold surface temperatures of the Saturnian

moons ( $\sim 60 - 90 K$  at Mimas) [Howett et al., 2012], the application of thermal conductivity and sintering models for the grain shape and material behavior is not straight forward.

Thermally driven molecular diffusion may also have an effect on the grain shape and sintering in the uppermost exposed grain layer when the moons are at their warmest ( $\sim 100 K$ ), and meteorite impacts from IDPs and E-ring grains will both melt and redistribute material across the surface. Since these effects should be roughly similar inside and outside the anomalies at the same longitude and since ions impact preferentially on the trailing hemispheres, we here assume that sintering within the thermal anomalies is caused by high energy electrons. As discussed further in Chapter 6, gardening of the regolith by IDPs and E-ring grains can effectively erase sintering effects. Thus, if the  $MeV$  electrons are responsible for the thermal anomalies, the sintering timescale should be smaller than the regolith gardening timescale at depths shallower than the thermal skin depth.

### 5.1.2 Regolith properties of the icy Saturnian moons

Using the thermal emission excursions measured by CIRS, values for thermal inertia inside and outside the anomalies were determined by Howett et al. [2011, 2012, 2014]. In order to compare the CIRS measurements with standard regolith thermal models, the thermal inertia can be converted to thermal conductivity following  $k = I^2/\rho c$  where  $I$  is the thermal inertia,  $\rho$  is the density, and  $c$  is the heat capacity of the regolith material. The regoliths are predominantly crystalline water ice [Smith et al., 1982; Filacchione et al., 2010] with small impurities of salts and organic materials such as those found in the Saturn E-ring grains [Postberg et al., 2008]. The source of surface material on the icy Saturnian moons is expected to be dominated by  $\sim \mu m$  sized E-ring grains which originate in the plumes of Enceladus [Spahn et al., 2006b]. These are expected to preferentially deposit on the trailing hemisphere of Mimas and the leading hemispheres of Tethys and Dione [Hamilton and Burns, 1994]. However, a complete description of the regolith growth rate due to E-ring grain deposition as

a function of surface location on each of the satellites has only very recently been carried out [Juhász and Horányi, 2015] and was not available for this analysis.

**Table 5.1:** Thermal characteristics and calculated thermodynamic values for the surface materials of Mimas, Tethys, and Dione. Particle radii,  $r_g$ , were determined using the Cassini observations and, assuming pure water ice regoliths, comparing the water ice absorption band depths at  $2.0\mu\text{m}$  and  $1.52\mu\text{m}$  to a model correlating absorption depth to grain size developed by Clark and Lucey [1984]. Using a regolith porosity of  $\phi = 50\%$ , the thermal skin depth,  $\delta = \frac{I}{\rho_{ice}(1-\phi)c_{ice}\sqrt{\omega}}$ , where  $I$  is the thermal inertia,  $\omega$  is the angular velocity of rotation of each moon and  $c_{ice} \sim 12.4 \text{ J}/(\text{mol K})$  and  $\rho_{ice} \sim 0.94 \text{ g}/\text{cm}^3$  are the heat capacity and density of ice at  $80 \text{ K}$ .

Body	Location	Grain radius [ $\mu\text{m}$ ]	Thermal inertia [ $\frac{\text{J}}{\text{m}^2\text{s}^{1/2}\text{K}}$ ]	Skin depth [cm]	Thermal cond. [ $\frac{\text{J}}{\text{m}\cdot\text{s}\cdot\text{K}}$ ]
Mimas	Inside anom.	10-40	$66 \pm 23$	$2.01 \pm 0.7$	$1.13 \left(\begin{smallmatrix} +0.94 \\ -0.65 \end{smallmatrix}\right) \times 10^{-2}$
	Outside anom.	5-25	$< 16$	$< 0.49$	$< 6.7 \times 10^{-4}$
	Herschel crater	25-50			
Tethys	Inside anom.	11-440	$25 \pm 3$	$0.76 \pm 0.09$	$1.63 (\pm 0.4) \times 10^{-3}$
	Anom. boundary		$11 \pm 1$	$0.34 \pm 0.03$	$3.16 (\pm 0.6) \times 10^{-4}$
	Outside anom.	( $\sim 15$ avg.)	$5 \pm 1$	$0.15 \pm 0.03$	$6.53 \left(\begin{smallmatrix} +2.9 \\ -2.4 \end{smallmatrix}\right) \times 10^{-5}$
Dione	Leading Hemi.	7-28	11	0.57	$3.24 \times 10^{-4}$
	Trailing Hemi.		8	0.42	$1.71 \times 10^{-4}$

The porosity of icy regoliths in the outer solar system is often debated, and values for Enceladus have been estimated at  $50 - 70\%$  [Verbiscer et al., 2005], while for the other icy satellites porosities of  $\phi > 90\%$  have been suggested [Filacchione et al., 2010; Buratti, 2014]. Alternatively, using far-UV data and assuming a lunar-like grain size distribution, Royer and Hendrix [2014] estimated very low surface porosities ( $< 5\%$ ) for Mimas and Dione, while for Tethys porosity varied from  $25\%$  to  $50\%$  between the leading and trailing hemispheres, respectively. The fits to the observational data are very sensitive to coherent backscattering effects and the assumed grain size distributions, which may lead to inaccurate estimates for the regolith porosity. Additionally, the different wavelength data sets probe different depths of the regolith grains, and porosity might vary significantly depending on the length scale considered. Assuming a porosity  $\phi = 50\%$ , the effective thermal conductivity,  $k_{eff}$ , and the skin depth,  $\delta_{therm}$ , inside and outside the anomalies are given in Table 5.1. The skin depths were calculated assuming that the conductivity is that of porous, crystalline ice regolith using an ice grain density of  $\rho_{grain} = 0.934 \text{ g}/\text{cm}^3$ , a specific heat of  $C_{H_2O} = 0.69 \text{ J}/\text{gK}$ , and published values for the angular velocity of rotation [Jaumann et al., 2009].

If the grains settle onto the surfaces at low relative velocities, then bonding between grains is initially weak, implying poor thermal contact or a small effective contact radius. Although somewhat different grain size distributions [Hendrix et al., 2012] and small porosity differences (A. Verbiscer, personal communication) have been measured inside and outside of the anomalies, because of their considerable uncertainties we will assume here that these are approximately unchanged across the relatively sharp anomaly boundaries. Annealing the ice from amorphous to crystalline can also increase thermal conductivity. However, this is likely insufficient to account for the measured differences, implying that the higher thermal inertia results primarily from growth of the contact region between grains.

A good deal of thermal modeling has been done to understand the structure of comets and the thermal inertia of bodies such as the Moon and Mars. However, the Saturnian moons are composed primarily of water ice as opposed to a rocky, silicate dominated regolith, and also lack the dark organic layer found on the surface of comets. In general, heat can be conducted through a granular regolith by radiative transfer between grains, convective transfer through gas in the pore space between grains, and conductive transfer through the solid phase. In the sections below, we first show that for cold, porous regoliths typical of airless solar system bodies in the outer solar system, radiative and convective heat transfer are negligible. Then, several thermal conductivity models are reviewed, and a simple model is used to determine the effective thermal conductivity of a granular regolith. For packed beds of regularly shaped rigid particles under vacuum, heat flow is typically limited by the size of the contact point between grains. Therefore, we review several of the published models to estimate the effective contact radius between grains based on the effective thermal conductivities reported for the icy Saturnian satellites.

## 5.2 Thermal conductivity in porous granular regoliths

In general, the effective thermal conductivity,  $k_{eff}$ , of a granular, uncemented (loose grained) sample under vacuum can be written as the sum of each of the individual heat transfer mechanisms [Watson, 1964]

$$k_{eff} = k_{rad} + k_{conv} + k_{cond} \quad (5.1)$$

and each term can be evaluated separately. The radiative term describes heat flow through the void space by thermal emission from grain surfaces and depends on both grain size and porosity. In an early empirical study of silicate powders (quartz, silica glass, olivine and hornblende) in size ranges from  $\sim 1 \text{ mm}$  to  $< 50 \mu\text{m}$  contained in vacuum at pressures of  $10^{-5}$  to  $10^{-6}$  Torr ( $\Rightarrow k_{conv} = 0$ ), Watson [1964] found  $k_{cond} \sim \frac{3000}{r_g} \text{ erg}/(\text{cm}^2 \text{ s K})$  where  $r_g$  is the grain radius in  $\mu\text{m}$ . Subsequent work has done much to constrain the  $k_{eff}$  dependence on the grain size, pore gas pressure, material thermal conductivity, porosity and average contact size between grains.

### 5.2.1 Radiative contribution to thermal conductivity

The contribution to the effective thermal conductivity from radiative heat emission from the grain/pore surfaces,  $k_{rad}$ , can be estimated as [Piqueux and Christensen, 2009a]

$$k_{rad} = 4\psi r_g \sigma T^3 \quad (5.2)$$

where  $r_g$  is the particle radius,  $T$  is the temperature,  $\sigma$  is the Stephan Boltzmann constant, and  $\psi$  is a heat transport coefficient defined by

$$\psi = \frac{2F + \epsilon'(1 - F)}{2(1 - F) - \epsilon'(1 - F)} \quad (5.3)$$

for which  $F$  is a constant equal to  $\approx 0.08$  and  $\epsilon'$  is related to the emissivity  $\epsilon$  of the material by  $\epsilon' = \frac{\epsilon}{\epsilon + 0.5(1-\epsilon)}$ . Taking  $r_g = 25\mu m$ , and  $\epsilon = 1$ , then the radiative contribution to the thermal conductivity can be estimated as  $k_{rad} \approx 6.3 \times 10^{-6} J/msK$ . Comparing this with the conductivity values derived for Mimas ( $k_{eff} \sim 10^{-3}$  outside the anomaly), we see that the radiative contribution is negligible. Radiative heat transfer is typically a  $< 1\%$  contribution to the total thermal conductivity and will be neglected in the remainder of our analysis.

### 5.2.2 Convective heat transfer

At the low surface gas pressures of the icy moons, heat transfer through the gas phase is assumed to be negligible. However, latent heat transfer through the pore space is due to enhanced molecular desorption from higher temperature grain surfaces and preferential migration of molecules. The latent heat contribution to the effective regolith thermal conductivity from the sublimation process can be estimated using the Hertz-Knudsen formula

$$k_{lat} = \left(\frac{m}{2\pi k_B T}\right)^{1/2} (LS) \frac{dP}{dT} \quad (5.4)$$

where  $T$  is the temperature,  $m$  is the molar mass of the gas molecule,  $k_B$  is the Boltzmann constant,  $L$  is the latent heat of sublimation per unit mass and  $S = \phi r_g$  is the average pore size dimension where  $\phi$  is the porosity and  $r_g$  the average particle diameter. The vapor pressure  $P$  of the gas of interest can be obtained from the Clausius-Clapeyron equation given in Equation 2.13. Assuming a temperature of  $80 K$ , the contribution to thermal conductivity from the latent heat is  $k_{lat} \sim 10^{-26} \frac{J}{msK}$ . Though at low temperatures this effect is negligible, Steiner and Koemle [1991] showed that it should be included at temperatures above  $\sim 170 K$ .

### 5.2.3 Solid state thermal conductivity

Models developed to simulate heat transport in planetary and cometary surfaces and in ‘packed-beds’ of grains typically assume idealized grain shapes and packing arrangements

[Chan and Tien, 1973; Piqueux and Christensen, 2009b], or use a mixture of analytical theory and fitting to experimental data to determine parameterized equations accounting for grain size, shape and packing [Gundlach and Blum, 2012]. Planar discontinuities at the grain contact point may also disrupt the heat flow, and these are rarely accounted for in models. When the conductance of the contact region between grains is much less than that of the grains, the effective heat flux,  $q_{eff}$ , is limited by the contact and is given by

$$q_{eff} \approx \sigma_{cem} \Delta T \quad (5.5)$$

where  $\Delta T$  is measured across the grain contact and  $\sigma_{cem}$  is the contact conductance. As discussed further below, the heat flow is limited by the contacts either when the contacts are very small or if the contact quality (meaning the structure of the material in the contact region) is far from a continuous, ordered, crystalline structure. Although a precise description of the contact region of regolith grains requires knowledge of the grain and contact geometries, the conductance  $\sigma_{cem}$  of the contact region can be defined in a simplified manner if the cementation region can be assumed to be uniform and there are no interface effects. In this case,  $\sigma_{cem}$  depends largely on the contact radius,  $R_{con}$  and the thermal conductivity of the cementation material,  $k_{cem}$ . Typical regolith heat transfer models use an effective regolith thermal conductivity,  $k_{eff}$ , which can be related to the contact conductance following

$$\sigma_{cem} t_{con} = k_{cem} \Psi(R_{con}, \phi, \chi, N_c, T) = k_{eff} \quad (5.6)$$

where  $t_{con}$  is the thickness of the contact and the structural parameter  $\Psi$  accounts for the porosity, packing arrangement, and grain shape, and temperature. For real grains, the ‘thickness’ of the contact may be difficult to define.

The volume fraction of cementation for non-deformed spherical grains is  $\chi = V_{cem}/V_{grain}$ , where  $V_{cem}$  is the total volume of the contact and  $V_{grain}$  is the average volume of a spherical grain. A typical idealized contact between spherical grains of thermal conductivity  $k_g$

connected by a material with thermal conductivity  $k_{cem}$  is shown in Fig. 5.2. In this model, when  $R_{con} \ll r_g$ , the cementation volume fraction,  $\chi$ , is related to  $R_{con}/r_g$  by

$$\chi \approx \frac{3}{16} N_c \left( \frac{R_{con}}{r_g} \right)^4 \quad (5.7)$$

where  $N_c$  is the number of neighboring grain contacts. For this simple model, the cementation uniformly fills the void space between spherical grains in contact at a single point and the surface of the neck has zero curvature. The number of grain-grain contacts, or coordination number, can be known exactly for regular packings of monodisperse spheres, where  $N_c = 6$  for simple cubic packing ( $\phi = 47.6\%$ ). However, random packings typically have smaller  $N_c$ , and for small ( $\sim 1 \mu m$ ), cohesive particles Yang et al. [2000] gave a functional relationship between the average coordination number and porosity as

$$N_c = 2.02 \left( \frac{1 + 87.38(1 - \phi)^4}{1 + 25.81(1 - \phi)^4} \right) \quad (5.8)$$

which closely matches modeled random packings, especially at  $\phi \geq 40\%$ . Using  $\phi = 50\%$ , Equation 5.8 yields  $N_c = 4.99$ . For polydispersed mixtures of randomly packed particles and for non-spherical grains the  $N_c$  may be different from Equation 5.8. In the following section, the parameters controlling the effective thermal conductivity of a granular regolith are explored in more detail. Models accounting for the grain size,  $r_g$ , and thermal conductivity,  $k_g$ , regolith porosity,  $\phi$ , and adhesion between grains as accounted for by the contact radius,  $R_{con}$ , will be described and their applicability to the icy regoliths of the Saturnian moons will be considered.

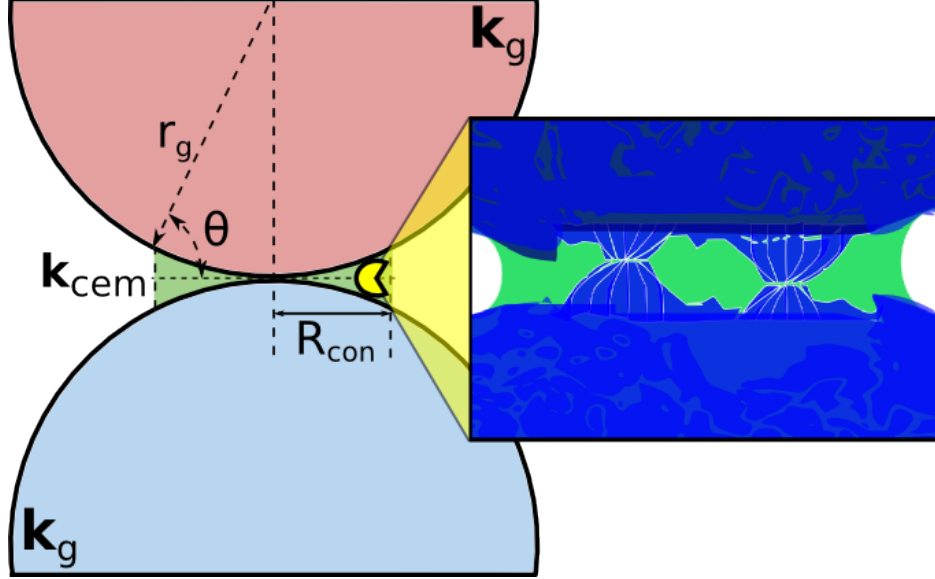


**Figure 5.2:** A simple model for spherical grains or radius,  $r_g$ , connected by a cementation phase of differing thermal conductivity. Effective conductivity of this system depends on the contact radius,  $R_{con}$ , and the thermal conductivities of the cementation phase,  $k_{cem}$ , and grain,  $k_g$ . The inset shows a rough grain or agglomerate (blue) that was subsequently sintered such that cementation (green) filled the contact region.

### 5.3 Thermal conductivity models applied to the icy moons

For airless bodies in the outer solar system, heat flow is likely determined by the quality and number of contacts between grains, and will increase as the connecting volume or effective contact radius,  $R_{con}$ , increases. As described in Ferrari and Lucas [2016], a general means of defining the contact conductivity without needing to directly specify the geometry is given by

$$k_{con}(r_g, \phi, T) = H_{Hertz}(R_{con}, r_g, T)\psi(\phi)k_g(T) \quad (5.9)$$

where  $H_{Hertz} = R_{con}/r_g$  is the oft discussed 'Hertz factor' defined as the ratio of the contact radius to the grain radius and the dimensionless structure factor,  $\psi(\phi)$ , accounts for the reduction in the bulk conductivity as a function of regolith porosity. As described in more detail below, the mechanistic model developed by S. Wood called MaxRTCM is also able to incorporate grain shape and it's corresponding influence on the number of neighbors,  $N_c(\phi)$ ,

and grain contact radius into  $\psi$ . Although in real grains  $R_{con}$  is dependent on the grain shape, roughness, and depth below the surface, the full range of these parameters for the regoliths of the icy satellites has not yet been determined from satellite remote sensing. If we assume that many bulk properties are the same inside and outside the anomalous regions on the Saturnian moons, the thermal inertia differences can be reduced to dependence on a single physical parameter, i.e. the contact radius.

### 5.3.1 Hertzian contact radius

At the  $\sim nm$  scale, heat transfer through dissimilar spheres with no rigid bonding (cementation) is due predominantly to the van der Waals interactions that mediate the phonon transfer, while for cemented grains heat is conducted directly through lattice vibrations. Although regolith grains on small silicate bodies and icy moons are expected to be highly porous and irregularly shaped, the effective contact area between dissimilar spheres provides an interesting point of reference. Deformation of curved, elastic surfaces in contact was first studied by Heinrich Hertz in 1882, and so-called 'Hertzian analysis' can be used to determine the intergranular contact area for dissimilar bodies. The contact radius between two equal sized spheres depends on the material properties and is related to an applied load  $F$  by

$$R_{con} = \left[ \frac{3}{4} \frac{1 - \mu(T)^2}{Y(T)} r_g F \right]^{1/3} \quad (5.10)$$

where  $\mu(T)$  and  $Y(T)$  are the temperature dependent Poisson's ratio and Young's modulus of the material, respectively. The applied load determines how strongly adjacent particles are bonded and the weight of the grains can be used to determine the force as a function of depth. However, for grains with little force pressing them together, such as those at the surface of a loose regolith, van der Waals bonding provides orders of magnitude greater adhesion than gravitational forces. Taking the adhesive force as the tensile force needed to separate the

spheres, this can be estimated by the so-called JKR theory as [Johnson et al., 1971]

$$F_{JKR}(T) = 3\pi\gamma_s(T)r_g \quad (5.11)$$

where  $\gamma_s$  is the specific surface energy of the material at the solid/solid interface.

Combining the JKR expression for adhesive force in the absence of external pressure with the Hertz expression for contact radius gives a measure of the contact size between spherical grains. The dimensionless Hertz factor can then be written as

$$H_{Hertz} = \frac{R_{con,JKR}}{r_g} = \left( \frac{9\pi}{4} \frac{1 - \mu^2}{Y} \frac{\gamma_s}{r_g} \right)^{1/3} \quad (5.12)$$

which can then be substituted into Equation 5.9 to relate the effective thermal conductivity to the grain size. However, this expression does not hold for a polydisperse mixture of grain sizes. The bulk properties of water ice at low temperatures taken from Hobbs [1974], as well as the contact force  $F_{JKR}$  and contact radius calculated assuming zero external pressure and van der Waals attractive force between grains,  $R_{con,JKR}$ , are shown for  $25 \mu m$  grains in Figure 5.3 as a function of temperature in the relevant ranges for the icy Saturnian satellites. Although the specific surface energy can be expected to vary as a function of the crystalline structure of the solid faces in contact, in addition to the temperature, a temperature dependent expression for  $< 100 K$  was not found, and so a constant value of  $\gamma_s = 65 \text{ erg/cm}^2$  was used to determine the Hertz factor.

### 5.3.2 Grain size dependence

Wechsler and Glaser [1965] measured the thermal conductivity for three size distributions of pumice powder ( $k_{pumice} \sim 0.43 \frac{J}{m.sK}$ ) and found that at low pressures the smallest grain size has the largest thermal conductivity and decreases with increasing grain size. Presley and Christensen [1997] gave data for lower pressures and a larger variety of materials and found similar results. However, neither study considered low enough pressures or temperatures such

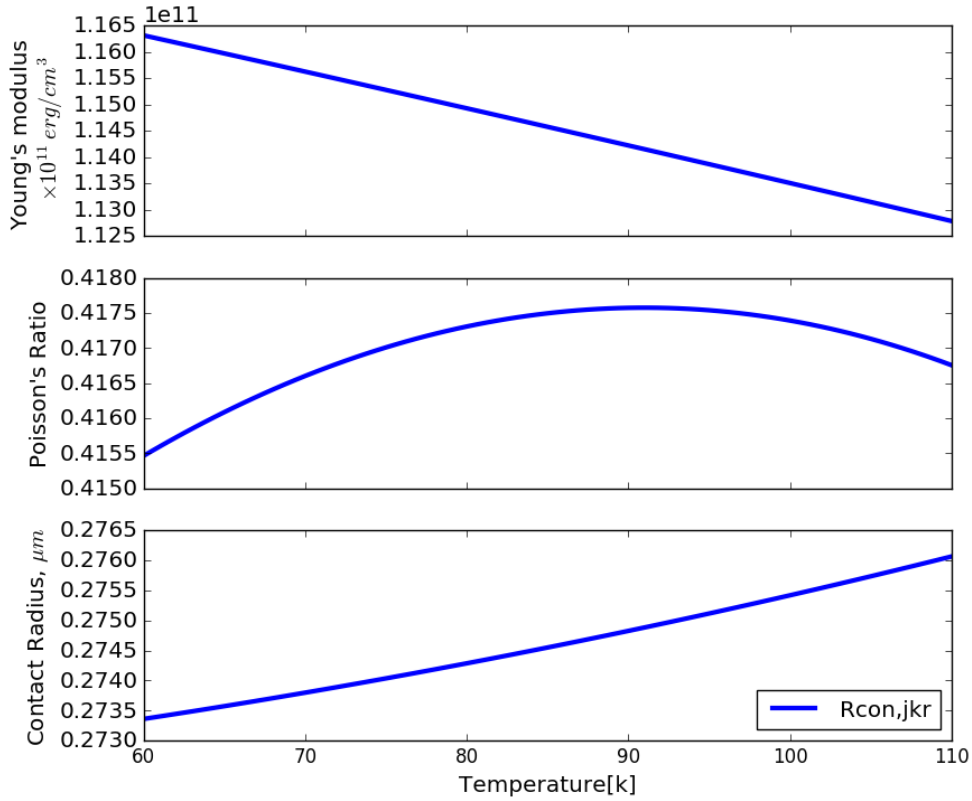


**Figure 5.3:** The Hertzian contact radius calculated from Equation 5.12 for 25  $\mu m$  grains was calculated using temperature dependent values for Young's modulus and Poisson's found in Hobbs [1974].

that the thermal conductivity through the void region between grains can be fully neglected. Piqueux and Christensen [2009b] calculated thermal conductivity of uncemented glass beads in a  $CO_2$  atmosphere and compared the results with experiment and saw that larger grain sizes correspond to greater thermal conductivity. Based on experimental modeling, the thermal conductivity for loose grains was related to the grain size and pore gas pressure as [Presley and Christensen, 1997]

$$k_{eff} = (AP^{0.6})(2r_g)^{(-0.11\log B/K)} \quad (5.13)$$

where the constants  $A \approx 0.0015$  and  $B \approx 8.1 \times 10^{-4}$  and  $P$  is the pore gas pressure. However, as shown in Equation 5.12, the thermal conductivity will have an inverse relationship on the

grain size. The difference can be explained by the pore gas pressure, as well as additional effects at higher temperatures where radiative heat transfer is important. The behavior at very low pressure and for irregularly shaped water ice grains such as those expected for the icy Saturnian regoliths requires further investigation.

### 5.3.3 Effective-medium thermal conductivity model

Thermal conductivity in porous granular regoliths has several similarities to percolation of electricity through mixed media of differing conductivities, and similar mathematical approaches can be used to study both. In this approach, conductive material can be viewed as an effective-medium or a random network of spherical grains arranged on a regular lattice. Assuming that heat can only flow through material in contact (i.e., the void conductivity is zero), then below a certain volume percentage of conductive material the effective conductivity of the mixture is effectively zero while past a critical concentration the conductivity increases sharply and continues to increase with increasing volume percent of conductive material. One such simple model is [Sirono and Yamamoto, 1997]

$$k_{eff} = \frac{\pi k_g}{g} \left( \frac{p - p_c}{1 - p_c} \right) \left( \frac{R_{con}}{r_g} \right)^2 \quad (5.14)$$

where  $r_g$  is the grain radius and  $g$  is a geometrical factor dependent on the packing structure and  $g \sim 1$  for random grain packings [Ferrari and Reffet, 2013]. The packing fraction,  $p$ , is related to the porosity by

$$p = \left( \frac{6}{\pi} \right) (1 - \phi)$$

and the critical packing fraction  $p_c = 1/3$  is the minimum necessary for a continuous thermal path. This model does not distinguish between the grain and cementation materials and assumes that the conductivity of the void space is zero.

### 5.3.4 Generalized regolith thermal conductivity model

Solutions of the heat transfer equation for spherical geometry are complicated by radiation-conduction coupling and complex packing geometries. Chan and Tien [1973] solved these equations analytically and derived explicit functional relationships between the thermal conductance of regularly packed spheres under vacuum and fundamental system parameters. This approach was adopted to describe thermal conductivity of granular regoliths composed of particle agglomerates and calibrated using experimental data acquired for basalt grains and lunar regolith [Gundlach and Blum, 2012, 2013; Ferrari and Lucas, 2016]. The effective thermal conductivity was given as

$$k_{eff}(r_g, T, \phi) = k_{ice}(T) \cdot R_{con}(T) \cdot \psi(r_g, \phi) \bar{\xi} \quad (5.15)$$

where  $R_{con}$  was determined using Hertzian analysis as described above and  $\bar{\xi}$  was introduced to describe the effects of polydisperse grain distributions and irregular grain shapes. The value of  $\bar{\xi} = 0.41$  gave the best fit to lunar regolith data, and was used for ‘tight’ contacts at the icy moons [Ferrari and Lucas, 2016]. The structure factor  $\psi$  was determined by fitting the analytical expressions derived in Chan and Tien [1973] with an exponential following

$$\psi(r_g, \phi) \cdot r_g = f_1 \exp(f_2(1 - \phi)) \quad (5.16)$$

where  $f_1 = 5.18 \pm 3.45 \times 10^{-2}$  and  $f_2 = 5.25 \pm 0.94$  were found by fitting to experimental data. This model explicitly assumes a linear dependence on the contact radius and requires either very high porosity or large grain sizes to explain the low thermal conductivity of the icy regoliths.

### 5.3.5 High parameter flexibility model: MaxRTCM

An interesting mechanistic model, referred to by the acronym MaxRTCM (Maxwellian Regolith Thermal Conductivity Model) and based on the Maxwell equation for effective conductivity of an isotropic, heterogeneous media consisting of a continuous phase and randomly dispersed particles of a second phase, is being developed by Dr. S. Wood to predict regolith thermal conductivities for a wide variety of Solar System regolith types [Wood, 2011, 2013, 2016]. For a continuous solid phase the maximum thermal conductivity is mainly a function of the porosity of the soil  $\phi$ , the cementation volume fraction  $\chi$ , thermal conductivity of the grain and cementation materials,  $k_g$  and  $k_{cem}$  respectively, while for a continuous gas or void phase either radiative or convective thermal conductivity must dominate. Since realistic regoliths cannot have a fully discontinuous solid phase, a structure factor,  $f_{sc}$ , is introduced to ensure that the effective thermal conductivity falls between the two extrema when thermal conductivity through the pore space is vanishingly small. Additionally, the structure factor has been formulated to account for reduced conductivity due to randomly packed porous regoliths and non-spherical grain shapes.

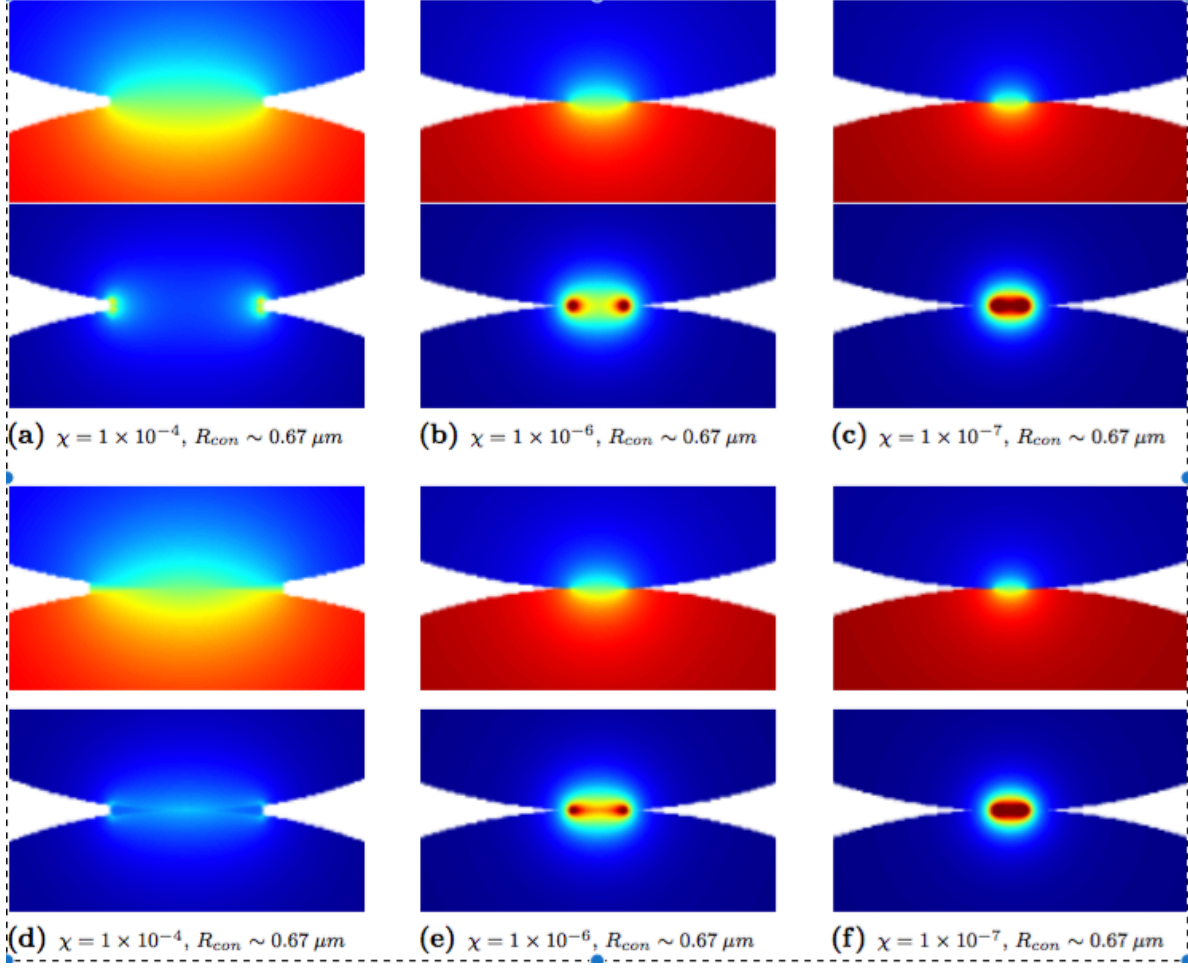
The MaxRTCM results indicate that the low thermal inertia measured on the icy Saturnian moons ( $\sim 10 J/m^2s^{1/2}K$  outside the thermal anomalies) results from either very high regolith porosity ( $> 95\%$ ), highly angular grain shapes, or predominantly amorphous ice grains (S. Wood, private communication). However, the dominant compositional end member on the icy satellites is crystalline water ice [Filacchione et al., 2016], and reported porosities are  $\leq 95\%$  [Filacchione et al., 2010], suggesting that for regolith structures such as those found on the icy satellites the low thermal conductivity must be due to inefficient thermal transport at the grain interfaces that is not easily accounted for by physical modeling. Due to uncertainty in the regolith parameters, it was decided to return to the MaxRTCM model in collaboration with Dr. Wood at a later time in order to more appropriately address the regolith thermal conductivity more comprehensively. In the meantime, the simple model in

Equation 5.14 was used to quantitatively estimate the grain contact radius as a function of porosity and grain size.

### 5.3.6 Continuum modeling of cemented spherical grains

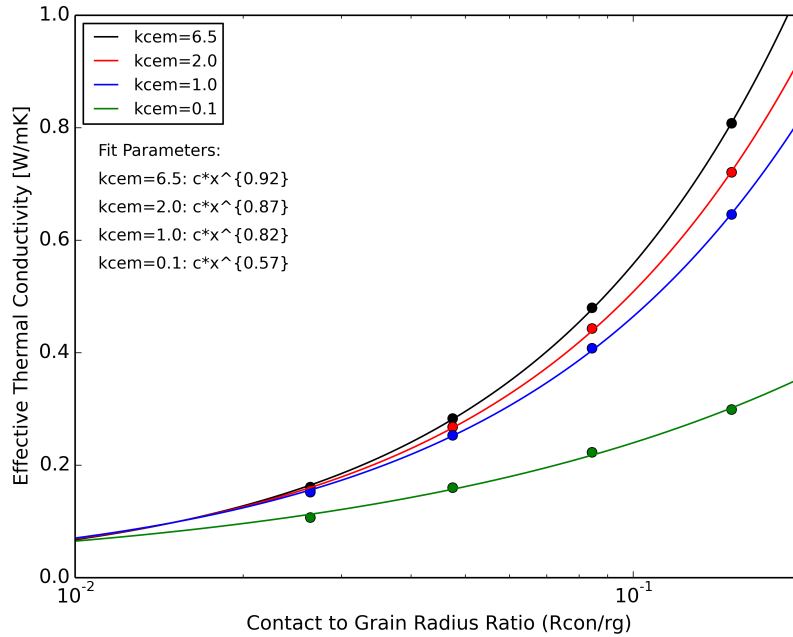
Inter-grain heat conduction can be studied using continuum techniques by assuming cylindrically symmetric pendular cementation regions connecting grains and regular grain packing using commercially available software, e.g. the COMSOL Multiphysics software. The continuum models developed in Piqueux and Christensen [2009b] for two spherical grains connected by an ideal contact volume, calculated using Equation 5.7, were used to determine the relative temperature and heat flux in the contact region. Calculations were run for cementation volume fractions of  $\chi = 1 \times 10^{-7}$  to  $1 \times 10^{-1}$ , and for a wide range of grain and cementation thermal conductivities [Piqueux and Christensen, 2009b]. By imposing an arbitrary temperature differential across grains and multiplying by the heat capacity of water, the computational results can be used to determine the effective thermal conductivity of the bulk.

Figure 5.4 gives simulation results where the thermal conductivity of the cementation and grain were taken to be equal ( $k_g = k_{cem} = k_{ice}$ ) and grains were arranged in a simple cubic configuration. The right hand column shows that for  $\chi \geq 1 \times 10^{-4}$  the heat flux is largest at the edges of the grain contact resulting in a linear dependence on  $R_{con}$  as expected for a sufficiently large contact. However, for the smallest cementation fraction simulated,  $\chi = 1 \times 10^{-7}$ , the heat flux is approximately uniform across the contact area as shown in the left hand columns of Fig. 5.4. Substituting  $\chi = 1 \times 10^{-7}$  into Eq. 5.7 with  $N_c = 6$  gives  $R_{con}/r_g \sim 0.018$  which is of the order or larger than the estimates obtained from Hertzian contact theory and suggests that for these very small contacts the area of the contact will control the heat flow. The smallest contacts estimated for spherical grains given in Table 5.2 are currently beyond the resolution of the simulations, and non-spherical grains or non-ideal grain contacts have not yet been well studied.



**Figure 5.4:** Continuum simulations of the equilibrium temperature and heat flux in the grain contact region for  $25\mu m$  radius water ice grains. For the top set of panels, the thermal conductivity of the grains and the cementation were both that of water ice,  $k_g = k_{cem} = k_{ice} = 6.5 W/m K$ . The upper images give the temperature maps and the lower images give the heat flux density. The cementation volume fraction and contact radius calculated using Equation 5.7 are given in the caption. For the bottom set of panels the thermal conductivity of the grains was that of water ice ( $k_g = 6.5 W/m K$ ), while the cementation thermal conductivity was set to  $k_{cem} = 1.0 W/m K$ . The color scale is relative and independent of the arbitrarily imposed temperature differential across the grains or the grain thermal properties.

The bulk thermal conductivities determined from the simulations performed for  $r_g = 25 \mu m$  water ice grains with varying amounts of cementation and cementation thermal conductivity are shown in Figure 5.5. It is seen that the bulk conductivity approaches a minimum at low  $k_{cem}$  and  $\chi$ . Converting  $\chi$  to  $R_{con}$  and fitting the bulk thermal conductivity derived from the simulations gives a functional dependence on the grain contact radius. When the cementation and grain are of similar thermal conductivity, the thermal conductivity varies approximately linearly with the grain radius. However, when the cementation thermal conductivity is much lower than the grains, heat transfer is heavily concentrated at the



**Figure 5.5:** Bulk thermal conductivity of a simple cubic packed bed of  $25 \mu m$  ideal water ice spheres connected by a pendular shaped cementation region such as that shown in Figure 5.2. Values were calculated using the continuum computational model of S. Piqueux and the ratio  $R_{con}/r_g$  can be related to the cementation volume fraction  $\chi$  using equation Equation 5.7. Lowering the thermal conductivity of the cementation region also lowers the bulk thermal conductivity significantly at higher cementation volume %, and the relationship between  $k_{eff}$  and  $R_{con}/r_g$  becomes sublinear. This is likely unphysical behavior due to the idealized grain geometries (no deformation at the contact point).

grain contact point and the dependence becomes sub-linear. However, this behavior is likely non-physical as grains would realistically be expected to deform upon contact and, for the water ice regolith of the icy moons, the grain and cementation thermal conductivities are likely similar.

## 5.4 Estimated grain contact sizes

As described above, models developed for heat transport in dust layers tend to fit experimental data for silicates and glass beads using a linear dependence on the  $R_{con}/r_g$  [Wood, 2013; Gundlach and Blum, 2012] as opposed to the quadratic dependence in Eq. 5.14. It has been shown [Cooper et al., 1969; Batchelor and O'Brien, 1977] that when the thermal conductivity of the contact material  $k_{cem} \gtrsim k_g$  and the effective contact radius is sufficiently large, the temperature of the two grains will be approximately uniform in the contact region. This

results in heat flux between the grains that varies as  $1/\sqrt{R_{con}^2 - r^2}$  [Cooper et al., 1969], where  $r$  is the distance from the center of the contact in Fig. 5.2, and implies that the effective thermal conductivity is proportional to the radius of the contact. However, if the thermal conductivity in the contact region is much lower than in the grain, either due to a rough grain boundary or a very small cementation radius, then the grain temperatures will differ on the two sides of the contact and will be approximately uniform within each grain. In this case, the temperature difference across the interface can be much larger than the temperature variation within a single grain and the flux through the contact is proportional to the contact area as in Eq. 5.14.

Models that assume linear dependence can reproduce the low thermal conductivities measured for the icy satellites only if high porosities or low grain thermal conductivities are assumed. Additionally, the relatively high  $k_{eff}$  determined from the continuum models assuming simple cubic packing suggests that regoliths such as those found on the Saturnian moons differ significantly from smoothly connected spherical grains. Therefore, the approximate model in Eq. 5.14 is used to estimate the effective contact radii to grain radius ratio, implying that contacts are either very small or have an average conductivity much smaller than the grains. Using the measured thermal inertia, the estimated ratios for  $R_{con}/r_g$  are given in Table 5.2 where several values of porosity and grain thermal conductivity were considered due to uncertainty in the actual regolith parameters [Hendrix et al., 2012; Filacchione et al., 2010; Scipioni et al., 2015b; Nelson et al., 2015]. It is seen that inside the anomalous regions  $R_{con}/r_g \ll 1$  and outside the anomalous regions this ratio can be much smaller than the ratio for Hertzian contacts. This suggests that spherical grains are only a crude approximation. Assuming uniform grain sizes, the grain contact sizes are largest at Mimas due to the larger thermal inertia measured there, thus implying that grain sintering is more efficient and/or resurfacing processes are less efficient than on Tethys and Dione. As described further Chapter 6, grain sintering rates are dependent on the grain geometry, and the values from Table 5.2 are used as limiting minimum and maximum values for  $R_{con}/r_g$  when calculating

the grain sintering timescales.

**Table 5.2:** Effective contact radii to grain radius ratio calculated using the Sirono and Yamamoto [1997] regolith thermal conductivity model for an average regolith temperature of 80 K. The porosity and grain thermal conductivities assumed are within the range of reasonable values expected for icy regoliths, and the error bounds are due to uncertainty in the thermal inertia measurements. For comparison, the Hertz factor calculated from Equation 5.12 for 25  $\mu\text{m}$  spherical grains is  $H_{Hertz} = 0.011$ , while  $H_{Hertz} =$  for 5  $\mu\text{m}$  grains.

$R_{\text{con}}/r_g$	$\phi = 0.5$ $k_g = 6.5 \text{ W/m/K}$	$\phi = 0.65$ $k_g = 6.5 \text{ W/m/K}$	$\phi = 0.5$ $k_g = 0.5 \text{ W/m/K}$
Mimas, In	$0.026 \pm 0.001$	$0.037 \pm 0.003$	$0.0089 \pm 0.033$
Mimas, Out	$\sim 0.01$	$\sim 0.01$	$\sim 0.02$
Tethys, In	$0.010 \pm 0.001$	$0.014 \pm 0.002$	$0.033 \pm 0.004$
Tethys, Out	$0.002 \pm 0.001$	$0.003 \pm 0.001$	$0.007 \pm 0.001$
Dione, In	$0.004 \pm 0.002$	$0.006 \pm 0.002$	$0.015 \pm 0.005$
Dione Out	$0.003 \pm 0.001$	$0.005 \pm 0.002$	$0.011 \pm 0.001$

Due to the dependence of  $R_{\text{con}}$  and  $\phi$  on  $r_g$ , the precise relationship between  $r_g$  and  $k_{\text{eff}}$  is more complicated than suggested by Eq. 5.14 [Presley and Christensen, 1997; Yang et al., 2000]. However, attempting to account for the differences in  $k_{\text{eff}}$  due only to grain size using the approximate relationships in Equation 5.12 or Equation 5.13 suggests that the grain size differences inside and outside the anomalous regions would need to be much larger than can be supported by the reflectance measurements. Although somewhat different grain size distributions [Hendrix et al., 2012] and small porosity differences [Annex et al., 2013; Verbiscer et al., 2014] have been measured inside and outside of the anomalies, because of their considerable uncertainties we will assume here that these quantities are approximately unchanged across the relatively sharp anomaly boundaries. Therefore, the higher thermal inertia in the anomalous regions can be taken to result primarily from growth of the contact region between grains. The grain sizes also represent a distribution of sizes, and reported observational values typically give best fit average sizes while thermal conductivity models also account for only a single grain size. It is currently unclear what result the incorporation of a true grain size distribution would have on the effective thermal conductivity values reported, and thus the sintering timescales calculated.

## 5.5 Conclusions

The PacMan thermal anomalies on the icy Saturnian moons present a unique opportunity to study the radiation effects on water ice regolith. Using a simple model which treats the regolith as an effective medium consisting of two independent phases and specifying the porosity, the effective contact radius between spherical grains in contact was calculated. However, the structure of a regolith is far from uniform or regular, and the contact between two grains may be thought of as consisting of several (or many) independent points of contact. Additionally, larger grain agglomerates of different porosity than the bulk regolith may further complicate the conductive path for heat moving through the regolith. There are many different approaches to modeling the effective thermal conductivity of a granular regolith accounting for grain size, shape, porosity, and temperature, and a full description of the icy regoliths in the outer solar system is still a work in progress. Additional IR observations and characterization of the thermal properties and in situ surface analysis using high resolution imagery would be the ideal means for studying surface structure, although much work can be done in the meantime using laboratory and computational techniques.

# Chapter 6

## Case 3b: Radiation sintering of water ice regoliths

### Abstract

Using the regolith properties and effective grain contact radii calculated in the previous chapter together with quantified electron excitation effects in water ice grains, the radiation induced sintering rates will be estimated. Electron excitation effects determine the distance from the surface or the edge of a grain at which an interaction can occur and cause either a surface migration or ejection event. The goal of this chapter is to describe how to correlate quantitatively the change in contact size (area or radius) with the effects caused by electron ionization and excitation of molecules in the water ice grains.

## 6.1 Introduction

On the surface of a moon or small ( $\lesssim 100 \text{ km}$ ) body, the effective grain contact radius is a minimum for freshly deposited or recently disturbed grains and is expected to grow as a result of radiation-induced diffusion or thermal processing. However, the specific nature of the growth mechanisms depends on the geometry and molecular bonding arrangement in the contact region. The very low thermal conductivity outside the anomalous regions on the icy Saturnian moons, introduced in Chapter 5, is difficult to explain unless the grain shapes are very irregular, and may require that the grains are highly disordered and porous at some scale. Radiation-induced diffusion tends to smooth the surfaces of grains and sintering occurs when an excited molecule moves into a defect site in the grain contact region, thereby reducing the local surface energy and increasing the contact volume. The electron interactions can also anneal highly amorphous ice producing crystallite regions with residual defects. The rate at which diffusion and annealing occur depends on the local ice structure (e.g. defect structure and vacancy concentration) where the ionization event takes place.

As described in Schaible et al. [2016], the measured electron properties in the inner Saturnian system are used together with simulations carried out using the Monte Carlo program PENELOPE and a theoretical approach to computing spherical grain sintering rates on the icy Saturnian satellites to estimate the grain sintering timescales required to produce the observed thermal differences described in Chapter 5. Section 6.1.2 introduces the basics of grain sintering and gives a basic approach to calculating the volume rate of change for grains in contact. Rough estimates of the sintering timescale based on experimental measurements and approximate surface ages determined from meteoroid-impact gardening calculations of asteroids are discussed further in Section 6.2. Then, in Section 6.3, the PENELOPE simulations of  $\sim \text{MeV}$  electron irradiation of water are described and estimates for the molecular excitation timescale and electron-induced heating of grains are given. A model for radiation-induced sintering of spherical grains is presented in Section 6.4 and used to

calculate approximate sintering timescales for each of the icy moons and for a variety of regolith properties. It is shown that, based on the rough estimates for the impact gardening rates, the icy regoliths must be relatively small grained or highly non-uniform in order for sintering to proceed rapidly enough for steady state features to form. Finally, growth of voids to the nanometer scale and their possible contribution to the observed enhancement in UV scattering in the anomalous regions is considered in Section 6.5.

### 6.1.1 Measured electron properties

The Saturnian moons Mimas, Tethys and Dione are embedded in an the energetic magnetospheric plasma where they are bombarded by electrons and ions, consisting primarily of protons and water product ions, in addition to E-ring grains. Since the moons are tidally locked and travel in the same direction as the faster rotating thermal plasma, deposition of low energy ( $< 500 \text{ keV}$ ) ions and electrons occurs preferentially on the trailing hemispheres [Roussos et al., 2007]. The ions penetrate up to  $\sim 100 \text{ nm}$  into the regolith and the electrons up to  $\sim \text{mm}$ . In addition to orbital motion, the plasma particles 'bounce' along magnetic field lines perpendicular to the orbital plane. For electrons with energies above  $\sim 10 \text{ keV}$ , the lateral drift during half a bounce period is less than the diameter of the moons, and it can be assumed that whenever the electron bounce motion crosses a body it is absorbed. At electron energies above the co-rotational resonance energy,  $\mathcal{E}_{cr}$ , gradient and curvature drifts are strong enough to cause electrons to move in a rotational direction opposite to that of the moons and the thermal plasma [Roussos et al., 2007; Paranicas et al., 2014]. These electrons impact preferentially on the leading hemisphere, penetrating to depths of  $\sim \text{cm}$ . The resulting deposition pattern is distinctly lens shaped with larger fluxes concentrated at the center.

The low energy magnetospheric measurements system (LEMMS) of the magnetosphere imaging instrument (MIMI) on the Cassini spacecraft [Krimigis et al., 2004] measured electron energy spectra in the vicinity of the moons. The measured spectra were used to calculate the

**Table 6.1:** Measured high energy electron fluxes [Paranicas et al., 2014] at the icy Saturnian Moons.

Body	Thermal Skin Depth [cm]	Grain Radius [ $\mu m$ ]	Co-rotational Resonance Energy [MeV]	Energy Deposition Flux [ $MeV/cm^2s$ ]	Electron Flux [ $elec/cm^2/s$ ]
Mimas In Out	$2.01 \pm 0.7$ < 0.49	10 – 40 5 – 25	$\sim 1.04$	$5.6 \times 10^4$	$\sim 1.45 \times 10^4$
Tethys In Out	$0.76 \pm 0.09$ $0.15 \pm 0.03$	$\sim 35$	$\sim .84$	$1.8 \times 10^4$	$\sim 1.18 \times 10^4$
Dione Leading Trailing	0.57 0.42	$\sim 30$	$\sim 0.63$	$\sim 1.8 \times 10^4$	$\sim 1.68 \times 10^4$

expected deposition profiles for electrons with energies above  $\mathcal{E}_{cr}$ , and the profiles were shown to closely match the shape and location of the anomalies as seen in Figure 5.1. The boundaries of the thermal anomalies were fit to the energy deposition fluxes given in Table 6.1 for Mimas and Tethys [Howett et al., 2011, 2012]. The thermal anomaly differences are much weaker on Dione and it is difficult to fit a specific energy flux contour to the anomaly boundary. Therefore, that of Tethys is used here. Furthermore, the skin depths of the thermal anomalies,  $\delta$ , and the estimated penetration depth of the electrons [ICRU, 1984] are both of the order of a centimeter. The depth of sensitivity for the UV3 filter on VIMS is  $\sim mm$ . The similar depth scales for the electron penetration, thermal skin depth, and enhanced UV scattering provides strong support for the hypothesis that high energy electrons are responsible for the increased thermal inertia in the anomalous regions. Similar weathering features due to trapped magnetospheric plasma have also been identified on Europa [Paranicas et al., 2001].

The CIRS and VIMS data did not reveal an anomaly on the leading hemisphere of Enceladus. This is likely due to the high rates of redeposited ejecta from the south pole plumes. The ejected grains that fall back onto the surface of Enceladus obscure any changes caused by the high energy electrons [Kempf et al., 2010] and lead to Enceladus having one of the highest albedos in the Solar System [Verbiscer et al., 2005]. However, microwave emission at  $2.17 cm$  measured by the RADAR instrument [Elachi et al., 2004] revealed a

anomaly on the leading hemisphere of Enceladus that was linked to anomalous microwave scattering [Ries and Janssen, 2015]. Since this anomaly was not linked to either electron or meteorite bombardment, further description of anomalous regions on the leading hemisphere of Enceladus is beyond the scope of this thesis.

### 6.1.2 Basics of grain contact growth

As described in Section 2.4, the primary energy loss mechanism for electrons in water ice is the ionization of a water molecule. Taking the volume surrounding the contact in which an electron/molecule interaction can occur and contribute to sintering to be  $V_{int}$  and using the average number of molecules mobilized per event from Equation 2.9, the number of molecules excited to energies greater than  $E_a$  per unit time within the volume  $V_{int}$  is

$$\frac{d\mathcal{N}}{dt} = \frac{N V_{int}}{\tau_0} n_{H_2O} \quad (6.1)$$

where  $N$  is the number of excited molecules per ionization,  $n_{H_2O}$  is the mean number density of the water ice particles and  $1/\tau_0$  is the event frequency. An excitation event which deposits average energy  $E_i$  per interaction can make  $N$  molecules mobile, meaning the energy transferred in the collision event is greater than the mean energy for creating a vacancy/interstitial pair. Then, we can write the average number of molecules made mobile per unit volume per unit time as

$$\dot{\mathcal{N}} = \frac{N\Phi_{elec}(dE/dz)}{W_{H_2O}} \quad (6.2)$$

where  $W_{H_2O}$  is the energy transferred by the incident electron to the water ice lattice in an ionization event,  $\Phi_{elec}$  is the incident electron flux, and  $dE/dz$  is the stopping power or energy lost per unit depth  $z$ .

As ionizations occur everywhere in the solid, including the contact region, with roughly equal probability, an abundance of mobile molecules are continuously created. The net effect

is radiation-induced diffusion of water molecules which can then be coupled to standard equations for thermal sintering to estimate contact volume and contact radius growth estimates. Taking the incident electron fluxes in Table 6.1, the ionization rate of molecules in the solid grains is

$$\frac{1}{\tau_0} = \left( \frac{dE}{dz} \right) \frac{\Phi_{elec}}{n_{H_2O} W_{H_2O}} \quad (6.3)$$

where  $n_{H_2O} \sim \ell_0^{-3}$  is the molecular number density and  $\ell_0$  is the mean lattice spacing.

However, not every molecule with energy greater than  $E_a$  in  $V_{int}$  will be mobilized and contribute to sintering, and thus we take the probability of a molecule diffusing into a lower energy site in the contact region,  $\varepsilon$ , times the volume of a molecule,  $\sim 1/n_{H_2O}$ , as the average increase of the contact volume per ionization event in the contact region. The resulting sintering rate estimate is then given by

$$\frac{dV_{con}}{dt} \sim V_{int} \frac{\varepsilon N}{\tau_0} = \frac{V_{int}}{\tau_{sint}} \quad (6.4)$$

where the quantity  $\varepsilon N$  depends in large part on the quality of the material in the vicinity of the contact. That is, irregular surfaces or the presence of poorly bound molecules means that  $\varepsilon$  and  $N$  are larger than, for instance, a highly annealed crystalline contact region. For surface or bulk diffusion the volume  $V_{int}$  in which an event can occur on either side of the contact and lead to sintering depends on the circumference of the contact, and the length scale for mobilizing molecules  $\lambda$  as

$$V_{int} \sim 2\pi R_{con}^2 \lambda \quad (6.5)$$

where  $\lambda$  is the approximate length scale of the excited region and can be estimated using Equation 2.12. If we assume that  $V_{int}$  is of the order  $V_{con}$ , then the sintering timescale

$$\tau_{sint} \sim \frac{\tau_0}{\varepsilon N}.$$

## 6.2 Preliminary surface modification timescales

In order to get a sense of whether it is possible for the high energy electrons to create sufficient mobilization and diffusion of molecules to sinter grains and increase the thermal conductivity of the icy regoliths, the basic growth equations discussed above are combined with experimental measurements for ion compaction of porous water ices to provide a first order estimate of the grain sintering rates. Additionally, the regolith resurfacing timescales are estimated following the methods described in Section 2.6. Such a first order comparison was carried out first to establish the validity of the electron-induced sintering hypothesis, and second to provide insight into the general regolith reformation processes.

### 6.2.1 Ion compaction of water ice

In recent experimental work, a large reduction in the porosity of vapor deposited laboratory ices was produced by energetic ions incident on ice films grown on a smooth *Au* substrate [Raut et al., 2008]. Although the laboratory ices were thin ( $< 1 \mu m$ ) with an initial porosity of only 26%, they can be considered crude proxies for a contact region with local roughness such as that shown in the Fig. 5.2 inset. As is the case for electrons, the incident ions (80 – 400 keV) deposited energy predominantly through ionizations which in turn drove molecular diffusion. Fitting the porosity measurements as a function of energy deposited in the ice with a decreasing exponential and ignoring any low energy thresholds [Dartois et al., 2013, 2015] results in a characteristic energy of  $E_c \sim 1.3 eV$ . This accounts for both the fraction of deposited energy converted into molecular motion and for the efficiency of the annealing process that leads to compaction of the porous sample.

Equating the sintering timescale given above with the compaction timescale,  $\tau_{comp} \sim \tau_0(E_c/W)$ , we see that the ‘compaction efficiency’  $\varepsilon N \lesssim 20$ , implying that each ionization creates a large number of mobilized molecules which subsequently move into more favorable binding sites. For comparison, using  $\Delta E \sim 5 eV$  in Eq. 2.9 and assuming  $E_a \sim 0.5 eV$ ,

which is a conservative value for surface diffusion activation energy of crystalline laboratory ices [Nie et al., 2009], then  $N \sim 6 - 8$ . Although these are similar orders of magnitude, the compaction measurements were made on ices deposited from the vapor at very low temperatures. Therefore, the molecular structure is highly disordered, consistent with the larger value of  $\varepsilon N$  above.

**Table 6.2:** Comparison of excitation, ion-induced compaction and resurfacing timescales (in *Myr*) for the icy Saturnian moons at a depth  $h$  below the regolith surface. The compaction estimates give a rough lower bound on the expected sintering timescales for the icy moons. The method of estimating regolith renewal timescales due to grain impacts are given in Section 2.6. No E-ring growth timescale is given for Mimas since grains deposit preferentially on the trailing hemisphere of that body.

Timescale [Myr]	Molecular Excitation $\tau_0 (h = 1mm)$	Compaction $\tau_{comp}$ (expt.)	IDP Gardening $\tau_{gar} (h = 1 cm)$	E-ring Growth $\tau_{gro} (h = 1 cm)$
Mimas	0.5	0.02	0.6	--
Tethys	0.7	0.03	1.9	0.004
Dione	0.7	0.03	4.9	0.046

Compaction not only reduces the porosity of the solid but, of interest here, it would improve the thermal contact between individual ice particles. The large value estimated for  $\varepsilon N$  suggests that the  $\Delta E$  contributing to the compaction could be a somewhat larger fraction of the deposited energy (equal to  $W_{H_2O}$  as described above) than that estimated for experiments on the sputtering of ice. Additionally, the activation energy for annealing in the amorphous and porous samples used in the compaction experiments is likely  $< 0.6 eV$ , the bulk diffusion activation energy for crystalline ice [Nasello et al., 2007; Livingston et al., 1998]. Although the energy deposition densities for the ions in the compaction experiments were typically higher on average than the *MeV* electrons considered here, the maximum energy deposition for the incident electrons is comparable to the lowest experimental values tested. Combined with the expectation that the experimental ice would have a high defect density and the suggestion that there may be a compaction threshold for the particular samples used, the compaction results represent a rough lower bound for the sintering timescale. Additional experiments using electron radiation together with realistic water ice grains in vacuum would be instructive.

## 6.2.2 Regolith growth timescale

Gardening due to impacts from small ( $0.5 - 100 \mu m$ ) interplanetary dust particles (IDPs) and meteorites, as well as the deposition of circumplanetary material such as E-ring grains ( $\lesssim \mu m$ ), compete with sintering and help determine the steady state regolith surface properties. In order for the observed anomalies to be stable on the icy satellites, the sintering timescale should be less than regolith turn over or renewal timescale,  $\tau_{ovr}$ , due to gardening and growth. The IDPs impact approximately uniformly across the surfaces, and impacts eject and distribute the surface material. The average yield per impact,  $Y = \text{mass of ejecta}/\text{mass of impactor}$ , depends on the mass and relative velocity of the impactor [Spahn et al., 2006a]. At Mimas, the E-ring grains deposit preferentially on the trailing side, whereas on Tethys and Dione these grains deposit preferentially on the leading side, modifying the anomalous regions [Hamilton and Burns, 1994]. The E-ring grains impact at lower velocities than IDPs and thus create less ejecta and mixing. Therefore, that we assume that E-ring grains primarily supply fresh water ice to the surface. The effect of the E-ring grains is a brightening of the surface albedo [Verbiscer et al., 2007].

The regolith gardening rate due to IDP grains is determined using the methods described in Section 2.6 where the impact ejecta yields for IDPs,  $Y_{IDP}$ , are given in Table 6.3 [Spahn et al., 2006a]. The IDP mass flux and velocity near Saturn are taken to be  $\sigma_{\infty} \sim 1 \times 10^{-18} g/cm^2/s$  [Poppe, 2016] and  $v_{\infty} \sim 9.5 km/s$  [Spahn et al., 2006a], respectively. The depth  $h$  to which the regolith grows in time  $t$  is then calculated using Equation 2.27. The rate at which E-ring grains cover the surface, given as a mass flux  $\sigma_{E-ring}$ , can be used to directly determine the total rate at which the regolith is coated. The growth rate of the regolith is determined by dividing the flux by the density of the regolith, and the timescale for the regolith to grow to a depth  $h$  can be written

$$\tau_{E-ring}(h) = \frac{h\rho_{reg}}{\sigma_{E-ring}}. \quad (6.6)$$

where the E-ring deposition fluxes are taken from Spahn et al. [2006a].

**Table 6.3:** Approximate gardening timescales assuming  $\rho_{reg} \sim 0.5\rho_{ice}$  corresponding to a 50% porous water ice surface. Orbital distances are given in Saturn radii,  $R_S$ . The IDP fluxes were corrected for gravitational focusing using recently published IDP fluxes at Saturn [Poppe, 2016], and the yields and E-ring flux were taken from Spahn et al. [2006a].

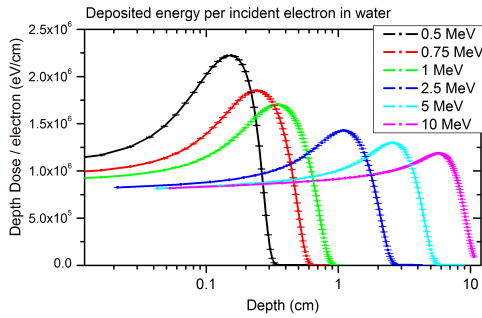
Satellite	Orbital distance [ $R_s$ ]	$Y_{IDP}$ ( $\times 10^4$ )	$\sigma_{IDP}$ ( $\times 10^{-18}$ ) [ $g/(cm^2s)$ ]	$\sigma_{E-ring}$ ( $\times 10^{-15}$ ) [ $g/(cm^2s)$ ]
Mimas	3.08	1.8	2.5	62
Tethys	4.89	1.2	2.0	230
Dione	6.26	0.98	1.6	27

The approximate IDP and E-ring grain resurfacing timescales to produce a regolith of 1 cm depth are given in Table 6.2. Although these estimates are rough and improved E-ring grain distribution modeling is needed to determine how deposition rates vary spatially across the moon surfaces. A comparison of the resurfacing timescales with the ion sintering timescale estimated from the compaction experiments suggests that the incident  $MeV$  electron flux is able to produce the requisite sintering in less than the expected regolith growth timescale. Thus, stable thermal anomalies can form. In order to further test these conclusions, we now consider sintering processes using standard models for spherical grains where diffusion is driven by electron radiation.

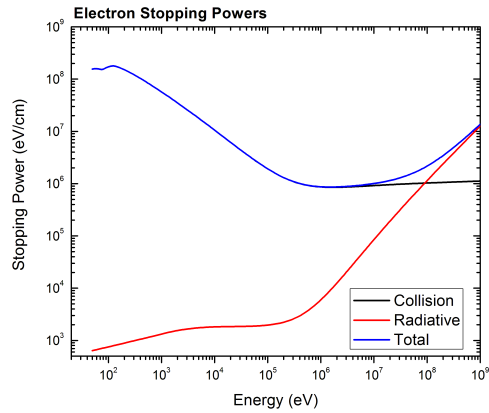
## 6.3 Electron irradiation effects on icy regolith grains

### 6.3.1 PENELOPE simulation software

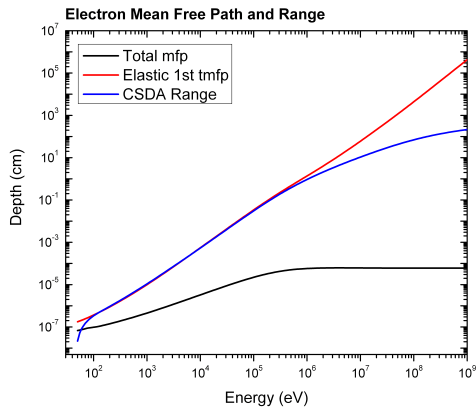
The PENELOPE (Penetration and ENergy LOss of Positrons and Electrons) Monte-Carlo program [F. Salvat and Sempau, 2011] was used to simulate the transport of  $MeV$  electrons through the water ice grain regolith. PENELOPE was developed to simulate energetic electron, positron, and photon interactions with materials. The electronic stopping power, range, and cross-section for electrons incident on a semi-infinite amorphous water target is shown in Figure 6.1. Although not studied in detail here, lower depths where the electron is able to react chemically with the material may also be of interest.



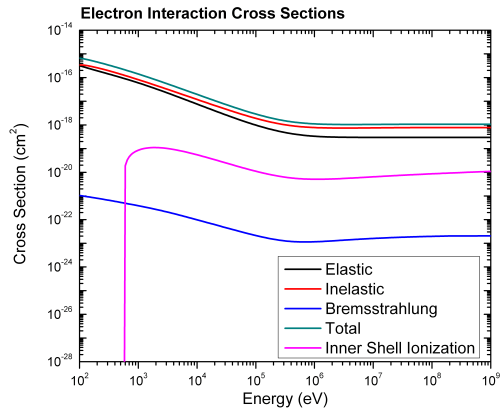
(a) Depth Dose



(b) Stopping Power



(c) Projected Range



(d) Cross Section

**Figure 6.1:** PENELOPE calculations for: (a) Electron energy deposition profile and stopping power calculated for 0.5–10 MeV electrons incident on 50% porous water; (b) The 'stopping power' which is the mean energy loss per unit path length and is similar to a force slowing down the electrons; (c) The the average path length an electron travels through the water ice or the CSDA range; and (d) The cross-section elastic and inelastic collisions, Bremsstrahlung, and inner-shell ionization processes.

The PENELOPE program uses tabulated values for reaction cross-sections as a function of energy to simulate the collision cascade and determine how the energy of the incident electron is deposited into the target. As electrons penetrate the ice regolith, they lose energy through elastic and inelastic collisions, ionization of the water molecules, and Bremsstrahlung interactions. As shown in Figure 6.1, the cross-section for inelastic and elastic collisions of electrons in water are similar to within a factor of a few for all energies less than  $\sim GeV$  and together account for the majority of the energy loss in the energy range relevant to the Saturnian magnetosphere. Inner-shell ionization and Bremsstrahlung radiation can also

occur, although these are negligible at energies below 10 *MeV*.

### 6.3.2 Electron energy profiles and excitation timescales

To simulate the irradiation of the Saturnian moons with high energy electrons, the measured electron energy spectra in the vicinity of the moons, given in Figure 6.2a, were used as the source input in the PENELOPE program. The simulations were run by sampling  $1 \times 10^8$  electrons from the measured electron energy distributions where the low energy cut off of the electron energy distribution was taken to be the co-rotation resonance energy and the upper cut off where the electron energy distributions fall to negligible levels ( $\leq 10$  *MeV*). PENELOPE directly calculates the average energy deposited per electron per unit depth into the regolith,  $dE/dz$ .

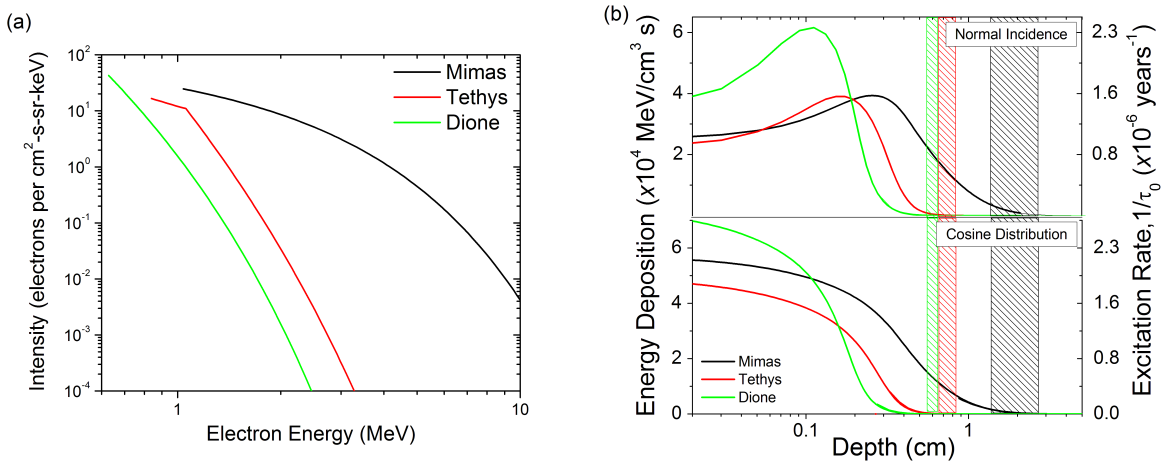


**Figure 6.2:** (a) Energy spectra of electrons in the vicinity of the icy moons based on LEMMS measurements taken from Paranicas et al. [2014] where the lower limit is taken as  $\mathcal{E}_{cr}$  given in Table 6.1. (b) The average energy flux deposited per unit length calculated with the PENELOPE program using the electron probability distributions shown in (a). The upper frame gives the deposition profile for normally incident electrons and the lower panel gives results for electrons averaged over a cosine distribution of incidence angles. The hashed boxes show the measured thermal skin depth and are consistent with the penetration depth of the electrons for a 50% porous regolith.

Although the incident electron fluxes,  $\Phi_{elec}$ , and energy distributions are typically measured by spacecraft instruments, the literature values are given in terms of the energy deposition fluxes as in Figure 5.1 [Paranicas et al., 2012; Paranicas et al., 2014]. Therefore, to determine  $\Phi_{elec}$ , the energy flux is divided by the mean electron energy,  $\langle E_{elec} \rangle$ , determined

from the electron energy spectra fits using the mean value theorem. The volumetric energy deposition rate in units of  $eV/cm^3s$  can be found by multiplying  $dE/dz$  by the incident electron flux, which is equivalent to

$$R_{Eng}(z) = \frac{dE}{dz} \times \frac{Q_{moon}}{\langle E_{elec} \rangle} \quad (6.7)$$

where  $Q_{moon}$  is the best fit energy deposition contour given in Table 6.1. The left hand axis of Fig. 6.2b shows the average energy deposited per unit volume per electron as a function of depth below the surface of a water ice regolith with  $\phi = 0.5$ , and the right hand axis gives the molecular excitation rate calculated from Equation 6.3. Results are given for both normal incidence and averaged over a cosine distribution of electron incidence angles. The hashed boxes represent the approximate thermal skin depth given in Table 6.1. Using the derived probabilities as a continuous energy distribution electron source in the PENELOPE program gives a unique depth-dose distribution for each of the moons. We can see that energy deposition into Dione peaks at a much shallower depth than at Mimas, and that at Mimas the energy deposited by incident electrons remains important to much greater depths.

### 6.3.3 Average heating per grain

Steiner and Kömle (1993) gave the energy balance at the surface of an uncovered, porous water ice regolith as

$$\Phi^{tot} = \left( -k_{eff} \frac{\partial T}{\partial z} \right) + Z^w L^w + \epsilon \sigma T_{surf}^4 \quad (6.8)$$

where  $\Phi^{tot}$  is the energy flux incident on the surface of the regolith,  $Z^w$  is the free sublimation rate of water ice given by the Hertz-Knudsen formula,  $L^w$  is the latent heat of water ice, and  $\epsilon$  is the IR emissivity. The Hertz-Knudsen formula gives the rate of phase change (i.e. rate of molecular desorption) for a given interface. However, as shown in Chapter 5, re-radiation from the surface and sublimation are negligible, and therefore all of the incident electron energy must be conducted into the regolith where it can heat grains.

Assuming that the energy is deposited uniformly throughout the grain, we can calculate the temperature change of a grain per incident electron following

$$\Delta T/electron = \frac{(dE/dz)d_g}{c_{ice}\rho_{ice}V_g} \quad (6.9)$$

where  $c_{ice}$  and  $\rho_{ice}$ , the heat capacity and density of ice, respectively, are given in Table 5.1, the average distance traveled by an electron through a grain is  $d_g$  and  $V_g$  is the volume of a grain. Using the energy deposition rate from figure Figure 6.2, we can calculate the average heating rate per grain as a function of depth. This is shown for each of the moons in Figure 6.3

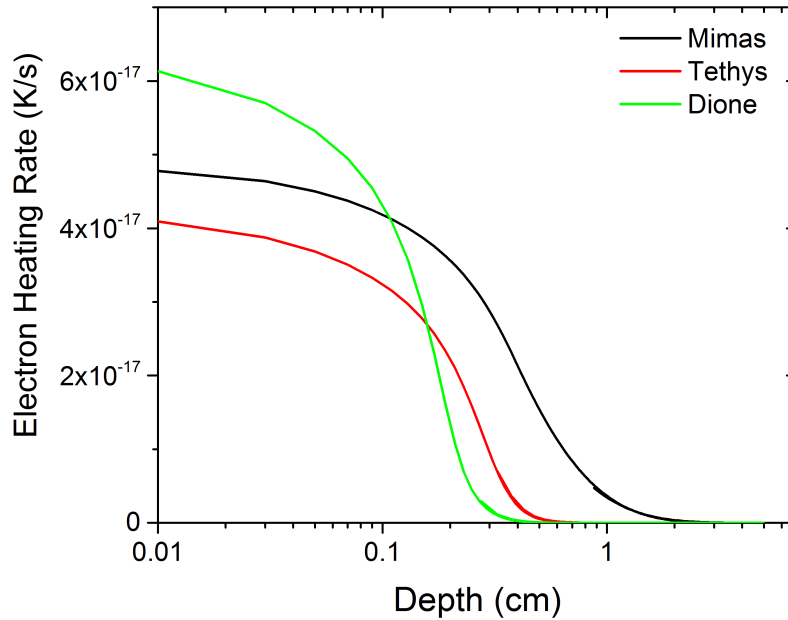


**Figure 6.3:** Average temperature change per second as a function of depth based on the Paranicas electron energy distributions. This calculation shows that any effect due to electron heating of the bulk is negligible.

Due to the small heating rates produced by the electrons, net heating of the regolith grains due to electron bombardment is negligible and produces no significant effect on the molecular diffusion rates. Therefore, sintering by individual excitation will be examined. Each excitation can be thought of as producing a small heat spike randomly situated in the grain

and causing surface or bulk molecules to become mobile as discussed in Chapter 2. In the following, the excitation rates for each of the moons, given in Figure 6.2, will be combined with a detailed description of the micro-heating events caused by electron interactions with water molecules. It will be shown that the so called 'heat-spike' caused by the electron ionization of the water molecules leads to the mobilization of the molecules, discussed previously in Section 2.4, in order to calculate the effective radiation-induced diffusion rates for the ice grains. Then, the radiation-induced diffusion model will be coupled with standard sintering equations for spherical grains so that grain contact growth rates can be calculated and the effective timescale for electron-induced sintering can be determined.

## 6.4 Radiation-induced sintering of spherical grains

Sintering is typically assumed to proceed by various molecular transport mechanisms as shown in Figure 6.4. Although models of sintering were originally developed in powder metallurgy [Kuczynski, 1972; Swinkels and Ashby, 1981], ionization events due to energetic radiation can eject molecules from grain surfaces into the gas phase and induce bulk, surface, and grain boundary diffusion. Molecules tend to accumulate in the grain contact region due to more available bonding arrangements caused by the inverted curvature, and thus desorption and diffusion processes lead to a growth in the contact volume. The sintering rates typically depend on the size of the grains, temperature, external pressure, and vapor pressure in the void space between grains. Equations governing the mechanisms leading to the formation and growth of the contact area between spherical grains in thermal equilibrium are given in A0.2.

Sintering models in the literature are primarily for idealized geometries under thermal equilibrium, and these models are applied here ignoring the fact that the grains are likely not spherical, the contacts not ideal, and that ionization events are inherently non-equilibrium. We also note that, at the low temperatures measured on these icy satellites, the thermal diffusion times are much greater than  $\sim 1 Myr$  [Mitchell et al., 2015] so that the defect

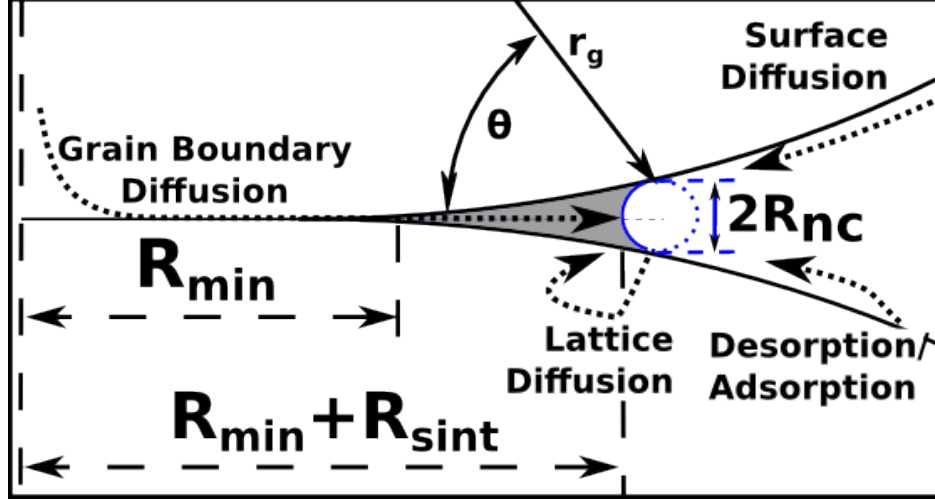


**Figure 6.4:** Diffusion paths and approximate contact shape for spherical grains in contact where  $R_{con}$  is the contact radius and increases as the contact grows. The inverted curvature where the grains come into contact results in preferential growth driven by surface energy minimization. Sintering rates increase as the radius of curvature,  $R_{nc}$ , decreases. Assuming that  $R_{con} \ll r_g$ , we see  $\theta \sim \pi/2$  and  $R_{nc} \sim R_{con}^2/2r_g$ .

densities may differ from those expected for well equilibrated ice grains as assumed in the sintering models. Therefore, the results described below provide rough upper limits to the sintering timescale.

### 6.4.1 Sputtering and redeposition

Sintering of ice grains is well studied at terrestrial and cometary temperatures where the dominant mechanism is typically found to be vapor transport of molecules [Blackford, 2007; Sirono, 2011]. The rate of change in the contact volume connecting equal sized grains caused by thermally driven gas phase sintering is given in Equation B-1. However, at 80K the water vapor pressure,  $P_v$ , is very low and the primary source of gas phase molecules is likely electron-induced desorption from grain surfaces, which we refer to here more generally as sputtering. Therefore, it isn't clear that vapor phase corrections such as those described in Section A0.2 can be directly applied to sputtering by electronic excitations since evaporation takes place from preferred positions on the surface, and since the energy necessary for an atom to leave the surface likely is transferred in several steps/collisions [Sigmund, 1969b].

For a rough, but on average flat, surface we estimate the electron-induced desorption flux as

$$\Phi_0 \sim \frac{\lambda n_0}{\tau_0} \quad (6.10)$$

where  $\lambda$ , given in Equation 2.12, is the weighted average distance from the surface at which an excitation can take place and lead to an ejection of a surface molecule. Although the linear dependence on the deposited energy in  $\lambda$  is observed in weakly bound condensed gas solids, it has not been well studied for ice [Johnson, 2011] and will be used here as a rough upper bound for the depth below the grain surface at which an interaction can occur and produce a sputtered molecule.

At  $< 100 K$  the sticking probability of water molecules is  $\sim 1$  [Gibson et al., 2011] and, accounting for electron-induced sputtering and thermal vapor pressure, the mean free path of the ejected molecules is much larger than the pore diameter. If there are no gas phase collisions and no scattering from grain surfaces, then only molecules with a direct line-of-site path to the grain contact will contribute to contact growth. Therefore, one might assume the local geometry of the regolith would be important. However, assuming a uniform grain size distribution, Sirono [2011] found little difference between the growth rates determined using a molecular mean free path much larger or much smaller than the grain radius. Noting that, on average, gas phase molecules in a spherical grain regolith originate on surfaces with curvature  $1/r_g$ , the net sputter flux at a point in the contact region is the difference in the deposition and ejection rates and is given by

$$\Phi_{net} = \Phi_0 \frac{\lambda}{2} \left( \frac{2}{r_g} - \frac{1}{R_{con}} + \frac{1}{R_{nc}} \right) = \Phi_0 \xi_{sput} \quad (6.11)$$

where  $\xi_{sput}$  is similar to the sintering 'efficiency factors' described in Section A0.2. For the case of  $r_g \gg R_{con}$ , the neck radius,  $R_{nc} \sim R_{con}^2/2r_g$ , dominates the curvature term and we can write  $\tau_{sint} \sim (R_{con}^3 \tau_0)/(\pi \lambda^2 r_g)$ . Taking approximate values of  $R_{con}/r_g \sim 0.01$  and  $\tau_0 \sim 0.5 Myr$  and using  $E_a \sim 0.5 eV$  in Eq. 2.12, then  $\tau_{sint} \sim 300 Myr$  and  $30 Myr$  for  $25 \mu m$

and  $5 \mu m$  grains, respectively. This is much longer than the regolith formation timescales, suggesting that the diffusion processes discussed below dominate grain sintering for the contact size ranges given in Table 5.2.

## 6.4.2 Diffusional sintering

In general, when a molecule in the water ice grains is excited by charged particle radiation, several regimes of induced diffusion can be identified [Myers, 1980]. The first, often referred to as the mixing phase, is driven by the mini-cascade produced when an excited molecule releases energy to the surroundings through a series of collisions. Mixing in this context differs from impact produced mixing in that it affects the solid only on the order of only  $nm$  as opposed to  $\mu m$  in the case of grain impacts. Following the mini-cascade, the heat diffuses away and can still, in principle, activate a sintering event. However, this thermal pulse has not been well modeled and more studies are needed to determine to what extent excitation energies below the diffusion activation energies can contribute to grain sintering in an icy grain. Finally, enhanced bulk diffusion occurs due to increased concentrations of vacancies and interstitials resulting from the electron radiation. As most previous studies of radiation-induced diffusion in solids have focused on ion bombardment of metals and semi-conductors, care must be exercised in adapting models to electron irradiation of a dielectric ice with non-equilibrium defect density.

**Table 6.4:** Thermal diffusion coefficients and activation energies where  $D = D_0 \exp(-E_a/kT)$ . The range of activation energies for each diffusion process represents uncertainty in the experimental measurements. The maximum and minimum activation energies can be thought to represent smooth and rough grains, respectively.

Diffusion Mechanism	$D_0$ [cm <sup>2</sup> /s]	$E_a$ [eV]
Bulk, $D_{bulk}$ <sup>1</sup>	$\sim 10^{-11} - 10^8$	0.6 – 0.75
Surface, $D_{surf}$ <sup>2</sup>	$1.4 \times 10^{-4} - 6.1 \times 10^{-3}$	0.1 – 0.5
Grain Boundary, $D_{gb}$ <sup>3</sup>	8.4	0.51
Vacancy, $D_v$ <sup>4</sup>	$1 \times 10^{-3}$	0.62

Radiation-induced diffusion occurs when the incident electron mobilizes molecules through ionization interactions. Mobilized molecules can produce defects in the ice lattice,

and when such events occur near the grain contact region diffusing molecules will on average move in such a way as to reduce the local surface energy. Therefore, events occurring within a diffusion length of the contact region can result in an increase in the contact volume. During the mini-cascade, on average  $N$  molecules, estimated using Equation 2.9, will become energetic enough to overcome diffusion activation energy  $E_a$ . Experimentally measured activation energies for each of the diffusion process depicted in Figure 6.4 are given in Table 6.4 where the range of values represents the large experimental uncertainty. The effective diffusion coefficient associated with the mini-cascades,  $D_{mc}$ , can be written

$$D_{mc} = \frac{N\ell_{eff}^2}{J\tau_0} \quad (6.12)$$

where  $\ell_{eff}$  is the mean diffusion length of molecules excited in the minicascade and  $J = 6$  or  $4$  for bulk and grain boundary diffusion or surface diffusion, respectively, and represents the degrees of freedom in which a molecule can diffuse.

As described in additional detail in Section A0.3, the diffusion length,  $\ell_{eff}$  can be estimated using the often applied thermal spike models [Kaoumi et al., 2008]. Spike models assume the energy deposited due to particle interactions is initially localized in a small number of nearby molecules and spreads uniformly outward. To obtain the effective diffusion coefficient,  $D_{eff}$ , the heat distribution is integrated over time assuming constant thermal conductivity and heat capacity of the material. Such models depend on the activation energy,  $E_a$ , and the jump frequency of molecules determined by fitting experimental data to the Arrhenius equation. However, due to difficulties in measuring molecular diffusion at low temperatures, differing growth conditions and dependence on crystal structure [Ghesquière et al., 2015], there is a large spread in the fitting parameters as seen in Table 6.4, leading to large spread in the estimated diffusion lengths. The theoretical effective diffusion coefficient can also be estimated using the entropy change in ice due to forming/annihilating a vacancy,

$\Delta S_f$ , plus the entropy of vacancy migration  $\Delta S_m$ , as given by

$$D_0 \sim \frac{1}{J} \ell_0^2 \nu_D N_j \exp\left(\frac{\Delta S_f + \Delta S_m}{k_B}\right) \quad (6.13)$$

where  $\nu_D \sim 10^{13} \text{ sec}^{-1}$  is the Debye frequency, which is approximately the frequency of vibration of a water molecule,  $N_j$  is the coordination number or number of possible jump directions, and  $k_B$  is the Boltzmann constant. Measurements of the total entropy change vary from  $50 - 100 \text{ J/mol/K}$  in water [Hobbs, 1974], giving a range of effective diffusion lengths  $\ell_{eff} \sim 1 - 50 \ell_0$ . Noting that the lower estimates of the effective diffusion length obtained from thermal spike models are similar to the approximate cascade size obtained using Equation 2.12, we use the latter as a conservative estimate of mean effective diffusion length.

Mini-cascade events will create on average  $N$  vacancy/interstitial pairs as estimated using the Kinchin-Pease approximation in Eq. 2.9. Thus, the electron radiation of the icy surfaces results in bulk defect concentrations that are greater than expected for a material in thermodynamic equilibrium and leads to enhanced bulk diffusion,  $D_{ebd}$ , of the vacancies and interstitials. The defects will remain in the solid until they either (a) recombine through thermal diffusion or (b) annihilate at a fixed sink such as a pore surface. Enhanced bulk diffusion can be estimated as [Myers, 1980]

$$D_{ebd} = \sqrt{\frac{N_{KP} D_v}{\pi n_{H_2O} \tau_0 R_{iv}}} \quad (6.14)$$

where  $D_v$  is the thermal diffusion coefficient for vacancies and  $R_{iv}$  is the vacancy-interstitial separation distance at which spontaneous recombination occurs. This model assumes that any spatial variations are small and that the vacancy and interstitial concentrations are in steady state (balanced annihilation and creation rates), although this may not be the case for the icy regoliths. Using the vacancy diffusion rate given in Table 6.4 indicates that this process is negligible at 80K.

### 6.4.3 Spherical grain sintering timescales

The radiation-induced surface, bulk, and grain boundary diffusion coefficients determined using Equation 6.12 and assuming the radiation conditions on Mimas are plotted in Figure 6.5a. For temperatures of 80  $K$ , radiation induced diffusion dominates thermal diffusion, although thermal grain boundary and surface diffusion become comparable at temperatures approaching 100  $K$ . Grain boundary sintering leads to densification by transport of defects from the interior of grains to the grain contact, and Figure 6.5b shows that it is much smaller than surface diffusion indicating that changes in porosity and grain size are small over the sintering lifetime.

Details of the sintering process are given in Section A0.2, and the sintering rates are estimated by replacing the thermal diffusion coefficients in Equation B-19 b-c with the radiation-induced diffusion coefficients. The sintering rate for spherical grains depends sensitively on the relative sizes of the grain and contact regions. Assuming  $R_{con} \ll r_g$ , it can be shown that  $\tau_{sint}$  varies as  $R_{con}^5/r_g^2$  for the bulk and  $R_{con}^7/r_g^3$  for the surface sintering mechanisms. The sintering timescales at Mimas,  $\tau_{sint} \sim V_{con}/(dV_{con}/dt)$ , are shown in Figure 6.5b. Surface diffusion tends to dominate in the size ranges of interest and smaller grain sizes have shorter sintering timescales due to the proportionately larger curvatures and an increased probability of an excitation occurring close to a grain contact. Assuming constant sintering rates in a regolith of uniform 25  $\mu m$  grains, an activation energy of  $E_a \sim 0.5 eV$ , and  $R_{con}/r_g \sim 0.01$  gives  $\tau_{sint} \sim 50 Myr$  for bulk and  $\sim 10 Myr$  for surface diffusion sintering timescales, respectively. For 5  $\mu m$  grains the surface diffusion sintering mechanism dominates with  $\tau_{sint} \sim 0.1 Myr$ .

The estimated contact/grain radius ratios inside and outside the anomalous region of Mimas, taken from Table 5.2, are indicated in Figure 6.5b, and the timescale for sintering is determined by numerically integrating the total sintering rate over this interval. This is done for each body assuming a constant average temperature of 80  $K$ , and the resulting timescales

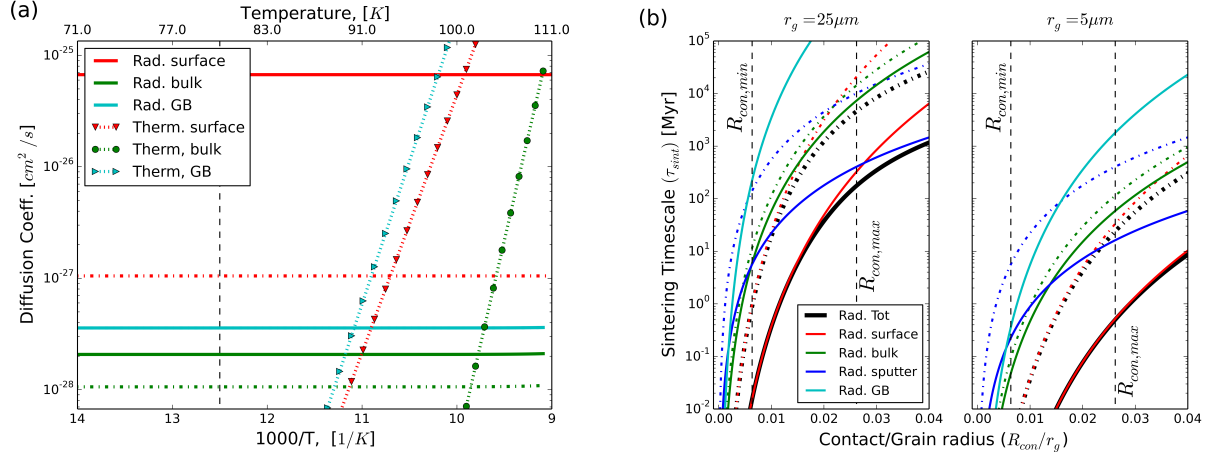


**Figure 6.5:** (a) Radiation-induced diffusion coefficients at Mimas calculated from Eq. 6.12 and compared with the bulk [Livingston et al., 1998], grain boundary [Goldsby and Kohlstedt, 2001], and surface [Kouchi et al., 1994] thermal diffusion coefficients. The dashed vertical line indicates 80 K. (b) Sintering timescales  $\tau_{sint} \sim V_{con}/(dV_{con}/dt)$  at 80 K calculated using the sintering model of Swinkels and Ashby [1981] and effective radiation-induced diffusion coefficients determined for the energy deposition rates at Mimas given in Table 6.1. Here, the vertical dashed lines represent the limits of  $R_{con}/r_g$  for Mimas taken from Table 5.2 assuming  $\phi = 0.5$  and  $k_g = 6.5 W/m/K$ . For both images, the solid lines are for the minimum activation energies given in Table 6.4 and can be thought to represent a 'rough' grain where radiation induced diffusion is efficient, while the dashed-dot lines were calculated using the maximum energies and represent smooth, crystalline grains.

are given in Table 6.5. The range of sintering timescales is determined from the uncertainty in the measured thermal inertia, and the *max* and *min* values correspond, respectively, to the upper and lower limits of the diffusion activation energies in Table 6.4. Since regolith grains are expected to deviate significantly from the smooth, spherical geometries assumed in the sintering model discussed above, the sintering timescales given here represent rough upper limits.

Assuming that the gardening and E-ring grain deposition rates in Table 6.2 dominate the regolith resurfacing processes and that the model for  $k_{eff}$  in Equation 5.14 gives reasonable estimate for the contact radii, the results in Table 6.5 indicate that only certain regolith geometries give reasonable sintering timescales. At Mimas and Tethys, this model suggests that either regolith growth/mixing timescales are longer than those in Table 6.2 or the regolith is relatively compact and composed of small, rough grains. That is, unless  $r_g \lesssim 5 \mu m$ ,  $\phi \lesssim 0.65$ , and the  $E_a$  for surface diffusion is near the lower limits established in experiments, the calculated sintering timescales for spherical grains are greater than the estimated regolith renewal timescales. However, these latter estimates also have considerable uncertainties. The

**Table 6.5:** Electron-induced sintering times in *Myr* for the icy Saturnian moons. The radiation enhanced sintering model is sensitive to  $R_{con}/r_g$  and the values given in Table 5.2 were used to determine the initial and final sintering rates. The *min* values correspond to the smallest activation energies given in Table 6.4 and can be thought represent a 'rough' grain with a high defect density, while the *max* values approximate smooth, crystalline grains.

$\tau_{sint}$ [ <i>Myr</i> ]	$r_g = 25 \mu m$ $\phi = 0.5$ $k_g = 6.5 W/m/K$	$r_g = 5 \mu m$ $\phi = 0.5$ $k_g = 6.5 W/m/K$	$r_g = 5 \mu m$ $\phi = 0.65$ $k_g = 6.5 W/m/K$	$r_g = 5 \mu m$ $\phi = 0.5$ $k_g = 0.5 W/m/K$
Mimas				
max	800 – 5000	3 – 30	30 – 300	> 1000
min	30 – 200	0.06 – 0.7	0.7 – 7	100 – 500
Tethys				
max	3 – 9	0.01 – 0.02	0.07 – 0.2	20 – 60
min	0.06 – 0.2	$\sim 10^{-4}$	$\sim 10^{-3}$	0.5 – 1
Dione				
max	0.007 – 0.1	$\sim 10^{-4}$	$\sim 10^{-3}$	0.06 – 1
min	$\sim 10^{-3}$	$< 10^{-6}$	$\sim 10^{-5}$	0.001 – 0.02

thermal anomalies on Dione and Tethys are much smaller than those on Mimas due to both the smaller penetration depth and lower incident fluxes of the electrons and more rapid regolith growth as seen in Table 6.2.

## 6.5 Void formation and enhanced UV scattering

Void formation in radiation damaged materials has been studied for a long time in relation to deterioration of nuclear reactor materials. Similar processes can occur in water ice grains, although the opposite (compaction) has also been observed as discussed in Section 6.2. Of course individual vacancies produced by the high energy electrons cannot account for the enhanced reflectance seen in the UV3 filter [Schenk et al., 2011] due to large difference in the size scales; vacancy diameters are  $\sim nm$  whereas the UV3 wavelength is  $\sim 0.3 \mu m$ , and thus the scattering from single vacancies is minor due to the much larger wavelength of light. However, much larger radiation-produced voids filled with gas bubbles can form by the coalescence of vacancies and interstitials [Gittus, 1978]. As discussed above, radiation-induced diffusion can drive vacancy migration leading to void growth. Radiation induced voids due to H and He bombardment are often found to contain trapped gasses due to the energy barrier

for resolvability in the material [Johnson and Jesser, 1997].

The maximum bubble radius ( $r_b$ ) for a given internal pressure ( $p$ ) is given by  $p \leq 2\gamma/r$ , where  $\gamma$  is the surface tension, and the average bubble radius produced by energetic ions varies roughly as

$$r \propto [D_v/(dE/dt)]^p \quad (6.15)$$

where  $D_v$  is the vacancy diffusion coefficient and  $dE/dt$  is the energy deposition rate. The exponent  $p$  ( $\sim 1/4$ ) [Gittus, 1978]. Since radiation forms and destroy such features, the average radius increases as energy deposition rate decreases although the time to form increases. For electrons which do not create extensive material damage or sputter molecules efficiently, the bubbles formed would be expected to be on average larger than for highly damaging ions Johnson and Jesser [1997]. Note that temperature is critical in determining the rate of vacancy aggregation to form voids and determines the gas pressure in a void. Due to the low vacancy diffusion rates for water ice at 80 K, it might be expected that the average void size remains small. However, less damaging radiation such as the incident  $MeV$  electrons can cause larger voids to form. Further work is needed to determine the equilibrium void size in the water grains on the icy Saturnian moons.

## 6.6 Summary

Thermal anomalies on the leading hemispheres of the icy Saturnian moons Mimas, Tethys and Dione have been spatially correlated with high energy electrons which preferentially impact the leading hemispheres of these bodies. The thermal inertia increase in the irradiated regions can be described as an increase in the effective size of the contacts connecting adjacent grains. We have shown here that the proposed radiation-induced sintering mechanism can produce the stable thermal anomalies consistent with grain impact resurfacing estimates. Estimates for the sintering times based on experimental results indicate that, under reasonable

approximations for grain structure and molecular excitation rates, the radiation-induced sintering is faster than the approximate regolith renewal rate.

The smaller thermal inertia differences measured on Tethys and Dione implies that E-ring grain infall limits the strength of the anomalies on these bodies, while IDP gardening limits the anomaly strength at Mimas. This is also consistent with the suggestion that the differences in the reflectance spectra inside and outside the anomalous regions observed by Voyager and Cassini are due to the electron radiation inside the anomalies. A standard spherical grain sintering model which depends on the regolith porosity, grain size, and grain thermal conductivity was also used to estimate radiation-induced diffusion and sintering rates. This model assumes idealized contacts between grains and defect densities that are at thermal equilibrium, and therefore gives only an approximate upper limit to the sintering timescale. Although the lower bound to the sintering timescale based on the compaction experiment was sufficiently short, the spherical grain models suggest that the regoliths have a porosity  $\lesssim 65\%$  and grain sizes of  $\lesssim 5 \mu m$ . This is somewhat lower than the grain sizes derived from VIMS observations ( $\sim 10 - 100 \mu m$ ) and suggests that grain shapes and scale dependent porosity may be important.

## 6.7 Future work

The radiation-induced sintering rates depend sensitively on how electron-deposited energy spreads in the grains and near the contact regions. Further work is needed for a variety of ice samples in order to better understand the microphysics of the sintering process. As discussed in the following chapter, MD simulations are under way which can be used to constrain the number of mobilized molecules per ionization event, the extent of the collision cascade, and the overall efficiency of the resulting radiation-induced sintering processes for non-spherical water ice grains. Continuum simulations can also be used to improve the description of thermal conductivity between irregular grains with irregular contact regions.

Such simulations are in progress and will be used to further improve the sintering calculations presented here and improve our understanding of weathering phenomena in ices, ultimately leading to a quantitative models able to provide independent constraints on regolith properties. Finally, the sintering models discussed are highly dependent on grain size, shape, and material crystalline structure, and more work should be done to determine the sintering rates for non-spherical grains and for a distribution of grain sizes in contact.

# Chapter 7

## Molecular Dynamics simulations of electron-induced excitations in water ice

### Abstract

It was previously shown that electron-induced sintering could account for the thermal anomalies observed on the icy moons of Saturn. However, the model relied on rough approximations for several key parameters, specifically the number of molecules excited above the diffusion activation energy per ionization event and the effective diffusion length of each molecule. Therefore, molecular dynamics simulations of molecular excitation in a water ice matrix have been carried out to constrain these parameters and provide a more accurate estimate of the radiation-induced sintering. Both hexagonal (Ih) and cubic (Ic) ice configurations have been simulated for both bulk ice and ice/vacuum interfaces (grain surfaces). These simulations allow the number of defects created per ionization event and the average displacement of molecules to be directly quantified.

## 7.1 Introduction

In order to better constrain the radiation induced sintering model introduced in Chapter 6, a series of molecular dynamics (MD) simulations were carried out to provide a direct measurement of the number of molecules,  $N$ , mobilized per excitation and the average diffusion length,  $\ell_{eff}$ , for mobilized molecules as a function of distance from the location of the initially excited molecule, crystalline ice structure, and the presence of grain surfaces. The values obtained from the simulations can then be used in Equation 6.12 to calculate the radiation induced diffusion coefficient during the mini-cascade phase of the electron energy deposition to the water ice grains. As mentioned in Section 6.4, there exist two additional mechanisms of radiation induced diffusion in the solid phase: the thermal pulse phase and enhanced bulk diffusion. However, due to the long computing times required to measure thermal diffusion at  $T < 100 K$ , MD cannot be used to better understand these additional diffusion processes.

### 7.1.1 LAMMPS, Rivanna, and TIP4P-ICE

The computational code used for these simulations was the LAMMPS (Large-scale Atomic/Molecular Massively Parallel Simulator) developed at Sandia National Laboratory (<http://lammps.sandia.gov>) [Plimpton, 1995]. The program can output values for the system such as temperatures, volume, and total energy, while the dump files can be used to output position, velocity, and energy on a per atom basis or as system wide averages. Several functions for calculating the mean squared displacement (MSD) and radial distribution functions (RDF) were implemented in the simulations using available LAMMPS options. The thermostat used to equilibrate the water ice configurations for bulk ice was a Nose-Hoover type NPT (isothermal-isobaric) integrator which uses non-Hamiltonian equations of motion to track particle motion for a given system temperature and pressure. For simulations involving grain surfaces (ice/vacuum interfaces), the thermostat used was an NVT (isothermal-isovolumetric) integrator. During

the particle excitation events, a NVE integrator was used which maintains the energy and volume of the system constant. The number of particles was held constant for all simulations. Periodic boundary conditions were used for all simulations.

Simulations were run on the Rivanna high performance computing cluster maintained by UVA Advanced Research Computing Services (ARCS). Rivanna allows the simulations to be run in parallel, greatly decreasing the time needed for each computation. The computing time was obtained through a generous grant from the Office for Research and Graduate Programs in the UVA School for Engineering and Applied Sciences (SEAS). LAMMPS was installed by ARCS on Rivanna and could quickly and easily be adapted to simulate water ice configurations, thereby greatly reducing the task of building the software to run on the specific cluster configuration while including non-standard build options. Typical computational runs used 20 – 40 processors on a single or multiple cluster nodes. The run times for the excitation sequence in thermally equilibrated water consisting of  $\sim 1600$  molecules required  $\sim 20$  min of simulation time.

The source code for LAMMPS contains several molecular potentials suited for the simulation of water (TIP3P, TIP4P, SPC), as well as calculating neighbor lists, long range Coulombic interactions, and spatial arrangements of atoms and molecules. The simulations presented here were carried out using the TIP4P-ICE potential [Abascal et al., 2005] to describe the interactions between water molecules. The TIP4P potential uses a standard Lennard-Jones (LJ) potential to determine the interactions between hydrogen and oxygen atoms and includes a massless dummy atom at a fourth site along the intersector of the H-O-H angle. To account for electrostatic effects, positive charges are added to the  $H$  atoms while the negative charge is placed on the dummy atom site. The TIP4P-Ice potential has been specifically parameterized to reproduce the bulk solid-phase properties of water ice and does an excellent job of matching the melting temperature, density, and melting enthalpy for water [Abascal et al., 2005]. The resulting phase diagram calculated over a wide range of temperature and pressure conditions closely resembles the experimentally determined phase

diagram. Coulombic interactions were accounted for using a long range particle-particle particle-mesh solver, ppm/tip4p, where a charge is added to a massless fourth site. For simulations including a free surface, the system boundaries normal to the surface were set to be much larger than the length of the block of atoms such that any long range interactions through the periodic boundaries in that direction could be effectively neglected.

### 7.1.2 Crystalline ice structures

It has long been assumed that ice in the outer Solar System should be predominantly amorphous due to the low temperatures (long annealing timescales) and ubiquitous, amorphizing radiation fields. However, the majority of explored bodies throughout the solar system show predominantly crystalline ice surfaces [Clark et al., 2014]. Various replenishment mechanisms such as micrometeorite annealing [Porter et al., 2010] and cryovolcanism [Cook et al., 2007] have been invoked to explain the presence of crystalline ice. The presence of crystalline ice on Charon has recently been explained as a balance between amorphizing radiation and thermal recrystallization [Holler et al., 2016].

Two polymorphs of crystalline water ice, hexagonal (Ih) and cubic (Ic), are used here to determine the effects of crystallinity on the collision cascade resulting from a molecular excitation. Bulk hexagonal (Ih) and cubic (Ic) proton-disordered ices were taken from the unit cell data available online (<http://www.fh.huji.ac.il/wiki/>) [Buch et al., 1998, 2005]. Representations of the equilibrium ice structures at 100 K are shown in Figure 7.1. These representations show crystalline ice when viewed along the c-axis. For Ih ice, the structure configuration file determined by V. Buch consisted of 1600 molecules, while for Ic ice the unit cell structure provided was only 216 molecules. Therefore, the Ic ice structure was repeated in a 2x2x2 pattern in order to generate a sufficient number of molecules so that energy transfer through the periodic boundaries was negligible.

In order to obtain stable ice structures, the minimum energy configurations from Buch et al. [1998, 2005] were given initially Gaussian velocity distributions corresponding to a

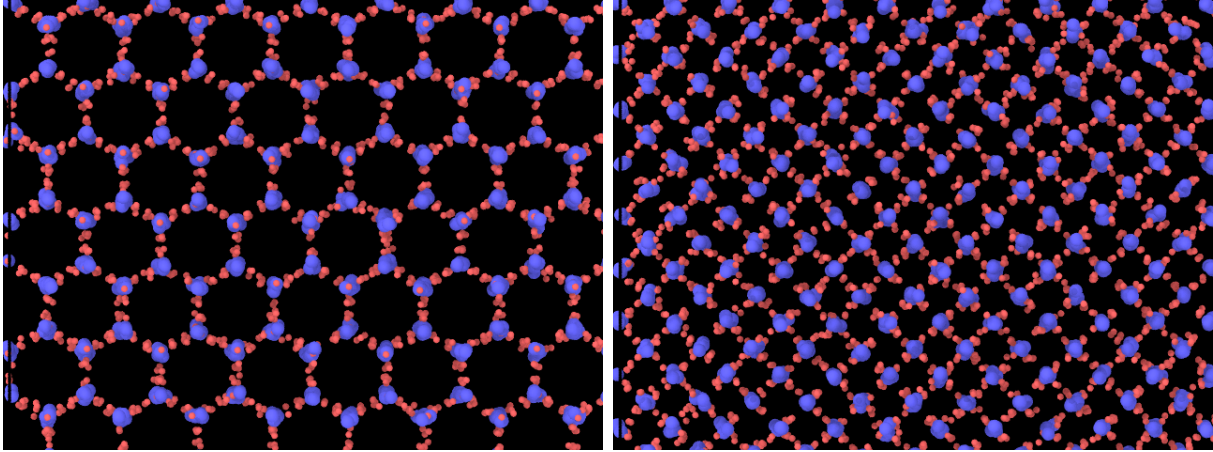


**Figure 7.1:** Atomic visualizations of (left) hexagonal and (right) cubic bulk ice at 100  $K$ .

temperature evenly distributed about 1  $K$ . Pressure during the bulk ice simulations was held constant at 0  $MPa$ , while for simulations including a free surface the volume of the system was held constant. The ices were then warmed sequentially in 10  $K$  increments over 100  $ps$  (100k steps) using a temperature damping parameter of 100  $fs$ . After each 10  $K$  increment, the system was stabilized for an additional 100  $ps$  at constant temperature. In this manner, the ice configuration remained stable throughout the warming process. The density is shown in Figure 7.2 for Ih and Ic ice during the warming process.

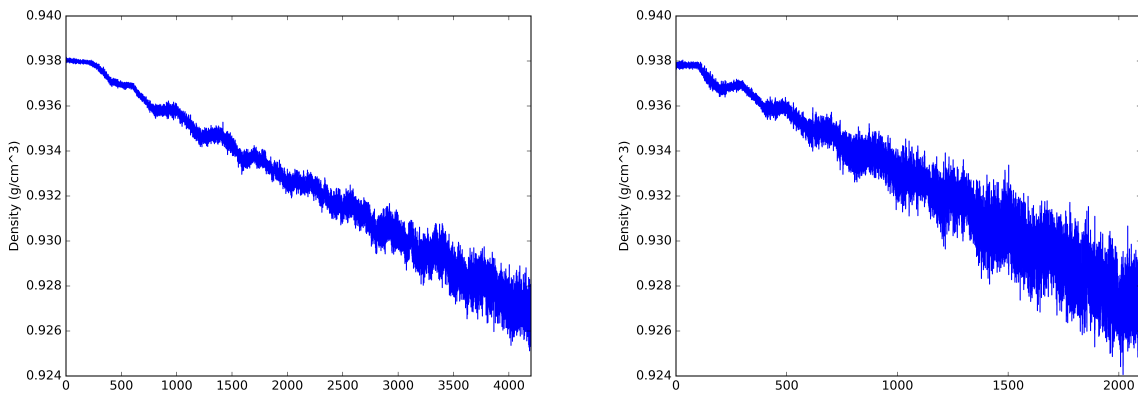


**Figure 7.2:** The density of (left) Ih and (right) Ic ice during warming of the bulk from 1  $K$  to 100  $K$ .

One commonly used means of characterizing the structure of solids is to use the radial distribution function (RDF). The RDF computes the average particle density as a function of distance from an arbitrary reference point. Similarly, the coordination number gives the

number of particles that are at a given distance from a reference point. Using LAMMPS output to determine the RDF for Ih and Ic ice, these can be compared with published results for these water ice polymorphs in order to confirm that the proper ice structures are being used in the simulations. The RDF is unique to each water ice polymorph and can be used to distinguish the crystalline form and proton ordering in the solid. The RDF calculated for  $O - O$  pairs,  $g_{OO}$ , and the integrated number of atomic neighbors, or coordination number, within a sphere of a given radius for proton disordered Ih and Ic water ice are given in Figure 7.3. These plots match previously published  $g_{OO}$  values for disordered ices at 170 K [Geiger et al., 2014]. The sharp peak at  $\sim 3 \text{ \AA}$  corresponds to the nearest neighbor distance, and Ih and Ic ice are very similar, although there are small differences at several nearest neighbor distances.

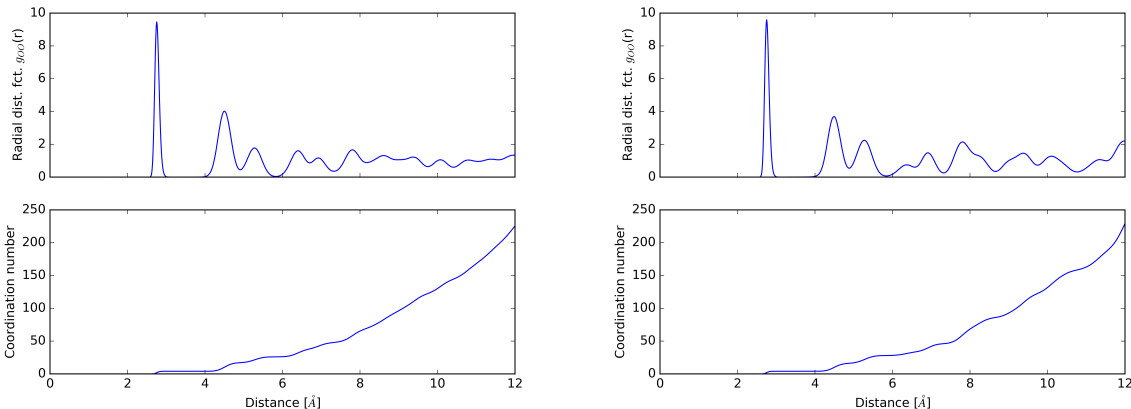


**Figure 7.3:** Radial distribution functions and coordination numbers calculated by LAMMPS for (left) Ih and (right) Ic ice at 100 K. The peak at  $\sim 3 \text{ \AA}$  corresponds to the nearest neighbor distance  $\ell_0$ .

## 7.2 Simulation of electron excitations in water ice

To simulate electron interactions with water molecules, a molecule, here called the IEM (initially excited molecule), was randomly chosen from a group of  $\sim 100$  molecules located near the center of the structure and given a randomly oriented velocity corresponding to 5 – 10 eV excitation. Since this artificial introduction of the momentum caused the entire

system to shift slightly in the direction of the initial particle velocity, a uniform correction was applied to the remaining molecules to maintain the net system displacement at zero. The collision cascade produced by the excitation was then tracked for  $\sim 10$  ps, and the positions, velocities, and potential energies of the atoms were output to a dump file every  $\sim 0.1$  ps for later analysis. Additional output included the total mean squared displacement (MSD) calculated for the system and the center of mass (COM) coordinates for all molecules. The COM coordinates were then used to calculate the MSD of individual molecules and to determine average MSD as a function of distance from the excited particle initial position.

In order to obtain visual representations of the atomic and molecular displacements both during and resulting from the molecular excitations, the visualization software Ovito was used to import the dump files and to generate rendered images and videos of the ice structures at various steps of the radiation process. The left hand image in Figure 7.4 shows a snapshot  $\sim 30$  fs after excitation where the color scale represents kinetic energy. Ovito can also be used to visualize the molecular displacement and defect formation due to excitation. The right hand image in Figure 7.4 shows the displacement vectors 30 fs after a 10 eV excitation event, overlaid on a grid of the initial molecular positions. In order to eliminate confusion due to rotation of the water molecules and changing positions of the *H* atoms, only *O* atoms were considered in the displacement analyses.

While the visualizations are useful qualitative tools for analyzing the molecular displacements, rigorous quantitative determination of the number and diffusion lengths of displaced particles are needed for the radiation-induced diffusion coefficient calculations. Therefore, in the following sections these parameters are calculated using the dump and COM files discussed above. For all simulations, the MSD was calculated as a function of distance from the IEM, and the number of vacancy/interstitial pairs can be calculated by determining the number of stable defects after  $\sim 100$  ps, at which the time system has largely returned to equilibrium.

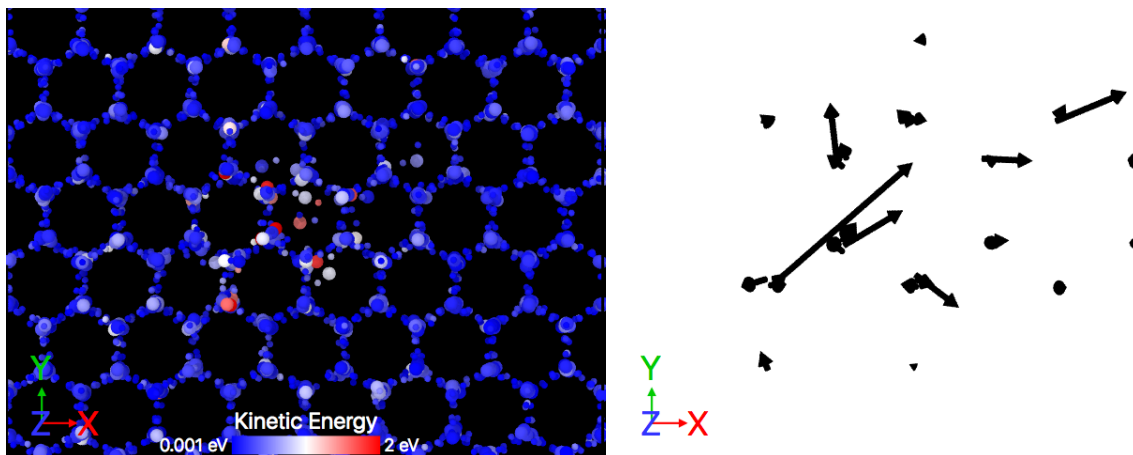


**Figure 7.4:** The left hand image shows a visualization of the mini-cascade 30 *ps* after the molecular excitation event. The color represents kinetic energy and the scale is shown in the color bar at the bottom of the image. The right hand image shows the total displacement of the initially excited and several nearby molecules. The largest displacement is for the excited molecule, and energy transfers during the mini-cascade process cause other molecules to become mobilized and diffuse away from their initial positions.

### 7.2.1 Excitations in bulk ices

For all simulations, the energy of the system was output as a function of time. Due to equipartition of energy, it was expected that, upon excitation, the kinetic energy of the system would initially rise a given amount (e.g., 10 *eV*), and gradually the energy would be lost through collisions so that when the system had returned to equilibrium half of the energy would remain kinetic while the other half would be converted to potential. An example of the average kinetic and potential energy per molecules are shown in the top panel of Figure 7.5 where it is clear that after  $\sim 2$  *ps* the system reaches an equilibrium stage with equipartition of energy. As seen in Figure 7.5 top panel, the average molecular kinetic energy is  $< 0.1$  *eV*, well below the bulk diffusion activation energies given in Table 6.4, and increases only  $\sim 10^{-3}$  *eV* as a result of the excitation such that the effect of excitation heating on the bulk diffusion can be neglected. The bottom panel shows the average molecule energy for 2 Å thick shells centered on the IEM where the number of molecules contained in each shell is indicated in the legend. The innermost shell (0 – 2 Å) contains only the IEM ( $N = 1$ ), and the number of molecules per shell increases with distance from the IEM as expected from Figure 7.3.

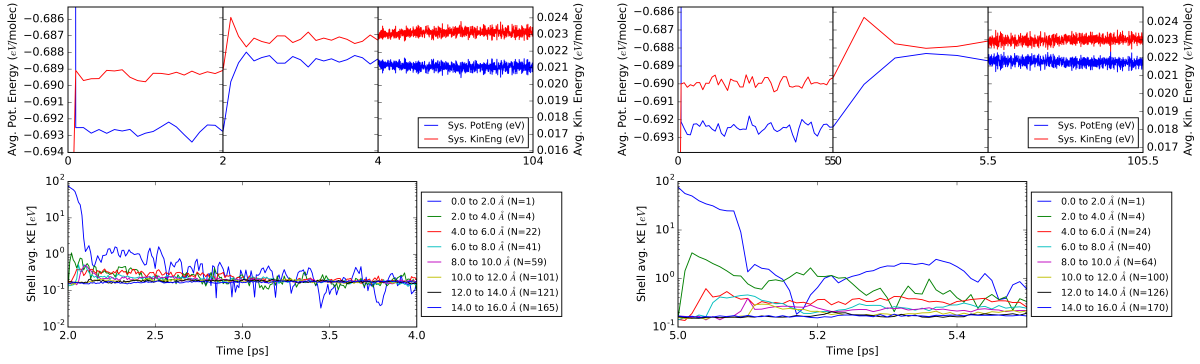


**Figure 7.5:** The top panels show the average kinetic and potential energies for Ih (left) and Ic (right) ices as a function of time. The IEM was given 10 eV of kinetic energy in a randomly oriented direction at 2 ps, and the system reached an equilibrium point at which energy was equally partitioned between kinetic and potential after < 10 ps. The bottom panels show the average energy for shells at the indicated distance from the IEM there the distance and number of molecules contained in each shell is shown in the legend.

In order to quantify the average displacement of molecules as a function of distance from the IEM, a Python script was written to read in the particle positions and energies from the COM files and calculate the displacement of individual molecules as a function of time. The average MSD for all molecules in the system, shown in the top panel of Figure 7.6, is small and the sharp increase at 2 ps represents the displacement of a relatively small number of molecules nearest the IEM. The slope of the average MSD both before and after the excitation is approximately zero, indicating that, as expected, thermal diffusion occurs on a time scale that cannot be reproduced by the MD simulations. The curves in the bottom panel of Figure 7.6 are the average displacement of molecules in uniform thickness shells measured outward from the initial position of the IEM. Both the MSD of each molecules and the molecules contained in each shell are calculated with respect their initial molecular positions, 2 ps before excitation. That is, a molecule that begins in a shell from 2 – 4 Å from the IEM will contribute to the MSD of that shell even if it moves out beyond the shell thickness defined at the beginning of the simulation.

Although the bottom panel of Figure 7.6 shows that the displacement is clearly the largest for the first shell (0 – 2 Å), containing only the IEM, this is not always the case. By changing the direction of the initial velocity, a variety of behaviors can be observed where occasionally the IEM returns to its original position and the largest displacement

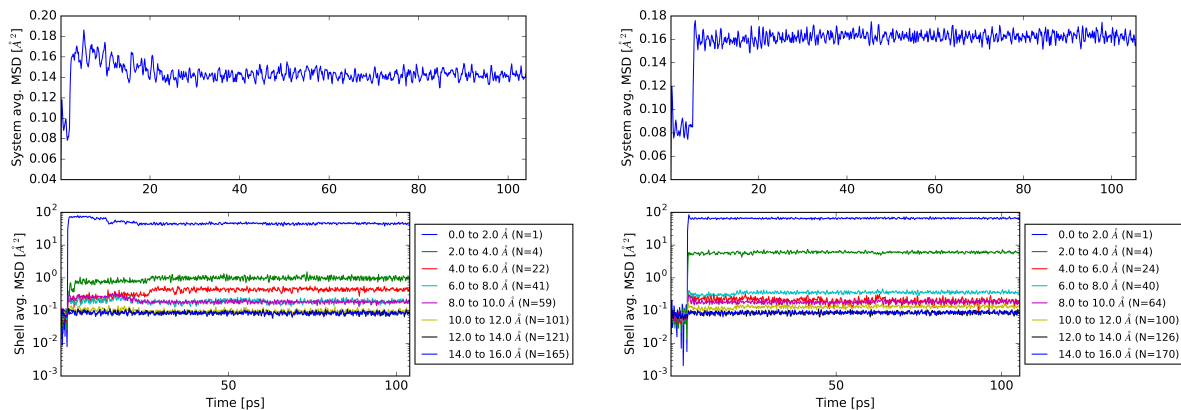


**Figure 7.6:** A typical example of the MSD for a  $10\text{ eV}$  excitation in (left) Ih and (right) Ic ice. The top panels represent the average MSD for the system, and the bottom panels show the average MSD calculated for equal thickness spherical shells centered on IEM. The number of molecules contained per shell and inner shell diameter are indicated in the legend, and the innermost shell contains only the IEM.

occurs in shells from  $2 - 8\text{ \AA}$ . In order to quantify this behavior, 10 simulations were run using the same initial excitation energy and material configuration, but randomly selecting a molecule near the center of the configuration and giving it a randomly oriented initial velocity. The systems were then run for  $\sim 100\text{ ps}$  at which time they had returned to an equilibrium state. Since periodic boundary conditions were being used in the simulations, the energy introduced by the excitation remained in the system, effectively heating the molecules. However, evenly distributing  $10\text{ eV}$  of energy between 1600 molecules leads to a mean increase of only  $\sim 0.01\text{ eV}$ , much less than the bulk diffusion activation energy. Therefore, the net increase in energy experienced by the system as a result of the excitation of a single molecule can be neglected. After the system reached equilibrium, the MSD of each shell was averaged over the final  $\sim 10\text{ ps}$ , and the average MSD of each shell is plotted in Figure 7.7. The variance is calculated by averaging the equilibrium MSD values for 10 simulation runs. The IEM tends to have the largest MSD, although the variance is also the largest and for Ih ice the displacement is occasionally very small indicating that the IEM returns to its original lattice position. The average IEM for all shells is larger for Ic ice than for Ih ice.

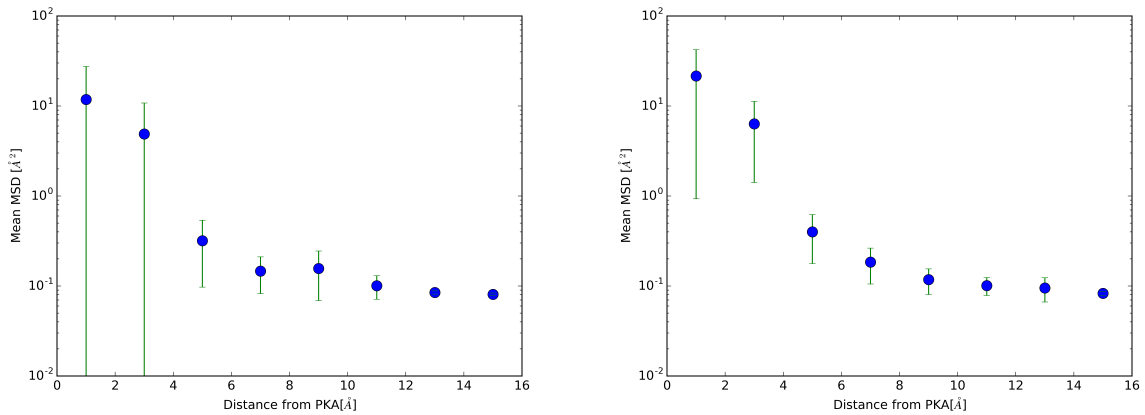


**Figure 7.7:** The average MSD for shells centered on the IEM

### 7.3 Conclusion

In this chapter I have used an MD program, which simulates bulk ice structures, to describe the number and diffusion length of molecules displaced by a molecular excitation event in crystalline ice. This work improves considerably on earlier MD work [Johnson and Liu, 1996] by using realistic molecular potentials and gives results that are directly relevant to excitations in water ice. The rough length scale for the mini-cascade region determined here is consistent with that found in Johnson and Liu [1996], but further work is needed to determine the dependence of the number and diffusion length of molecules on the sample crystallinity and presence of materials defects. However, it is shown that the length scale of the excitations is similar to the estimates used in the sintering model of Chapter 6, thus confirming the analytical approach used there. The simulations can additionally give the spatial distribution of defects produced by the release of energy in an ice lattice and the nature of molecular desorption from the surface. Further work is needed to determine these quantities from the simulation data. Since the principal quantity used in the sintering estimates, the length scale, is consistent with that used here, the more detailed results will be used in future modeling of sintering near a contact. Future work will simulate events in amorphous ice to account for the amorphous fraction found in icy bodies. Additionally, excitations will be carried out in

the presence of grain boundaries to directly measure the rate of molecular migration into the contact region. Finally, a more realistic simulation of the ionization and dissociation of the ionized water ice molecule will be used to improve agreement with experimental and astrophysical environments.

# Chapter 8

## Conclusion

In this thesis I have presented several examples of radiation induced space weathering processes that occur on solar system bodies with very thin or essentially no atmospheres. The combined experimental, computational, and theoretical approaches presented here allow for quantitative predictions for radiation induced effects for a number of objects. Such methods can be combined with returned spacecraft data to inform the development of new solar system exploration missions and the search for valuable resources in our solar neighborhood. Furthermore, by observing distant gas and dust nebula, we can in principal infer what the primordial components of our solar system might have been and, by observing contemporary solar system bodies, we can better understand the materials present in the early solar system and understand the processes that lead to the origin of life. In addition, the observational data can be combined with ground truth obtained from laboratory studies of meteorites and model materials or in situ on small bodies and moons in the Solar System, thus leading to a more complete picture of solar system evolution. By understanding how our Solar System developed, we can better understand observations of distant protoplanetary disks and exoplanet systems and the potential for life to exist elsewhere in the galaxy.

The radiolysis processes that break and reform bonds can potentially be important in protoplanetary discs where gas and dust are exposed to solar radiation, and in accreting

planetary bodies where the presence of hydrogen can have significant effects on the mechanical strength of the materials. It was previously suggested that solar wind hydrogen can combine with oxygen in silicates to form hydroxyl [Schaible and Baragiola, 2014], and this process was used to explain the  $2.8 \mu\text{m}$  absorption at the equator of the Moon. Previous experiments bombarded  $\alpha\text{-SiO}_2$  and the mineral olivine and saw clear increase in the  $\sim 3 \mu\text{m}$  region of the spectra. The absorption was seen to increase rapidly and saturate after fluences of  $\sim 5 \times 10^{16} \text{ cm}^{-2}$  in  $\alpha\text{-SiO}_2$ , but olivine was seen to saturate only at fluences  $> 2 \times 10^{17} \text{ cm}^{-2}$ . Whether the differences in saturation behavior were due to composition or crystalline structure was not determined. The laboratory work presented here attempted to produce a change in the  $OH$  band absorption in lunar soil 15058. However, any change in the  $3 \mu\text{m}$  region of the spectra was below the sensitivity of the experiments. The lunar soil samples were far more granular, meaning increased scattering of light from grain surfaces, and more opaque than the previous sample. Therefore, the lack of a detectable signal does not imply that solar wind hydrogen was not the source of the observed lunar absorption, but that more sensitive experimental methods are needed to observe this effect in lunar soils. Further work with improved IR sensitivity and additional samples will be needed to fully describe the solar wind hydrogen effects on silicates.

Sputtering of surfaces and production of secondary ions was shown to be a viable means of determining the refractory composition of small bodies exposed to solar wind irradiation via an orbiting spacecraft or a flyby of a small body. The SDTrimSP Monte Carlo program was used to calculate sputtering yields for both simple oxides and complex meteorite compositions. These simulations are a significant improvement on prior work using the TRIM which gives inaccurate yields for solar system minerals sputtered by the low energy ( $\sim \text{keV}$ ) ions that dominate the solar wind. The SDTrimSP simulations gave much better agreement to experimentally measured sputtering yields for  $\text{SiO}_2$  and  $\text{Al}_2\text{O}_3$ . Furthermore, the SDTrimSP program dynamically updates the sample composition to account for preferentially sputtering of light, weakly bound species such as  $O$  and  $Na$ , and thus

can provide a better analog to the solar wind sputtering processes. The computations were combined with experimentally measured relative secondary ion yields to provide a means of estimating secondary ion fluxes from small bodies exposed to solar wind irradiation. Since the experimental measurements contained significant uncertainties, additional experiments, combined with the simulations, can help to better constrain the relative secondary ion yield dependence on sample composition and incident ion mass and energy. Although enhanced secondary ion yields were observed under  $H^+$  bombardment of lunar soils, further work is needed to determine the cause of this effect which is important for solar wind sputtering of surfaces. The work presented here is now being used, in collaboration with colleagues at NASA's Goddard Space Flight Center to develop a mission that will send cube satellites to the moons of Mars.

Finally, sintering processes in icy regoliths were studied using combined computational and analytical modeling approach. The PacMan thermal anomalies on the icy Saturnian moons were suggested to result from high energy electron bombardment of these bodies. By examining the productions of the excitation events driven by the incident electrons and subsequent radiation-induced diffusion and sintering of grains, we showed that this process is quantitatively viable. However, the results presented are preliminary and further improvements to the modeling of the thermal conductivity of a regolith composed of irregular icy grains is needed. Such modelling is important for placing constraints on the grain sizes, shapes, and porosity. Although many aspects of the electron effects in water ice are known the spatial production and diffusion of defects is well modeled. Chapter 7 presents a preliminary study on the electron excitation effects in a crystalline ice sample. This work will be continued and expanded to configurations with a free surface (ice/vacuum interface), amorphous materials and small irregular grains. The ultimate goal of the MD modeling is to quantify the radiation induced diffusion effects. Such results can then be used to accurately predict the sintering timescales for realistic grains in an icy satellite regolith.



# Chapter 9

## Appendices

### A0.1 Meteorite gardening

Using the equations outlined in Section 2.6, the rate of removal of surface material from Phobos and Deimos and the surface ages of the Saturnian satellites as determined by crater counting can be determined.

### A Meteorite impact production of secondary ions

The main source of error in determining the micrometeorite vapor flux is knowing the density, velocity, and size distribution of micrometeorites in the interplanetary environment. One method to circumvent this issue, used in Cintala [1992], is to scale the vaporization rates measured in the upper atmosphere of Earth to the environment of interest. The amount of evaporated mass flux can be estimated by [Bruno et al., 2006]

$$M_{vap} = \rho_s \int_{\nu_{min}}^{\nu_{max}} \int_{\mu_{min}}^{\mu_{max}} f(\nu) h(\mu) V_{vap}(\nu, \mu) d\nu d\mu \quad (\text{A-1})$$

where  $\rho_s$  is the surface density of the larger body and  $h(\mu)$  and  $f(\nu)$  are the differential mass and velocity distributions, respectively, of the incident meteorites. The volume of regolith,

$V_{vap}$ , vaporized by an impacting spherical projectile of mass  $\mu$ , velocity  $\nu$ , and density  $\rho_p$  is determined according to

$$V_{vap} = \frac{\mu}{\rho_p}(c + d\nu + e\nu^2) \quad (\text{A-2})$$

where  $c$ ,  $d$ , and  $e$  are constants dependent on the target temperature and composition [Cintala, 1992]. Cipriani et al. [2011] considered micrometeorite sputtering around Phobos and Deimos explicitly. They assumed an average of  $10^{-6}$  meteoroids  $\text{km}^{-2} \text{hr}^{-1}$  [Domokos et al., 2007; Molina-Cuberos et al., 2003]. The number of atoms of species  $i$  vaporized during an impact was then determined from

$$S_a = M_{vap} \frac{F_i}{m_i} N_A \quad (\text{A-3})$$

where  $M_{vap}$  is the mass of vaporized material,  $F_i$  is the fraction and  $m_i$  the mass of species  $i$  in the regolith, and  $N_A$  is Avagadro's number [Bruno et al., 2007]. Although not carried out in detail here, the above equations can be used together with impact rate estimates at Mars to estimate the impact ejecta flux into the exosphere. However, secondary ion fractions in the ejecta produced are currently unknown, and the contribution of micrometeorites to the secondary ion flux around Phobos, Deimos, and silicate dominated asteroids remains unknown. See Cipriani et al. [2011] for total vaporization flux estimates.

## B Cratering studies on the icy Saturnian satellites

Using the equations in Section 2.6 for determining the surface age of a solar system body based on the cumulative crater distribution observed on the surface, estimates for the surface age of the icy Saturnian satellites are given here. Early Voyager studies of the Saturn system suggested that two separate populations of impactors were responsible for the cratering seen [Smith et al., 1981, 1982]. Population I impactors were thought to be heliocentric in origin and consisted of a relatively high abundance of larger ( $\sim 20\text{km}$ ) objects. Population II craters were identified on the younger terrains of Dione and Tethys and dominated the surface of Mimas [Kirchoff and Schenk, 2009, 2010]. These were characterized by an abundance of small

**Table A-1:** Cumulative and differential crater size distribution slopes where cp stands for cratered planes and sp for smooth planes.

Satellite	Diameter range [km]	Cumulative slope, $b$	Differential slope, $b'$
Mimas	4-10	$1.548 \pm 0.004$	$2.1 \pm 0.1$
	10-30	$2.23 \pm 0.02$	$2.8 \pm 0.3$
Tethys	0.2-10	$1.701 \pm 0.002$	$-2.71 \pm 0.3$
	10-65	$2.22 \pm 0.02$	$3.2 \pm 0.2$
Dione - cp	0.25-4	$1.640 \pm 0.007$	$2.56 \pm 0.07$
	4-10	$1.166 \pm 0.004$	$2.02 \pm 0.09$
	10-30	$2.31 \pm 0.02$	$3.2 \pm 0.2$
	30-150	$2.9 \pm 0.1$	$3.8 \pm 0.4$
Dione - sp	5-10	$2.21 \pm 0.02$	$2.5 \pm 0.2$
	10-45	$2.57 \pm 0.08$	$3/6 \pm 0.4$

(< 20 km) craters and general absence of large craters and thought to be formed by material circum-Saturnian in origin [Chapman and McKinnon, 1986]. As described in Section 2.6, the size distributions of craters can be used to estimate the surface ages and regolith depths. The cumulative crater size distribution slopes for the icy Saturnian satellites are given in Table A-1 Kirchoff and Schenk [2010].

Cratering studies can be used to date the surface of solar system bodies and several different chronologies have been developed. The *Neukum lunar chronology* assumes that the same family of impactors created the primary crater populations on both the lunar and gas giant satellites [Neukum et al., 2001]. This model fits lunar data using the linear combination of a constant plus an exponential cratering rates which represent steady state and early (fresh) cratering rates, respectively, and is valid when the diameter of the craters considered are  $D > 1$ km. An alternative is a power law fit to the measured data [Neukum et al., 2001; Hartmann, 1964]. The *cometary chronology*, on the other hand, uses the number of 'comets' crossing Saturn's orbit to estimate resurfacing rates [Zahnle et al., 2003]. The cometary model extrapolates current crossing rates to earlier times either assuming the change in the number of craters with time,  $dN/dt$ , is constant or assuming the population of impactors crossing the orbits of the gas giants has decreased inversely with time [Zahnle et al., 2003]. The cometary chronology can be discussed under two bounding impactor size distributions,

**Table A-2:** Meteorite impact time scales

Satellite	Cratering times [Myr]		Surface age [Gyr] ( $D \geq 5\text{km}$ )		Surface age [Gyr] $D \geq 10\text{km}$	
	$\tau_{rs,A}$	$\tau_{rs,B}$	$t_{surf,A}$	$t_{surf,B}$	$t_{surf,A}$	$t_{surf,B}$
Mimas	80	17	4.39	0.75	4.35	1.33
Herschel crater	–	–	–	–	0.9	0.1
Tethys	25	6.5	4.56	1.66	4.44	2.10
Odysseus basin	–	–	–	–	3.76	1.06
Dione - sp	34	10	4.56	2.60	4.56	3.22
Dione - cp			4.55	2.60	4.56	3.22

where (A) the low small crater counts [Bierhaus et al., 2005] on the Galilean satellites are used to set an upper lifetime or (B) the relatively high small crater counts (based on high resolution imaging) seen on Triton [McKinnon et al., 2000] are taken as a lower lifetime bound (younger surface). Finally, the *Nice model chronology* assumes that the majority of the large impacts occurred during the epoch of high solar system instability when Jupiter and Saturn crossed their 1:2 orbital resonance [Tsiganis et al., 2005]. This instability causes rapid migration of the giant planets and destabilizes the orbits of planetesimals (asteroid to Pluto sized objects) and can account for a large spike in the cratering of inner Solar System bodies typically known as the Late Heavy Bombardment [Gomes et al., 2005] and the origin of the Jupiter trojans [Morbidelli et al., 2005].

The icy Saturnian satellite surfaces are characterized by population II type crater distributions, mean a high density of small craters, and general hemispheric uniformity of craters, thus suggesting the bulk of the impacting material is planetocentric in orbit [Dones et al., 2009]. However, in order to account for the larger craters present, heliocentric comets should be considered as well. Using the *cometary chronology* limits discussed above, where for case A the majority of the small craters are produced by planetocentric impactors, the cratering time scales,  $\tau_{rs}$ , are given in Tab. A-2 for  $D > 20\text{km}$  [Dones et al., 2009]. Using Cassini images to determine the size frequency distributions and again assuming the cometary chronology applies, the assumed crater retention time or 'surface age',  $t_{surf}$ , inferred from crater sizes larger than 5 and 10 km in diameter are given in Table A-2 [Kirchoff and Schenk,

2009, 2010].

Integrating to a maximum cratering size of infinity and taking the lunar value for slope distribution of  $b_{lunar} = 2.93$ , Phillips and Chyba [2001], following Melosh [1989] and [Shoemaker et al., 1970], estimated the overturn rates at a depth  $h$  below the regolith surface for Europa as

$$\tau_{ovr} = t_{surf} \frac{4(b-2)}{\pi b c} (4h)^{(b-2)} \quad (\text{A-4})$$

where it was assumed that  $D = 4h$ . However, cumulative distribution slope,  $b$ , is often  $< 2$  for large crater populations, and these are the only type available for the outer solar system bodies. The small crater populations on Saturnian satellites suggest size frequency distributions such as those given by Eq. 2.18 where  $b \sim 0.9 - 1.2$  [Dones et al., 2009]. Likewise, taking either the cumulative number density slopes or the differential slopes gives regolith overturn timescales that are all negative Kirchoff and Schenk [2009].

We can use Eq. 2.23 to estimate the overturn timescale by assuming that  $h_{eq} \gg h$  and that  $c_{eq}$  is of order unity [Phillips and Chyba, 2001; Melosh, 2011]. These are likely good approximations at small depths ( $\ll \text{km}$ ) and since the surface of Mimas appears to be in equilibrium with only a small range of  $\sim \text{km}$  crater sizes visible [Dones et al., 2009]. Then, taking the approximate equilibrium crater size to be  $\sim 10 \text{ km}$  [Dones et al., 2009] and using a crater size distribution slope for Mimas of  $b \sim 1.6$  and the surface ages are given in Table A-2. The estimated overturn timescale at Mimas is  $\tau_{ovr} > 100 \text{ Myr}$  and similar for Tethys and Dione. Since these are much larger than the micrometeorite gardening rates or the sintering timescales calculated in Chapter 6, crater counting methods are not considered in determining the steady state conditions of the icy moon surfaces.

## A0.2 Sintering at grain contacts: General processes

When grains come into contact, free energy variations and concentration gradients cause molecular and atomic diffusion across the surfaces, and materials tend to accumulate at the

grain contact where there is a free energy minimum due to the curvatures at that point. A total of six such mechanisms were identified by Swinkels and Ashby [1981]. These can be further classified into densifying and non-densifying mechanisms. If regolith porosity (density) is assumed to be the same inside and outside the anomalous region, we can neglect the densifying mechanisms and take the linear shrinkage rate (columnarization) to be zero. This assumption means all species which migrate to the contact point must originate at a surface point. Thus, the rate of increase in the cementation phase at the neck is determined by bulk and surface diffusion and equilibrium vapor pressure. Relevant water properties for calculating the various diffusion rates are given in table A-10.

## A Vapor phase sintering

When grains come into contact, free energy variations and concentration gradients cause molecular and atomic diffusion, and molecules tend to accumulate in the contact region and sinter grains together. The sintering of spherical grains under various conditions of temperature and pressure can be calculated using equations given in Swinkels and Ashby [1981], and the mechanisms that are important for radiation sintering of ice grains in the upper  $\sim mm$  of the regolith are shown in Fig. 6.4. The equation for vapor phase sintering is

$$\left(\frac{dV_{con}}{dt}\right)_{vapor} = \dot{V}_{vapor} = 2\pi R_{con}R_{nc}\theta\frac{\Phi_v}{n_0}\xi_{vapor} \quad (\text{B-1})$$

where  $\xi$  is the 'sintering efficiency' and  $n_0$  is the material number density. The net vapor flux at the surface due to thermal desorption and absorption,  $\Phi_v$ , is given by

$$\Phi_v = \frac{P_v(T)}{(2\pi mkT)^{(1/2)}}$$

where  $P_v(T)$  is the temperature dependent vapor pressure,  $m$  is the mass of the gas species (=18 amu for water),  $k$  is the Boltzmann constant,  $T$  the average temperature of the gas, and  $\gamma_{sv}$  is the specific surface energy of the surface/vapor interface. The sintering efficiency

depends on the difference in curvatures between the grain and the neck regions, and

$$\xi_{vapor} = \frac{\gamma_s}{n_0 k T} \left( \frac{2}{r_g} - \frac{1}{R_{con}} - \frac{1}{R_{nc}} \right). \quad (\text{B-2})$$

where, assuming that the grain interpenetration depth is zero,  $R_{nc} = R_{con}^2 / [2(r_g - R_{con})]$  is the curvature of a smoothly connected neck as shown in Fig. 6.4. The rate of change in contact radius is the volume sintering rate divided by the area of the neck region,  $\sim 2\pi R_{con} R_{nc} \theta$ . Assuming  $r_g \gg R_{con} \gg R_{nc}$  gives

$$\left( \frac{dR_{con}}{dt} \right)_{vapor} = \frac{2\Phi_v \gamma_s}{n_0^2 k T} \frac{1}{R_{nc}} \quad (\text{B-3})$$

which implies that, while the contact radius is much smaller than the grain radius, the vapor phase sintering rate will be dominated by the curvature of the neck region and will decrease as the contact region grows larger. Kossacki gave an estimate for the neck surface area of

$$A_n = 4\pi\rho \left[ (R_{con} + \rho) \arcsin \left( \frac{r_a}{\rho} \right) - r_a \right] \quad (\text{B-4})$$

where  $r_a$  and  $\rho$  are defined by

$$\rho = \frac{R_{con}^2}{2(r_g - R_{con})} \quad (\text{B-5})$$

and

$$r_a = \frac{r_g \rho}{r_g + \rho} \quad (\text{B-6})$$

If it is assumed that the mean free path of a molecule is much smaller than the pore diameter, molecules will undergo multiple collisions before condensing, and the condensation rate can be assumed to be dominated by  $\phi_{gas}$ . Then the rate of change of the surface with  $R_s$  can be written

$$\frac{dR_s}{dt} = (\phi_{con} - \phi_{sub}) V_m = \beta (P_{gas} - P_s(K)) V_m \quad (\text{B-7})$$

where  $\beta = 1/(2\pi m k T)^{1/2}$ . Noting that the vapor pressure  $P_{gas}$  relaxes in a short time scale

to a point where the sublimation and condensation rates are on average equal, we can write  $P_{gas} = P_{ev}[1 + K_{av}(\gamma_s)/(n_0kT)]$  where  $K_{av} \sim 1/r_g$  is the area-averaged surface curvature of the whole aggregate surface. Writing the curvature difference  $\bar{K} = K_{av} - K$  and noting that the sublimation rate from a surface (molecules per unit time) is given by  $\phi_{sub} = \beta P_s(K)$ , the growth rate of the surface rate can be written

$$\frac{dR_{vapor}}{dt} = \frac{\Phi\gamma_{sv}}{n_0^2kT}\bar{K} \quad (\text{B-8})$$

where  $\Phi = \beta P_{ev}$ . Under the assumption that the contribution from surrounding grains to the condensation rate can be neglected and neglecting any grain size distribution, Sirono finds no difference between the growth rates determined assuming the molecular mean free path is much larger or much smaller than the grain radius.

When the mean free path of a molecule is much larger than the pore diameter, which implies that the ambient gas pressure  $P_{gas}$  is negligible, the condensation rate is due to absorption of molecules sublimed with a straight line of site path of the surface site

$$\phi_{con} = \frac{\Phi}{\pi} \int \bar{K}(\Omega) \cos \theta d\Omega \quad (\text{B-9})$$

where  $\bar{K}(\Omega)$  is the surface curvature of the grain surface viewed in the direction  $\Omega$  from the surface onto which the molecule condenses and the integration of  $d\Omega$  covers the solid angle which does not point at surfaces from the immediately adjacent grains.

## B Solid state diffusion sintering mechanisms

The diffusional sintering equations can essentially be determined from Fick's law of diffusion. That is, the flux of molecules into favorable binding sites in the contact region is

$$J = D \frac{dc}{dz} \quad (\text{B-10})$$

where  $c$  is the concentration of binding sites in the contact region. Migration of molecules originally on the grain surface into the contact region results in a decrease in chemical potential, meaning that the material becomes more thermodynamically stable by molecules moving into the contact region. Thus, we can write

$$\frac{dc}{dz} = \frac{c}{kT} \frac{d\mu}{dz} \Rightarrow J = -\frac{cD}{kT} \frac{d\mu}{dz} \quad (\text{B-11})$$

but

$$\frac{d\mu}{kT} \sim \frac{\gamma_{sv}}{nkT} * \frac{1}{R_{nc}} \sim \xi \quad (\text{B-12})$$

where  $1/R_{nc}$  is the curvature in the neck region. Thus, the flux of molecules into the contact region is given by

$$J = -\frac{c}{dz} * D_{eff} * \xi \quad (\text{B-13})$$

Using the geometry described in Swinkels and Ashby (1981), the flux can be converted into a contact growth rate. Writing the average distance to the edge of  $R_{con}$  times the volume of the added molecule

$$\frac{dz}{c} \sim b \frac{R_{con}}{n} \quad (\text{B-14})$$

where  $b < 1$ , the molecular growth rate per unit time for lattice diffusion can be written as

$$n \left( \frac{dV}{dt} \right)_{Bulk} \sim 3\pi b (R_{con})^2 * J \quad (\text{B-15})$$

or, writing it as a radial growth rate

$$\left( \frac{dR}{dt} \right)_{Bulk} = \frac{3}{2} * b * \frac{R_{con}}{R_{nc}\theta} * J \quad (\text{B-16})$$

Substituting for  $J$ , we get

$$\left( \frac{dR}{dt} \right)_{Bulk} = \frac{3}{2R_{nc}\theta} * D_{eff} * f \quad (\text{B-17})$$

where  $D_{eff}$  for radiation-induced sintering has been substituted for the thermal diffusion coefficient. Similarly, the growth rate for surface diffusion can be written

$$\left(\frac{dR}{dt}\right)_{Surf} = \frac{3\delta_s}{2d_2R_{nc}\theta} * D_{eff} * \frac{\gamma_{sv}}{nkT} * (K_3 - K_2) \quad (\text{B-18})$$

where  $\delta_s \sim a$  is the effective surface thickness and  $d_2$ ,  $K_3$  and  $K_2$  are defined by the geometry.

For the surface and bulk sintering mechanisms, as in vapor phase sintering, material is redistributed from the grain surfaces into the contact region resulting in no net change in regolith density or porosity. The bulk, surface, and grain boundary sintering mechanisms depend on the diffusion rate of molecules, and are given by Swinkels and Ashby [1981].

$$\text{Bulk diffusion: } \left(\frac{dV_{con}}{dt}\right)_{Bulk} = 3\pi R_{con} D_{bulk} \xi_{bulk} \quad (\text{B-19a})$$

$$\text{Surface diffusion: } \left(\frac{dV_{con}}{dt}\right)_{Surf} = 3\pi R_{con} D_{surf} \xi_{surf} \quad (\text{B-19b})$$

$$\text{Grain boundary: } \left(\frac{dV_{con}}{dt}\right)_{GB} = 16\pi \frac{D_{gb}}{R_{con}} \xi_{GB} \quad (\text{B-19c})$$

The sintering efficiency for bulk sintering is the same as for vapor phase,  $\xi_{bulk} = \xi_{vapor}$ , while the efficiency for surface diffusion sintering is given by

$$\xi_{surf} = \frac{\gamma_s}{n_0 kT} \frac{\delta_s}{d_s} \left(\frac{2}{r_g} - K_s\right) \quad (\text{B-20})$$

where  $\delta_s$  is the approximate surface thickness and  $d_s$ , and  $K_s$  are described in Swinkels and Ashby [1981]. Noting that for  $r_g \gg R_{con}$  the neck curvature simplifies to  $R_{nc} \sim R_{con}^2/2r_g$ , then we can write an approximate analytical solution for  $K_s$ , the averaged surface curvature, as

$$K_s \sim \sqrt{10} \left(\frac{r_g}{R_{con}^2}\right) \quad (\text{B-21})$$

and the length scale in the contact region over which surface diffusion is important,  $d_s$ , is given by

$$d_s \sim 0.2 \frac{R_{con}^2}{r_g}. \quad (\text{B-22})$$

The grain boundary diffusion sintering mechanism is due to the transport of defects from the interior of a grain along the grain boundary to the contact region and leads to densification (porosity reduction) of the regolith and grain size reduction. The sintering efficiency for the grain boundary mechanism is given by

$$\xi_{GB} = \frac{\gamma_s}{n_0 k T} \delta_{GB} \left( 1 - \frac{K_m^2 R_{con}}{2K_s} \right) \quad (\text{B-23})$$

where  $\delta_{GB}$  is the approximate grain boundary thickness [Goldsby and Kohlstedt, 2001]. In order to calculate the thermal equilibrium sintering rates, the various curvature radii are needed in addition to the water ice parameters given in table A-10.

Assuming that there is no inter-penetration of the grains (i.e. all grains in contact remain spherical throughout the sintering process. The radii of curvature of the contact neck is

$$\rho = \frac{R_{con}^2}{2(r_g - R_{con})} \quad (\text{B-24})$$

In the absence of densification, the size of the source region from which material can originate and diffuse to the contact region is simply the distance between grain contacts.

$$d_{source} = r_g(\theta - \pi/3) \quad (\text{B-25})$$

where

$$\theta = \tan^{-1} \left( \frac{r_g - y}{R_{con} + \rho} \right) \quad (\text{B-26})$$

For aggregates of roughly spherical grains, the equations of curvature are slightly modified as compared to sintering of two spheres in order to account for porosity of the medium. However,

when the particles are initially in contact and throughout the early stages of sintering the contact growth equations are effectively the same. The equations below are given for spherical grains and can be simplified by assuming that no sintering has occurred ( $y = 0$ ).

### A0.3 Thermal spike estimates of the radiation-induced diffusion length-scale

Using the spherical spike solution to determine the temperature,  $T(r, t)$ , as a function of distance and time from an initial heating event and then integrating over the relevant diffusion coefficient using the simple diffusion formula  $D = D_0 \exp(-E_a/k_B T(r, t))$  gives the transient diffusion coefficient due to the heat spike,  $D_{spike}$ . The expression for  $T(r, t)$  can be solved for using the Green's function solution to the heat diffusion equation with a point source concentrated at  $r = r_0$  and acting at time  $t = t_0$  and is given by [Haberman, 2004]

$$\Delta T(r, t) = \frac{\Delta E C_0^{1/2}}{(4\pi k_0 t)^{3/2}} \exp\left(\frac{C_0 r^2}{4k_0 t}\right) \quad (\text{D-1})$$

where it was assumed that the heat capacity  $C_0$  and the thermal conductivity  $k_0$  were constant with temperature. Although in reality both  $C_0$  and  $k_0$  vary with temperature, solutions accounting for this variability are not available.

Taking the heating rate to be  $(\Delta E n_0 / \tau_0)$  where  $n_0$  and  $\tau_0$  are the number density and heating event frequency, respectively, the equation for the thermal spike diffusion coefficient is given by

$$D_{spike} = \left(\frac{n_0}{\tau_0}\right) \int \int D_0 \exp\left(\frac{-E_a}{k_B T}\right) 4\pi r^2 dr dt \quad (\text{D-2})$$

where a spherically symmetric heat spike was assumed. However, the diffusion coefficient used are assumed to have a simple exponential dependence over a limited temperature range. For the energy deposition estimates described in Chapter 6, the energy deposited in an ionization event  $k_B T \sim 5 \text{ eV}$  is concentrated in a small number of molecules for only a very short time,

and the dispersion of the energy initially has a  $1/E^2$  dependence, not a Maxwellian. Also, since we are using  $T$  to find when a molecule overcomes  $E_a$ , instead of the cascade, a larger fraction of the total deposited energy  $W_{H_2O}$  may contribute. Although the cascade cools rapidly, it is not clear that using an equilibrium quantity like  $D(T)$  is reasonable.

Ignoring the above, the analytic solution for  $D_{spike}$  can be found to be [Kaoumi et al., 2008]

$$D_{spike} = \frac{\sqrt{3/5}D_0(n_0/\tau_0)\Delta E^{5/3}}{10\pi C_0^{2/3}k_0} \left(\frac{k_b}{E_a}\right)^{5/3} \Gamma\left(\frac{5}{3}\right) \quad (D-3)$$

which assumes the heat capacity has the form  $C = C_0T^{(n-1)}$ , the thermal conductivity has the form  $k = k_0T^{(n-1)}$ , and  $n=1$ . Using values for the number density, heat capacity, and thermal conductivity of ice from Table A-10 and taking the excitation rate  $\tau_0 = 1.5 \times 10^{13}$  s, the effective diffusion coefficient due to the thermal spike can be written  $D_{spike} \sim D_0(l_0^2/\tau_0)(0.1 \text{ s/cm}^2)(\Delta E/E_a)^{5/3}$ . The activation energies  $E_a$  and the diffusion coefficient pre-factors  $D_0$  can be taken from Table A-10. Experimental data is typically fit to an Arrhenius equation and is valid only over a small temperature range. Note that the spike result varies as  $\sim E_a^{5/3}$  whereas the thermal  $D(T)$  varies much more rapidly as  $\exp(-E_a/k_B T)$ . The results obtained for the thermal spike diffusion coefficient  $D_{spike}$  vary greatly depending on what parameters are used for  $D_0$  and  $E_a$ .

## A0.4 Full listing of meteorite sample compositions

Table A-3: Lunar compositions

	H	C	O	Na	Mg	Al	Si	S	K	Ca	Ti	Mn	Fe	Ni
MM	1.008	12.011	15.994	22.99	24.305	26.982	29.0855	32.066	39.0993	40.078	47.867	54.938	55.847	58.3964
SBE (SDTrimSP)	1.1	7.37	2.58	1.11	1.51	3.39	4.72	2.85	0.93	1.84	4.84	2.92	4.28	4.44
LS15058	x	x	x	x	x	x	x	x	x	x	x	x	x	x
LS69999	x	x	0.6824	0.0020	0.0316	0.0548	0.1575	x	0.0002	0.0539	0.0010	0.0003	0.0162	x
LS15999	x	x	0.6711	0.0017	0.0509	0.0356	0.1626	x	0.0004	0.0392	0.0038	0.0006	0.0341	x
LS10089	x	x	0.6510	0.0022	0.0417	0.0319	0.1590	x	0.0002	0.0448	0.0208	0.0006	0.0478	x
LS65901	x	x	0.6806	0.0016	0.0321	0.0542	0.1570	x	0.0002	0.0558	0.0016	0.0002	0.017	x
LS65901	x	x	0.6124	0.0016	0.0210	0.0940	0.1850	x	0.000	0.053	0.0016	0.0002	0.031	x
LS62231	x	x	0.6848	0.0014	0.0319	0.0535	0.1553	x	0.0003	0.0569	0.0016	0.0003	0.0141	x
LS62231	x	x	0.6554	0.0020	0.0070	0.0960	0.1840	x	0.0003	0.0310	0.0010	0.0003	0.0230	x
LS62231	x	x	0.6244	0.0030	0.0250	0.1310	0.1420	x	0.0003	0.0530	0.0020	0.0003	0.0190	x
LS10084	x	x	0.6487	0.0016	0.0438	0.0298	0.1568	x	0.0003	0.0478	0.0212	0.0007	0.0493	x
LS10084	x	x	0.6637	0.0020	0.0120	0.0700	0.1580	x	0.0003	0.0220	0.0080	0.0030	0.0610	x
LS10084	x	x	0.5917	0.0080	0.0420	0.0840	0.1510	x	0.0003	0.0530	0.0170	0.0030	0.0500	x

Table A-4: Mars compositions

	H	C	O	Na	Mg	Al	Si	S	K	Ca	Ti	Mn	Fe	Ni
MM	1.008	12.011	15.994	22.99	24.305	26.982	29.0855	32.066	39.0993	40.078	47.867	54.938	55.847	58.3964
SBE (SDTrimSP)	1.1	7.37	2.58	1.11	1.51	3.39	4.72	2.85	0.93	1.84	4.84	2.92	4.28	4.44
ALHA77005	x	x	0.591	0.003	0.158	0.013	0.159	x	0.000	0.013	0.001	x	0.063	x
EETA79001 lithology A	x	x	0.607	0.006	0.089	0.026	0.185	x	0.000	0.029	0.002	x	0.057	x
EETA79001 lithology B	x	x	0.613	0.013	0.037	0.050	0.186	x	0.000	0.044	0.003	x	0.055	x
Shergotty	x	x	0.610	0.010	0.052	0.031	0.194	x	0.001	0.039	0.002	x	0.061	x
ALH 84001	x	x	0.604	0.001	0.136	0.006	0.193	x	0.000	0.007	0.001	x	0.053	x
Nakhla	x	x	0.600	0.003	0.070	0.008	0.189	x	0.001	0.061	0.001	x	0.067	x
Chassigny	x	x	0.578	0.001	0.182	0.004	0.144	x	0.000	0.003	0.000	x	0.088	x
Adirondack	x	x	0.609	0.018	0.061	0.048	0.173	x	0.000	0.031	0.001	x	0.059	x
Humphrey	x	x	0.609	0.020	0.053	0.048	0.175	x	0.001	0.033	0.002	x	0.059	x
Humphrey	x	x	0.609	0.019	0.059	0.048	0.174	x	0.000	0.032	0.002	x	0.059	x
Mazatzal Brooklyn	x	x	0.610	0.020	0.055	0.048	0.173	x	0.001	0.032	0.002	x	0.060	x

**Table A-5:** HED compositions

	H	C	O	Na	Mg	Al	Si	S	K	Ca	Ti	Mn	Fe	Ni
MM	1.008	12.011	15.994	22.99	24.305	26.982	29.0855	32.066	39.0993	40.078	47.867	54.938	55.847	58.3964
SBE (SDTrimSP)	1.1	7.37	2.58	1.11	1.51	3.39	4.72	2.85	0.93	1.84	4.84	2.92	4.28	4.44
Haraiya	x	x	0.616	0.003	0.039	0.053	0.183	x	x	0.039	0.002	x	0.065	x
Sioux	x	x	0.612	0.003	0.041	0.054	0.188	x	x	0.041	0.002	x	0.059	x
SerraMage	x	x	0.614	0.002	0.041	0.090	0.171	x	x	0.051	x	x	0.031	x
Y-791195	x	x	0.611	0.003	0.043	0.058	0.187	x	x	0.041	0.001	x	0.056	x
Johnstown	x	x	0.605	x	0.140	0.006	0.194	x	x	0.005	x	x	0.050	x
Bholghati	x	x	0.616	0.002	0.085	0.036	0.182	x	x	0.024	0.001	x	0.054	x
EET87503	x	x	0.610	0.002	0.072	0.041	0.186	x	x	0.030	0.002	x	0.057	x
Bialystok	x	x	0.616	0.002	0.044	0.056	0.184	x	x	0.039	0.002	x	0.057	x
Petersburg	x	x	0.608	0.003	0.063	0.048	0.185	x	x	0.034	0.002	x	0.057	x
Polymict Eucrite	x	x	0.7117	0.0033	0.0461	0.0529	0.1837	0.0023	x	0.0414	x	x	0.0606	x

**Table A-6:** Unique compositions

	H	C	O	Na	Mg	Al	Si	S	K	Ca	Ti	Mn	Fe	Ni
MM	1.008	12.011	15.994	22.99	24.305	26.982	29.0855	32.066	39.0993	40.078	47.867	54.938	55.847	58.3964
SBE (SDTrimSP)	1.1	7.37	2.58	1.11	1.51	3.39	4.72	2.85	0.93	1.84	4.84	2.92	4.28	4.44
Tagish Lake	0.2470	0.0498	0.5331	0.0032	0.0737	0.0061	0.0674	0.0197	x	0.0041	x	x	0.0574	0.0033
Kaidun	0.1930	0.0327	0.5690	0.0071	0.0788	0.0072	0.0828	0.0294	x	0.0047	x	x	0.0761	0.0044
Murchison	0.2056	0.0321	0.5567	0.0016	0.0905	0.0075	0.0888	0.0172	x	0.0064	x	x	0.0729	0.0043
Brachina	0.0036	0.0014	0.5650	0.0047	0.1572	0.0097	0.1472	0.0133	x	0.0087	x	x	0.0862	0.0032

**Table A-7:** Aubrite compositions

	H	C	O	Na	Mg	Al	Si	S	K	Ca	Ti	Mn	Fe	Ni
MM	1.008	12.011	15.994	22.99	24.305	26.982	29.0855	32.066	39.0993	40.078	47.867	54.938	55.847	58.3964
SBE (SDTrimSP)	1.1	7.37	2.58	1.11	1.51	3.39	4.72	2.85	0.93	1.84	4.84	2.92	4.28	4.44
Aubres	x	x	0.6178	0.0008	0.1873	0.0018	0.1868	0.0017	x	0.0020	x	x	0.0018	x
Bishopville	x	x	0.6134	0.0062	0.1770	0.0056	0.1864	0.0039	x	0.0052	x	x	0.0023	x
Bustee	x	x	0.6150	0.0026	0.1861	0.0014	0.1846	0.0024	x	0.0059	x	x	0.0020	x
Khor Temiki	x	x	0.6167	0.0033	0.1823	0.0026	0.1872	0.0008	x	0.0019	x	x	0.0052	x
Mayo Belwa	x	x	0.6193	0.0109	0.1655	0.0092	0.1894	0.0023	x	0.0016	x	x	0.0018	x
Norton County	x	x	0.6042	0.0020	0.2108	0.0011	0.1678	0.0020	x	0.0041	x	x	0.0080	x
Pena Blanca Spring	x	x	0.6083	0.0176	0.1798	0.0028	0.1848	0.0012	x	0.0044	x	x	0.0011	x
Shallowater	x	x	0.5874	0.0041	0.1771	0.0042	0.1739	0.0021	x	0.0008	x	x	0.0504	x

**Table A-8:** Ureilite compositions

	H	C	O	Na	Mg	Al	Si	S	K	Ca	Ti	Mn	Fe	Ni
MM	1.008	12.011	15.994	22.99	24.305	26.982	29.0855	32.066	39.0993	40.078	47.867	54.938	55.847	58.3964
SBE (SDTrimSP)	1.1	7.37	2.58	1.11	1.51	3.39	4.72	2.85	0.93	1.84	4.84	2.92	4.28	4.44
ALHA77257 ureilite	0.0021	0.0583	0.5432	0.0002	0.2058	0.0001	0.1432	0.0013	0.0001	0.0040	x	x	0.0395	0.0023
ALH84136 ureilite	0.0101	0.0419	0.5542	0.0004	0.2029	0.0011	0.1536	0.0031	0.0001	0.0085	x	x	0.0221	0.0022
Dingo Pup Donga ureilite	0.0449	0.0532	0.5442	0.0004	0.1551	0.0014	0.1311	0.0039	0.0002	0.0051	x	x	0.0576	0.0030
North Haig polymict ureilite	0.0383	0.0694	0.5309	0.0005	0.1746	0.0008	0.1245	0.0042	0.0002	0.0045	x	x	0.0498	0.0024

Table A-9: Chondrite compositions

	H	C	O	Na	Mg	Al	Si	S	K	Ca	Ti	Mn	Fe	Ni
MM	1.008	12.011	15.994	22.99	24.305	26.982	29.0855	32.066	39.0993	40.078	47.867	54.938	55.847	58.3964
SBE (SDTrimSP)	1.1	7.37	2.58	1.11	1.51	3.39	4.72	2.85	0.93	1.84	4.84	2.92	4.28	4.44
CI	0.3038	0.0436	0.4452	0.0033	0.0605	0.0049	0.0574	0.0256	x	0.0035	x	x	0.0494	0.0028
CM	0.2395	0.0316	0.4699	0.0029	0.0815	0.0072	0.0780	0.0145	x	0.0055	x	x	0.0658	0.0036
CV	0.0627	0.0100	0.5253	0.0033	0.1327	0.0140	0.1261	0.0155	x	0.0104	x	x	0.0949	0.0051
CO	0.0164	0.0086	0.5488	0.0043	0.1405	0.0122	0.1325	0.0162	x	0.0093	x	x	0.1055	0.0057
CK	x	0.0043	0.5794	0.0032	0.1426	0.0129	0.1327	0.0125	x	0.0100	x	x	0.0971	0.0053
CR	x	0.0387	0.5676	0.0033	0.1309	0.0099	0.1241	0.0138	x	0.0075	x	x	0.0990	0.0052
CH	x	0.0174	0.5120	0.0021	0.1243	0.0104	0.1285	0.0029	x	0.0087	x	x	0.1820	0.0117
H	x	0.0042	0.5446	0.0064	0.1404	0.0095	0.1474	0.0151	x	0.0074	x	x	0.1179	0.0071
L	x	0.0049	0.5585	0.0070	0.1438	0.0101	0.1554	0.0161	x	0.0078	x	x	0.0914	0.0050
LL	x	0.0059	0.5736	0.0068	0.1433	0.0100	0.1532	0.0149	x	0.0075	x	x	0.0807	0.0041
R	x	0.0012	0.5475	0.0070	0.1293	0.0096	0.1563	0.0310	x	0.0056	x	x	0.1065	0.0060
EH	x	0.0089	0.4828	0.0082	0.1202	0.0083	0.1610	0.0476	x	0.0058	x	x	0.1487	0.0085
EL	x	0.0092	0.5039	0.0065	0.1458	0.0096	0.1725	0.0249	x	0.0066	x	x	0.1145	0.0065
A	x	x	0.5377	0.0068	0.1559	0.0108	0.1531	0.0205	x	0.0067	x	x	0.1023	0.0062
K	x	x	0.5043	0.0074	0.1584	0.0121	0.1505	0.0429	x	0.0076	x	x	0.1106	0.0062



**Table A-10:** Properties for various polymorphs, cubic, hexagonal, and low density amorphous (LDA), of water ice near versus temperature and calculated for 80K). Note R = gas constant = 8.134 J/mol/K. Temperature dependent equations use temperature in Kelvin (K).

	Description	Value for $H_2O$	@80K	Source
$D_s$	$I_c$ ice surface diffusion ( $cm^2/s$ ) (0001) surface of $I_h$ ( $cm^2/s$ )	$1.74 \times 10^5 \exp(-\frac{38.2 \times 10^3}{RT})$ $4.46 \times 10^{-2} \exp(-\frac{10.2 \times 10^3}{RT})$	$1.98 \times 10^{-20}$ $9.75 \times 10^{-9}$	Kouchi et al, 1994 Kouchi et al, 1994
$D_t$	LDA ice lattice self-diffusion ( $cm^2/s$ ) $I_h$ ice lattice self-diffusion ( $cm^2/s$ ) Bulk ice diffusion ( $cm^2/s$ ) Volume diffusion ( $cm^2/s$ )	$7 \times 10^{-6} \exp(-\frac{15 \times 10^3}{RT})$ $1 \times 10^{-10} \exp(-\frac{9 \times 10^3}{RT})$ $4.2 \times 10^8 \exp(-71.1 \times 10^3/RT)$ $9.10 \exp(-59.4 \times 10^3/RT)$	$1.12 \times 10^{-15}$ $1.33 \times 10^{-16}$ $1.5 \times 10^{-38}$ $1.5 \times 10^{-38}$	Ghesquiere et al, 2015 Ghesquiere et al, 2015 Livingston et al, 1998 Ramseier, 1967
$D_b$	grain boundary diffusion ( $cm^2/s$ )	$\sim 8.4 \exp(-\frac{49 \times 10^3}{RT})$	$8.5 \times 10^{-32}$	Goldsby and Kohlstedt, 2001
$k_{Tcr}$	Crystalline ice thermal conductivity [W/mK]	$488.12/T + 0.4685$	6.57	Ellsworth and Schubert, 1983
$k_A$	Amorphous ice thermal conductivity [W/mK] Amorphous ice thermal conductivity [W/mK]	$567/T$ $7.1 \times 10^{-8} * T$	7.08 $6 \times 10^{-6}$	Kossacki et al., 1994 Haruyama, 1993 Klinger, 1975
$\gamma_{ss}$	$I_h$ ice/vacuum surface free energy ( $erg/cm^2$ )	109	1.2 90K and 0.1 GPa 109 273K	Andersson and Suga, 2002 Ketcham and Hobbs, 1969
$\gamma_{sl}$	$I_h$ ice/liquid free energy ( $erg/cm^2$ )	43	43	Henry, 2003
$\gamma_{gb}$	$I_h$ grain boundary free energy ( $erg/cm^2$ )	33	33 273K	Ketcham and Hobbs, 1969
$\delta_b$	$I_h$ grain boundary width (A)	65 $\sim 9.04$	65 273K	Ketcham and Hobbs, 1969 Goldsby and Kohlstedt, 2001
$\ell_{Ic}$	Cubic Ice Lattice Spacing (A)	6.355		Kumai, 1967
$\ell_{Ih}$	Hexagonal ice lattice spacing (A)	$a = 4.501, c = 7.348$		Kimai, 1967
$\rho_b$	$I_h/I_c/LDA$ bulk density ( $g/cm^3$ )	$\sim 0.92 - 0.94$	$\sim 0.94$	Loerting and Giovambattista, 2006
$\Omega$	$I_h$ molecular volume at -20C ( $cm^3$ )	$3.25 \times 10^{-23}$		Petrenko and Whitworth, 1999
$Y$	Young's modulus (GPa)	$f(T)$	11.5	Hobbs, 1974
$\nu$	Poisson's ratio	$f(T)$	0.42	Hobbs, 1974
$N_o$	equilibrium dislocation density ( $cm^{-3}$ )	$\sim 0.74 \pm 0.025$		Watkins et al, 2011
$E_{vac}$	bulk ice vacancy formation energy (eV/vacancy)			
$E_{int}$	interstitial formation energy (eV)	0.4		Hondoh et al., 1987
$S_{int}$	interstitial formation entropy ( )	4.9		Hondoh et al., 1987
$CH_2O$	specific heat [J/gK]	$0.09 + 0.00749 * T$	0.69	Klinger, 1981
$P_{ev}$	equilibrium vapor pressure (dyne/cm <sup>2</sup> )	$10h - 2445.5646/T + 8.2312 \log_{10}(T) - 0.01677006 * T + 1.20514 \times 10^{-5} * T^2 - 3.63227$	$1.6 \times 10^{-20}$	Yamamoto et al, 1983



# Bibliography

- J. L. F. Abascal, E. Sanz, R. García Fernández, and C. Vega. A potential model for the study of ices and amorphous water: TIP4P/Ice. *Journal of Chemical Physics*, 122(23): 234511–234511, June 2005. doi: 10.1063/1.1931662.
- M. A. Allodi, R. A. Baragiola, G. A. Baratta, M. A. Barucci, G. A. Blake, P. Boduch, J. R. Brucato, C. Contreras, S. H. Cuyllé, D. Fulvio, M. S. Gudipati, S. Ioppolo, Z. Kaňuchová, A. Lignell, H. Linnartz, M. E. Palumbo, U. Raut, H. Rothard, F. Salama, E. V. Savchenko, E. Sciamma-O’Brien, and G. Strazzulla. Complementary and Emerging Techniques for Astrophysical Ices Processed in the Laboratory. *Space Science Reviews*, 180:101–175, December 2013. doi: 10.1007/s11214-013-0020-8.
- K. Altwegg, H. Balsiger, U. Calmonte, M. Hässig, L. Hofer, A. Jäckel, B. Schläppi, P. Wurz, J. J. Berthelier, J. De Keyser, B. Fiethe, S. Fuselier, U. Mall, H. Rème, and M. Rubin. In situ mass spectrometry during the Lutetia flyby. *Planetary and Space Science*, 66:173–178, June 2012. doi: 10.1016/j.pss.2011.08.011.
- C. A. Andersen and J. R. Hinthorne. Ion Microprobe Mass Analyzer. *Science*, 175:853–860, February 1972. doi: 10.1126/science.175.4024.853.
- D. J. Andrews, A. D. Morse, S. J. Barber, M. R. Leese, G. H. Morgan, S. Sheridan, J. C. Zarnecki, C. T. Pillinger, and I. P. Wright. Ptolemy operations and results during the Lutetia flyby. *Planetary and Space Science*, 66:179–186, June 2012. doi: 10.1016/j.pss.2011.09.005.
- A. Annex, A. J. Verbiscer, P. Helfenstein, C. Howett, and P. Schenk. Photometric properties of thermally anomalous terrain on icy Saturnian satellites. In *AAS/Division for Planetary Sciences Meeting Abstracts*, volume 45 of *AAS/Division for Planetary Sciences Meeting Abstracts*, page 417.02, October 2013.
- C. Arasa, S. Andersson, H. M. Cuppen, E. F. van Dishoeck, and G.-J. Kroes. Molecular dynamics simulations of the ice temperature dependence of water ice photodesorption. *Journal of Chemical Physics*, 132(18):184510–184510, May 2010. doi: 10.1063/1.3422213.
- J. R. Arnold. Ice in the lunar polar regions. *Journal of Geophysical Research*, 84:5659–5668, September 1979. doi: 10.1029/JB084iB10p05659.
- H. Bach. Determination of bond energy of silica glass by means of ion sputtering investigations. *Nuclear Instruments and Methods*, 84:4–12, July 1970. doi: 10.1016/0029-554X(70)90728-7.

- H. Balsiger, K. Altwegg, P. Bochsler, P. Eberhardt, J. Fischer, S. Graf, A. Jäckel, E. Kopp, U. Langer, M. Mildner, J. Müller, T. Riesen, M. Rubin, S. Scherer, P. Wurz, S. Wüthrich, E. Arijs, S. Delanoye, J. de Keyser, E. Neefs, D. Nevejans, H. Rème, C. Aoustin, C. Mazelle, J.-L. Médale, J. A. Sauvaud, J.-J. Berthelier, J.-L. Bertaux, L. Duvet, J.-M. Illiano, S. A. Fuselier, A. G. Ghielmetti, T. Magoncelli, E. G. Shelley, A. Korth, K. Heerlein, H. Lauche, S. Livi, A. Loose, U. Mall, B. Wilken, F. Gliem, B. Fiethe, T. I. Gombosi, B. Block, G. R. Carignan, L. A. Fisk, J. H. Waite, D. T. Young, and H. Wollnik. Rosina: Rosetta Orbiter Spectrometer for Ion and Neutral Analysis. *Space Science Reviews*, 128:745–801, February 2007. doi: 10.1007/s11214-006-8335-3.
- A. F. Barghouty, F. W. Meyer, P. R. Harris, and J. H. Adams. Solar-wind protons and heavy ions sputtering of lunar surface materials. *Nuclear Instruments and Methods in Physics Research B*, 269:1310–1315, June 2011. doi: 10.1016/j.nimb.2010.12.033.
- G. K. Batchelor and R. W. O’Brien. Thermal or Electrical Conduction Through a Granular Material. *Royal Society of London Proceedings Series A*, 355:313–333, July 1977. doi: 10.1098/rspa.1977.0100.
- H. L. Bay, J. Roth, and J. Bohdansky. Light-ion sputtering yields for molybdenum and gold at low energies. *Journal of Applied Physics*, 48:4722–4728, November 1977. doi: 10.1063/1.323538.
- R. Behrisch and W. Eckstein. *Sputtering by particle bombardment: Experiments and computer calculations from threshold to MeV energies*. Topics in Applied Physics. Springer Berlin Heidelberg, 2007. ISBN 9783540445029. URL <http://books.google.com/books?id=TSVcpzx30XcC>.
- M. Benna, P. R. Mahaffy, J. S. Halekas, R. C. Elphic, and G. T. Delory. Variability of helium, neon, and argon in the lunar exosphere as observed by the LADEE NMS instrument. *Geophysical Research Letters*, 42:3723–3729, May 2015. doi: 10.1002/2015GL064120.
- Chris J. Bennett, Claire Pirim, and Thomas M. Orlando. Space-weathering of Solar System bodies: A laboratory perspective. *Chemical Reviews*, 113(12):9086+, DEC 2013. ISSN 0009-2665. doi: {10.1021/cr400153k}.
- A. Benninghoven. Comparative study of Si(111), silicon oxide, SiC and Si<sub>3</sub>N<sub>4</sub> surfaces by secondary ion mass spectroscopy (SIMS). *Thin Solid Films*, 28:59–64, July 1975. doi: 10.1016/0040-6090(75)90275-8.
- A. Benninghoven, P. Beckmann, K. H. Müller, and M. Schemmer. Investigation of multi-component surface reactions by SIMS: The interaction between hydrogen and oxygen on polycrystalline nickel. *Surface Science*, 89:701–709, 1979. doi: 10.1016/0039-6028(79)90649-6.
- M. J. Berger, J. S. Coursey, M. A. Zucker, and J. Chang. ESTAR, PSTAR, and ASTAR: Computer Programs for Calculating Stopping-Power and Range Tables for Electrons,

- Protons, and Helium Ions (version 1.2.3). National Institute of Standards and Technology, Gaithersburg, MD, 2005. URL <http://physics.nist.gov/Star>.
- S. Besse, J. Sunshine, M. Staid, J. Boardman, C. Pieters, P. Guasqui, E. Malaret, S. McLaughlin, Y. Yokota, and J.-Y. Li. A visible and near-infrared photometric correction for Moon Mineralogy Mapper (M<sup>3</sup>). *Icarus*, 222:229–242, January 2013. doi: 10.1016/j.icarus.2012.10.036.
- G. Betz and G. K. Wehner. *Sputtering of multicomponent materials*, page 11. 1983. doi: 10.1007/3-540-12593-0\_2.
- E. B. Bierhaus, C. R. Chapman, and W. J. Merline. Secondary craters on Europa and implications for cratered surfaces. *Nature*, 437:1125–1127, October 2005. doi: 10.1038/nature04069.
- J.P. Biersack and W. Eckstein. Sputtering studies with the monte carlo program trim.sp. *Applied Physics A*, 34(2):73–94, 1984. ISSN 0947-8396. doi: 10.1007/BF00614759. URL <http://dx.doi.org/10.1007/BF00614759>.
- J. R. Blackford. Sintering and microstructure of ice: A review. *Journal of Physics D Applied Physics*, 40:355, November 2007. doi: 10.1088/0022-3727/40/21/R02.
- E. M. Bringa and R. E. Johnson. A New Model for Cosmic-Ray Ion Erosion of Volatiles from Grains in the Interstellar Medium. *The Astrophysical Journal*, 603:159–164, March 2004. doi: 10.1086/381382.
- R. H. Brown, K. H. Baines, G. Bellucci, J.-P. Bibring, B. J. Buratti, F. Capaccioni, P. Ceroni, R. N. Clark, A. Coradini, D. P. Cruikshank, P. Drossart, V. Formisano, R. Jaumann, Y. Langevin, D. L. Matson, T. B. McCord, V. Mennella, E. Miller, R. M. Nelson, P. D. Nicholson, B. Sicardy, and C. Sotin. The Cassini Visual And Infrared Mapping Spectrometer (VIMS) Investigation. *Space Science Reviews*, 115:111–168, December 2004. doi: 10.1007/s11214-004-1453-x.
- W. L. Brown and R. E. Johnson. Sputtering of ices: a review. *Nuclear Instruments and Methods in Physics Research B*, 13:295–303, March 1986. doi: 10.1016/0168-583X(86)90516-1.
- M. Bruno, G. Cremonese, and S. Marchi. Neutral sodium atoms release from the surface of the Moon induced by meteoroid impacts. *Monthly Notices of the Royal Astronomical Society*, 367:1067–1071, April 2006. doi: 10.1111/j.1365-2966.2006.10029.x.
- M. Bruno, G. Cremonese, and S. Marchi. Neutral sodium atoms release from the surfaces of the Moon and Mercury induced by meteoroid impacts. *Planetary and Space Science*, 55:1494–1501, September 2007. doi: 10.1016/j.pss.2006.10.006.
- V. Buch, P. Sandler, and J. Sadlej. Simulations of h<sub>2</sub>o solid, liquid, and clusters, with an emphasis on ferroelectric ordering transition in hexagonal ice. *The Journal of Physical Chemistry B*, 102(44):8641–8653, 1998. doi: 10.1021/jp980866f. URL <http://dx.doi.org/10.1021/jp980866f>.

- V. Buch, R. Martonak, and M. Parrinello. A new molecular-dynamics based approach for molecular crystal structure search. *Journal of Chemical Physics*, 123(5):051108–051108, August 2005. doi: 10.1063/1.2000230.
- A. Buemi, G. Cimino, G. Leto, and G. Strazzulla. On the observability of -SiH vibrational stretch on solid objects in the Solar System. *Icarus*, 108:169–171, March 1994. doi: 10.1006/icar.1994.1049.
- B. J. Buratti. Icy Satellite Science Today and in Cassini’s Final Three Years. *AGU Fall Meeting Abstracts*, December 2014.
- B. J. Buratti, J. A. Mosher, and T. V. Johnson. Albedo and color maps of the Saturnian satellites. *Icarus*, 87:339–357, October 1990. doi: 10.1016/0019-1035(90)90138-Y.
- M. H. Burger, R. M. Killen, W. E. McClintock, A. W. Merkel, R. J. Vervack, T. A. Cassidy, and M. Sarantos. Seasonal variations in Mercury’s dayside calcium exosphere. *Icarus*, 238:51–58, August 2014. doi: 10.1016/j.icarus.2014.04.049.
- D. J. Burke, C. A. Dukes, J.-H. Kim, J. Shi, M. Famá, and R. A. Baragiola. Solar wind contribution to surficial lunar water: Laboratory investigations. *Icarus*, 211:1082–1088, February 2011. doi: 10.1016/j.icarus.2010.11.007.
- T. A. Cassidy, R. E. Johnson, M. A. McGrath, M. C. Wong, and J. F. Cooper. The spatial morphology of Europa’s near-surface O<sub>2</sub> atmosphere. *Icarus*, 191:755–764, November 2007. doi: 10.1016/j.icarus.2007.04.033.
- TA Cassidy and RE Johnson. Monte Carlo model of sputtering and other ejection processes within a regolith. *Icarus*, 176(2):499–507, AUG 2005. ISSN 0019-1035. doi: {10.1016/j.icarus.2005.02.013}.
- C.K. Chan and C.L. Tien. Conductance of packed spheres in vacuum. *Journal of Heat Transfer - Transactions of the ASME*, 95(3):302–308, 1973. ISSN 0022-1481.
- C. R. Chapman and W. B. McKinnon. *Cratering of planetary satellites*, pages 492–580. 1986.
- M. J. Cintala. Impact-induced thermal effects in the lunar and Mercurian regoliths. *Journal of Geophysical Research*, 97:947–973, January 1992. doi: 10.1029/91JE02207.
- F. Cipriani, O. Witasse, F. Leblanc, R. Modolo, and R. E. Johnson. A model of interaction of Phobos’ surface with the Martian environment. *Icarus*, 212(2):643–648, APR 2011. ISSN 0019-1035. doi: {10.1016/j.icarus.2011.01.036}.
- R. N. Clark. Detection of adsorbed water and hydroxyl on the Moon. *Science*, 326:562, October 2009. doi: 10.1126/science.1178105.
- R. N. Clark and P. G. Lucey. Spectral properties of ice-particulate mixtures and implications for remote sensing. I - Intimate mixtures. *Journal of Geophysical Research*, 89: 6341–6348, July 1984. doi: 10.1029/JB089iB07p06341.

- R. N. Clark, C. M. Pieters, R. O. Green, J. W. Boardman, and N. E. Petro. Thermal removal from near-infrared imaging spectroscopy data of the Moon. *Journal of Geophysical Research (Planets)*, 116:E00G16, June 2011. doi: 10.1029/2010JE003751.
- R. N. Clark, G. A. Swayze, R. Carlson, W. Grundy, and K. Noll. Spectroscopy from Space. *Reviews in Mineralogy and Geochemistry*, 78:399–446, January 2014. doi: 10.2138/rmg.2014.78.10.
- A. Colaprete, P. Schultz, J. Heldmann, D. Wooden, M. Shirley, K. Ennico, B. Hermalyn, W. Marshall, A. Ricco, R. C. Elphic, D. Goldstein, D. Summy, G. D. Bart, E. Asphaug, D. Korycansky, D. Landis, and L. Sollitt. Detection of water in the LCROSS ejecta plume. *Science*, 330:463, October 2010. doi: 10.1126/science.1186986.
- J. C. Cook, S. J. Desch, T. L. Roush, C. A. Trujillo, and T. R. Geballe. Near-Infrared Spectroscopy of Charon: Possible Evidence for Cryovolcanism on Kuiper Belt Objects. *The Astrophysical Journal*, 663:1406–1419, July 2007. doi: 10.1086/518222.
- J. F. Cooper, R. E. Johnson, B. H. Mauk, H. B. Garrett, and N. Gehrels. Energetic ion and electron irradiation of the icy Galilean satellites. *Icarus*, 149:133–159, January 2001. doi: 10.1006/icar.2000.6498.
- M. G. Cooper, B. B. Mikic, and M. M. Yovanovich. Thermal contact conductance. *International Journal of heat and mass transfer*, 12(3):279–300, 1969.
- J. N. Cuzzi and P. R. Estrada. Compositional evolution of Saturn’s rings due to meteoroid bombardment. *Icarus*, 132:1–35, March 1998. doi: 10.1006/icar.1997.5863.
- E. Dartois, J. J. Ding, A. L. F. de Barros, P. Boduch, R. Brunetto, M. Chabot, A. Domaracka, M. Godard, X. Y. Lv, C. F. Mejía Guamán, T. Pino, H. Rothard, E. F. da Silveira, and J. C. Thomas. Swift heavy ion irradiation of water ice from MeV to GeV energies. Approaching true cosmic ray compaction. *Astronomy and Astrophysics*, 557:A97, September 2013. doi: 10.1051/0004-6361/201321636.
- E. Dartois, I. Alata, C. Engrand, R. Brunetto, J. Duprat, T. Pinot, E. Quirico, L. Remusat, N. Bardin, G. Briani, S. Mostefaoui, G. Morinaud, B. Crane, N. Szwec, L. Delauche, F. Jamme, C. Sandt, and P. Dumas. Interstellar and interplanetary solids in the laboratory. *Bulletin de la Societe Royale des Sciences de Liege*, 84:7–14, January 2015.
- K. Demyk, L. d’Hendecourt, H. Leroux, A. P. Jones, and J. Borg. IR spectroscopic study of olivine, enstatite and diopside irradiated with low energy H<sup>+</sup> and He<sup>+</sup> ions. *Astronomy and Astrophysics*, 420:233–243, June 2004. doi: 10.1051/0004-6361:20040091.
- Z. Djouadi, F. Robert, L. Le Sergeant D’Hendecourt, S. Mostefaoui, H. Leroux, A. P. Jones, and J. Borg. Hydroxyl radical production and storage in analogues of amorphous interstellar silicates: A possible ”wet” accretion phase for inner telluric planets. *Astronomy and Astrophysics*, 531:A96, July 2011. doi: 10.1051/0004-6361/201116722.

- A. Domokos, J. F. Bell, P. Brown, M. T. Lemmon, R. Suggs, J. Vaubaillon, and W. Cooke. Measurement of the meteoroid flux at Mars. *Icarus*, 191:141–150, November 2007. doi: 10.1016/j.icarus.2007.04.017.
- L. Dones, C. R. Chapman, W. B. McKinnon, H. J. Melosh, M. R. Kirchoff, G. Neukum, and K. J. Zahnle. *Icy Satellites of Saturn: Impact Cratering and Age Determination*, page 613. 2009. doi: 10.1007/978-1-4020-9217-6\_19.
- M. N. Drozdovskaya, C. Walsh, E. F. van Dishoeck, K. Furuya, U. Marboeuf, A. Thiabaud, D. Harsono, and R. Visser. Cometary ices in forming protoplanetary disc mid-planes. *Monthly Notices of the Royal Astronomical Society*, 462:977–993, October 2016. doi: 10.1093/mnras/stw1632.
- C. A. Dukes and R. A. Baragiola. The lunar surface-exosphere connection: Measurement of secondary-ions from Apollo soils. *Icarus*, 255:51–57, July 2015. doi: 10.1016/j.icarus.2014.11.032.
- CA Dukes, RA Baragiola, and LA McFadden. Surface modification of olivine by H(+) and He(+) bombardment. *Journal of Geophysics Research-Planets*, 104(E1):1865–1872, JAN 25 1999. ISSN 0148-0227. doi: {10.1029/98JE02820}.
- C. Elachi, M. D. Allison, L. Borgarelli, P. Encrenaz, E. Im, M. A. Janssen, W. T. K. Johnson, R. L. Kirk, R. D. Lorenz, J. I. Lunine, D. O. Muhleman, S. J. Ostro, G. Picardi, F. Posa, C. G. Rapley, L. E. Roth, R. Seu, L. A. Soderblom, S. Vetrilla, S. D. Wall, C. A. Wood, and H. A. Zebker. Radar: The Cassini Titan Radar Mapper. *Space Science Review*, 115:71–110, December 2004. doi: 10.1007/s11214-004-1438-9.
- C. Elder, P. Helfenstein, P. Thomas, J. Veverka, J. A. Burns, T. Denk, and C. Porco. Tethys’ mysterious equatorial band. In *AAS/Division for Planetary Sciences Meeting Abstracts #39*, volume 39 of *Bulletin of the American Astronomical Society*, page 429, October 2007.
- R. C. Elphic, H. O. Funsten, III, B. L. Barraclough, D. J. McComas, M. T. Paffett, D. T. Vaniman, and G. Heiken. Lunar surface composition and solar wind-induced secondary ion mass spectrometry. *Geophysics Research Letters*, 18:2165–2168, November 1991. doi: 10.1029/91GL02669.
- S. Epstein and H. P. Taylor, Jr. D/H and O-18/O-16 ratios of H<sub>2</sub>O in the ‘rusty’ breccia 66095 and the origin of ‘lunar water’. In *Lunar and Planetary Science Conference Proceedings*, volume 5 of *Lunar and Planetary Science Conference Proceedings*, pages 1839–1854, 1974.
- J.M. Fernández-Varea F. Salvat and J. Sempau. *PENELOPE-2011: A Code System for Monte Carlo Simulation of Electron and Photon Transport*. OECD-NEA, Issy-les-Moulineaux, France, 2011.
- C. Ferrari and A. Lucas. Low thermal inertias of icy planetary surfaces. Evidence for amorphous ice? *Astronomy and Astrophysics*, 588:A133, April 2016. doi: 10.1051/0004-6361/201527625.

- C. Ferrari and E. Reffet. The dark side of Saturn’s B-ring: Seasons as clues to its structure. *Icarus*, 223:28–39, March 2013. doi: 10.1016/j.icarus.2012.12.006.
- G. Filacchione, F. Capaccioni, R. N. Clark, J. N. Cuzzi, D. P. Cruikshank, A. Coradini, P. Cerroni, P. D. Nicholson, T. B. McCord, R. H. Brown, B. J. Buratti, F. Tosi, R. M. Nelson, R. Jaumann, and K. Stephan. Saturn’s icy satellites investigated by Cassini-VIMS: II. Results at the end of nominal mission. *Icarus*, 206:507–523, April 2010. doi: 10.1016/j.icarus.2009.11.006.
- G. Filacchione, E. D’Aversa, F. Capaccioni, R. N. Clark, D. P. Cruikshank, M. Ciarniello, P. Cerroni, G. Bellucci, R. H. Brown, B. J. Buratti, P. D. Nicholson, R. Jaumann, T. B. McCord, C. Sotin, K. Stephan, and C. M. Dalle Ore. Saturn’s icy satellites investigated by Cassini-VIMS: IV. Daytime temperature maps. *Icarus*, 271:292–313, June 2016. doi: 10.1016/j.icarus.2016.02.019.
- F. M. Flasar, V. G. Kunde, M. M. Abbas, R. K. Achterberg, P. Ade, A. Barucci, B. Bézard, G. L. Bjoraker, J. C. Brasunas, S. Calcutt, R. Carlson, C. J. Césarsky, B. J. Conrath, A. Coradini, R. Courtin, A. Coustenis, S. Edberg, S. Edgington, C. Ferrari, T. Fouchet, D. Gautier, P. J. Gierasch, K. Grossman, P. Irwin, D. E. Jennings, E. Lellouch, A. A. Mamoutkine, A. Marten, J. P. Meyer, C. A. Nixon, G. S. Orton, T. C. Owen, J. C. Pearl, R. Prangé, F. Raulin, P. L. Read, P. N. Romani, R. E. Samuelson, M. E. Segura, M. R. Showalter, A. A. Simon-Miller, M. D. Smith, J. R. Spencer, L. J. Spilker, and F. W. Taylor. Exploring The Saturn System In The Thermal Infrared: The Composite Infrared Spectrometer. *Space Science Review*, 115:169–297, December 2004. doi: 10.1007/s11214-004-1454-9.
- J. L. Fox. The chemistry of protonated species in the Martian ionosphere. *Icarus*, 252:366–392, May 2015. doi: 10.1016/j.icarus.2015.01.010.
- K. Franzreb, J. Lörinčák, and P. Williams. Quantitative study of oxygen enhancement of sputtered ion yields: I. Argon ion bombardment of a silicon surface with O<sub>2</sub> flood. *Surface Science*, 573:291–309, December 2004. doi: 10.1016/j.susc.2004.10.001.
- Philipp Geiger, Christoph Dellago, Markus Macher, Cesare Franchini, Georg Kresse, Jürgen Bernard, Josef N. Stern, and Thomas Loerting. Proton ordering of cubic ice ic: Spectroscopy and computer simulations. *The Journal of Physical Chemistry C*, 118(20):10989–10997, 2014. doi: 10.1021/jp500324x. URL <http://dx.doi.org/10.1021/jp500324x>.
- P. Ghesquière, T. Mineva, D. Talbi, P. Theulé, J. A. Noble, and T. Chiavassa. Diffusion of molecules in the bulk of a low density amorphous ice from molecular dynamics simulations. *Physical Chemistry Chemical Physics*, 17:11455–11468, 2015. doi: 10.1039/C5CP00558B.
- K. D. Gibson, D. R. Killelea, H. Yuan, J. S. Becker, and S. J. Sibener. Determination of the sticking coefficient and scattering dynamics of water on ice using molecular beam techniques. *Journal of Chemical Physics*, 134(3):034703–034703, January 2011. doi: 10.1063/1.3528116.

- J. Gittus. *Irradiation effects in crystalline solids*. Applied Science Publishers LTD, London, U.K., 1978.
- D. L. Goldsby and D. L. Kohlstedt. Superplastic deformation of ice: Experimental observations. *Journal of Geophysical Research*, 106:11017, June 2001. doi: 10.1029/2000JB900336.
- R. Gomes, H. F. Levison, K. Tsiganis, and A. Morbidelli. Origin of the cataclysmic Late Heavy Bombardment period of the terrestrial planets. *Nature*, 435:466–469, May 2005. doi: 10.1038/nature03676.
- N. B. Gontareva, E. A. Kuzicheva, and V. N. Shelegedin. Synthesis and characterization of peptides after high-energy impact on the icy matrix: Preliminary step for further UV-induced formation. *Planetary and Space Science*, 57:441–445, April 2009. doi: 10.1016/j.pss.2008.10.009.
- B. Gundlach and J. Blum. Outgassing of icy bodies in the Solar System - II: Heat transport in dry, porous surface dust layers. *Icarus*, 219:618–629, June 2012. doi: 10.1016/j.icarus.2012.03.013.
- B. Gundlach and J. Blum. A new method to determine the grain size of planetary regolith. *Icarus*, 223:479–492, March 2013. doi: 10.1016/j.icarus.2012.11.039.
- A. Gupta and G. N. Parsons. Bond strain, chemical induction, and OH incorporation in low-temperature (350–100°C) plasma deposited silicon dioxide films. *Journal of Vacuum Science Technology B: Microelectronics and Nanometer Structures*, 18:1764, May 2000. doi: 10.1116/1.591468.
- R. Haberman. *Applied Partial Differential Equations: With Fourier Series and Boundary Value Problems*. Pearson Prentice Hall, 2004. ISBN 9780130652430. URL <https://books.google.com/books?id=alp0QgAACAAJ>.
- J. S. Halekas, M. Benna, P. R. Mahaffy, R. C. Elphic, A. R. Poppe, and G. T. Delory. Detections of lunar exospheric ions by the LADEE neutral mass spectrometer. *Geophysical Research Letters*, 42:5162–5169, July 2015. doi: 10.1002/2015GL064746.
- D. T. Hall, D. F. Strobel, P. D. Feldman, M. A. McGrath, and H. A. Weaver. Detection of an oxygen atmosphere on Jupiter’s moon Europa. *Nature*, 373:677–679, February 1995. doi: 10.1038/373677a0.
- D. P. Hamilton and J. A. Burns. Origin of Saturn’s E-ring: Self-sustained, naturally. *Science*, 264:550–553, April 1994. doi: 10.1126/science.264.5158.550.
- B. Hapke. Space weathering from Mercury to the asteroid belt. *Journal of Geophysical Research*, 106:10039–10074, May 2001. doi: 10.1029/2000JE001338.
- B. W. Hapke. Laboratory Photometric Studies Relevant to the Lunar Surface. *Astrophysical Journal*, 70:322, 1965. doi: 10.1086/109534.

- W. K. Hartmann. On the Distribution of Lunar Crater Diameters. *Communications of the Lunar and Planetary Laboratory*, 2:197–204, 1964.
- A. R. Hendrix, T. A. Cassidy, B. J. Buratti, C. Paranicas, C. J. Hansen, B. Teolis, E. Roussos, E. Todd Bradley, P. Kollmann, and R. E. Johnson. Mimas’ far-UV albedo: Spatial variations. *Icarus*, 220:922–931, August 2012. doi: 10.1016/j.icarus.2012.06.012.
- T. Henning and D. Semenov. Chemistry in Protoplanetary Disks. *Chemical Reviews*, 113: 9016–9042, December 2013. doi: 10.1021/cr400128p.
- U. Hincelin, Q. Chang, and E. Herbst. A new and simple approach to determine the abundance of hydrogen molecules on interstellar ice mantles. *Astronomy and Astrophysics*, 574:A24, February 2015. doi: 10.1051/0004-6361/201424807.
- P.V. Hobbs. *Ice Physics*. Clarendon Press, 1974. ISBN 9780198519362.
- S. Hofmann. Evaluation of concentration-depth profiles by sputtering in SIMS and AES. *Applied Physics*, 9:59–66, January 1976. doi: 10.1007/BF00901910.
- H. Hofsäss, K. Zhang, and A. Mutzke. Simulation of ion beam sputtering with SDTrimSP, TRIDYN and SRIM. *Applied Surface Science*, 310:134–141, August 2014. doi: 10.1016/j.apsusc.2014.03.152.
- B. J. Holler, L. A. Young, M. W. Buie, W. M. Grundy, J. E. Lyke, E. F. Young, and H. G. Roe. Measuring temperature and ammonia hydrate ice on Charon in 2015 from Keck/OSIRIS spectra. *ArXiv e-prints*, June 2016.
- R. M. Housley. XPS Studies of the Surface Chemistry of Lunar Highlands Regolith. In *Lunar and Planetary Science Conference*, volume 23 of *Lunar and Planetary Science Conference*, March 1992.
- C. J. A. Howett, J. R. Spencer, P. Schenk, R. E. Johnson, C. Paranicas, T. A. Hurford, A. Verbiscer, and M. Segura. A high-amplitude thermal inertia anomaly of probable magnetospheric origin on Saturn’s moon Mimas. *Icarus*, 216:221–226, November 2011. doi: 10.1016/j.icarus.2011.09.007.
- C. J. A. Howett, J. R. Spencer, T. Hurford, A. Verbiscer, and M. Segura. PacMan returns: An electron-generated thermal anomaly on Tethys. *Icarus*, 221:1084–1088, November 2012. doi: 10.1016/j.icarus.2012.10.013.
- C. J. A. Howett, J. R. Spencer, T. Hurford, A. Verbiscer, and M. Segura. Thermophysical property variations across Dione and Rhea. *Icarus*, 241:239–247, October 2014. doi: 10.1016/j.icarus.2014.05.047.
- D. M. Hurley, D. J. Lawrence, D. B. J. Bussey, R. R. Vondrak, R. C. Elphic, and G. R. Gladstone. Two-dimensional distribution of volatiles in the lunar regolith from space weathering simulations. *Geophysics Research Letters*, 39:L09203, May 2012. doi: 10.1029/2012GL051105.

- A. S. Ichimura, A. P. Zent, R. C. Quinn, M. R. Sanchez, and L. A. Taylor. Hydroxyl (OH) production on airless planetary bodies: Evidence from H<sup>+</sup>/D<sup>+</sup> ion-beam experiments. *Earth and Planetary Science Letters*, 345:90–94, September 2012. doi: 10.1016/j.epsl.2012.06.027.
- ICRU. *Stopping Powers for Electrons and Positrons*. Number 37 in 1956-1964: National Bureau of Standards handbook. International Commission on Radiation Units and Measurements, Bethesda, MD, USA, 1984.
- R. Jaumann, R. N. Clark, F. Nimmo, A. R. Hendrix, B. J. Buratti, T. Denk, J. M. Moore, P. M. Schenk, S. J. Ostro, and R. Srama. *Icy Satellites: Geological Evolution and Surface Processes*, pages 637–681. 2009. doi: 10.1007/978-1-4020-9217-6\_20.
- K. L. Johnson, K. Kendall, and A. D. Roberts. Surface Energy and the Contact of Elastic Solids. *Royal Society of London Proceedings Series A*, 324:301–313, September 1971. doi: 10.1098/rspa.1971.0141.
- R. E. Johnson. *Energetic Charged-Particle Interactions with Atmospheres and Surfaces*, volume 19 of *Physics and Chemistry in Space*. Springer-Verlag Berlin Heidelberg, 1990.
- R. E. Johnson and W. A. Jesser. O<sub>2</sub>/O<sub>3</sub> Microatmospheres in the Surface of Ganymede. *Astrophysical Journal, Letters*, 480:L79–L82, May 1997. doi: 10.1086/310614.
- R. E. Johnson and M. Liu. Molecular dynamics studies of minicascades in electronically stimulated sputtering of condensed-gas solids. *Journal of Chemical Physics*, 104:6041–6051, April 1996. doi: 10.1063/1.471340.
- R. E. Johnson and T. I. Quickenden. Photolysis and radiolysis of water ice on outer solar system bodies. *Journal of Geophysics Research*, 102:10985–10996, 1997. doi: 10.1029/97JE00068.
- R. E. Johnson and E. C. Sittler, Jr. Sputter-produced plasma as a measure of satellite surface composition - The Cassini mission. *Geophysics Research Letters*, 17:1629–1632, September 1990. doi: 10.1029/GL017i010p01629.
- R. E. Johnson, R. M. Killen, J. H. Waite, Jr., and W. S. Lewis. Europa’s surface composition and sputter-produced ionosphere. *Geophysical Research Letters*, 25:3257–3260, 1998. doi: 10.1029/98GL02565.
- R.E. Johnson and R.A. Baragiola. Lunar Surface - Sputtering and secondary ion mass spectrometry. *Geophysics Research Letters*, 18(11):2169–2172, NOV 1991. ISSN 0094-8276. doi: {10.1029/91GL02095}.
- Robert E. Johnson. PHOTOLYSIS AND RADIOLYSIS OF WATER ICE. In Khriachtchev, L, editor, *PHYSICS AND CHEMISTRY AT LOW TEMPERATURES*, pages 297–339. 2011. ISBN 978-9-81426-782-3.
- A. Juhasz and M. Horanyi. Dust Delivery from Enceladus to the Moons of Saturn. *AGU Fall Meeting Abstracts*, December 2015.

- D. Kaoumi, A. T. Motta, and R. C. Birtcher. A thermal spike model of grain growth under irradiation. *Journal of Applied Physics*, 104(7), OCT 1 2008. ISSN 0021-8979. doi: {10.1063/1.2988142}.
- S. Kempf, U. Beckmann, and J. Schmidt. How the Enceladus dust plume feeds Saturn's E ring. *Icarus*, 206:446–457, April 2010. doi: 10.1016/j.icarus.2009.09.016.
- M. R. Kirchoff and P. Schenk. Crater modification and geologic activity in Enceladus' heavily cratered plains: Evidence from the impact crater distribution. *Icarus*, 202:656–668, August 2009. doi: 10.1016/j.icarus.2009.03.034.
- M. R. Kirchoff and P. Schenk. Impact cratering records of the mid-sized, icy saturnian satellites. *Icarus*, 206:485–497, April 2010. doi: 10.1016/j.icarus.2009.12.007.
- M. R. Kirchoff and P. Schenk. Dione's resurfacing history as determined from a global impact crater database. *Icarus*, 256:78–89, August 2015. doi: 10.1016/j.icarus.2015.04.010.
- R. L. Korotev. Further Examination of the Geochemistry of Apollo 16 Soils. In *Lunar and Planetary Science Conference*, volume 13 of *Lunar and Planetary Science Conference*, pages 403–404, March 1982.
- R. L. Korotev and J. J. Gillis. A new look at the Apollo 11 regolith and KREEP. *Journal of Geophysical Research*, 106:12339–12354, June 2001. doi: 10.1029/2000JE001336.
- R. L. Korotev, M. M. Lindstrom, and L. A. Haskin. Apollo 16 samples: compositional trends and relationship to the lunar highlands. In O. B. James and F. Hörz, editors, *Workshop on Apollo 16*, page 67, 1981.
- A. Kouchi, T. Yamamoto, T. Kozasa, T. Kuroda, and J. M. Greenberg. Conditions for condensation and preservation of amorphous ice and crystallinity of astrophysical ices. *Astronomy and Astrophysics*, 290, October 1994.
- S. M. Krimigis, D. G. Mitchell, D. C. Hamilton, S. Livi, J. Dandouras, S. Jaskulek, T. P. Armstrong, J. D. Boldt, A. F. Cheng, G. Gloeckler, J. R. Hayes, K. C. Hsieh, W.-H. Ip, E. P. Keath, E. Kirsch, N. Krupp, L. J. Lanzerotti, R. Lundgren, B. H. Mauk, R. W. McEntire, E. C. Roelof, C. E. Schlemm, B. E. Tossman, B. Wilken, and D. J. Williams. Magnetosphere Imaging Instrument (MIMI) on the Cassini Mission to Saturn/Titan. *Space Science Reviews*, 114:233–329, September 2004. doi: 10.1007/s11214-004-1410-8.
- G.C. Kuczynski. Physics and chemistry of sintering. *Advances in Colloid and Interface Science*, 3(3):275 – 330, 1972. ISSN 0001-8686. doi: [http://dx.doi.org/10.1016/0001-8686\(72\)85005-X](http://dx.doi.org/10.1016/0001-8686(72)85005-X).
- L. Le Roy, K. Altwegg, H. Balsiger, J.-J. Berthelier, A. Bieler, C. Briois, U. Calmonte, M. R. Combi, J. De Keyser, F. Dhooghe, B. Fiethe, S. A. Fuselier, S. Gasc, T. I. Gombosi, M. Hässig, A. Jäckel, M. Rubin, and C.-Y. Tzou. Inventory of the volatiles on comet 67P/Churyumov-Gerasimenko from Rosetta/ROSINA. *Astronomy and Astrophysics*, 583: A1, November 2015. doi: 10.1051/0004-6361/201526450.

- Y. Liu, Y. Guan, Y. Zhang, G. R. Rossman, J. M. Eiler, and L. A. Taylor. Direct measurement of hydroxyl in the lunar regolith and the origin of lunar surface water. *Nature Geoscience*, 5:779–782, November 2012. doi: 10.1038/ngeo1601.
- F. E. Livingston, G. C. Whipple, and S. M. George. Surface and bulk diffusion of HDO on ultrathin single-crystal ice multilayers on Ru(001). *Journal of Chemical Physics*, 108:2197–2207, February 1998. doi: 10.1063/1.475600.
- M. J. Loeffler and R. A. Baragiola. Photolysis of solid  $\text{NH}_3$  and  $\text{NH}_3\text{-H}_2\text{O}$  mixtures at 193 nm. *Journal of Chemical Physics*, 133(21):214506, December 2010. doi: 10.1063/1.3506577.
- M. J. Loeffler, C. A. Dukes, and R. A. Baragiola. Irradiation of olivine by 4 keV  $\text{He}^+$ : Simulation of space weathering by the solar wind. *Journal of Geophysical Research (Planets)*, 114:E03003, March 2009. doi: 10.1029/2008JE003249.
- T. E. Madey, R. E. Johnson, and T. M. Orlando. Far-out surface science: Radiation-induced surface processes in the solar system. *Surface Science*, 500:838–858, March 2002. doi: 10.1016/S0039-6028(01)01556-4.
- P. R. Mahaffy, R. Richard Hodges, M. Benna, T. King, R. Arvey, M. Barciniak, M. Bendt, D. Carigan, T. Errigo, D. N. Harpold, V. Holmes, C. S. Johnson, J. Kellogg, P. Kimvilakani, M. Lefavor, J. Hengemihle, F. Jaeger, E. Lyness, J. Maurer, D. Nguyen, T. J. Nolan, F. Noreiga, M. Noriega, K. Patel, B. Prats, O. Quinones, E. Raaen, F. Tan, E. Weidner, M. Woronowicz, C. Gundersen, S. Battel, B. P. Block, K. Arnett, R. Miller, C. Cooper, and C. Edmonson. The Neutral Mass Spectrometer on the Lunar Atmosphere and Dust Environment Explorer Mission. *Space Science Reviews*, 185:27–61, December 2014. doi: 10.1007/s11214-014-0043-9.
- G. G. Managadze, V. T. Cherepin, Y. G. Shkuratov, V. N. Kolesnik, and A. E. Chumikov. Simulating OH/ $\text{H}_2\text{O}$  formation by solar wind at the lunar surface. *Icarus*, 215:449–451, September 2011. doi: 10.1016/j.icarus.2011.06.025.
- P. L. Mattern. Hydrogen and helium implantation in vitreous silica. *Journal of Vacuum Science Technology*, 13:430, January 1976. doi: 10.1116/1.568938.
- J. Maul and K. Wittmaack. Secondary ion emission from silicon and silicon oxide. *Surface Science*, 47:358–369, January 1975. doi: 10.1016/0039-6028(75)90300-3.
- P. W. May, G. Pineau des Forêts, D. R. Flower, D. Field, N. L. Allan, and J. A. Purton. Sputtering of grains in C-type shocks. *Monthly Notices of the Royal Astronomical Society*, 318:809–816, November 2000. doi: 10.1046/j.1365-8711.2000.03796.x.
- T. B. McCord, L. A. Taylor, J.-P. Combe, G. Kramer, C. M. Pieters, J. M. Sunshine, and R. N. Clark. Sources and physical processes responsible for OH/ $\text{H}_2\text{O}$  in the lunar soil as revealed by the Moon Mineralogy Mapper ( $\text{M}^3$ ). *Journal of Geophysical Research (Planets)*, 116:E00G05, April 2011. doi: 10.1029/2010JE003711.

- F. M. McCubbin, B. L. Jolliff, H. Nekvasil, P. K. Carpenter, R. A. Zeigler, A. Steele, S. M. Elardo, and D. H. Lindsley. Fluorine and chlorine abundances in lunar apatite: Implications for heterogeneous distributions of magmatic volatiles in the lunar interior. *Geochimica et Cosmica Acta*, 75:5073–5093, September 2011. doi: 10.1016/j.gca.2011.06.017.
- W. B. McKinnon, P. M. Schenk, and S. A. Stern. New Constraints on the Small Kuiper Belt Object Population from High-Resolution Images of Triton. In *IAU Joint Discussion*, volume 4 of *IAU Joint Discussion*, 2000.
- H. J. Melosh. *Impact cratering: A geologic process*. 1989.
- H.J. Melosh. *Planetary Surface Processes*. Cambridge Planetary Science. Cambridge University Press, 2011. ISBN 9781139498302. URL <https://books.google.com/books?id=3bQD1DJgliIC>.
- F. W. Meyer, P. R. Harris, C. N. Taylor, H. M. Meyer, III, A. F. Barghouty, and J. H. Adams. Sputtering of lunar regolith simulants by protons and singly and multicharged Ar ions at solar wind energies. *Nuclear Instruments and Methods in Physics Research B*, 269:1316–1320, June 2011. doi: 10.1016/j.nimb.2010.11.091.
- E. H. Mitchell, U. Raut, D. Fulvio, M. J. Schaible, C. A. Dukes, and R. A. Baragiola. Ultraviolet photodesorption as a driver of water migration on the lunar surface. *Planetary and Space Science*, 89:42–46, December 2013. doi: 10.1016/j.pss.2013.02.002.
- E. H. Mitchell, U. Raut, and R. A. Baragiola. Porosity effects on crystallization kinetics of Amorphous Solid Water: Implications for cold icy objects in the Outer Solar System. In *AAS/Division for Planetary Sciences Meeting Abstracts*, volume 47 of *AAS/Division for Planetary Sciences Meeting Abstracts*, page 508.07, November 2015.
- G. Mitri, A. P. Showman, J. I. Lunine, and R. D. Lorenz. Hydrocarbon lakes on Titan. *Icarus*, 186:385–394, February 2007. doi: 10.1016/j.icarus.2006.09.004.
- G. J. Molina-Cuberos, O. Witasse, J.-P. Lebreton, R. Rodrigo, and J. J. López-Moreno. Meteoric ions in the atmosphere of Mars. *Planetary and Space Science*, 51:239–249, March 2003. doi: 10.1016/S0032-0633(02)00197-6.
- M. H. Moore, T. Tanabe, and J. A. Nuth. The SiH vibrational stretch as an indicator of the chemical state of interstellar grains. *Astrophysical Journal Letters*, 373:L31–L34, May 1991. doi: 10.1086/186044.
- A. Morbidelli, H. F. Levison, K. Tsiganis, and R. Gomes. Chaotic capture of Jupiter’s Trojan asteroids in the early Solar System. *Nature*, 435:462–465, May 2005. doi: 10.1038/nature03540.
- A. D. Morse, K. Altwegg, D. J. Andrews, H. U. Auster, C. M. Carr, M. Galand, F. Goesmann, S. Gulkis, S. Lee, I. Richter, S. Sheridan, S. A. Stern, M. F. A’Hearn, P. Feldman, J. Parker, K. D. Retherford, H. A. Weaver, and I. P. Wright. The Rosetta campaign to detect an exosphere at Lutetia. *Planetary and Space Science*, 66:165–172, June 2012. doi: 10.1016/j.pss.2012.01.003.

- W. W. Mullins. Theory of Thermal Grooving. *Journal of Applied Physics*, 28:333–339, March 1957. doi: 10.1063/1.1722742.
- A. Mutzke, R. Schneider, W. Eckstein, and R. Dohmen. SDTrimSP Version 5.0. volume 12/8 of *IPP Report*. Max-Planck-Inst. für Plasmaphysik, 2011.
- S. M. Myers. Ion-beam-induced migration and its effect on concentration profiles. *Nuclear Instruments and Methods*, 168:265–274, January 1980. doi: 10.1016/0029-554X(80)91264-1.
- O. B. Nasello, S. Navarro de Juarez, and C. L. Di Prinzio. Measurement of self-diffusion on ice surface. *Scripta Materialia*, 56(12):1071–1073, JUN 2007. ISSN 1359-6462. doi: {10.1016/j.scriptamat.2007.02.023}.
- R. M. Nelson, M. D. Boryta, B. W. Hapke, K. S. Manatt, A. Nebedum, D. Kroner, Y. Shkuratov, V. Psarev, and W. D. Smythe. Jupiter’s Satellite Europa: Evidence for an Extremely Fine-Grained, High Porosity Surface. In *AAS/Division for Planetary Sciences Meeting Abstracts*, volume 47 of *AAS/Division for Planetary Sciences Meeting Abstracts*, page 405.02, November 2015.
- G. Neukum, B. A. Ivanov, and W. K. Hartmann. Cratering Records in the Inner Solar System in Relation to the Lunar Reference System. *Space Science Reviews*, 96:55–86, April 2001.
- S. Nie, N. C. Bartelt, and K. Thürmer. Observation of Surface Self-Diffusion on Ice. *Physical Review Letters*, 102(13):136101, April 2009. doi: 10.1103/PhysRevLett.102.136101.
- L. R. Nittler, T. J. McCoy, P. E. Clark, M. E. Murphy, J. I. Trombka, and E. Jarosewich. Bulk element compositions of meteorites: A guide for interpreting remote-sensing geochemical measurements of planets and asteroids. *Antarctic Meteorite Research*, 17:231, 2004.
- C. Paranicas, R. W. Carlson, and R. E. Johnson. Electron bombardment of Europa. *Geophysical Research Letters*, 28:673–676, 2001. doi: 10.1029/2000GL012320.
- C. Paranicas, E. Roussos, N. Krupp, P. Kollmann, A.R. Hendrix, T. Cassidy, R.E. Johnson, P. Schenk, G. Jones, J. Carbary, D.G. Mitchell, and K. Dialynas. Energetic charged particle weathering of saturn’s inner satellites. *Planetary and Space Science*, 61(1):60 – 65, 2012.
- C. Paranicas, E. Roussos, R. B. Decker, R. E. Johnson, A. R. Hendrix, P. Schenk, T. A. Cassidy, J. B. Dalton, C. J. A. Howett, P. Kollmann, W. Patterson, K. P. Hand, T. A. Nordheim, N. Krupp, and D. G. Mitchell. The lens feature on the inner Saturnian satellites. *Icarus*, 234:155–161, May 2014. doi: 10.1016/j.icarus.2014.02.026.
- E. M. Parmentier and J. W. Head. Viscous relaxation of impact craters on icy planetary surfaces - Determination of viscosity variation with depth. *Icarus*, 47:100–111, July 1981. doi: 10.1016/0019-1035(81)90095-6.

- C. B. Phillips and C. F. Chyba. Impact Gardening Rates on Europa: Comparison with Sputtering. In *Lunar and Planetary Science Conference*, volume 32 of *Lunar and Planetary Science Conference*, March 2001.
- C. M. Pieters, E. M. Fischer, O. Rode, and A. Basu. Optical effects of space weathering: The role of the finest fraction. *Journal of Geophysical Research*, 98:20817, November 1993. doi: 10.1029/93JE02467.
- C. M. Pieters, J. Boardman, B. Buratti, R. Clark, R. Green, J. W. Head, S. Lundeen, E. Malaret, T. B. McCord, J. F. Mustard, C. Runyon, M. Staid, J. Sunshine, L. Taylor, S. Tompkins, and P. Varanasi. M3 on Chandrayaan-1: Strategy for Mineral Assessment of the Moon. In *Lunar and Planetary Science Conference*, volume 38 of *Lunar and Planetary Science Conference*, page 1295, March 2007.
- C. M. Pieters, J. N. Goswami, R. N. Clark, M. Annadurai, J. Boardman, B. Buratti, J.-P. Combe, M. D. Dyar, R. Green, J. W. Head, C. Hibbitts, M. Hicks, P. Isaacson, R. Klima, G. Kramer, S. Kumar, E. Livo, S. Lundeen, E. Malaret, T. McCord, J. Mustard, J. Nettles, N. Petro, C. Runyon, M. Staid, J. Sunshine, L. A. Taylor, S. Tompkins, and P. Varanasi. Character and Spatial Distribution of OH/H<sub>2</sub>O on the Surface of the Moon Seen by M<sup>3</sup> on Chandrayaan-1. *Science*, 326:568–569, October 2009. doi: 10.1126/science.1178658.
- S. Piqueux and P. R. Christensen. A model of thermal conductivity for planetary soils: 1. Theory for unconsolidated soils. *Journal of Geophysical Research (Planets)*, 114:E09005, September 2009a. doi: 10.1029/2008JE003308.
- S. Piqueux and P. R. Christensen. A model of thermal conductivity for planetary soils: 2. Theory for cemented soils. *Journal of Geophysical Research (Planets)*, 114:E09006, September 2009b. doi: 10.1029/2008JE003309.
- S. Plimpton. Fast Parallel Algorithms for Short-Range Molecular Dynamics. *Journal of Computational Physics*, 117:1–19, March 1995. doi: 10.1006/jcph.1995.1039.
- F. Poitrasson, A. N. Halliday, D.-C. Lee, S. Levasseur, and N. Teutsch. Iron isotope differences between Earth, Moon, Mars and Vesta as possible records of contrasted accretion mechanisms. *Earth and Planetary Science Letters*, 223:253–266, July 2004. doi: 10.1016/j.epsl.2004.04.032.
- A. R. Poppe. An improved model for interplanetary dust fluxes in the outer Solar System. *Icarus*, 264:369–386, January 2016. doi: 10.1016/j.icarus.2015.10.001.
- A. R. Poppe and S. M. Curry. Martian planetary heavy ion sputtering of Phobos. *Geophysical Research Letters*, 41:6335–6341, September 2014. doi: 10.1002/2014GL061100.
- C. C. Porco, R. A. West, S. Squyres, A. McEwen, P. Thomas, C. D. Murray, A. Del Genio, A. P. Ingersoll, T. V. Johnson, G. Neukum, J. Veverka, L. Dones, A. Brahic, J. A. Burns, V. Haemmerle, B. Knowles, D. Dawson, T. Roatsch, K. Beurle, and W. Owen.

- Cassini Imaging Science: Instrument Characteristics And Anticipated Scientific Investigations At Saturn. *Space Science Reviews*, 115:363–497, December 2004. doi: 10.1007/s11214-004-1456-7.
- S. B. Porter, S. J. Desch, and J. C. Cook. Micrometeorite impact annealing of ice in the outer Solar System. *Icarus*, 208:492–498, July 2010. doi: 10.1016/j.icarus.2010.01.031.
- F. Postberg, S. Kempf, J. K. Hillier, R. Srama, S. F. Green, N. McBride, and E. Grün. The E-ring in the vicinity of Enceladus. II. Probing the moon’s interior: The composition of E-ring particles. *Icarus*, 193:438–454, February 2008. doi: 10.1016/j.icarus.2007.09.001.
- M. A. Presley and P. R. Christensen. Thermal conductivity measurements of particulate materials 2. Results. *Journal of Geophysical Research*, 102:6551–6566, March 1997. doi: 10.1029/96JE03303.
- U. Raut, M. Famá, M. J. Loeffler, and R. A. Baragiola. Cosmic Ray Compaction of Porous Interstellar Ices. *The Astrophysical Journal*, 687:1070–1074, November 2008. doi: 10.1086/592193.
- P. A. Ries and M. Janssen. A large-scale anomaly in Enceladus’ microwave emission. *Icarus*, 257:88–102, September 2015. doi: 10.1016/j.icarus.2015.04.030.
- J. Roth, J. Bohdansky, R. S. Blewer, and W. Ottenberger. Data on low energy light ion sputtering. volume 9-26 of *IPP Report*. Max-Planck-Inst. fur Plasmaphysik, 1979.
- E. Roussos, G. H. Jones, N. Krupp, C. Paranicas, D. G. Mitchell, A. Lagg, J. Woch, U. Motschmann, S. M. Krimigis, and M. K. Dougherty. Electron microdiffusion in the Saturnian radiation belts: Cassini MIMI/LEMMS observations of energetic electron absorption by the icy moons. *Journal of Geophysical Research (Space Physics)*, 112: A06214, June 2007. doi: 10.1029/2006JA012027.
- E. M. Royer and A. R. Hendrix. First far-ultraviolet disk-integrated phase curve analysis of Mimas, Tethys and Dione from the Cassini-UVIS data sets. *Icarus*, 242:158–171, November 2014. doi: 10.1016/j.icarus.2014.07.026.
- C. T. Russell, J. G. Luhmann, K. Schwingenschuh, W. Riedler, and Y. Yeroshenko. Upstream waves at Mars - PHOBOS observations. *Geophysical Research Letters*, 17:897–900, May 1990. doi: 10.1029/GL017i006p00897.
- A. E. Saal, E. H. Hauri, M. L. Cascio, J. A. van Orman, M. C. Rutherford, and R. F. Cooper. Volatile content of lunar volcanic glasses and the presence of water in the Moon’s interior. *Nature*, 454:192–195, July 2008. doi: 10.1038/nature07047.
- M. Sarantos, R. E. Hartle, R. M. Killen, Y. Saito, J. A. Slavin, and A. Glozer. Flux estimates of ions from the lunar exosphere. *Geophysical Research Letters*, 39:L13101, July 2012a. doi: 10.1029/2012GL052001.

- M. Sarantos, R. M. Killen, D. A. Glenar, M. Benna, and T. J. Stubbs. Metallic species, oxygen and silicon in the lunar exosphere: Upper limits and prospects for LADEE measurements. *Journal of Geophysical Research (Space Physics)*, 117:A03103, March 2012b. doi: 10.1029/2011JA017044.
- D. W. Savin, N. S. Brickhouse, J. J. Cowan, R. P. Drake, S. R. Federman, G. J. Ferland, A. Frank, M. S. Gudipati, W. C. Haxton, E. Herbst, S. Profumo, F. Salama, L. M. Ziurys, and E. G. Zweibel. The impact of recent advances in laboratory astrophysics on our understanding of the cosmos. *Reports on Progress in Physics*, 75(3):036901, March 2012. doi: 10.1088/0034-4885/75/3/036901.
- M. J. Schaible. The role of solar wind in the formation of hydroxyl on airless silicate bodies in space. Master's thesis, University of Virginia, 2014.
- M. J. Schaible and R. A. Baragiola. Hydrogen implantation in silicates: The role of solar wind in sioh bond formation on the surfaces of airless bodies in space. *Journal of Geophysical Research: Planets*, pages n/a–n/a, 2014. ISSN 2169-9100. doi: 10.1002/2014JE004650. URL <http://dx.doi.org/10.1002/2014JE004650>.
- M. J. Schaible, R. E. Johnson, L. V. Zhigilei, and S. Piqueux. High energy electron sintering of icy regoliths: Formation of the pacman thermal anomalies at saturn. *Icarus*, Jul 2016. doi: 10.1016/j.icarus.2016.08.033. URL <http://dx.doi.org/10.1016/j.icarus.2016.08.033>.
- M. J. Schaible, C. A. Dukes, R. E. Johnson, A.H. Hutcherson, P. Lee, and M. R. Collier. Solar wind sputtering rates of small bodies and ion mass spectrometry detection of secondary ions. *Journal of Geophysical Research*, in preparation.
- P. Schenk, D. P. Hamilton, R. E. Johnson, W. B. McKinnon, C. Paranicas, J. Schmidt, and M. R. Showalter. Plasma, plumes and rings: Saturn system dynamics as recorded in global color patterns on its midsize icy satellites. *Icarus*, 211(1):740–757, JAN 2011.
- Helmut Schirrwitz. Kathodenzerstäubung bei beschuß verschiedener metalle mit argon-ionen im mittleren energiebereich. *Beiträge aus der Plasmaphysik*, 2(3):188–204, 1962. ISSN 1521-3986. doi: 10.1002/ctpp.19620020305. URL <http://dx.doi.org/10.1002/ctpp.19620020305>.
- B. Schläppi, K. Altwegg, and P. Wurz. Asteroid exosphere: A simulation for the ROSETTA flyby targets (2867) Steins and (21) Lutetia. *Icarus*, 195:674–685, June 2008. doi: 10.1016/j.icarus.2007.12.021.
- B. Schläppi, K. Altwegg, H. Balsiger, M. HäSsig, A. JäCkel, P. Wurz, B. Fiethe, M. Rubin, S. A. Fuselier, J. J. Berthelier, J. de Keyser, H. RèMe, and U. Mall. Influence of spacecraft outgassing on the exploration of tenuous atmospheres with in situ mass spectrometry. *Journal of Geophysical Research (Space Physics)*, 115:A12313, December 2010. doi: 10.1029/2010JA015734.

- F. Scipioni, P. Schenk, and F. Tosi. Spectroscopic Variation of Water Ice Abundance and Sub-Micron Ice Grains Across Enceladus, Mimas, and Tethys' Surface Using Cassini VIMS Data. In *Lunar and Planetary Science Conference*, volume 46 of *Lunar and Planetary Science Conference*, page 1919, March 2015a.
- F. Scipioni, P. Schenk, F. Tosi, R. Clark, C. Dalle Ore, and J.-P. Combe. Discovering sub-micron ice particles across Dione's surface. In *AAS/Division for Planetary Sciences Meeting Abstracts*, volume 47 of *AAS/Division for Planetary Sciences Meeting Abstracts*, page 508.03, November 2015b.
- Z. D. Sharp, C. K. Shearer, K. D. McKeegan, J. D. Barnes, and Y. Q. Wang. The Chlorine Isotope Composition of the Moon and Implications for an Anhydrous Mantle. *Science*, 329:1050, August 2010. doi: 10.1126/science.1192606.
- E. M. Shoemaker, M. H. Hait, G. A. Swann, D. L. Schleicher, D. H. Dahlem, G. G. Schaber, and R. L. Sutton. Lunar Regolith at Tranquillity Base. *Science*, 167:452–455, January 1970. doi: 10.1126/science.167.3918.452.
- M. T. Sieger and T. M. Orlando. Probing low-temperature water ice phases using electron-stimulated desorption. *Surface Science*, 451:97–101, April 2000. doi: 10.1016/S0039-6028(00)00013-3.
- P. Sigmund. Theory of Sputtering. I. Sputtering Yield of Amorphous and Polycrystalline Targets. *Physical Review*, 184:383–416, August 1969a. doi: 10.1103/PhysRev.184.383.
- P. Sigmund. On the Number of Atoms Displaced by Implanted Ions or Energetic Recoil Atoms. *Applied Physics Letters*, 14:114–117, February 1969b. doi: 10.1063/1.1652730.
- S.-i. Sirono. The Sintering Region of Icy Dust Aggregates in a Protoplanetary Nebula. *The Astrophysical Journal*, 735:131, July 2011. doi: 10.1088/0004-637X/735/2/131.
- S.-i. Sirono and T. Yamamoto. Thermal conductivity of granular materials relevant to the thermal evolution of cometary nuclei. *Planetary Space Science*, 45:827–834, July 1997. doi: 10.1016/S0032-0633(97)00069-X.
- B. A. Smith, L. Soderblom, R. F. Beebe, J. M. Boyce, G. Briggs, A. Bunker, S. A. Collins, C. Hansen, T. V. Johnson, J. L. Mitchell, R. J. Terrile, M. H. Carr, A. F. Cook, J. N. Cuzzi, J. B. Pollack, G. E. Danielson, A. P. Ingersoll, M. E. Davies, G. E. Hunt, H. Masursky, E. M. Shoemaker, D. Morrison, T. Owen, C. Sagan, J. Veverka, R. Strom, and V. E. Suomi. Encounter with Saturn - Voyager 1 imaging science results. *Science*, 212:163–191, April 1981. doi: 10.1126/science.212.4491.163.
- B. A. Smith, L. Soderblom, R. M. Batson, P. M. Bridges, J. L. Inge, H. Masursky, E. Shoemaker, R. F. Beebe, J. Boyce, G. Briggs, A. Bunker, S. A. Collins, C. Hansen, T. V. Johnson, J. L. Mitchell, R. J. Terrile, A. F. Cook, J. N. Cuzzi, J. B. Pollack, G. E. Danielson, A. P. Ingersoll, M. E. Davies, G. E. Hunt, D. Morrison, T. Owen, C. Sagan, J. Veverka, R. Strom, and V. E. Suomi. A new look at the Saturn system - The Voyager 2 images. *Science*, 215:504–537, January 1982. doi: 10.1126/science.215.4532.504.

- F. Spahn, N. Albers, M. Hörning, S. Kempf, A. V. Krivov, M. Makuch, J. Schmidt, M. Seiß, and Miodrag Sremčević. E-ring dust sources: Implications from Cassini's dust measurements. *Planetary Space Science*, 54:1024–1032, August 2006a. doi: 10.1016/j.pss.2006.05.022.
- F. Spahn, J. Schmidt, N. Albers, M. Hörning, M. Makuch, M. Seiß, S. Kempf, R. Srama, V. Dikarev, S. Helfert, G. Moragas-Klostermeyer, A. V. Krivov, M. Sremčević, A. J. Tuzzolino, T. Economou, and E. Grün. Cassini dust measurements at Enceladus and implications for the origin of the E-Ring. *Science*, 311:1416–1418, March 2006b. doi: 10.1126/science.1121375.
- L. V. Starukhina. Computer simulation of sputtering of lunar regolith by solar wind protons: Contribution to change of surface composition and to hydrogen flux at the lunar poles. *Solar System Research*, 37:36–50, January 2003.
- G. Steiner and N. I. Koemle. A model of the thermal conductivity of porous water ice at low gas pressures. *Planetary Space Science*, 39:507–513, March 1991. doi: 10.1016/0032-0633(91)90009-Y.
- S. A. Stern, F. Bagenal, K. Ennico, G. R. Gladstone, W. M. Grundy, W. B. McKinnon, J. M. Moore, C. B. Olkin, J. R. Spencer, H. A. Weaver, L. A. Young, T. Andert, J. Andrews, M. Banks, B. Bauer, J. Bauman, O. S. Barnouin, P. Bedini, K. Beisser, R. A. Beyer, S. Bhaskaran, R. P. Binzel, E. Birath, M. Bird, D. J. Bogan, A. Bowman, V. J. Bray, M. Brozovic, C. Bryan, M. R. Buckley, M. W. Buie, B. J. Buratti, S. S. Bushman, A. Calloway, B. Carcich, A. F. Cheng, S. Conard, C. A. Conrad, J. C. Cook, D. P. Cruikshank, O. S. Custodio, C. M. Dalle Ore, C. Deboy, Z. J. B. Dischner, P. Dumont, A. M. Earle, H. A. Elliott, J. Ercol, C. M. Ernst, T. Finley, S. H. Flanigan, G. Fountain, M. J. Freeze, T. Greathouse, J. L. Green, Y. Guo, M. Hahn, D. P. Hamilton, S. A. Hamilton, J. Hanley, A. Harch, H. M. Hart, C. B. Hersman, A. Hill, M. E. Hill, D. P. Hinson, M. E. Holdridge, M. Horanyi, A. D. Howard, C. J. A. Howett, C. Jackman, R. A. Jacobson, D. E. Jennings, J. A. Kammer, H. K. Kang, D. E. Kaufmann, P. Kollmann, S. M. Krimigis, D. Kusnierkiewicz, T. R. Lauer, J. E. Lee, K. L. Lindstrom, I. R. Linscott, C. M. Lisse, A. W. Lunsford, V. A. Mallder, N. Martin, D. J. McComas, R. L. McNutt, D. Mehoke, T. Mehoke, E. D. Melin, M. Mutchler, D. Nelson, F. Nimmo, J. I. Nunez, A. Ocampo, W. M. Owen, M. Paetzold, B. Page, A. H. Parker, J. W. Parker, F. Pelletier, J. Peterson, N. Pinkine, M. Piquette, S. B. Porter, S. Protopapa, J. Redfern, H. J. Reitsema, D. C. Reuter, J. H. Roberts, S. J. Robbins, G. Rogers, D. Rose, K. Runyon, K. D. Retherford, M. G. Ryschkewitsch, P. Schenk, E. Schindhelm, B. Sepan, M. R. Showalter, K. N. Singer, M. Soluri, D. Stanbridge, A. J. Steffl, D. F. Strobel, T. Stryk, M. E. Summers, J. R. Szalay, M. Tapley, A. Taylor, H. Taylor, H. B. Throop, C. C. C. Tsang, G. L. Tyler, O. M. Umurhan, A. J. Verbiscer, M. H. Versteeg, M. Vincent, R. Webbert, S. Weidner, G. E. Weigle, O. L. White, K. Whittenburg, B. G. Williams, K. Williams, S. Williams, W. W. Woods, A. M. Zangari, and E. Zirnstein. The Pluto system: Initial results from its exploration by New Horizons. *Science*, 350:aad1815, October 2015. doi: 10.1126/science.aad1815.

- P. J. Stooke. Tethys: Volcanic and Structural Geology. In *Lunar and Planetary Science Conference*, volume 20 of *Lunar and Planetary Inst. Technical Report*, page 1071, March 1989.
- P. J. Stooke. Tethys and Dione: New geological interpretations. In *Lunar and Planetary Science Conference*, volume 33 of *Lunar and Planetary Science Conference*, March 2002.
- J. M. Sunshine, T. L. Farnham, L. M. Feaga, O. Groussin, F. Merlin, R. E. Milliken, and M. F. A'Hearn. Temporal and spatial variability of lunar hydration as observed by the Deep Impact spacecraft. *Science*, 326:565, October 2009. doi: 10.1126/science.1179788.
- FB Swinkels and MF Ashby. Overview 11: A 2nd report on sintering diagrams. *Acta Metallurgica*, 29(2):259–281, 1981. ISSN 0001-6160. doi: {10.1016/0001-6160(81)90154-1}.
- J. R. Szalay and M. Horányi. Annual variation and synodic modulation of the sporadic meteoroid flux to the Moon. *Geophysical Research Letters*, 42:10, December 2015. doi: 10.1002/2015GL066908.
- L. A. Taylor, G. R. Rossman, and Q. Qi. Where Has All the Lunar Water Gone? In *Lunar and Planetary Science Conference*, volume 26 of *Lunar and Planetary Science Conference*, March 1995.
- K. Thiel, U. Sassmannshausen, H. Kulzer, and W. Herr. Ion sputtering of minerals and glasses: A first step to the simulation of solar wind erosion. *Radiation Effects*, 64:83–88, 1982.
- M. W. Thompson. II. The energy spectrum of ejected atoms during the high energy sputtering of gold. *Philosophical Magazine*, 18:377–414, August 1968. doi: 10.1080/14786436808227358.
- R. L. Tokar, R. E. Johnson, M. F. Thomsen, E. C. Sittler, A. J. Coates, R. J. Wilson, F. J. Crary, D. T. Young, and G. H. Jones. Detection of exospheric  $O_2^+$  at Saturn's moon Dione. *Geophysical Research Letters*, 39:L03105, February 2012. doi: 10.1029/2011GL050452.
- K. Tsiganis, R. Gomes, A. Morbidelli, and H. F. Levison. Origin of the orbital architecture of the giant planets of the Solar System. *Nature*, 435:459–461, May 2005. doi: 10.1038/nature03539.
- Herbert M. Urbassek, R. Mark Bradley, Maureen L. Nietiadi, and Wolfhard Moeller. Sputter yield of curved surfaces. *Physical Review B*, 91(16), APR 20 2015. ISSN 1098-0121. doi: {10.1103/PhysRevB.91.165418}.
- A. Verbiscer, R. French, M. Showalter, and P. Helfenstein. Enceladus: Cosmic graffiti artist caught in the act. *Science*, 315:815, February 2007. doi: 10.1126/science.1134681.
- A. J. Verbiscer, R. G. French, and C. A. McGhee. The opposition surge of Enceladus: HST observations 338-1022 nm. *Icarus*, 173:66–83, January 2005. doi: 10.1016/j.icarus.2004.05.001.

- A. J. Verbiscer, P. Helfenstein, C. Howett, A. Annex, and P. Schenk. Spectrophotometric properties of thermally anomalous terrain on Mimas. In *AAS/Division for Planetary Sciences Meeting Abstracts*, volume 46 of *AAS/Division for Planetary Sciences Meeting Abstracts*, page 502.08, November 2014.
- J. H. Waite, W. S. Lewis, W. T. Kasprzak, V. G. Anicich, B. P. Block, T. E. Cravens, G. G. Fletcher, W.-H. Ip, J. G. Luhmann, R. L. McNutt, H. B. Niemann, J. K. Parejko, J. E. Richards, R. L. Thorpe, E. M. Walter, and R. V. Yelle. The Cassini Ion and Neutral Mass Spectrometer (INMS) investigation. *Space Science Reviews*, 114:113–231, September 2004. doi: 10.1007/s11214-004-1408-2.
- J. H. Waite, M. R. Combi, W.-H. Ip, T. E. Cravens, R. L. McNutt, W. Kasprzak, R. Yelle, J. Luhmann, H. Niemann, D. Gell, B. Magee, G. Fletcher, J. Lunine, and W.-L. Tseng. Cassini Ion and Neutral Mass Spectrometer: Enceladus Plume Composition and Structure. *Science*, 311:1419–1422, March 2006. doi: 10.1126/science.1121290.
- M. Watkins, D. Pan, E. G. Wang, A. Michaelides, J. Vandevondele, and B. Slater. Large variation of vacancy formation energies in the surface of crystalline ice. *Nature Materials*, 10:794–798, October 2011. doi: 10.1038/nmat3096.
- K. Watson, B. Murray, and H. Brown. On the possible presence of ice on the Moon. *Journal of Geophysical Research*, 66:1598–1600, May 1961. doi: 10.1029/JZ066i005p01598.
- Kenneth Watson. *I. The thermal conductivity measurements of selected silicate powders in vacuum from 150 degrees-350 degrees K. II. An interpretation of the moon's eclipse and lunation cooling as observed through the earth's atmosphere from 8-14 microns*. PhD thesis, California Institute of Technology, 1964.
- A. E. Wechsler and P. E. Glaser. Pressure Effects on Postulated Lunar Materials. *Icarus*, 4: 335–352, September 1965. doi: 10.1016/0019-1035(65)90038-2.
- G.K. Wehner and C.E. KenKnight. Investigation of sputtering effects on the Moon's surface: Final report. volume 3107 of *NASA Report*. Office of Lunar and Planetary Programs, 1967.
- Q. Wei, M. Eddy, K.-D. Li, and L. Wang. Influence of surface morphology on sputtering yields. *Journal of Physics D Applied Physics*, 42(16):165304, August 2009. doi: 10.1088/0022-3727/42/16/165304.
- M. S. Westley, R. A. Baragiola, R. E. Johnson, and G. A. Baratta. Photodesorption from low-temperature water ice in interstellar and circumsolar grains. *Nature*, 373:405–407, February 1995. doi: 10.1038/373405a0.
- K. Wittmaack. Reliability of a popular simulation code for predicting sputtering yields of solids and ranges of low-energy ions. *Journal of Applied Physics*, 96:2632–2637, September 2004. doi: 10.1063/1.1776318.
- S. Wood. A general analytic model for the thermal conductivity of planetary regolith: 1. uncemented and cohesive non-spherical particulates. (0):–, 2016.

- S. E. Wood. A General Analytic Model for the Thermal Conductivity of Loose, Indurated or Icy Planetary Regolith. In *Lunar and Planetary Science Conference*, volume 42 of *Lunar and Planetary Inst. Technical Report*, page 2795, March 2011.
- S. E. Wood. An analytic model for the thermal conductivity of planetary regolith: Uncemented, non-spherical particulates. In *Lunar and Planetary Science Conference*, volume 44 of *Lunar and Planetary Inst. Technical Report*, page 3077, March 2013.
- P. Wurz and H. Lammer. Monte-Carlo simulation of Mercury's exosphere. *Icarus*, 164:1–13, July 2003. doi: 10.1016/S0019-1035(03)00123-4.
- P. Wurz, U. Rohner, J. A. Whitby, C. Kolb, H. Lammer, P. Dobnikar, and J. A. Martin-Fernandez. The lunar exosphere: The sputtering contribution. *Icarus*, 191(2):486–496, NOV 15 2007. ISSN 0019-1035. doi: {10.1016/j.icarus.2007.04.034}.
- R. Y. Yang, R. P. Zou, and A. B. Yu. Computer simulation of the packing of fine particles. *Physical Review E*, 62:3900, September 2000. doi: 10.1103/PhysRevE.62.3900.
- K. Zahnle, P. Schenk, H. Levison, and L. Dones. Cratering rates in the outer Solar System. *Icarus*, 163:263–289, June 2003. doi: 10.1016/S0019-1035(03)00048-4.
- E. J. Zeller, L. B. Ronca, and P. W. Levy. Proton-induced hydroxyl formation on the lunar surface. *Journal of Geophysical Research*, 71:4855, October 1966.
- J.F. Ziegler, J.P. Biersack, and M.D. Ziegler. *SRIM, the stopping and range of ions in matter*. SRIM Company, 2008. ISBN 9780965420716. URL <http://books.google.com/books?id=JSN63qxPG5MC>.